Informatics Control Measurement
in Economy and Environment Protection

1/2020

Informatyka Automatyka Pomiary

w gospodarce i ochronie środowiska

www.e-IAPGOS.pl

ISSN 2083-0157

Kwartalnik Naukowo-Techniczny

Yuriy Fedkovych Chernivtsi National University
(Chernivtsi, Ukraine)

fot. Andriy Samila

1/2020

styczeń – marzec

Wydanie pod redakcją naukową
prof. dr hab. inż. Waldemara Wójcika

INFORMATYKA AUTOMATYKA POMIARY
W GOSPODARCE i OCHRONIE ŚRODOWISKA
Informatics Control Measurement in Economy and Environment Protection

p-ISSN 2083-0157, e-ISSN 2391-6761, www.e-iapgos.pl

INTERNATIONAL PROGRAMME COMMITTEE – RADA PROGRAMOWO-NAUKOWA

EDITORIAL OFFICE – REDAKCJA

Redakcja czasopisma
Informatyka, Automatyka, Pomiary w Gospodarce i Ochronie Środowiska
Katedra Elektroniki i Technik Informacyjnych
Politechnika Lubelska
ul. Nadbystrzycka 38A, 20-618 Lublin
tel. +48 81 53 84 309, fax: +48 81 53 84 312
iapgos@pollub.pl
www.e-iapgos.pl
iapgos.pollub.pl
ph.pollub.pl/index.php/iapgos

PUBLISHER – WYDAWCA

Politechnika Lubelska
ul. Nadbystrzycka 38D
20-618 Lublin
tel. +48 81 53 84 100
www.pollub.pl
ph.pollub.pl

PRINTING HOUSE – DRUKARNIA

DjaF – Naświetlarnia B1+
ul. Kmietowicza 1/1
30-092 Kraków
http://www.djaf.pl
nakład: 100 egzemplarzy

OTHER INFORMATION – INNE INFORMACJE

Czasopismo jest indeksowane w bazach:

BazTech:	baztech.icm.edu.pl
IC Journals Master List:	www.journals.indexcopernicus.com
Google Scholar	scholar.google.pl
POL-index	pbn.nauka.gov.pl

Czasopismo *Informatyka, Automatyka, Pomiary w Gospodarce i Ochronie Środowiska* zostało objęte finansowaniem przez Ministerstwo Nauki i Szkolnictwa Wyższego w ramach programu *Wsparcie dla czasopism naukowych* w latach 2019-2020.

Czasopismo znajduje się w wykazie czasopism naukowych opublikowanym w Komunikacie Ministra Nauki i Szkolnictwa Wyższego z dnia 31 lipca 2019 r., pozycja 27864 – z przypisaną liczbą punktów przyznawanych za publikację równą 20.

Zasady publikowania artykułów, przygotowania tekstów, zasady etyczne, procedura recenzowania, wykazy recenzentów oraz pełne teksty artykułów dostępne są na stronie internetowej czasopisma:

www.e-iapgos.pl

W celu zwiększenia oddziaływania czasopisma w środowisku naukowym redakcja zaleca:

- w artykułach publikowanych w IAPGOS cytować artykuły z renomowanych czasopism międzynarodowych (szczególnie indeksowanych w bazach Web of Science oraz Scopus) używając oficjalnych skrótów nazw czasopism,
- w artykułach publikowanych w innych czasopismach (zwłaszcza indeksowanych w bazach Web of Science oraz Scopus) cytować prace publikowane w IAPGOS – zwłaszcza posługując się numerami DOI, np.:
  Kluszczyński K. *Modelowanie – umiejętność czy sztuka?* Informatyka, Automatyka, Pomiary w Gospodarce i Ochronie Środowiska – IAPGOS, 1/2016, 4–15, DOI: 10.5604/20830157.1193833.

CONTENTS – SPIS TREŚCI

http://doi.org/10.35784/iapgos.921

APPLICATION OF HURST INDICATOR TO CHOOSE AN ALGORITHM FOR RESOURCE CONTROL OF A TELECOMMUNICATION NETWORK

Anton Vrublevskiy, Ivan Lesovoy, Gennadij Pylypenko
Odessa National Academy of Telecommunication named after O.S. Popov, Department of Telecommunications Systems, Odessa, Ukraine

Abstract. *It has been shown that fuzzy integrals (Sugeno and Shocke) have special properties and are suitable for a fuzzy system for managing the resources of a telecommunication network. The form of choosing a method for calculating the Hurst coefficient in a fuzzy control system for telecommunication network resources is proposed.*

Keywords: traffic, Hurst coefficient, membership function, fuzzy integral, fuzzy measure

ZASTOSOWANIE WSKAŹNIKA HURSTA W SIECI TELEKOMUNIKACYJNEJ DLA WYBORU ALGORYTMU STEROWANIA

Streszczenie. *Wykazano, że całki rozmyte (Sugeno i Shock) mają szczególne właściwości i są odpowiednie dla systemu rozmytego do zarządzania zasobami sieci telekomunikacyjnej. Zaproponowano formę wyboru metody obliczania współczynnika Hursta w systemie sterowania rozmytego dla zasobów sieci telekomunikacyjnych.*

Słowa kluczowe: ruch, współczynnik Hursta, funkcja przynależności, całka rozmyta, miara rozmyta

Introduction

Functioning of telecommunication network is characterized by a number of indicators, such as: parameters of the quality of network operation (packet delay, jitter, packet loss ratio, etc.), and economic parameters (capital costs, operating costs). To ensure functioning of telecommunication network with specified parameters, it is necessary to manage the resources of telecommunication network. A system for managing resources of a telecommunication network means a set of software and hardware that ensures the operation of a network with specified parameters: time delay, packet loss rate, which can be associated with a certain type of traffic on the channel, and with the network load as a whole.

One of the important tasks of ensuring a given quality of service is the control of telecommunication network resources. With increasing traffic intensity TCP overload prevention mechanisms and tools built into the operating systems do not work effectively. A packet is dropped only in the event of actual buffer overflow. This reduces the current traffic, but subsequently leads to a wave-like change in the queue length and causes network overload, which increases jitter and reduces the network bandwidth.

The research in the field of traffic analysis of modern networks with packet switching indicates that data traffic, in contrast to a classical representation of traffic by a Poisson stream, it manifests variability in a wide range of time scales (presents the property of self-similarity).

The algorithms for processing traffic created to work with the simplest threads are not enough effective for streams that have the property of self-similarity.

Thus, a need is required to improve methods for operational resource allocation of the data link multi-service network based on the prediction of the Hurst coefficient and methods for assessing its probabilistic time characteristics in the presence of self-similarity properties of the incoming load.

This will ensure increased efficiency traffic processing in terms of improving indicators such as values of delay, packet loss, and coefficient channel use.

1. Fuzzy traffic management system

The resources of telecommunication network are managed under the conditions of changing the parameters of transmission paths, loading buffers, characteristics of load flows, time intervals, etc. over a wide range. The main reasons for these changes are the constant impact of internal and external factors: the variation in the parameters of the equipment of telecommunication systems, information distribution systems, changes in the conditions of operation of the telecommunication network, etc. This creates multi-criteria uncertainty, which makes it impossible to correctly solve the problem of optimal management of telecommunication network resources without taking into account the interests of stakeholders.

The important factor in managing the resources of telecommunication network is a degree of congestion of output interfaces of routers, which determines expediency of dropping a packet or directing it over a longer route on which the buffers are not so loaded. In the process of managing resources, it is advisable to take into account not only the distance, but also the load dynamics of output buffer of the drive corresponding to the interface and a number of other factors.

Usually, when studying a telecommunication network, to establish the connection between the total (full) assessment of an object and the partial estimates of the constituent elements, the object under study is decomposed into its constituent elements and a linear mathematical model is applied:

$$z = \sum_{i=1}^{n} a_i h(x_i),$$

where $U = \{x_1, x_2, ..., x_n\}$ is the set of information elements, function $h{:}U \to [0,1]$ represents measurement results of information elements, and a_i are constants expressing the coefficients of importance of the corresponding information elements. The linear criterion is a weighted sum of particular criteria.

However, a different mathematical model is needed for the tasks of managing the resources of a telecommunication network in fuzzy conditions. The fuzzy Sugeno integral [3, 11] can be used as a mathematical model.

The control algorithm based on fuzzy logic allows taking into account the influence of many factors when managing the resources of a telecommunication network. The main advantage of fuzzy regulators for a telecommunication network resource management system is the use of qualitative information, which cannot be formalized when traditional management methods are implemented, the low sensitivity of fuzzy regulators to disturbances in a certain range and better characteristics compared to classical regulators.

The resource management in a telecommunication network is carried out with fuzzy parameters, in real time. Given convenience of formalizing information about procedures and conditions for their use, when describing the knowledge, it is advisable to use a set of fuzzy production rules. Each fuzzy production rule allows putting a certain action in accordance with the current situation.

The main difficulty in creating a resource management system for a telecommunication network based on fuzzy logic is that changing the parameters of a telecommunication network (control object) entails modifying the control rules with their subsequent iterative adjustment, which takes time.

There is a problem of ensuring the optimal characteristics of telecommunication network resource management system and, in particular, their stability and dynamics. In order to dynamically manage the resources of a telecommunication network, special technical tools are needed that adapt to constantly changing conditions, that is, adaptive control systems. The main goal of adaptation or adaptive management of telecommunication network resources is to improve the quality of service in the changing conditions of its operation.

A promising direction in the development of fuzzy regulators is the creation of adaptive and self-organizing fuzzy regulators. In the process of managing the resources of a telecommunications network, a fuzzy adaptive controller, based on traffic prediction, status of information distribution devices and transmission paths, determines the values of parameters necessary to stabilize the quality of service at a given level.

In order to dynamically control the resources of telecommunication network, special technical tools are required that adapt to changing conditions, that is, adaptive control systems. The main purpose of adaptation or adaptive management of telecommunication network resources is to improve the quality of service in terms of its operation.

The advantage of fuzzy regulators for a telecommunication network resource management system is the use of qualitative information, which cannot be formalized when traditional management methods are implemented, the low sensitivity of fuzzy regulators to disturbances in a certain range and better characteristics compared to classical regulators. In the process of managing the resources of telecommunication network, a fuzzy adaptive controller, based on the prediction of the status of information distribution devices and transmission paths, determines the values of parameters necessary to stabilize the quality of service at a given level. The main difficulty in creating fuzzy regulators is that changing the parameters of the telecommunication network (control object) entails modifying the control rules with their subsequent iterative adjustment, which takes time.

Self-similarity of traffic is manifested in the fact that with the increase in aggregation interval, the traffic structure of lower levels of hierarchy is preserved and, as a rule, depends on efficiency of the use of transmission paths [2, 4, 5, 6, 8, 10, 12]. The presence of self-similarity or scale invariance allows forecasting, by analyzing the traffic over a relatively short period of time, to predict its behavior over longer time intervals [7]. These forecasts can be used to select the method of managing the resources of a telecommunication network in the presence of traffic surges for its efficient operation.

Hurst index H, which is a measure of self-similarity of the stochastic process, allows estimating the traffic self-similarity, takes values from 0 to 1 and allows establishing the difference between random processes with independent increments (at $H = 0.5$), with statistically dependent values, manifestation. There is a so-called persistent (supporting) behavior ($H > 0.5$), and with statistically dependent values that show anti-persistent behavior ($H < 0.5$).

There are several methods used to determine the Hurst index: analysis of R/S statistics, analysis of variance changes, first analysis, analysis of the auto-correlation function, Whittle estimation, analysis based on the wavelet function, and analysis of the dispersion index for samples. The value of Hurst coefficient can be determined using the methods:

- theory of probability;
- statistical theory;
- based on the theory of fuzzy sets (fuzzy measures).

It should be noted that when studying the same experimental traffic data, the value of Hurst index depends on the estimation method, sample size, the number of load sources, etc.

To calculate the Hurst coefficient by a probabilistic method, it is necessary to know the density of its distribution in the H_E region. In order to determine the value of Hurst coefficient by a statistical method, with an acceptable probability, a sufficiently large sample is necessary. As a rule, in traffic control problems, the law of distribution of the Hurst index in a region is not defined, and a full sample of data, that is, complete information about the behavior, its value in a given region is also absent. Therefore, in a fuzzy system for managing the resources of a telecommunication network, an assessment of the value of Hurst index is advisable to be carried out using the theory of fuzzy sets.

For each current value of the input variable, the degree of belonging (truth value) to these terms (fuzzy sets) characterizing a specific linguistic variable is determined. Each of these fuzzy subsets consists of elements along with their degrees of belonging. The number of terms j for each linguistic variable is desirable to choose the same.

The graphs of membership functions (MF) of fuzzy sets may have a different shape depending on the preferences and developer experience. In the tasks of managing the resources of a telecommunication network based on fuzzy logic, it is advisable to use simple linear and triangular membership functions, which simplify the calculations.

We write the membership function in the form

$$\mu(X) = \sum_i \mu_i / x_i$$

where: $\sum$ – the union of elements; μ_i – the degree of belonging of the element x_i to the set.

If the distribution of the fuzzy density of weights of these values $g(H_j)$, $H_j \in H_E$ is determined a priori, by means of an examination, it is possible to determine the expected value of the Hurst coefficient H_j from the H_E region from the experimental results using the fuzzy integral.

2. Fuzzy integral

Fuzzy integral is a non-linear functional. By analogy with the mathematical expectation of probability theory, a fuzzy integral is sometimes called a fuzzy mathematical expectation. The fuzzy Sugeno integral of the function h on the set U by a fuzzy measure g is determined from the expression

$$\int h \circ g = \sup\left(a \wedge g\left(F_a\right)\right),\ F_a = \left\{x \in U : h(x) \geq a\right\},\ a \in [0,1]$$

where the symbol $\int$ – denotes a fuzzy integral, $\circ$ – is the sign of the composition.

Let the integration be performed on the set $A \subseteq U$, then the fuzzy integral describes the expression

$$\int_A h(x) \circ g = \sup\left(a \wedge g\left(A \cap F_a\right)\right),\ a \in [0,1]$$

For a set of information elements $U = \{x_1, x_2, \ldots x_n\}$, fuzzy integral

$$(h(x_i) \wedge g(E_i)),\ E_i = \{x_i, \ldots, x_n\},$$

$$a_i = \max\{a_i\},$$

if the condition is met $h(x_i) \leq \ldots \leq h(x_n)$, and

$$(h(x_i) \wedge g(E_i)),\ E_i = \{x_1, \ldots, x_i\} \text{ if a } h(x_1) \geq \ldots \geq h(x_n).$$

The fuzzy integral of the function h over a fuzzy measure g is a general estimate in the form of a non-linear convolution of the partial estimates of information elements, but it does not exclude the possibility of information elements interconnection.

If the posteriori membership function of a region is determined, then the most expected value of H_j is determined by the expression [3]

$$H = \arg \int_{H_\ni} h(H_j) \circ g(F_j),$$

where $\int$ – is the sign of a fuzzy integral; ∘ – sign of the composition; $h(H_j)$ is the function of the membership function ordered in descending powers $\mu(H_j)$; $g(F_j)$ is a fuzzy measure of a set

$$F_j = < H_{j1}, H_{j2}, ..., H_{ji} > .$$

The procedure for calculating a fuzzy integral for U which is a finite set $U = \{x_1, ... x_n\}$ is laid down in its definition:

$$(h(x_i) \wedge g(E_i)),$$

$$E_i = \{x_i, x_{i+1}, ,, x_n\},\ E_1 \supset E_2 \supset ... E_n, E_1 = U.$$

$$\int h(x) \circ g = h(x_i) \wedge g(E_j),$$

then and only then ever

$$h(x_{j-1}) \le g(E_j) \le h(x_j).$$

or

$$g(E_{j+1}) \le h(x_j) \le g(E_j).$$

Thus, the value of a fuzzy integral can be obtained without calculating

$$h(x_i) \wedge g(E_i)$$

for all i.

Let as a result of traffic analysis using the R/S statistics estimation method, the value of the Hearst coefficient $H_1 = 0.84$ is obtained; method of estimating the spectral functions $H_2 = 0.93$ and the method of estimating the correlation coefficient $H_3 = 0.65$. In order to determine the most possible value of the Hurst coefficient, we calculate the fuzzy integral.

Let the following membership function be known, written according to:

$$\mu(H_j) = 0.84/0.4 + 0.93/0.9 + 0.65/0.8$$

Ordered by decreasing powers membership function

$$h(H_j)\text{: } h(H_2) = 0.9;\ h(H_3) = 0.8;\ h(H_1) = 0.4.$$

Fuzzy measures:

$$g(F_1) = 0.5;\ g(F_2) = 0.81;\ g(F_3) = 0.75.$$

To this end, the ordering of of the function h value, we make the change of variables, taking

$$y_1 = H_1, y_2 = H_3, y_3 = H_2.$$

Then, $h(y_1) < h(y_2) < h(y_3)$ and according to the definition of a fuzzy integral, we calculate

$$h(y_i) \wedge g(E_i), E_i = \{y_1, ..., y_3\}, i = 1,2,3.$$

$$when\ i = 1, h(y_1) \wedge g(E_1) = 0.4 \wedge 1.0 = 0.4.$$

$$when\ i = 2, h(y_2) \wedge g(E_2) = 0.8 \wedge 0.81 = 0.8.$$

$$when\ i = 3, h(y_3) \wedge g(E_3) = 0.9 \wedge 0.75 = 0.75.$$

Consequently,

$$(h(y_i) \wedge g(E_i)) = \max(0.4; 0.8; 0.75) = 0.8$$

Thus, the most possible value of the Hurst coefficient is 0.65 with an expected measure of 0.81. Therefore, the fuzzy adaptation system will perform the calculation of the Hurst coefficient by the method of estimating the correlation coefficient.

In order to determine the most expected value of H_j for continuous functions, according to [1], it is possible to present it graphically (Fig. 1).

The solution of the fuzzy integral allows us to determine [1]:

- the expected fuzzy measure of the set NOT;
- the most likely value of the Hurst coefficient in the area is NOT with its fuzzy estimate;
- coefficient value (the boundary of the region is NOT into two sub-regions H_1 and H_2).

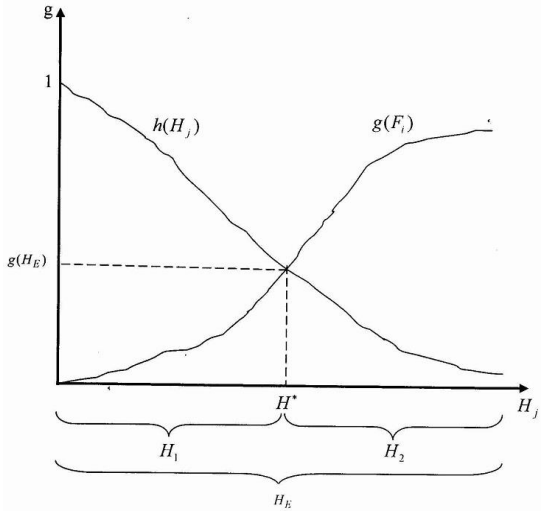

Fig. 1. Graphic solution of a fuzzy integral

Knowing this limit allows you to specify the most likely value of the Hurst coefficient obtained from the results of the experiment.

For a graphical solution of a fuzzy integral, we construct a graph applying the traffic analysis data using the method of estimating R/S statistics; the value of the Hurst coefficient $H_1 = 0.84$; method of estimating the spectral functions $H_2 = 0.93$ and the method of estimating the correlation coefficient $H_3 = 0.65$.

Let the following membership function be known, written according to:

$$\mu(H_j) = 0.84/0.4 + 0.93/0.9 + 0.65/0.8.$$

Ordered by decreasing powers membership function

$$h(H_j)\text{: } h(H_2) = 0.9;\ h(H_3) = 0.8;\ h(H_1) = 0.4.$$

Fuzzy measures:

$$g(F_1) = 0.8;\ g(F_2) = 0.5;\ g(F_3) = 0.75.$$

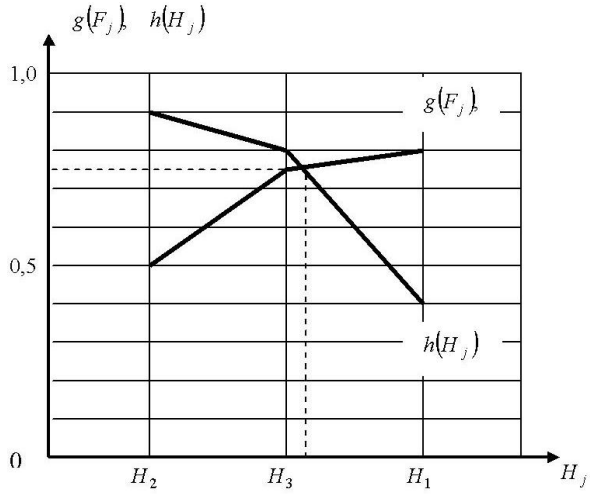

Fig. 2. An example of a graphical determination of the most possible value of H using a fuzzy integral

Many properties of telecommunication networks are fuzzy, which makes fuzzy methods applicable for monitoring their parameters. Fuzzy analysis is more efficient than traditional data processing methods, which are usually inaccurate and ambiguous. Fuzzy methods are able to classify model errors in a non-dichotomous way, similar to the way a person processes inaccurate information. The concepts of fuzzy measure and fuzzy integral are taken from the classical theory of sets, the theory of fuzzy sets and the theory of measure.

The important properties of fuzzy measures and fuzzy integrals are the ability to reflect the importance of criteria and to represent certain interactions between the criteria. Fuzzy measures

and fuzzy integrals may reflect the importance of criteria and represent certain interactions between the criteria. These properties make fuzzy measures and fuzzy integrals the most rational for choosing the function and mechanisms of state and control of a telecommunication network.

Fuzzy integrals (Sugeno and Choke) are suitable for managing the resources of a telecommunication network [10]. The use of a fuzzy integral is constrained by the difficulty of defining a fuzzy measure.

3. Conclusion

The presence of self-similarity or scale invariance allows forecasting, by analyzing traffic over a relatively short period of time, to predict its behaviour over longer time intervals. These forecasts can be used to select the method for managing the resources of a telecommunication network in the presence of traffic surges to ensure its efficient operation.

The application of the Hurst index in order to select the algorithm for managing the resources of a telecommunication network requires the complex use of fractal analysis methods in the study of time series of small length.

The fuzzy analysis is more efficient than traditional data process-sing methods, which are generally inaccurate and ambiguous. Fuzzy methods allow us to classify model errors in a nondichotonous way, which is similar to the way human information is processed.

Fuzzy measures and fuzzy integrals provide an insight into the importance of each parameter and some of the relationships between parameters. These properties allow the fuzzy measure and the theory of fuzzy integrals to apply in adaptive systems for managing resources of a telecommunication network based on fuzzy logic.

References

[1] Bychkov Ye. D.: Prilozheniye teorii nechetkikh (FUZZY) mnozhestv v matematicheskikh modelyakh sistem svyazi. Izd-vo Omskoy Gos. Med. Akademii, Omsk 2000.

[2] Dang T. D., Sonkoly B., Molnar S.: Fractal Analysis and Modelling of VoIP Traffic. NETWORKS-2004. Vienna. Austria. 2004, 95–104.

[3] Dubois D., Prad H.: Fuzzy Sets and Systems: Theory and applications. Acad. Press, New York 1980.

[4] Ghaderi M.: On the Relevance of Self-Similarity in Network Traffic Prediction. School of Computer Science, University of Waterloo, Waterloo 2003.

[5] Ilnickis S.: Research of the Network Server in Self-Similar Traffic Environment. Scientific proceedings of Riga Tecnical University Telecommunication and Electronics. Computer Science l/2004, 78–81.

[6] Karasaridis A., Hatzinakos D.: Network Heavy Traffic Modeling Using a-stable Self-Smilar Process. IEEE Transactin on Communications 49(7)/2001, 1203–1214.

[7] Neyman V. I.: Novoye napravleniye v teorii teletrafika. Elektrosvyaz' 7/1998, 27–29.

[8] Osin A. V.: Vliyaniye samopodobnosti rechevogo trafika na kachestvo obsluzhivaniya v telekommunikatsionnykh setyakh. PhD thesis, Moscow 2005.

[9] Pospelov D. A.: Nechetkiye mnozhestva v modelyakh upravleniya i iskusstvennogo intellekta. Nauka, Moscow 1986.

[10] Shelukhin O. I. (red.): Fraktal'nyye protsessy v telekommunikatsiyakh. Radiotekhnika, Moscow 2003.

[11] Sugeno M.: Fuzzy measures and fuzzy integrals: a survey. Fuzzy automata and decision processes. North-Holland Publishning Company, Amsterdam 1977, 89–102.

[12] Tsybakov B. S., Georganas N. D.: Self-Similar Processes in Communications Networks. IEEE Trans. on Information Theory 44(5)/1998, 1713–1725.

M.Sc. Anton Vrublevskiy
e-mail: vrublevskiyar@gmail.com

Vrublevskiy Anton Romanovych postgraduate student of the department of Telecommunication Systems, Institute of Information and Communication Technologies and Computer Engineering of Odessa National Academy of Telecommunications, the name of A.S. Popov. Author of 11 scientific works. Research interests is packet network traffic management on the fuzzy logic base.

http://orcid.org/0000-0002-6488-3418

D.Sc. Ivan Lesovoy
e-mail: ur5fo55@gmail.com

Lesovoy Ivan Pavlovich doctor of Technical Sciences (2005), Professor (2008). Professor of the Department of Telecommunication Systems, Institute of Information and Communication Technologies and Computer Engineering of Odessa National Academy of Telecommunications the name of A.S. Popov. Author of more than 100 scientific works, including 10 monographs, 5 textbooks. Research interests: fuzzy logic in telecommunications, digital processing and signal generation in telecommunication systems.

http://orcid.org/0000-0002-3807-2099

M.Sc. Gennadij Pylypenko
e-mail: gvpilipenko@gmail.com

Pylypenko Gennadij Viktorovych postgraduate student of the department of Telecommunication Systems, Institute of Information and Communication Technologies and Computer Engineering of Odessa National Academy of Telecommunications, the name of A.S. Popov. Author of 9 scientific works. Research interests is packet network traffic management on the fuzzy logic base.

http://orcid.org/0000-0002-8635-9019

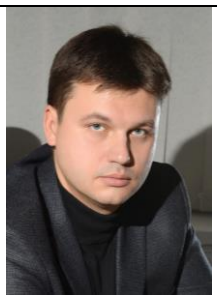

otrzymano/received: 15.11.2019 *przyjęto do druku/accepted: 15.02.2020*

http://doi.org/10.35784/iapgos.919

BLOCK CIPHERS ON THE BASIS OF REVERSIBLE CELLULAR AUTOMATA

Yuliya Tanasyuk, Petro Burdeinyi
Yuriy Fedkovych Chernivtsi National University, Department of Computer Systems and Networks, Chernivtsi, Ukraine

Abstract. *The given paper is devoted to the software development of block cipher based on reversible one-dimensional cellular automata and the study of their statistical properties. The software implementation of the proposed encryption algorithm is performed in C# programming language in Visual Studio 2017. The paper presents specially designed approach for key generation. To ensure a desired cryptographic stability, the shared secret parameters can be adjusted in order to contain information needed for creating substitution tables, defining reversible rules, and hiding the final data. For the first time, it is suggested to create substitution tables based on iterations of a cellular automaton that is initialized by the key data.*

Keywords: block cipher, symmetric encryption algorithm, reversible cellular automata

SZYFRY BLOKOWE NA PODSTAWIE ODWRACALNYCH AUTOMATÓW KOMÓRKOWYCH

Streszczenie. *Niniejszy artykuł poświęcony jest rozwojowi oprogramowania szyfrów blokowych opartych na odwracalnych jednowymiarowych automatach komórkowych oraz badaniu ich właściwości statystycznych. Zastosowanie oprogramowania w proponowanym algorytmie kodowania wykonywane jest w języku programowania C# w Visual Studio 2017. Artykuł przedstawia specjalnie zaprojektowane podejście do generowania klucza. Aby zapewnić pożądaną stabilność kryptograficzną, dostosowane mogą zostać wspólne tajne parametry w taki sposób, aby zawierały informacje wymagane dla stworzenia tabel substytucyjnych, określające zasady odwracalne oraz ukrywające dane końcowe. Po raz pierwszy, proponowane jest tworzenie tabeli substytucyjnych w oparciu o iterację automatów komórkowych, które zostają zainicjowane poprzez dane klucza.*

Słowa kluczowe: szyfr bloku, algorytm szyfrowania symetrycznego, odwracalny automat komórkowy

Introduction

The increased use of computers, converged networks with high-speed Internet access and IoT deployment resulted in an urgent need for means to protect information and to provide various security services. Encryption is known to be a primary method of protecting valuable electronic information. A cryptographic algorithm, or cipher, is a set of well-defined but complex mathematical instructions used to encrypt or decrypt data. The encryption and decryption processes depend on a cryptographic key selected by the parties participating in the communication process. Typically, details of the algorithm are publicly open. However, operation of the algorithm and security of the encrypted message relies on the cryptographic key used in the encryption and decryption process.

The transformation of a message from plaintext to cipher-text occurs through a substitution or a transposition process, or a combination of both. A substitution cipher replaces a digit or a data block in a message with another arbitrarily chosen digit or data portion. A transposition cipher implies different permutations of a data block. Based on how cryptographic algorithms are applied on the plaintext, they are categorized as block ciphers and stream ciphers.

As the name implies, the block ciphers work on a fixed-length segment of plaintext, typically a 64- or 128-bit block as input, and produces a fixed length cipher text, usually of the same size as the input. The message is broken into blocks, and each block is processed in the same manner. Where there is insufficient data to fill a block, the blank space will be padded prior to the encryption. Block ciphers are mostly used in the symmetric key encryption. DES, Triple DES and AES are some of the well-recognized examples of block ciphers [4, 7].

Cellular automata (CA) are typically considered as a regular grid of cells, with each presenting a finite number of possible states. These automata cells are modified independently by the transition function on a discrete time step. The application of the function to each cell in the grid leads to the next generation for the grid. The outcome of the transition function depends on states of the cell itself and of their neighbors. Every cell follows the same rule for determining these transitions. Types of their interaction are simple and diverse, while their implementation imposes low demands for computational complexity. Some of the CAs are reversible, enabling one to restore the information processed through direct transformations [7].

1. Reversible cellular automata

A number of papers are dedicated to the application of CA in cryptography [1–3, 5–7]. Namely, they are considered as promising candidates for symmetric and asymmetric enciphering. Security of the latter was based on the complexity to solve non-linear polynomial equations. Stream enciphering with the use of CA was first proposed by Wolfram [11]. The idea consists in usage of CA as the generator of pseudorandom numbers. The considerations were further embodied in the algorithms, developed by Seredynski [7] and Tomassini [8]. The block cipher using both reversible and irreversible rules was reported in [1, 3].

As a dynamic system CA can be represented as follows [7]:

$$A = \{S, Z^d, f, V\}, \tag{1}$$

where S is a finite number of states; Z is the set of integers; d is the size of automation; Z^d is the space of CA (the number of cells), f is a rule (transition function), V is the set of neighbours (including the current cell and the neighbours involved in interaction).

The simplest CA can be represented as one-dimensional array of 0 and 1, as the states of cells. Each cell has its network environment of three cells: left, right and a current cell itself. Normally, finite CA are used with cyclic edge conditions, when the first and the last cells are treated as neighbours. The CA consists of a number of steps. When calculating the next state of a cell, the step changes. In order to execute the next function of the state, three states of the interacting cells are applied as an input, producing the next state of the cell on the output.

A CA space denotes the number of the cells, which are updated according to some rule f [11]. In total, the 256 rules of CA interaction are defined. For example, the rule 30 in terms of Boolean functions is given as follows:

$$C[i]' = C[i\text{-}1] \oplus (C[i] \vee C[i+1]) \tag{2}$$

where C[i] is a current cell, C[i]′ is the value of the current cell after the rule application, C[i-1], C[i+1] are previous and next neighbor cells, and ⊕, ∨ denote the bitwise XOR and OR operations, respectively. As shown in Fig. 1, the rule 30 is called so since all possible combinations of cell states at step t produce a sequence of 00011110 which when converted to the decimal system gives a value of 30.

t	1	1	1	1	1	0	1	0	1	1	0	0	0	1	1	0	1	0	0	0	1	0	0	0
t + 1		**0**			**0**			**0**			**1**			**1**			**1**			**1**			**0**	

Fig. 1. CA cell states resulted from application of rule 30

Some CA rules possess an interesting property of being reversible, providing not only a direct but also a reverse iteration. When applying reversible rule, this enables the CA getting back to the initial state. To be applicable for cryptographic purpose the reverse rules must comply with the following criteria: they must be numerous and exhibit complex behavior. When analyzing elementary CA, it turns out that only a small number of rules are known to be reversible. For example, of all the 256 elementary radius rules, only six are stated to be reversible. In addition, their behavior is very simple [3, 7]. For this reason, standalone elementary reversible rules cannot be used for encryption.

In order to accomplish this task, it is proposed to use a class of reversible rules, first described by Wolfram in [9, 11]. Each rule belonging to this class can be described by two elementary CA transition rules. The first one determines the state of transition in the case when at step *t*-1 the cell is in the state of 0, and the second rule applies for the cell state of 1. These two rules depend on each other. By knowing one rule, we can derive another one using the following formula:

$$R_2 = 2^n - R_1 - 1, \tag{3}$$

where R is the elementary rule; n is the neighborhood of the cell. Fig. 2. shows the reversible rule consisting of rule 57 $(00111001)_2$ and 198 $(11000110)_2$, inverse to it.

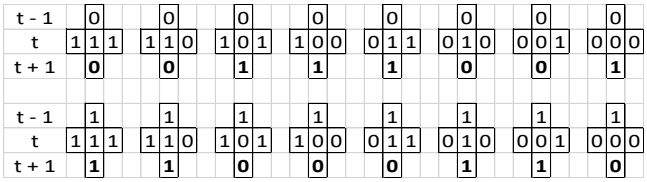

Fig. 2. Reversible rule, including CA transformation rules 57 and 198

2. Cryptographic application of the reversible CA

Since the reversible rule depends on a previous step, the initial state of the CA must consist of two consecutive configurations. The text to be encrypted comes as a second configuration, while the first configuration is populated with random data (Fig. 3). Traditionally, the encryption is performed by direct iteration of the CA. However, the final outcome consists of two configurations and both of them must be used in the decryption. The first is encrypted text and the second is called the final data. During decryption, these operations are executed in reverse order [10].

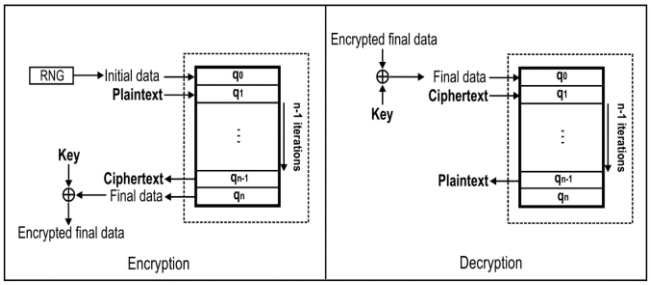

Fig. 3. Basic scheme of encryption and decryption process [9]

A rule used for both encryption and decryption is considered as a secret key. The end data must be kept in secret, since knowing two consecutive configurations (end data and encrypted message) one can easily define the rule, applied for the encryption.

There are two approaches for processing the final data generated in the encryption process. The most secure one assumes that this information is kept private, and therefore it becomes a part of a key. Now, the key consists of the rule and final configuration. The drawback of this option is that after each encryption the key is to be changed and shared with the message recipient. According to the second option the end data is encrypted with the use of Vernam algorithm [5] applying logical bitwise operation of XOR to the final data and the key portion as follows:

$$efd_i = k_i \oplus fd_i, \tag{4}$$

where k_i is the *i*-th bit of the key, fd_i is the *i*-th bit of the end data, efd_i is the *i*-th bit of the encrypted end data, $\oplus$ denotes XOR operation.

Now, the encrypted final data should be no longer kept in secret and can be added to the cipher text.

3. Software implementation of the block cipher on the basis of reversible one-dimensional CA

The paper aimed at development of the block cipher on one-dimensional CA, processed by reversible CA transformation rules. Software implementation of the proposed encryption algorithm has been performed in the C# programming language in the integrated application development environment of Visual Studio 2017.

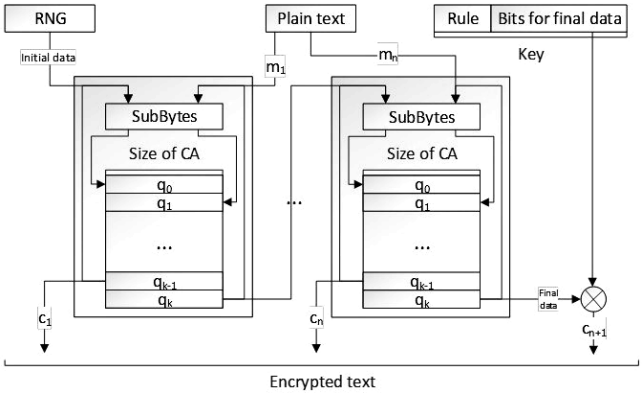

Fig. 4. Generalized representation of the chosen encryption approach

The designed algorithm uses the single reversible one-dimensional CA and the corresponding rules. To achieve basic cryptographic strength, we have proposed a novel approach to key formation, when the rule to use for CA transformation and specific bits for concealing the final data are contained inside the key. Depending on the needs the rule may be implemented with different radii (1, 2, 3). The larger the radius of the rule, the more time the calculations take, yet producing more tangled output.

The block size may acquire values of 128, 256 and 512 bits. The key may be 384, 512 or 640 bits long. The standard algorithm leans upon one reversible rule, however, its modification implies utilization of several transition functions. The number of iterations and rounds may vary. The size of CA equals the doubled size of the block, since the reversible rule depends not only on the neighbours on the right or left, but on the state of the cell at previous iteration. Schematically, the implemented encryption algorithm is shown in Fig. 4.

To utilize the algorithm, input messages are read and padded to the size multiple of the block *S* size. Then some random value (Initial data) of *S* bits in size is generated. The CA is initialized with this initial data and a block of information to be encrypted (m_1).

Before being supplied to the CA, the data undergo procedure of byte substitution, denoted as SubBytes, with the use of the AES substitution tables. The algorithm implies utilization of the alternative substitution tables which should be generated and transmitted together with the secret key. After that, the CA is processed with the reversible rule of radius 3 obtained from the key. The *h* rounds produce a portion of encrypted information (c_1) and data that can be used to initialize the cellular automaton when encrypting the next block of information. In this way all blocks of information are encrypted. The last piece of the encrypted message (c_n), i.e. final data, should be hidden because their discovery may provide a clue for deciphering all the information. For this reason, XOR operation is additionally applied to the final data and specific bits of the key, producing the outcome which supplements the encrypted message (c_{n+1}) [7].

The decryption algorithm includes the same steps of the encryption algorithm in the reverse order.

4. The function creating a key and substitution tables

The cryptographic key consists of the following components:

- bits for initialization of the CA, generated by the substitution tables (128 bits);
- CA rules with the radius of 3 (128 bits);
- special bits for hiding the CA final data (the size is equal to the block size).

The size of the key is calculated using a formula:

$$L = 128 + 128 + S, \tag{5}$$

where S is the size of the block.

Thus, the key may be 384, 512 or 640 bits long.

For key generation the System.Security.Cryptography module of NET Framework has been used. The data generated, experience 1000 iterations on the CA with rule 30 and radius 1. As a result, the encryption key of the algorithm is obtained.

The function of substitution tables formation creates two S-Box tables and one Inverse S-Box, providing protection against attacks based on simple algebraic properties. In fact, this is an example of common cipher of the simple substitution.

The substitution tables are generated on the basis of the CA operating with the application of rule 30 with the radius 1 and the key bits used for the CA initialization (Fig. 5).

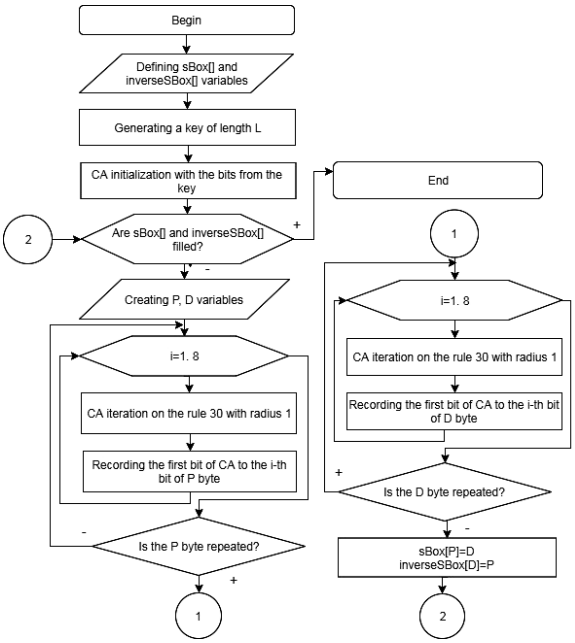

Fig. 5. The flow chart of generating substitution tables using the reversible CA

The procedure forming the substitution tables is as follows. First, the CA is initialized with the specific part of the key to generate the tables. The CA are processed until direct and inverse tables are completed.

With each iteration the first bit of CA is written to form a location byte P, pointing to a cell in the substitution table. If this cell appears to be already used, new location byte will be generated. After the location byte is formed, another byte D is derived. If its value is already in use, a new byte value will be formed. In parallel, the inverse substitution table is created. In this table the byte-value (D) becomes a location byte (P) and vice versa. As a result, two inverted substitution tables are formed. Repeating this function forms the identical substitution tables.

Depending on demands, the designed algorithm can be easily modified. The key comprises additional reversible CA rule with radius 3 to be applied. Eq. 5 used to calculate the key size is altered as follows:

$$L = 128 + 128N + S, \tag{6}$$

where N is the number of the additional reversible CA rules.

5. Scattering properties of the designed block cipher

Pseudorandom behavior is generally considered as a good indicator of a secure block cipher. We have used a technique of NIST STS statistical testing in order to check randomness properties of the developed encryption algorithm. Good encryption algorithm should also satisfy the Strict Avalanche Criterion [6]. This means that each output bit should change with a probability of one half when-ever a single input bit is complemented.

Investigation of the scattering properties of the block cipher based on reversible one-dimensional cellular automata has been performed on the binary file of 12.3 MB resulted from the programmed encryption procedure through the designed algorithm applied to cellular automata of the corresponding length. The statistical suit of NIST STS v.2.1.2 divided generated binary sequences into 100 equal parts of 10^6 bits each. The bit strings were tested against 15 statistical tests with different parameters. The randomness properties were assessed in terms of probability of the tests being passed. As a result, a vector of 189 values of probability was formed. Ideally, only one sequence out of a hundred can be rejected, providing a coefficient of the test passing of 99%. However, this requirement is rather strict. In most cases the evaluation is conducted within a confidence interval, the lower limit of which is assumed to be at the level of 96% [10].

The following initial parameters were used during the testing:

- binary file of 12.3 MB;
- sequences of 103.4 Mbits.

The performance of the selected set of transformations was evaluated on a following hardware platform: AMD Athlon X4 740 Quad Core Processor 3.2 GHz, AMD Radeon HD 7700 (1050 MHz), 8 GB RAM.

When studying the block cipher encryption algorithm based on reversible one-dimensional cellular automata, we used a combination of one (RCA1), two (RCA2) and three (RCA3) reversible rules with a radius of 3. The results presented in Table 1 consider the block size of 256 bits, 5 processing rounds and 5 iterations.

Table 1. Statistical and performance parameters of the designed block ciphers

Parameters	RCA1	RCA2	RCA3
The number of tests passed by at least 99% of the sequences	68.6%	72.3%	73.9%
The number of tests passed by at least 96% of the sequences	100%	99.5%	99.5%
Minimal proportion of the tests passed	96%	95%	95.5%
12.3 MB file encryption time	7 min 55 sec	15 min 22 sec	23 min 26 sec

Fig. 6. shows the results of the conducted statistical testing. The obtained data prove that the least ratio of bit sequences that successfully passed the tests, is at the level of 96% – 97%, pointing out satisfactory scattering properties of the developed encryption algorithm.

Investigating scattering properties of the proposed block cipher built on the basis of reversible one-dimensional cellular automata with NIST STS revealed the applying three transformation rules to be most effective. Inclusion of additional processing rules to the algorithm ensures better scattering properties. However, the most optimal in terms of performance and statistical properties is a one-way design with a radius of 3, using 5 rounds and 5 iterations. Avalanche effect investigations should be further performed.

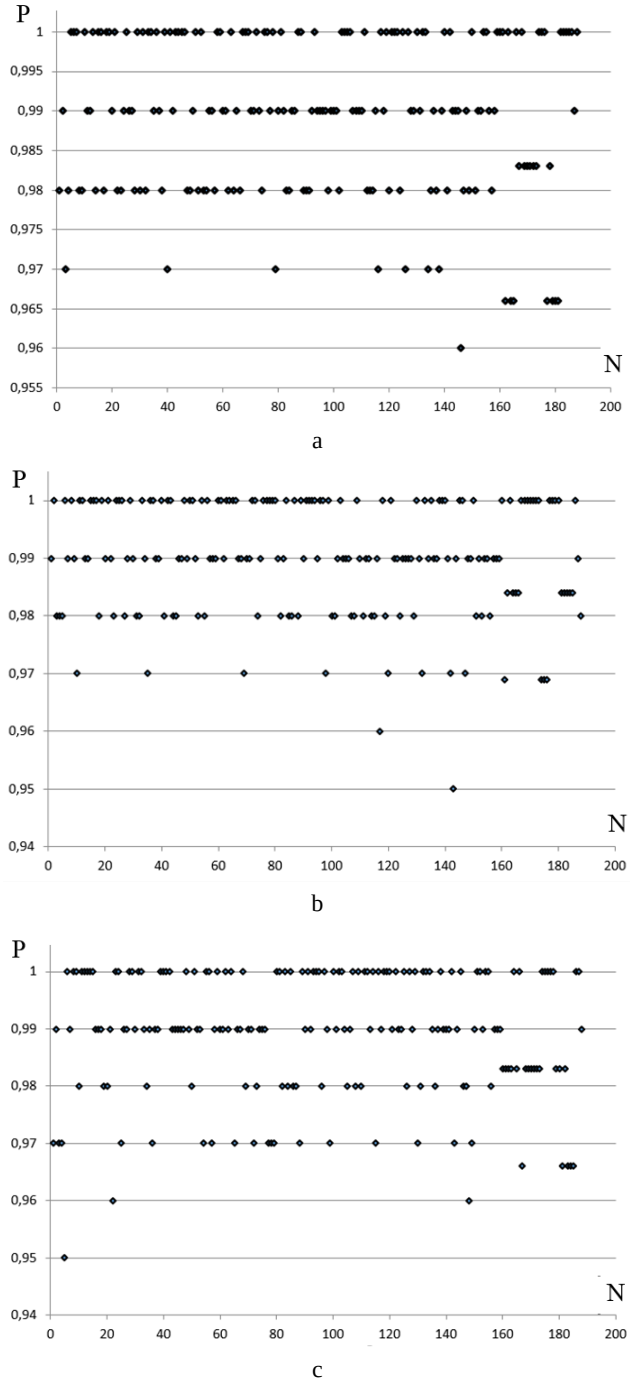

Fig. 6. Statistical portraits of the block cipher on the reversible one-dimensional CA, processed by one (a), two (b) and three (c) transformation rules with a radius of 3. The block is 256 bits long. The chosen reversible rules were applied for 5 round including 5 iterations. N is a number of a test, P is the portion of sequences under study that passed the test

6. Conclusions

Thus, summarizing the investigations carried out, the following conclusions can be made:

1) By means of the C# programming language, a software implementing the block cipher on reversible one-dimensional cellular automata has been developed, which allows to process files of arbitrary types.
2) In order to ensure the cryptographic stability, a key generation approach has been developed. The key is designed to contain information about processing rules, data to create substitution tables, and information to hide the final data.
3) For the first time we have proposed to form substitution tables based on iterations of the cellular automaton, initialized by the key data. This may allow for additional protection against attacks in case when the applied reversible rules are revealed.
4) To enhance cryptographic strength, the basic encryption algorithm with the use of single one-dimensional CA and one reversible rule with radius 3 can be complemented with two or three reversible rules.
5) The created block cipher design uses blocks of 128, 256, 512 bits, and allows one to generate the keys of 384, 512 and 640 bits.
6) Investigations of the scattering properties of the block cipher based on one-dimensional CA using NIST STS statistical tests revealed that the minimum portion of studied bit sequences, meeting the requirements of the tests, fell within 96% – 97%, indicating the qualitative statistical characteristics of the developed cryptosystem.
7) According to the research conducted, for the same number of processing rounds, the use of three reversible rules with a radius of 3 appeared to be most effective, ensuring better scattering characteristics. However, in terms of performance a one-rule design with a radius of 3, turned out to be more appropriate.

References

[1] Bouchkaren S., Lazaar S.: A fast cryptosystem using reversible cellular automata. International Journal of Advanced Computer Science and Applications 5(5)/2014, 207–210.
[2] Debasis D., Abhishek R.: A parallel encryption algorithm for block ciphers based on programmable reversible cellular automata. J. Computer Science and Engineering 1(1)/2010, 82–90.
[3] Gutowitz H.A.: Cryptography with Dynamical Systems: Cellular Automata and Cooperative Phenomena. Kluwer Academic Press, Dordrecht 1993.
[4] Paar C., Peltz J.: Understanding cryptography. Springer-Verlag, Berlin Heidelberg 2010.
[5] Leporati A., Mariot L.: Cryptographic properties of bipermutive cellular automata rules. J. Cellular Automata 9/2014, 437–475.
[6] Seredynski M., Bouvry P.: Block cipher based on cellular automata. New Generation computing 23(3)/2005, 245–258.
[7] Seredynski F., Bouvry P., Zomaya A. Y.: Cellular automata and secret key cryptography. Parallel Computing 30(5-6)/2004, 753–766, [http://doi.org/10.1016/j.parco.2003.12.014].
[8] Tomassini M., Perrenoud M.: Stream Cyphers with One- and Two-Dimensional Cellular Automata. Parallel Problem Solving from Nature PPSN VI. PPSN. Lecture Notes in Computer Science 1917. Springer, Berlin, Heidelberg, 2000, 722–731.
[9] Wolfram S.: Cryptography with Cellular Automata.: Advances in Cryptology: Crypto'85, Springer-Verlag LNCS 218, 1985, 429–432.
[10] NIST SP 800-22: Documentation and Software. Random bit generation. Guide to the statistical tests, https://csrc.nist.gov/Projects/Random-Bit-Generation/Documentation-and-Software/Guide-to-the-Statistical-Tests
[11] Wolfram S.: A New Kind of Science.: Wolfram Media, Inc, 2002, 1197, http://www.wolframscience.com/nksonline/toc.html

Ph.D. Yuliya Tanasyuk
e-mail: y.tanasyuk@chnu.edu.ua

Associate professor at Department of Computer Systems and Networks, Physical, Technical and Computer Sciences Institute, Yuriy Fedkovych Chernivtsi National University, Chernivtsi, Ukraine. Research interests and academic activities: programming, network information technologies, cryptography.

http://orcid.org/0000-0001-8650-0521

M.Sc. Petro Burdeinyi
e-mail: pburdeyniy@gmail.com

Master in Computer Engineering, Department of Computer Systems and Networks, Physical, Technical and Computer Sciences Institute, Yuriy Fedkovych Chernivtsi National University, Chernivtsi, Ukraine. Research interests and academic activities: cryptography, information technologies, software engineering.

http://orcid.org/0000-0002-3859-7522

otrzymano/received: 15.11.2019 *przyjęto do druku/accepted: 15.02.2020*

http://doi.org/10.35784/iapgos.908

TIME INTERVAL SWITCHING DEVICE

Ruslan Politanskyi[1], Andrij Veryga[2]
[1]Lviv Polytechnic National University, Institute of Telecommunications, Lviv, Ukraine, [2]Yuriy Fedkovych Chernivtsi National University, Department of Radio Engineering and Information Security, Chernivtsi, Ukraine

Abstract. *The proposed electronic switching device, which is a replacement (analogue) of the electromechanical switch KEP-12. The status and time settings are set for each channel separately through the device menu. It is characterized by less time and ease of reconfiguration.*

Keywords: microcontroller, switch, voltage, semistor

URZĄDZENIE PRZEŁĄCZAJĄCE INTERWAŁ CZASOWY

Streszczenie. *Proponowane jest elektroniczne urządzenie przełączające, które jest zamiennikiem (analogowym) przełącznika elektromechanicznego KEP-12. Status oraz ustawienia czasu zostają wyznaczone dla każdego kanału osobno poprzez menu urządzenia. Charakteryzuje się ono zmniejszoną czasochłonnością i łatwością rekonfiguracji.*

Słowa kluczowe: mikro-kontroler, przełącznik, napięcie, semistor

Introduction

The mechanical part of the vacuum units of the UV-800 type under the correct conditions of operation and timely maintenance present a great resource of work (decades). The electrical part has large dimensions, some of the circuits are obsolete. The logic of the circuit is provided by many electromagnetic relays. Resource of relays and actuators due to the burning of contacts and mechanical wear of their moving parts is limited, which leads to a deterioration of the efficiency of the control circuit, reduces the reliability of working out the scheme of technological operations.

In such installations, the KEP-12 electromechanical switch is used to automate the technological process [1]. Such devices are characterized by large dimensions, high power consumption, low functionality.

The use of modern radio electronic components (including programmable digital circuits) eliminates the above disadvantages. The proposed device allows you to control eight devices. It also has the ability to extend managed modules.

1. Technical characteristics of the UV-800 plant

The UV-800 vacuum metallization plant is designed for the metallization of plastic, glass and metal parts by vacuum evaporation. The plant provides a uniform metal film having good adhesion with the base material on the surface of the product. Other types of coating can be applied to the metallized layer. The plant has the following basic technical parameters:

1) dimensions L×W×H, mm — 2720×1240×1710
2) Internal dimensions of the vacuum chamber:
   - Diameter, mm — 800
   - Length of cylindrical part, mm — 925
   - Volume, liter — 550
3) Plant weight, kg — 1267
4) Vacuum, mmHg:
   - Operational — $5\cdot10^{-4}$
   - Limit in empty barrel — $1\cdot10^{-4}$
5) Estimated cycle duration, min — 15
6) Speed of rotation of the drum, rpm — 16
7) Power supply voltage, V — 280/220 (50 Hz)
8) Power, kW — 15
9) Consumption of cooling water, l / h — 500

   It is possible to metallize products with the following data:
   - Maximum width, mm — 300
   - Maximum length, mm — 800
   - Maximum height, mm — 50
   - The thickness of the applied layer, μm — 0,08…0,12
   - Maximum productivity (for products of the largest size), product/hour — 24

The coating is carried out by thermal evaporation on the basis of the property of metal atoms in high vacuum conditions to move in a straight line and to settle on the surface in its path.

Before spraying, the metal which is applied to the articles is placed on a heater in the central part of the vacuum chamber. The heaters heat the metal to the temperature of intense evaporation.

The required length of free path of vapor of metal atoms (> 450 mm) is provided when creating in the chamber of high vacuum of the order of $5\cdot10^{-4}$ mm Hg.

The scheme of plant is shown in Fig. 1.

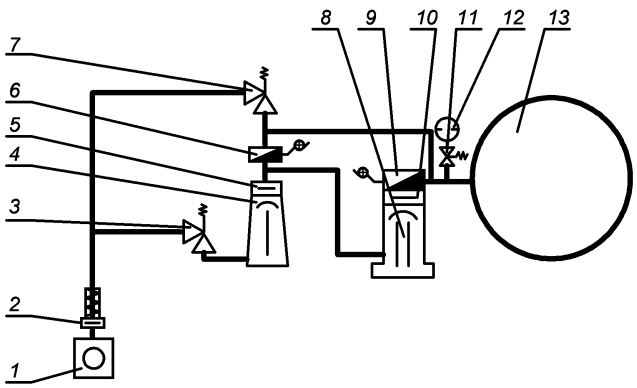

Fig. 1. The scheme of pumping of air: 1 – the pump is vacuum, 2 – the trap is vacuum, 3 – the valve is electromagnetic, 4 – the pump is booster steam-oil, 5 – the trap is vacuum, 7 – the valve is electromagnetic, 8 – the pump is high-vacuum, 6, 9 – the valve is vacuum, 10 – cooling trap, 11 – air intake valve, 12 – air intake filter, 13 – vacuum chamber

The separate units and technological processes are controlled by an electrical circuit, which includes a system of the cycle remote control as a whole and a system of programmed control following the pumping, subsequent, technological operations.

The semi-automatic program control is provided by the KEP-12U command electric apparatus. Built in the KEP program is designed for 2 min 51 s and is executed in the same sequence and with the same equipment as in the remote mode according to the work diagram.

The evaporator heating time and the metal evaporation time are determined by the type of evaporated metal for which the KEP contacts are adjusted accordingly. Since this appliance is electromechanical, the adjustment process is not convenient and takes a long time. And you need to switch the mode switch to the "off" position after the start of the KEP. These shortcomings are eliminated in the proposed electronic time switching device.

2. Electrical structural scheme of the switching device

The structure electrical scheme of the time switching device is shown in Fig. 2.

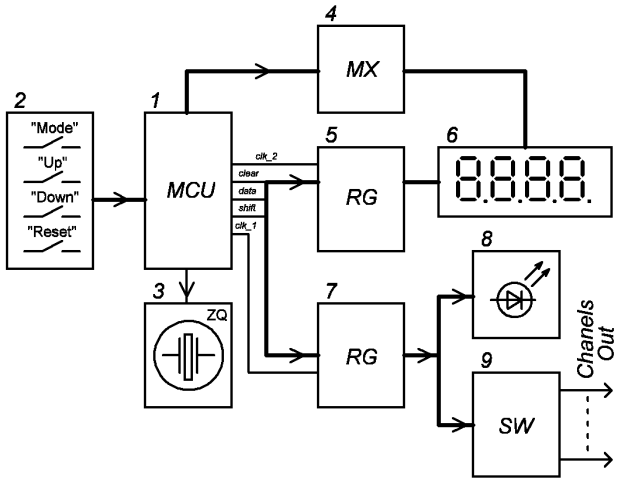

Fig. 2. The structure electrical scheme of device: 1 – microcontroller, 2 – keyboard, 3 – piezoelectric sound resonator, 4 – display switch, 5 – shift register, 6 – seven-segment four-character display, 7 – shift register, 8 – LEDs, 9 – electronic or electromechanical key

The main unit of the instrument is the microcontroller (1) (MCU). Its application simplifies the process of adjusting the device parameters and allows you to update the software to improve its functionality. Entering the menu mode and maintaining the time interval parameters is made from the keyboard (2) with the buttons "Mode", "Up", "Down". The reset of the microcontroller is done by the "Reset" button.

The sound signaling was made by the acoustic resonator (3).

The microcontroller control program and the device menus have a simple algorithm. Therefore, you can use a microcontroller without built-in peripherals and a small amount of program memory (up to 2 K).

Such chips usually have a small number of pins. Shift registers (5, 7) with sequential data input and parallel output were used to extend their number. The "clear" (clear the contents of the registers), "data" (sequential data entry), "shift" (moving the recorded data to the register in its output buffer) signals are common to both registers, and the "clk_1" and "clk_2" clock signals – separate. The clock pulses are fed to the register in which the recording is made. This ensures the "addressing" of the data written to the registers. The "clear" signal is sent to the registers when the microcontroller control program is started after the power is turned on. The "shift" signal is given after the data has been written to the register. The register in which the record was not recorded will not be changed and simply copied back to the output buffer.

The first shift register (5) is used to output a seven-segment four-digit mapping (6). Characters are displayed alternately. The symbol visible on the display is controlled by the switch (4). Key switching time is determined by the inertia of human vision. Each character's switching frequency must be greater than 48 Hz. Given the number of characters four, switching times are accepted every 20 ms / 4 = 5 ms.

The display shows information about the work time in mode "Comutation", and the channel number, time slot number, channel status, slot time in the "Menu" mode.

The second register (7) is the main register. It records the channel status at a given point in time. When the state is off, the logical level at the output of the channel is equal to logical "0", when enabled – logical "1". The status of the channel is indicated by the LEDs (8).

Switching by controlled devices is carried out with switches (9). As the latter the relays, transistors, triacs can be used. The type of switch is selected depending on the type of load. The relay is convenient to use for switching low-current devices, otherwise they will "burn" the switching contacts. At high DC currents, it is convenient to use transistors (field or IGBT). For alternating currents it is more convenient to use the triacs.

3. The electrical scheme of time interval switching device

The electrical scheme of the device consists of two modules: the main and the subordinate. This separation makes the scheme of the device universal. The slave module can be designed on the basis of other switch radio elements (electromechanical DC relays, solid state relays, transistors) to control the loads which are powered by AC or DC.

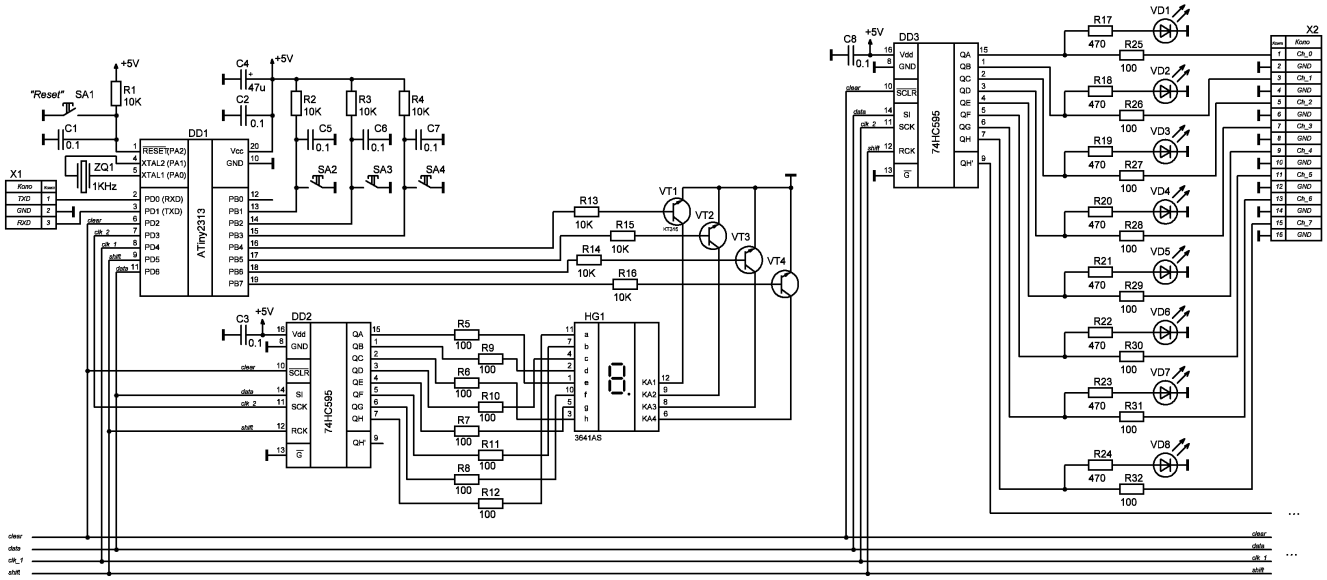

Fig. 3. The main module principal scheme of the switching device

The main module is shown in Fig. 3. The module is based on the widespread ATiny2313A microcontroller [7]. It has an internal clock generator that does not require the connection of an external quartz resonator, and allows you to use alternative functions of these pins. The microcontroller of this family and brand is optimal among ATMEL microcontrollers for this purpose. Since no interaction with the complex periphery is required, the number of legs used is sufficient.

The four-digit seven-segment 3641AS general cathode display [2] displays information regarding operating modes ("start-up", "on / off channel", "end-of-work", time from the start of the process), menu items and channel time values in "Programming" mode. Dynamic control of the display is carried out through the ports of the microcontroller (PB4… PB7).

The sound signaling is performed by a piezo resonator connected to two microcontroller pins (PA0, PA1). In this way bridging into the circuit is organized and thus it provides a higher volume of audio signals.

Entering the menu, navigating through menu items, programming the timings of the device control time is made using the buttons SA2 ... SA4 (SA2 – "less / down", SA3 – "more / up", SA4 – "input"). The SA1 button is introduced into the scheme to "reset" the microcontroller, but the program provides for the use of hardware "anti-hang" of the microcontroller.

The parallel output shift registers 74HC595 [6] have been used to control the channels and output the display symbol code. They are connected to the microcontroller via a serial bus. It contains the following control signals: CLK1, CLK2, CLEAR, DATA, SHIFT. Two channels are formed on this bus: one channel is the main channel for transmitting status data (on / off) of control devices to shift registers; another channel for transmitting data to the display.

The CLEAR, DATA, SHIFT signals are common to the managed devices and the display, and the clock signals of the registers CLK1, CLK2 are separated – the clock signal is applied to the channel for which the data is intended. This approach allows the use of a microcontroller with fewer legs.

LEDs indicate the channel is on.

You can control and configure your device from your computer using USART. As the data volumes are small, it is advisable to use a microcontroller with such a module.

The schema can be expanded to connect new slave modules.

The slave module principal scheme is shown in Fig. 4 and is a classic for triacs.

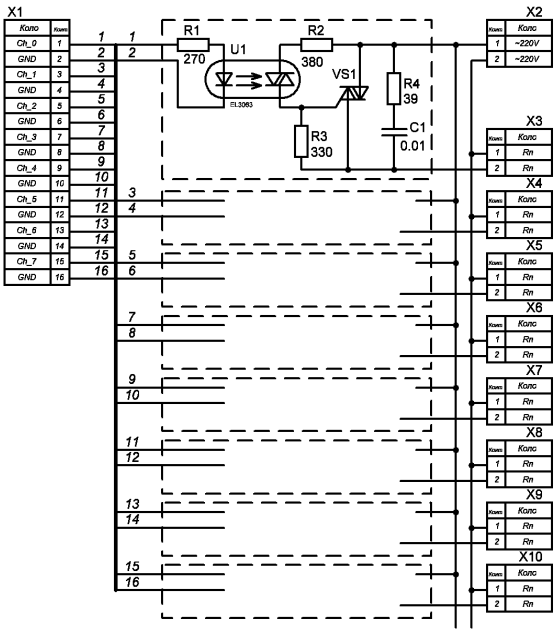

Fig. 4. The slave module principal scheme on the triacs

This module is intended for the control of devices powered by 220 volt AC.

As the switches the triacs are used. In this scheme, unlike relays, there is no sparking of contacts and there is no further decrease in the reliability of switching.

Part of the high voltage circuit (~ 220 V) is separated from the low voltage (+5 V) part by the MOC3063 optocoupler [5] which in the event of failure of any element (breakdown) in the high voltage circuit prevents damage to the low voltage circuits.

The scheme of the main module is designed in such a way that it is possible to connect subordinate modules of other types. The relay module is shown in Fig. 5. It is also assembled according to a typical scheme.

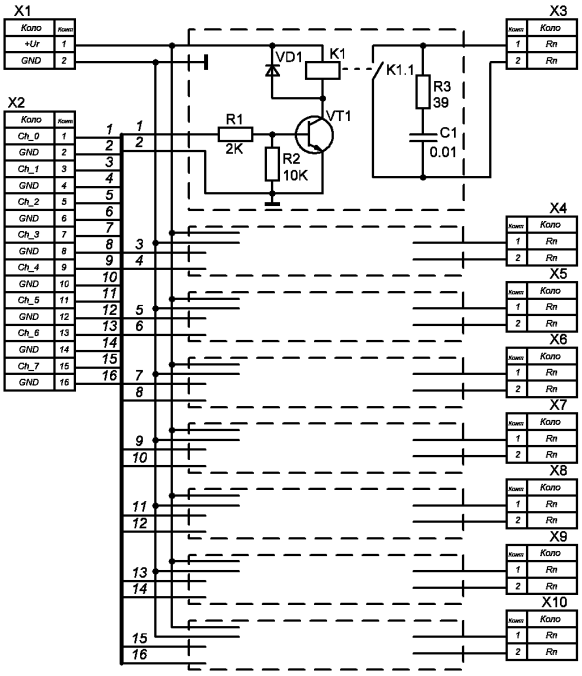

Fig. 5. The slave module principal scheme on the relay

This module is designed to control devices with separate power buses where voltages have different values or do not have a common conductor. The relays are used here as switches. The relay is controlled by a transistor switch to reduce the load on the outputs of the microcontroller. The parallel included a diode to relay and prevents damaging the transistor by self-induction voltage during tripping. A series of connected resistor and capacitor on the relay contacts reduces their sparking.

The look of the developed device is shown in Fig. 6.

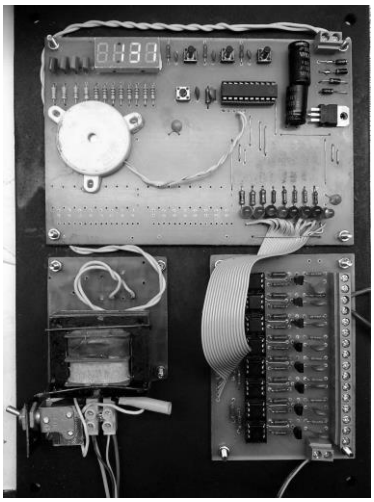

Fig. 6. The look of the developed device

4. Microcontroller control program algorithm flowchart

Microcontroller control program algorithm flowchart of the main module is shown in Fig. 7.

The described device allows you to control eight devices. For each device, the allotted time block is divided into eight time intervals. One byte of data in the flash memory of the microcontroller is assigned to each interval. The higher bit indicates the state in which the channel is to be turned in this interval (1-off, 0-on), and the remaining lower bits set the time directly. Thus, the length of the time interval can be set from 0 to 127 seconds, and the duration of the entire block from 0 to 8 · 127 = 1016 s.

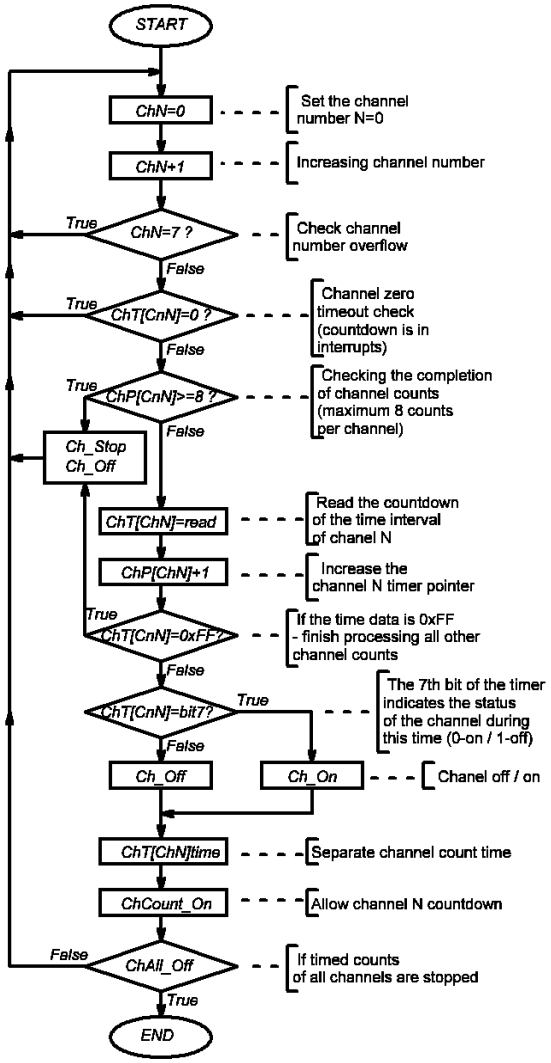

Fig. 7. Microcontroller control program algorithm flowchart of the main module

The microcontroller control program algorithm flowchart of the menu module is not shown. You can enter the Menu mode by pressing the "Mode" button, exit only by restarting the microcontroller by pressing the "Reset" button.

The algorithm is constructed in such a way that it is continuously executed in a circle. Entering time parameters is broken down into actions (Action). Depending on the established action, there is a cyclic entry into the corresponding branch of the algorithm. In each action the reaction follows by pressing of one of the device buttons ("Up", "Down", "Mode"). In the first step, the "Up" and "Down" buttons select the channel to edit the time parameters. In the second step – the time interval is selected. The third step – is to set the time interval state (on / off). In the fourth step – time is set within the time interval.

By the "Mode" button moves to the next step. Upon completion of the fourth action, the transition goes to the third. This is done for the convenience of sequentially entering the time interval parameters of one channel. Long press (> 100 ms) of the "Mode" button will go to the channel selection action.

The program is written on C programming language (GCC Compiler [6]) in the AVR Studio IDE [7].

5. Conclusions

By refining the code and correcting the hardware, the number of managed devices can be increased to a maximum of 32.

The developed device allows you to conveniently and quickly reconfigure time parameters. When completed, it automatically stops.

The proposed device can also be used in "Smart house" systems, if necessary, changing the microcontroller's control program.

References

[1] Command Electrical Device KEP-12M Manual.
[2] Segment Digit LED Display. http://www.wayjun.com/Datasheet/Led/Segment%20Digit%20LED%20Display.pdf
[3] https://gcc.gnu.org
[4] http://ww1.microchip.com/downloads/archive/NEWas5installer-stable-5.1.208-full.exe
[5] 6 PIN DIP Zero-Cross Triac Driver Photocoupler. http://www.everlight.com/file/ProductFile/EL303X_EL304X_EL306X_EL308X.pdf
[6] 8−Bit Serial−Input/Serial or Parallel−Output Shift Register with Latched 3−State Outputs. http://www.ti.com/lit/ds/symlink/sn74hc595.pdf
[7] 8-bit Microcontroller with 2/4K Bytes In-System Programmable Flash. http://ww1.microchip.com/downloads/en/DeviceDoc/doc8246.pdf

Ph.D. Ruslan Politanskyi
e-mail: polroos@mail.ru

Received M.Sc. degrees in applied mathematics and physics/qualification of an engineer-physicist from Moscow Institute Physics and Technologies, Russia, in 1994. He received a Ph.D. in solid state physics from Yuriy Fedkovych Chernivtsi National University. He is currently a post doctoral student of the Institute of Telecommunications, of Lviv Polytechnic National University. His research interests include signal processing, coding theory, pseudorandom sequence systems with chaotic dynamics (differential equations and circuits, including own invention) and their synchronization, fractal Brownian signals.

http://orcid.org/0000-0003-0015-7123

Ph.D. Andrij Veryga
e-mail: veriga@ukr.net

Received B.Sc. and M.Sc. degrees in Radio Engineering from Yuriy Fedkovych Chernivtsi National University, Ukraine. He received a Ph.D. in Radio Engineering from Yuriy Fedkovych Chernivtsi National University. He is currently an assistant of the Radio Engineering Department of Yuriy Fedkovych Chernivtsi National University. His research interests include signal processing, development of electronic circuits.

http://orcid.org/0000-0002-2616-3057

otrzymano/received: 15.11.2019 *przyjęto do druku/accepted: 15.02.2020*

http://doi.org/10.35784/iapgos.917

ENVIRONMENT OF ELECTROMAGNETIC COMPATIBILITY OF RADIO-ELECTRONIC COMMUNICATION MEANS

Heorhii Rozorinov[1], Oleksandr Hres[2], Volodymyr Rusyn[2], Petro Shpatar[2]
[1] National Technical University of Ukraine "Igor Sikorsky Kyiv Politechnic Institute", Kyiv, Ukraine, [2]Yuriy Fedkovych Chernivtsi National University, Department of Radio Engineering and Information Security, Chernivtsi, Ukraine

***Abstract**. The conditions of ensuring electromagnetic compatibility of radio electronic means of mobile radio service have been analyzed. The stages of such analysis are outlined and a list of measures to be taken at each stage is given. The types of scenarios (paired, group) of interfering radio electronic means of mobile radio service are described. The technical specifications of the radiocommunication service equipment and antennas, which provide a statement of validation of the electromagnetic compatibility of the radiocommunication electronic means radiocommunication, are provided. An algorithm for determining the electromagnetic environment is proposed and recommendations for providing electromagnetic compatibility are offered.*

Keywords: electromagnetic compatibility, electromagnetic environment, electronic means, radio communication, mobile service, interference

ŚRODOWISKO KOMPATYBILNOŚCI ELEKTROMAGNETYCZNEJ ŚRODKÓW KOMUNIKACJI RADIOELEKTRONICZNEJ

***Streszczenie**. Analizie poddane są warunki zapewnienia kompatybilności elektromagnetycznej środków radioelektronicznych mobilnych usług radiowych. Przedstawione zostają etapy takich analiz oraz podana jest lista środków do realizacji na każdym etapie. Opisane są rodzaje scenariuszy (parami, grupami) interferujących środków radioelektronicznych mobilnych środków radiowych. Podane zostają techniczne specyfikacje sprzętu usług radiokomunikacyjnych oraz anten, które przedstawiają oświadczenie o ważności kompatybilności elektromagnetycznej elektronicznych środków radiokomunikacji. Sugerowany jest algorytm dla określenia środowiska elektromagnetycznego oraz przedstawione zostają zalecenia dla świadczenia kompatybilności elektromagnetycznej.*

Słowa kluczowe: kompatybilność elektromagnetyczna, środowisko elektromagnetyczne, środki elektroniczne, komunikacja radiowa, usługi mobilne, interferencja

Introduction

The analysis of electromagnetic compatibility (EMC) of radio-electronic devices (RED) is currently relevant during the calculation of frequency assignments and is defined by the legislation of the country [7]. The problem of securing EMC RED can be solved in two ways, individually or in combination: technical measures, organizational measures. There are three main stages [9, 10, 11].

The first stage – the decisions that are made during the design phase of the RED. At this stage, for a given model of electromagnetic environment, the EMC problem can be solved sufficiently accurately and effectively. However, the model cannot really consider all the related factors related to the engineering implementation and production technology (for example, compatibility with adjacent electronic systems, interference from side frequencies and intrinsic heterodyne paths, i.e. intra-system EMC, difficult predictions of related equipment). Therefore, a complete solution to the problem of providing EMC is achieved in the last stages of development and design, manufacture and testing.

The second stage – to perform tests on the EMC criteria and to measure the parameters of the individual RED units and the finished product.

The third stage is the operation, where as a result of various reasons, the REDs operate in conditions different from the calculated ones.

The problem of EMC RED forecasting is traditionally divided into two parts:

1) intra-system EMC, which is characterized by the close location of the RED, accounting for their interaction within a single radio complex and analysis of the characteristics of the antennas in the near and far zones, considering the influence of configuration of the media surface or surrounding devices;
2) intersystem EMC, which is characterized by electrodynamics' interaction of antennas of different radio engineering complexes in the far zone, considering the underlying surface and the conditions of propagation of radio signals through the intermediate medium.

The purpose of the paper is to consider the organizational measures that simplify the analysis of EMC RED mobile service and allow new frequency assignments.

1. Theory of electromagnetic compatibility

An increase in the number of radio-electronic devices (REDs), as well as high-frequency generators for industrial, scientific, medical and electro technical devices, which by their functional purpose are not foreseen by sources of radio waves create industrial radio interference. Expanding the scope of REDs led to the gradual saturation of the radio frequency spectrum (RMS) with electromagnetic fields of artificial origin, and together with sources of radio emission (SRE) of natural origin created the problem of electromagnetic compatibility (EMC) of REDs and radio radiation devices (RRD) problems in their design and operation. In general, electromagnetic compatibility is the ability of REDs and RRDs to function simultaneously with conditioned quality in actual operating conditions, taking into account the effects of unintended radio interference on them, without creating unacceptable radio interference with other REDs and RRDs.

The causes and ways of occurrence of electromagnetic interference. The electromagnetic radiation of any RED is concentrated both in the band of its operating frequency (main radiation) and outside of this band (non-basic radiation). Both basic and non-basic radiation when used, for example, directional antennas can propagate both in the direction of the main petal of the radiation pattern and in the lateral and posterior petals. Despite the fact that the gain of directional antennas in the direction of the main petal reaches 50 dB, the gain in the directions of the posterior and lateral petals of the radiation pattern remains quite high (from minus 20 to minus 40 dB). As a result, for example, high-power radar stations can emit power outputs of 1 kW or more along the back and side lobes. And in the direction of the main and side 27 of the antenna petals the electromagnetic waves are emitted with both working polarization and polarization, the parameters of which are different from the working. In this regard, in the receiving antenna and the subsequent paths of the radio receiving device (RRD) for the selection of electromagnetic oscillations of the working radio channel it is necessary to apply the different types of selection – frequency, spatial, polarization, etc. The electromagnetic situation also depends on the radiation that accompanies the main radiation, such as a radio transmitter, and it is manifested by the nonlinear properties of the volt-ampere characteristics of its individual elements. This further complicates the real electromagnetic environment at the receiving point.

Thus, in order to achieve the EMC when more than one RED is required simultaneously within the same radio frequency space, it is necessary to increase the electromagnetic efficiency of the RED, i.e. to improve certain radiation and / or reception parameters. Ideally, by improving these RED parameters and bringing them to perfection, as well as by optimizing the "placement" of RED frequencies in the RF space, it is possible to obtain its maximum capacity. Under such ideal conditions, the transmitting REDs emit only the necessary signals in the required frequency band and with minimal power only at a given point in space, and the receiving REDs receive signals at the tuning frequency and only from the specified direction.

2. Methodology for calculation of the EMC RED

The EMC RED calculation of the mobile radio service is carried out in accordance with a procedure consisting of six consecutive steps, namely [7, 8]:

1) preliminary assessment of the electromagnetic environment (EME) in the planning area of the new frequency assignment;
2) preliminary assessment of the proper quality of functioning of individual RESs or the totality of REDs in a given EME;
3) identification of scenarios of interfering RED interaction in the area of planning of new frequency assignment;
4) determination of the characteristics of the RED for the EMC calculations of the RED;
5) calculation of the EMC RED in accordance with the defined interference interaction scenarios;
6) estimation of providing the EMC RED on the results of the performed calculations.

In the first stage, a preliminary evaluation of the EME is carried out within the area of planning of new frequency assignment by territorial and frequency selection of potentially incompatible REDs [1, 3, 4].

In the analysis of EMC RED of duplex radio communications, the EME is evaluated in two steps. In the first stage, the cases of possible interference with existing REDs are evaluated with a new RED. The second stage considers the cases when a new RED may be a source of interfering RED.

In the second stage, the preliminary evaluation of the quality of functioning of individual REDs or their totality is carried out on the basis of basic requirements for the operation of REDs and the quality of communication taking into account the technical characteristics of the REDs and EMEs studied within the area of planning of new frequency assignment [3].

The third stage is the determination of the interaction scenario for the planned REDs and REDs that have fallen into the calculation zone, and is carried out according to the results of a preliminary assessment of the interference situation in the frequency assignment planning area [9]. The scenarios of interfering interaction between the RED of the mobile radio service and the RED of other radio services are divided into pairs and groups. In the paired scenarios, the effect of one unintentional interference (one RED) on one receptor (the other RED) is investigated. In the group scenarios, the effect of a set of interference sources (several REDs) on one receptor is investigated. This must take into account the deployment conditions, antenna directional characteristics, territorial diversity and spatial orientation of the planned and operational RED.

Taking into account that:

1) in the most typical cases, the main factors determining the obstacles in the land mobile service include:
   - products in the band of intermodulation frequencies generated by two (or more) powerful interfering signals;
   - unwanted radiation that may occur in the transmitter when third-party signals from another transmitter appear in its output RF cascades;
   - levels of useful interfering signals are random variables;
2) two (or more) unwanted signals must have such specific frequencies that the products of their intermodulation fall into the frequency band of the receiver;
3) the likelihood of intermodulation interference caused by the interaction of more than two powerful undesired signals is very low;
4) intermodulation interference calculation procedures are a useful tool to ensure more efficient use of spectrum in the land mobile service;

recommended that the intermodulation model of the receiver shown in Fig. 1 to be used in the calculation of intermodulation interference in the land mobile service, and intermodulation interference calculations were performed using intermodulation models in the transmitter and receiver.

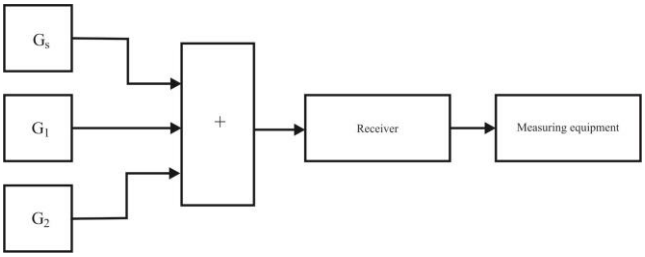

Fig. 1. Block scheme of measurements of intermodulation in the receiver

When measuring the intermodulation characteristics of the receiver, two signals of the same level from the generators G_1 and G_2 and a useful signal from the generator G_S with the level P_c are fed to its input. The frequency disorder of the first generator is selected equal to Δf_0, and the second generator is approximately equal to $2\Delta f_0$. The levels of both generators at the input of the receiver are increased until the level is reached, when the quality of the reception of the useful signal does not start to fall below some set level. The reception quality is clearly related to the protective ratio $A = P_C - P_I$, where P_I is the equivalent interference power listed before the receiver input (dBm).

The general formula for calculating intermodulation interference in a receiver is as follows:

$$P_{\mathrm{IM}} = 2(P_1 - \beta_1) + (P_2 - \beta_2) - K_{2,1} \tag{1}$$

where P_1 and P_2 are the interference power of the frequencies f_1 and f_2, respectively; P_{3i} is the power of third-order intermodulation products at frequency f_0 ($f_0 = 2 f_1 - f_2$); $K_{2,1}$ is the third order intermodulation coefficient, which can be calculated by means of third order intermodulation measurements, or obtained from the description of equipment characteristics; β_1 and β_2 are radio frequency selectivity parameters at deviations of frequency Δf_1 and Δf_2 from operating frequency f_0, respectively.

Values β_1 and β_2, for example, can be obtained from the equation to calculate the attenuation of the signal at a non-tuned frequency

$$\beta(\Delta f) = 60\log\left[1 + \left(\frac{2\Delta f}{B_{\mathrm{RF}}}\right)^2\right], \tag{2}$$

where B_{RF} is the bandwidth of the receiver on the radio frequency.

It should be noted that for a certain set of third-order intermodulation measurements for analogue terrestrial mobile radio receivers operating in the UHF band and the lower frequency of the UHF band, equation (1) can be converted to the form:

$$P_{\mathrm{IM}} = 2P_1 + P_2 + 10 - 60\log(\sigma f), \tag{3}$$

where σf is the average frequency deviation (MHz), equal $(\Delta f_1 + \Delta f_2)/2$.

The power P_i of the products of intermodulation arising in the transmitter and then entering on the receiver input, can be determined by the formula:

$$P_i = P_2^o - \beta_{12} - \beta_{10} - K_{(2),1} - L_{10}, \tag{4}$$

where P_2^o is the power of the interfering transmitter (at frequency f_2) at the output of the faulty transmitter (operating at frequency f_1) in which occur the intermodulation products (dBW); β_{12}, β_{10} are suppression performed by the output circuits of the faulty transmitter at the frequency f_1 and feeders of its antenna with respect to the interfering transmitter at the frequency f_2, and to the products of intermodulation at the frequency f_0, respectively (dB); $K_{(2),1}$ is the losses of intermodulation transformation in the

transmitter (dB), which differ from $K_{2,1}$ in formula (1); L_{10} is the attenuation of intermodulation products on-track between transmitter that work on the frequency f_1 and the receiver (dB).

Interference caused by the transmitter occurs if $P_S - P_i < A$.

In the fourth stage, the technical characteristics of the RED for which the new frequency assignment is planned and used in the calculations of the EMC RED will be submitted by the applicant together with the application for the issuance of an opinion on the EMC RED of the mobile radio communication. The application is sent directly to the Radio Frequency Center (RFC). At the same time the following technical characteristics of RED are provided: range of working frequencies of RED, MHz; duplicate radio frequency diversity; frequency grid step or channel formation formula; polarization; radiation bandwidth at -30 dB; radiation class.

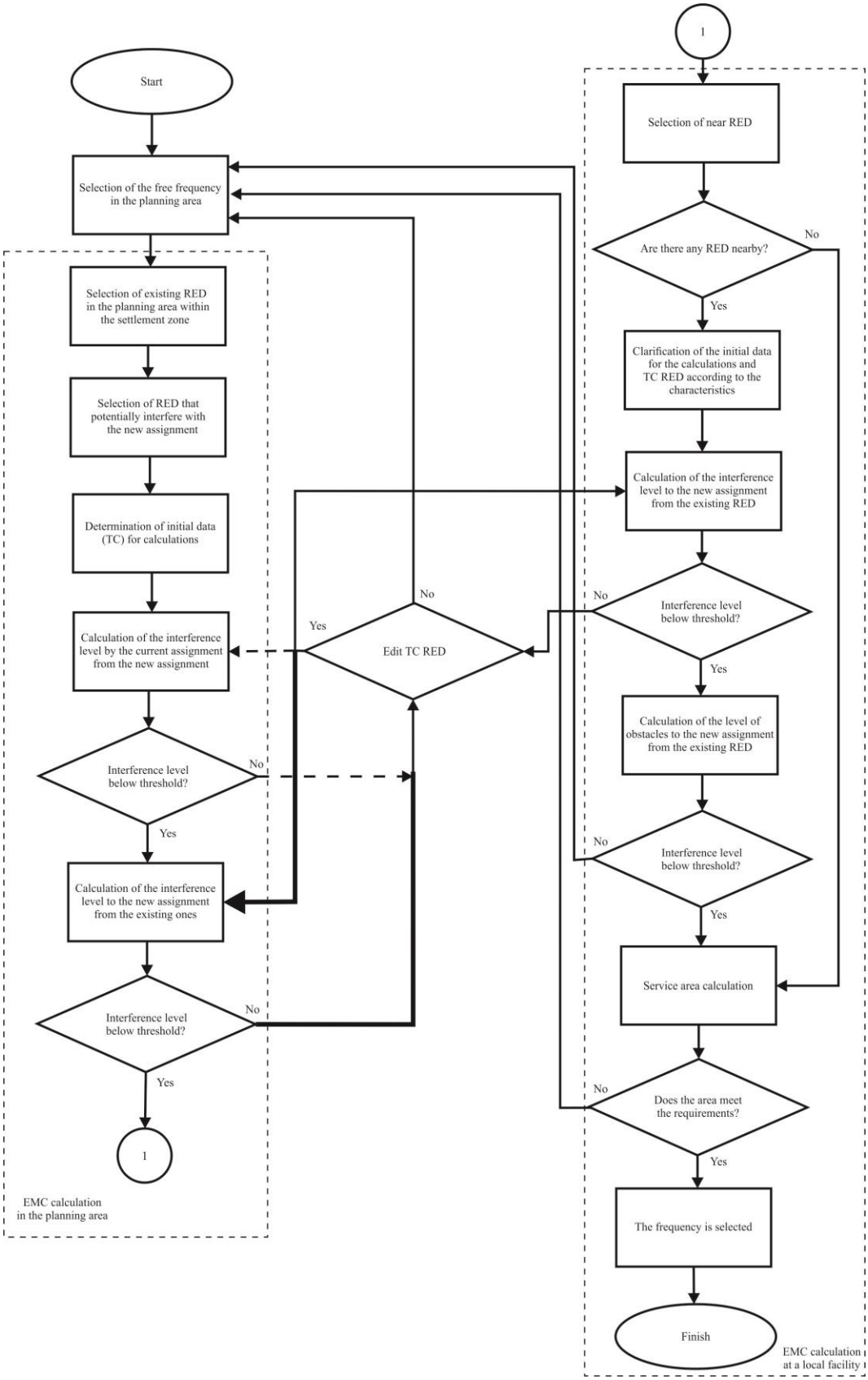

Fig. 2. Block scheme of the generalized algorithm for EMC calculating for implementation and new radio frequency assignments of the RED of Mobile Radio Service

In the fifth stage, the EMC RED of the mobile radio communication is calculated in accordance with the algorithm, the block diagram of which is shown in Fig. 2 [2]. In this paper, this algorithm has been refined and corrected. The EMC calculations of REDs necessarily take into account the type of scenario of interfering RED interaction, which are considered as potential conflicts, types of interferences, channels of possible penetration of interferences (main and non-fundamental) and negative phenomena, which are determined by the frequency selection of conflicting REDs.

In the sixth stage, the provision of the EMC RED is evaluated by checking the fulfillment of the generalized energy criterion of the EMC RED, according to the formula [5, 6]: $P_S/P_i \geq A(\Delta f)$, where P_S is the useful signal power at the receiver input; P_i is the power of interference at the input of the receiver (for group scenarios – the total level of interference at the input of the receiver); $A(\Delta f)$ is the protective ratio of the receiver to the interference receptor. The following parameters should be considered when checking the fulfillment of a certain EMC RED criterion: the percentage of time during which communication deterioration is observed due to interference and non-compliance with the EMC RED conditions; the percentage of places that do not meet the conditions of EMC RED; permissible intensity of the interference signal field at the border of the service area; field strength of the payload signal, which guarantees the proper quality of operation of the subscriber terminals in the service area of the base station.

In the international coordination of frequency assignments, the verification of the EMC RED conditions is carried out by the following indicators: the permissible intensity of the interference signal field at a certain point; the maximum range of the interference signal.

3. Algorithm calculation for the EMC RED

The EMC RED calculation of the mobile service is performed according to the algorithm (Fig. 2). For the selected radio frequency, consecutive calculations are carried out to evaluate the impact of the new RED on the existing RED and the impact of the existing RED on the new RED depending on the scenario selected [2]. The obtained results of the calculations check the fulfillment of the EMC criterion RED, defined by the formula (the sixth stage).

If the aforementioned EMC RED criterion is not fulfilled, the possibility of changing the technical characteristics of the RED is determined or a decision is made to select another frequency for the new planned RED.

This algorithm can be used in different programming languages, such as Delphi, C++.

4. Conclusions

The paper determines the relevance of the analysis of the EMC RED mobile radio service when making frequency assignments. The stages of calculating the EMC RED of the mobile radio service, as well as the list of measures taken at each stage, are outlined. An algorithm for calculating the EMC RED of a mobile radio service is proposed. The suggestions provided make it possible to calculate the EMC RED parameters of the mobile radio service. This analysis should be used when assigning radio frequencies to the mobile radio service RED, as well as during the practical calculations and determining the EMC conditions of the mobile radio service RED.

References

[1] Burrell J.: Disruptive Effects of Electromagnetic Interference on Communication and Electronic Systems, http://citeseerx.ist.psu.edu/viewdoc/download?doi=10.1.1.196.1450&rep=rep1&type=pdf

[2] GOST 29037-91. Electromagnetic compatibility of technical means. Certification test. General rules. Moscow 2006, http://gostrf.com/normadata/1/4294825/4294825646.pdf

[3] Recommendation P.452: Prediction procedure for the evaluation of interference between stations on the surface of the Earth at frequencies above about 0.1 GHz Managed by R00-SG03, https://www.itu.int/dms_pubrec/itu-r/rec/p/R-REC-P.452-16-201507-I!!PDF-E.pdf (available 01.12.2017).

[4] Recommendation P.530: Propagation data and prediction methods required for the design of terrestrial line-of-sight systems. Managed by R00-SG03, https://www.itu.int/dms_pubrec/itu-r/rec/p/R-REC-P.530-17-201712-I!!PDF-E.pdf (available 01.12.2017).

[5] Recommendation SM.1134 : Intermodulation interference calculations in the land-mobile service. Managed by R00-SG01, https://www.itu.int/rec/R-REC-SM.1134/en (available 01.02.2007).

[6] Recommendation SM.337-6: Frequency and distance separations. Status: In force (Main), http://www.itu.int/dms_pubrec/itu-r/rec/sm/R-REC-SM.337-6-200810-I!!PDF-E.pdf (available 22.10.2008).

[7] Rishennya N2151 (02.12.2008) Pro zatverdzhennya Poryadku rozrobky vysnovkiv shchodo elektromahnitnoyi sumisnosti radioelektronnykh zasobiv movlennya, neobkhidnykh dlya stvorennya ta rozvytku kanaliv movlennya, merezh movlennya ta telemerezh, https://zakon.rada.gov.ua/rada/show/vr215295-08/ed20160210.

[8] Rozorinov G. M., Lazarenko S. V.: The analysis of electromagnetic compatibility of radio-electronic devices of mobile radio service for frequency assignments Scientific Proceeding of Ukrainian Research Institute of Communication 1(41)/2016, 14–19.

[9] Schneider-Electric: Vol. 32. EMC www.schneider-electric.com.ua (available 10.02.2016).

[10] Sedelnikov Yu.E.: Electromagnetic compatibility of radio electronic means: a training manual. New Knowledge, Kazan 2006 (in Russian).

[11] Suman M., Saini E-M., Sharma A.: Electromagnetic Interference and Compatibility – A Review. International Journal of Advanced Research in Computer Science 8(4)/2017, 355–357.

D.Sc. Heorhii Rozorinov
e-mail: grozoryn@gmail.com

National Technical University of Ukraine "Igor Sikorsky Kyiv Politechnic Institute"
Department of Audiotechnic and Information Registration. D.Sc. (Engineering Sciences) Professor of Department of Audiotechnic and Information Registration. Research interests: pseudorandom sequence generators; encryption information, acoustics.
Author of nearly 120 publications.

http://orcid.org/0000-0002-6095-7539

M.Sc. Oleksandr Hres
e-mail: o.hres@chnu.edu.ua

Yuriy Fedkovych, Chernivtsi National University Department of Radio Engineering and Information Security. Assistant Professor of Department of Radio Engineering and Information Security.
Research interests: pseudorandom sequence generators; encryption information. Author of nearly 35 publications.

http://orcid.org/0000-0002-8465-193X

Ph.D. Volodymyr Rusyn
e-mail: rusyn_v@ukr.net

Yuriy Fedkovych Chernivtsi National University Department of Radio Engineering and Information Security. Ph.D. (Engineering Sciences) Assistant Professor of Department of Radio Engineering and Information Security. Research interests: modeling of nonlinear equations and chaotic generators; control of chaotic oscillations. Author of nearly 60 publications.

http://orcid.org/0000-0001-6219-1031

Ph.D. Petro Shpatar
e-mail: p.shpatar@chnu.edu.ua

Yuriy Fedkovych Chernivtsi National University Department of Radio Engineering and Information Security. Ph.D. (Engineering Sciences) Associate Professor of Department of Radio Engineering and Information Security. Research interests: pseudorandom sequence generators; encryption information. Author of nearly 60 publications.

http://orcid.org/0000-0003-4088-1458

otrzymano/received: 15.11.2019 *przyjęto do druku/accepted: 15.02.2020*

http://doi.org/10.35784/iapgos.916

THE GENERATING RANDOM SEQUENCES WITH THE INCREASED CRYPTOGRAPHIC STRENGTH

Volodymyr Korchynskyi, Vitalii Kildishev, Oleksandr Riabukha, Oleksandr Berdnikov
Odessa National Academy of Telecommunication named after O.S. Popov, Institute of Radio, Television and Information Security, Department of Information Security, Odessa, Ukraine

Abstract. *Random sequences are used in various applications in construction of cryptographic systems or formations of noise-type signals. For these tasks there is used the program generator of random sequences which is the determined device. Such a generator, as a rule, has special requirements concerning the quality of the numbers formation sequence. In cryptographic systems, the most often used are linearly – congruent generators, the main disadvantage of which is the short period of formation of pseudo-random number sequences. For this reason, in the article there is proposed the use of chaos generators as the period of the formed selection in this case depends on the size of digit net of the used computing system. It is obvious that the quality of the chaos generator has to be estimated through a system of the NIST tests. Therefore, detailed assessment of their statistical characteristics is necessary for practical application of chaos generators in cryptographic systems. In the article there are considered various generators and there is also given the qualitative assessment of the formation based on the binary random sequence. Considered are also the features of testing random number generators using the system. It is determined that not all chaos generators meet the requirements of the NIST tests. The article proposed the methods for improving statistical properties of chaos generators. The method of comparative analysis of random number generators based on NIST statistical tests is proposed, which allows to select generators with the best statistical properties. Proposed are also methods for improving the statistical characteristics of binary sequences, which are formed on the basis of various chaos generators.*

Keywords: dynamic chaos, generator, sequence, encryption

GENEROWANIE SEKWENCJI LOSOWYCH O ZWIĘKSZONEJ SILE KRYPTOGRAFICZNEJ

Streszczenie. *Sekwencje losowe wykorzystywane są do tworzenia systemów kryptograficznych lub do formowania sygnałów zakłócających. Do tych zadań wykorzystywany jest generator sekwencji losowych, który jest urządzeniem deterministycznym. Taki generator z reguły ma specjalne wymagania dotyczące jakości tworzenia sekwencji liczbowej. W systemach kryptograficznych najczęściej stosuje się generatory liniowo-przystające, których główną wadą jest krótki okres formowania pseudolosowych sekwencji liczbowych. Z tego powodu w artykule zaproponowano użycie generatora chaotycznego, jako że okres próbkowania w tym przypadku zależy od rozmiaru siatki bitowej w używanym systemie obliczeniowym. Oczywistym jest, że należy oszacować jakość generatora chaotycznego za pomocą systemu testów NIST, dlatego też do praktycznego zastosowania generatorów chaotycznych w systemach kryptograficznych wymagana jest szczegółowa ocena ich cech statystycznych. W artykule rozważono różne generatory, a także podano ocenę jakościową procesu formacji na podstawie losowej sekwencji binarnej. Rozważano również funkcje testowania generatorów liczbowych przy użyciu systemu. Stwierdzono, że nie wszystkie generatory chaotyczne spełniają wymagania testów NIST. W artykule zaproponowano metody poprawy właściwości statystycznych generatorów chaotycznych, tak jak również metodę analizy porównawczej generatorów liczb losowych, która oparta jest na testach statystycznych NIST, i która pozwala wybrać generatory o najlepszych cechach statystycznych. Przedstawiono także metody poprawy właściwości statystycznych sekwencji binarnych, które powstają na podstawie różnych generatorów chaotycznych.*

Słowa kluczowe: chaos dynamiczny, generator, sekwencja, szyfrowanie

Introduction

The protection of the transmitted information from unauthorized access is carried out at different levels of OSI models [2, 4, 6] by means of cryptographic systems and noise-like signals. The confrontation between cryptography and cryptanalysis allows to conclude that the reliability of the cryptographic system decreases over time and its compromise becomes apparent. Therefore, it is possible to guarantee the high cryptographic stability of the encryption systems by their constant improvement.

Another purpose of random numbers is to expand the spectrum of digital signals to form noise-like signals, on which based are various implemented indicators of transmission stealth. It is obvious that the cryptographic strength of encryption systems, and the level of energy and structural secrecy of noise-like signals are affected by the quality of the used random number generators [5, 8]. It is known [8] that in cryptographic systems, as a rule, used are the linear congruent generators. The main disadvantage of such generators is a short period of formation of random numerical sequences.

The implementation of the dynamic chaos phenomenon [1, 4, 7] into the field of information and communication technologies not only opened new prospects for the synthesis of signal structures, which are providing high potential stealth of transmission, but also expanded the possibilities for developing effective cryptocoding systems. For this reason, it is expedient to improve the methods for generating random sequences and this substantiates the relevance of this research. Therefore, the aim of this work is to develop methods for the formation of pseudorandom sequences based on dynamic chaos with improved statistical characteristics and increased cryptographic strength.

1. The features of testing random sequences

The random sequences based on dynamic chaos should satisfy the corresponding statistical properties of the generated processes. Dynamic chaos [7] has all the basic properties of a random process and is an irregular, aperiodic change in the state of a nonlinear dynamic system. An insignificant change in the initial parameters of the chaos generator leads to a significant change in the values of the generated oscillations, which makes it possible to form different trajectories of the chaotic process. This property allows one to create almost unlimited number of random sequence combinations of various lengths.

For cryptographic tasks and noise-like signals, it is advisable to use program generators with a uniform distribution law of numbers [3]. Such generators are implemented in accordance with a certain algorithm, according to which each successive random number is calculated from the previous one. This method of forming a sequence has the following advantages:

1) the selection of a sample of numbers with tested statistical properties, which provides the necessary stability of the numbers generation and does not require regular testing of the sequence;
2) the repeated reproduction of a numerical sequence from the desired position;
3) the minimum number of operations that is necessary for the formation of each member of the numerical sequence;
4) the computational process does not occupy large amounts of memory;
5) the sequence period must be no less than the specified process.

The research of generators with a uniform distribution law [8] shows that the search for samples with the required quality indicators is a difficult task and requires rather large laborious calculations. There are various statistical criteria for checking

random and pseudo-random number generators [2]: criteria χ^2 (Pearson), Kolmogorov-Smirnov criteria, Student criteria, and others. The most convenient and universal is the criteria χ^2, the advantages of which are independent of the distribution of a random variable.

As noted in [2], using statistical criteria, you can implement such verification tests as distribution check (test frequencies), series check (test pairs), intervals check (testing intervals), combinations check (poker test) etc. For the task of testing random numbers, the National Institute of Standards and Technologies (NIST) has developed 16 special tests: the seriality test (Runs Test); test for maximum batch size; matrix-rank test (Random Binary Matrix Rank Test); spectral test; test with non-overlapping non-periodic patterns (Nonoverlapping (Aperiodic) Template Matching Test); test for overlapping periodic patterns (Overlapping (Periodic)); universal statistical test (Maurer's Universal Statistical Test); comprehensive test Lempel-Ziv (Lempel-Ziv Complexity Test); linear test (Linear Complexity Test); serial test (Serial Test); with – approximate entropy test (Approximate Entropy Test); summing test (Cumulative Sum (Cusum) Test); random deviation test (Random Excursions Test and Random Excursions Variant Test).

The method of comparative analysis of random sequences generators requires the following actions:

1) with the help of NIST tests, sample testing of the number generators under study is carried out;
2) counting the number of values that went beyond the limits of the confidence interval;
3) according to the number of internal local deviations Z, an analysis of the quality indicators of generators, for which the Z values are ranked in ascending order.

2. Generation and testing of binary sequence based on the dynamic chaos

Consider the method of improving the qualitative realizations of chaotic oscillations [7]. To solve the experiment, we consider several discrete mappings in chaos generators [5]:

1) static

$$x_{n+1} = a(1-|1-2x_n|^l) \tag{1}$$

where $x_0 = 0.8$, $a = 0.9$, $l = 0.8$;

2) logistic

$$x_{n+1} = ax_n(1-x_n) \tag{2}$$

where $x_0 = 0.9$, $a = 3.9$;

3) cubic

$$x_{n+1} = (1-4a)x_n + 4ax_n^3 \tag{3}$$

where $x_0 = 0.5$, $a = 0.92$;

4) shear

$$x_{n+1} = ax_n \bmod 1 \tag{4}$$

where $x_0 = 0.8$, $a = 3.0$.

For generators (1-4), Fig. 1 shows the graphs of dependence $P(\chi^2)$ on the values n, which are calculated in the process of generating numbers through the interval $\Delta n = 2\cdot 10^3$ for the implementation lengths of 450,000 values.

The graph of the dependence $P(\chi^2)$ on the values n of the sequence for the length $\overline{y_n}$ of the implementation of 450,000 values is shown in Fig. 2 (a). In Fig. 2 (b) there is the graph of the dependence $P(\chi^2)$ on the values n of the sequence $\overline{z_n}$.

From the analysis of the dependency graphs $P(\chi^2)$, we see that the bottom line with the accepted criterion, as the base random generator, should be taken by the generator sequence $\overline{z_n}$. We can assume that the implementation of pseudorandom numbers based on such a generator is a random distribution. As shown in [1], the sequence $\overline{z_n}$ represents a noise signal. Thus, the noise signal can be considered a truly casual process, for the purpose of generating random numbers. By applying a sign function $signx$, which is conditioned as $signx = 1$ at $x \geq 0$ and $signx = -1$ at $x < 0$, we will form a binary sequence based on the chaos generator.

The resulting sequence $\ddot{z}_n$ of 450000 bits is initially generated to form a desired length through the dilution procedure. For example, by double-thinning with a different step, we will generate a binary sequence 20000 bits long and check it randomly with a frequency test. This test is based on the equality of frequencies "1" and "-1" in a truly random binary sequence.

If X marks the amount of "1" i "−1" in binary sequences, then in the experiment under consideration

$$X = \sum_{i=0}^{20000} \ddot{z}_i = -1 \tag{5}$$

indicates that the frequency test of a random binary sequence has been successfully completed.

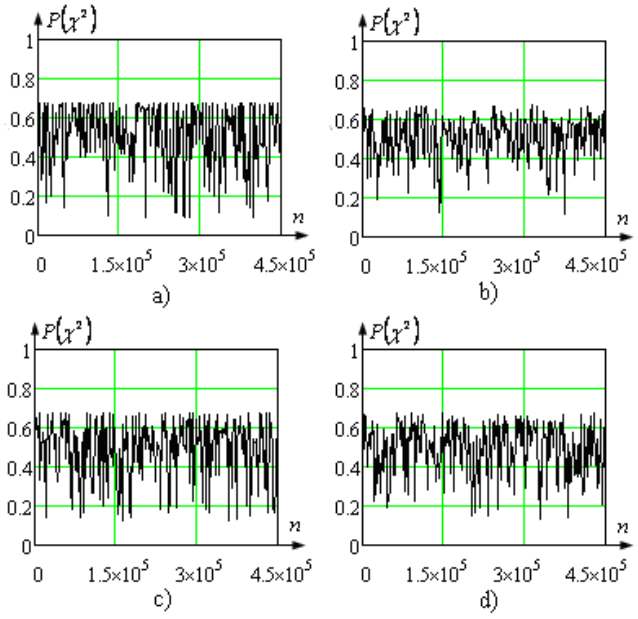

Fig. 1. The graphs of dependency $P(\chi^2)$ *from the quantity of numbers n generators of discrete mappings: static (a), logistic (b), cubic (c) and shift (d)*

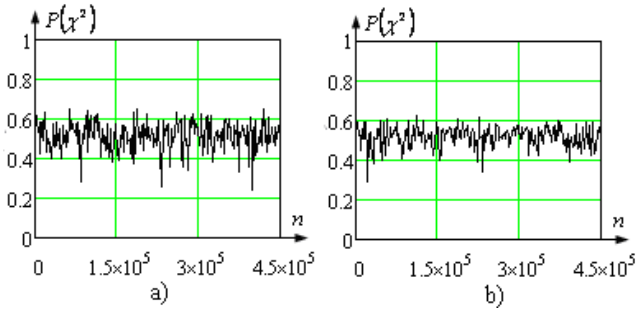

Fig. 2. The graphs of dependency $P(\chi^2)$ *from the quantity of numbers n to (a) and after (b) mixing*

Thus, we can conclude that the chaos generator $\overline{z_n}$ is the ideal basis for the formation of the random binary sequence that provides reproduction and the required length of a random sequence. The application of such sequences in transmission algorithms will increase the noise immunity, structural and informational concealment of signal structures in the confidential communication systems.

With the help of the various NIST system tests, there can be considered the process of statistical evaluation $P(\chi^2)$ of binary sequences formed on the basis of chaos generators (1-4). Fig. 3 shows the values $P(\chi^2)$ that depends on the NIST system tests. Based on the results of values $P(\chi^2)$ deviations in the zone of the

confidence interval, it can be concluded that not all samples of chaos generators meet the requirements of the NIST test system. For example, chaos generators with a logistic (Fig. 4) and cubic (Fig. 5) mapping, as well as a chaos generator with a shift type display (Fig. 6), do not pass all tests on randomness, as a series of values obtained $P(\chi^2) < 0.05$. Satisfactory results for NIST tests were obtained for a power chaos generator (Fig. 3).

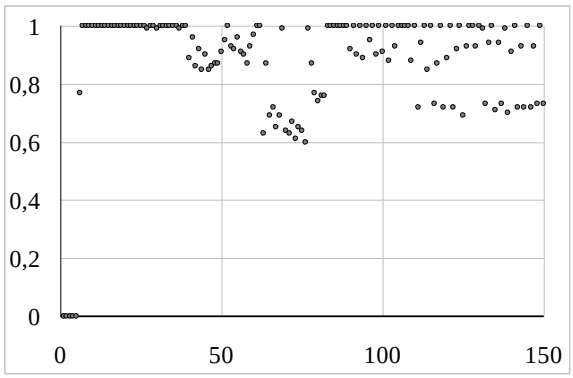

Fig. 3. The results of testing the power chaos generator

To increase the stability of the statistical characteristics of a binary sequence, it was proposed to use several chaos generators. For this purpose, the XOR operation was used to form the final binary sequence. Fig. 7 shows the results of testing such sequence, which is formed on the basis of a shift type generator and a cubic generator. The test results show that the quality of the obtained sample has significantly improved, since most of the tests are in the zone of the confidence interval, i.e. $P(\chi^2) > 0.05$.

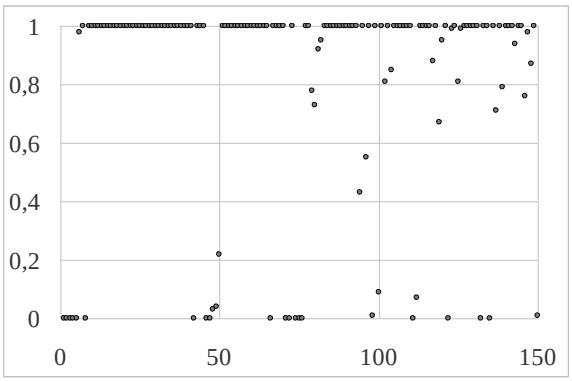

Fig. 4. The results of testing the chaos generator with the logistic display

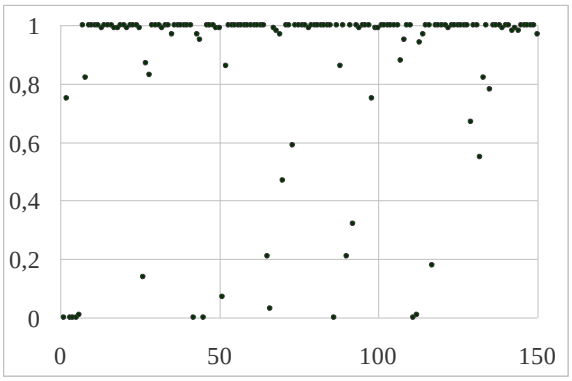

Fig. 5. The results of testing the chaos generator with a cubic map

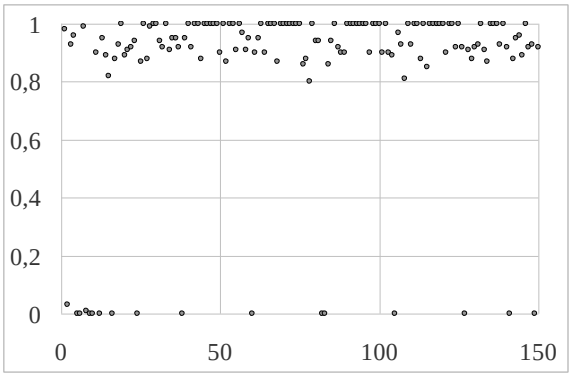

Fig. 6. The results of testing the chaos generator with mapping type shift

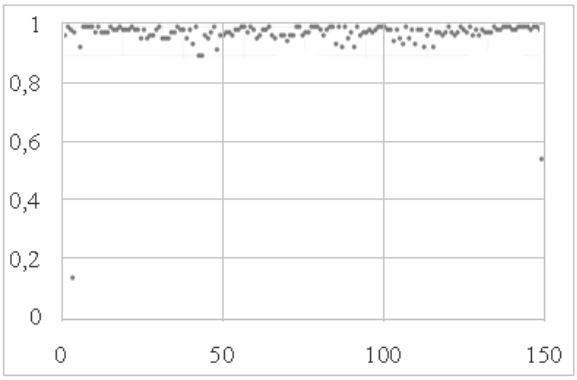

Fig. 7. The results of testing the sequence generated on the basis of a shift type generator and a cubic generator

3. The generation of sequences with increased cryptographic strength

The cryptographic resistance of encryption systems depends directly on the degree of randomness of the used numbers sequence. Provided that the random sequence of the generator satisfies the tests using statistical tests, then it can be considered random. However, this is not sufficient enough condition to ensure the cryptographic strength of the random number generation algorithm. It is considered that the sequence is cryptographically safe if it has the property of unpredictability of the next generated number. As a rule, a random number generator has this property.

Let us consider the algorithm for generating random number sequences with increased cryptographic strength. The essence of the method is as follows:

1) using the first chaos generator, forming the set of N random numbers in the interval]0;1[:

$$x_1, x_2, x_3, \ldots, x_N \tag{6}$$

2) the interval from 0 to 1 is divided into z equal parts (for example, $z = 2$, or $z = 3$, or $z = 4$, etc.);
3) the first subset is selected from z numbers, for example, with $z = 3$ selected are numbers x_1, x_2, x_3, and x_1 corresponds to the 1st interval, x_2 – 2nd interval, x_3 – 3rd interval;
4) using the second generator, random number y_j is formed in the interval]0;1[;
5) if $0 < y_j < 0.33$, then selected is the number x_1, if $0.33 < y_j < 0.66$, then x_2, if $0.66 < y_j < 1$, then x_3;

If $0.33 < y_1 < 0.66$, then selected is number x_2. Similarly, the next number is selected from the subset $\{x_4, x_5, x_6\}$. If $0.66 < y_2 < 1$, then selected is number x_6. When $0 < y_3 < 0.33$ the selected number is x_7, etc.

The process of the random sequence generation when $z = 3$ is shown in Fig. 8.

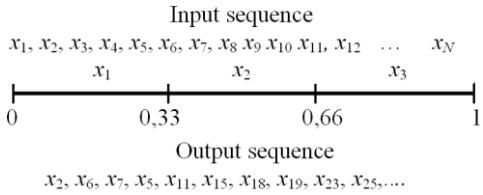

Fig. 8. The process of generating random sequence when z = 3

Thus, as the result obtained will be a random sequence

$$x_v, x_{z+v}, x_{2z+v}, x_{3z+v}, \cdots, ; \quad (7)$$

where $v = 1 \ldots z$ – the number of the selected numeric in the subset.

Next, the sequence (6) is converted into a binary sequence, taking into account the system of the following conditions: $x_i < 0.5$, then $s_i = 0$; $x_i \geq 0.5$, then $s_i = 1$.

Obviously, the degree of randomness of the generated numbers depends on the amount of the Z numbers in the used subset.

4. Conclusion

The results of the research have shown that not all chaos generators fully satisfy the requirements of the NIST test system. It means that the use of chaos generators for the formation of binary sequences may be limited. The chaos generators with logistic (2) and cubic (3) mappings, and also the chaos generators with a shift type display (4), did not pass the tests for randomness in full, because the number of values $P(\chi^2)$ went beyond the limit of the confidence interval.

It has been proposed to improve the qualitative characteristics of the binary sample due to the XOR operation and the use of several source sequences formed using chaos generators. For the task of the experiment there were used a shift type generator and a cubic generator, which showed unsatisfactory results during testing.

The sample obtained while using XOR received higher marks than while conducting tests using the NIST system (Fig. 5), because for the most tests the value $P(\chi^2)$ is in the zone of the confidence interval. It can be supposed that the use of the large number of chaos generators (2-4) significantly stabilizes the statistical characteristics of a binary sample. However, the number of operations for the formation of one bit will increase. This must be considered when constructing the source of a binary sequence.

Proposed is the algorithm for increasing the cryptographic stability of the generator due to the uncertainty of the number appearance in a random sequence. It is achieved by the use of subsets from Z numbers over the entire interval of the formation sequence. With the increasing Z, the cryptographic strength of the algorithm for generating random sequence of numbers rises. However, more implementation is required.

References

[1] Ipatov V. P.: Broadband Systems and Code Separation of Signals. Principles and Applications. Tech-Nosfera, Moscow 2007.
[2] Knuth D.: The Art of Programming. Williams, 2000.
[3] Korchynskyi V., Filkin K.: Analysis of Models of Primary Sensors of Pseudo-random Numbers. Proc. of Semin. young science students and students of the Advanced Telecommunications Technology and Information Technology, 2007, 20–24.
[4] Korchynskyi V.: A Method of Increasing the Secrecy of Transmission by Timer Signals in Communication Systems with Code Division of Channels. Visnik of the V. Dahl East Ukrainian National University 15(204)/2013, 93–99.
[5] Korchynskyi V: A Model of a Noise Signal for Transmitting Confidential Information. Bulletin of NTU "KhPI" 11(985)/2013, 89–94.
[6] Kupriyanov A. I., Sakharov A.: Theoretical Foundations of Electronic Warfare, University Book, Moscow 2007.
[7] Kuznetsov S. P.: Dynamic Chaos. Physico-mathematical literature, Moscow 2006.
[8] Zakharchenko M., Korchynskyi V.: Transmission Secrecy in Communication Systems with Chaotic Signals Measuring and enumerated technology in technological processes. International science and technology technical magazine 3/2013, 161–164.

D.Sc. Volodymyr Korchinskyi
e-mail: vladkorchin@ukr.net

Associate Professor, Department of Information Security and Data Transmission.
In 2007, he defended a dissertation on the specialty "Telecommunication systems and networks". In 2012, he was awarded the academic title of Associate Professor of the Department of Information Security and Data Transmission at Odessa National Academy of Telecommunication named after O.S. Popov. In 2014, he defended a doctoral dissertation on the specialty "Information Security Systems".

http://orcid.org/0000-0003-3972-0585

Ph.D. Vitalii Kildishev
e-mail: kildishev@ukr.net

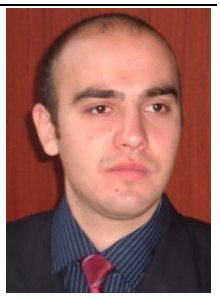

Associate Professor, Department of Information Security and Data Transmission.
In 2008, he defended a dissertation on the specialty "Telecommunication systems and networks". In 2013, He was awarded the academic title of Associate Professor of the Department of Information Security and Data Transmission. The field of his scientific interests covers the enhancing security of information transmission in telecommunication systems based on integrated processing methods.

http://orcid.org/0000-0002-7121-4060

Ph.D. Oleksandr Riabukha
e-mail: ryabukha@gmail.com

Senior Lecturer, Department of Information Security and Data Transmission.
In 2012, he defended a dissertation on the specialty "Telecommunication systems and networks".
The field of his scientific interests covers the enhancing security of information transmission in telecommunication systems based on integrated processing methods. He is the author of over 20 scientific papers in the field of communication and information protection.

http://orcid.org/0000-0001-7402-0395

M.Sc. Oleksandr Berdnikov
e-mail: berdnikov2000@gmail.com

In 2001, he graduated from the department of multichannel telecommunications ONAT them. A.S. Popova. Since 2017, He is studying at the graduate school of the Odessa National Academy of Communications named after A.S. Popov, specialty 125 – Cybersecurity. The field of his scientific interests covers the protection of transmitted information from unauthorized access based on dynamic chaos.
He have authored over 7 scientific papers in the field of communication and information protection.

http://orcid.org/0000-0003-0058-9997

otrzymano/received: 15.11.2019 *przyjęto do druku/accepted: 15.02.2020*

http://doi.org/10.35784/iapgos.914

THE INCREASE OF THE ENERGY EFFICIENCY OF THE RADIO EQUIPMENT BASED ON THE USE OF MODULATION BY ORTHOGONAL HARMONIC CARRIERS

Sergey Toliupa[1], Vladimir Nakonechnyi[1], Alexander Trush[2]
[1]Taras Shevchenko National University of Kyiv, Department of Cybersecurity and Information Protection, Kyiv, Ukraine
[2]Taras Shevchenko National University of Kyiv, Department of Network and Internet Technologies, Kyiv, Ukraine

Abstract. *Most of the theoretical results, as well as methods using OFDM modulation, are obtained in order to increase the rate of information transmission with energy constraints and the bandwidth. For broadband radio access systems, this task is primarily due to the commercial purpose of these systems and the desire of the communications developers to provide high-speed wireless access to the Internet as much as possible at the same time. This article is devoted to the issue of increasing the energy efficiency of radio equipment using modulation orthogonal harmonic carriers under conditions of intentional interference and frequency-selective fading while ensuring a given level of reliability and speed of information transmission.*

Keywords: radio communication, carrier, signal, noise, energy efficiency

ZWIĘKSZENIE WYDAJNOŚCI ENERGETYCZNEJ SPRZĘTU RADIOWEGO W OPARCIU O STOSOWANIE MODULACJI PRZEZ ORTOGONALNE HARMONICZNE

Streszczenie. *Większość wyników teoretycznych, a także metod wykorzystujących modulację OFDM, uzyskuje się w celu zwiększenia szybkości transmisji informacji z ograniczeniami energetycznymi i przepustowością. W przypadku szerokopasmowych systemów dostępu radiowego zadanie to wynika przede wszystkim z komercyjnego celu tych systemów i chęci twórców komunikacji, aby zapewnić szybki bezprzewodowy dostęp do Internetu w jak największym stopniu w tym samym czasie. Artykuł poświęcony jest zwiększeniu wydajności energetycznej urządzeń radiowych z wykorzystaniem modulacji ortogonalnych nośników harmonicznych w warunkach zamierzonego zakłócania i selektywnego opadania częstotliwości, przy jednoczesnym zapewnieniu określonego poziomu niezawodności i prędkości transmisji informacji.*

Słowa kluczowe: komunikacja radiowa, nośna, sygnał, hałas, efektywność energetyczna

Introduction

Methods of optimizing OFDM signals, improvement of algorithms for their formation and processing have been the subject of intensive theoretical research in recent years. However, most of the theoretical results, as well as methods implemented in existing radio communication systems (SRZs) using OFDM modulation, are obtained to increase the speed of information transmission with energy constraints and bandwidth (increasing the frequency efficiency of the system). For broadband radio access systems, this task is primarily due to the commercial purpose of these systems and the desire of the communications developers to provide high-speed wireless access to the Internet as much as possible at the same time. For radio communication systems, where, as a rule, the information load on communication lines is known, the task of increasing energy efficiency with restrictions on bandwidth, bandwidth and reliability [1–3] is more relevant.

Consequently, the task of increasing the energy efficiency of SRH in the conditions of multipath of radio waves is relevant and has not only a theoretical but also a great application value for ensuring the necessary level of readiness of radio communication systems by increasing the timeliness, probability and concealment of management.

1. Theoretical indicators for improving energy efficiency of radio communication systems (SRZ)

An important indicator of the effectiveness of radio communication systems (SRZ) is energy efficiency, which, the greater it is, the less energy is needed to transmit one bit of information. Advantages of increasing energy efficiency are obvious: a minimization of transmitter radiation power, an improvement of electromagnetic compatibility of radio-electronic means, an increase of concealed transmission of information, a minimization of power consumption [4].

The essence of the proposed method is to adapt the values of the parameters of the OFDM signal of the radio communication means of destination, which are optimal for the criterion of the maximum of the energy efficiency indicator with a given reliability of information transmission and throughput.

Setting objectives.

Specified: parameters of the transmitter and the communication channel $\Psi = \{\psi_i\}$, $i = \overline{1, 10}$, where $\psi_1 \ldots \psi_{10}$ – the number of subcarriers, the power of the useful signal, the ratio of the signal/noise in the channel, the operating frequency, the type of modulation, the rate of information transmission (required bandwidth), set of correcting codes with appropriate parameters: length of the code combination, the speed of the correction code, the value of the code distance, the limit value of the signal-to-noise ratio in the channel, at which the correction code begins to win with modulation without coding. The initial mode of operation, which provides the required speed of information $v_{i\ parm}$ transmission, involves the use of all subcarriers and the least speed correction code.

It is necessary: to determine the optimal values of the signal parameters (the number of active subcarriers and their numbers, the correction code, the transmitter power and its distribution among the subchannels), at which the energy efficiency of the SRZ β_E is maximized when the limitations on the probability of a false signal $P_b \le P_{\text{b parm}}$ reception and the rate of transmission in the channel $v_i \ge v_{i\ parm}$.

Restrictions: the type of correction code – ergonomic codes with speed R = 0.5–0.9; type of signal – FM-4; number of subcarriers N = 256; the maximum acceptable probability of the false reception of signals $P_{\text{b parm}} = 10^{-5}$.

Assumption: the state of the transmission characteristic of the H connection channel is known and does not change during the transmission of the symbol before transmitting the next OFDM symbol:

$H_{\text{zag}} = H_1, H_2, \ldots, H_N = \sum_{i=1}^{N} H_i$, where H_i is the transfer characteristic of the i-subchannel; the amplitude characteristic of the power amplifier of the transmitter is linear – there are no nonlinear distortions of the signal.

The task of determining the values of the parameters of the OFDM signal with the maximum energy efficiency indicators is reduced to a typical optimization problem [6]. The system of equations for solving the optimization problem has the form

$$\begin{cases} \beta_E = F_1(v_{\mathrm{i}}, \Delta F, M, n, R, d, P_{\mathrm{s}}, N_{\mathrm{A}}) \to \max \\ P_{\mathrm{b}} = F_2(P_{\mathrm{s}}, M, n, R, d, N_{\mathrm{A}}) \le P_{\mathrm{b\,parm}} \\ v_{\mathrm{i}} = F_3(M, R, N_{\mathrm{A}}) \ge v_{\mathrm{i\,parm}} \end{cases} \tag{1}$$

where n is the length of the code combination, P_s is the signal strength, M is the signal strength dimension, R is the correction code rate $R = k / n$, k is the number of information bits in the code combination length n, d is the code distance, N_A is the number of active subcarriers, ΔF – the width of the spectrum of the signal.

Let's expand the function of the system of equations (1). Information speed is defined as

$$v_i = \frac{B}{T_S} = \frac{N \cdot \log_2 M \cdot R}{T_S} \tag{2}$$

where T_s – duration of the symbol; B is the number of information bits transmitted in one OFDM character. In the case of adaptive power distribution (ARP), the signal/noise ratio at the input of the receiver is aligned in all sub-channels and will take values Q^2_{mid}. Let's express the value of the average of all sub-channels of the signal/noise ratio:

$$Q^2_{\mathrm{mid}} = P_s \cdot \frac{k}{n} / \sum_{i=1}^{N_A} G_{0i} \tag{3}$$

where G_{0i} is the spectral density of the noise power in the i-th sub-channel.

Energy efficiency is determined by [2] as

$$\beta_E = v_i / Q^2_{mid} \tag{4}$$

The probability of an error in the formula when applying the correction code is determined by the expression

$$P_{\mathrm{pom}} \ge \sum_{j=s_{\mathrm{vip}}+1}^{n} C_n^j P_{\mathrm{pom}}^j (1 - P_{\mathrm{pom}})^{n-j} \tag{5}$$

where P – the probability of erroneous decoding of the code combination $s_{\mathrm{vip}} = (d-1)/2$ – the multiplicity of errors that the code corrects, j – the multiplicity of the error in the block of n elements, P^j_{pom} – the probability of error occurrence in the sequence of transmitted code elements, $C_n^j = n! / j!(n-j)!$ – the binomial coefficient, which is equal to the number of different combinations of j errors in the block with n characters. The value is determined by the type of signal modulation and is calculated taking into account the encoding rate R:

$$P_{\mathrm{pom}} = \left[1 - \Phi\left[\sqrt{2Q^2_{\mathrm{mid}} R}\right]\right]$$

where Φ is the Krampa function [2].

Then, taking into account the formulas (3) and (4)

$$P_{\mathrm{b}} = \sum_{j=(d+1)/2}^{n} C_n^j \cdot \left[1 - \Phi\sqrt{2Q^2_{\mathrm{mid}}}\right]^j \cdot \left[1 - \left(1 - \Phi\sqrt{2Q^2_{\mathrm{mid}}}\right)\right]^{n-j}$$

From the analysis of system (1), it follows that its computational complexity in real time is not acceptable. However, if you somehow change the order of the task, the desired result can be obtained more easily. First, with fixed power P_s, the values of the parameters that provide the minimum probability of error P_b are found. Since the values of ΔF, M, T_S, according to the output data are constant, they can be replaced by B. Thus, the system of equations for solving the optimization problem is transformed into the form:

$$\begin{cases} P_{\mathrm{pom}} = \sum_{j=(d+1)/2}^{n} C_n^j \cdot \left[1 - \Phi\sqrt{2Q^2_{\mathrm{mid}}}\right]^j \cdot \\ \cdot \left[1 - \left(1 - \Phi\sqrt{2Q^2_{\mathrm{mid}}}\right)\right]^{n-j} \to \min \\ B = N_{\mathrm{A}} \cdot R \ge B_{\mathrm{parm}} \\ Q^2_{\mathrm{mid}} \ge Q^2_{\mathrm{bor}} \\ P_{\mathrm{s}} = \mathrm{const} \end{cases} \tag{6}$$

It is advisable to solve the presented problem of conditional discrete optimization using a directed selection of valid variants using an iterative algorithm.

The technique of choosing the optimal values of the OFDM signal parameters, the block diagram of the implementation, algorithm of which is presented in Fig. 1, consists of the following steps.

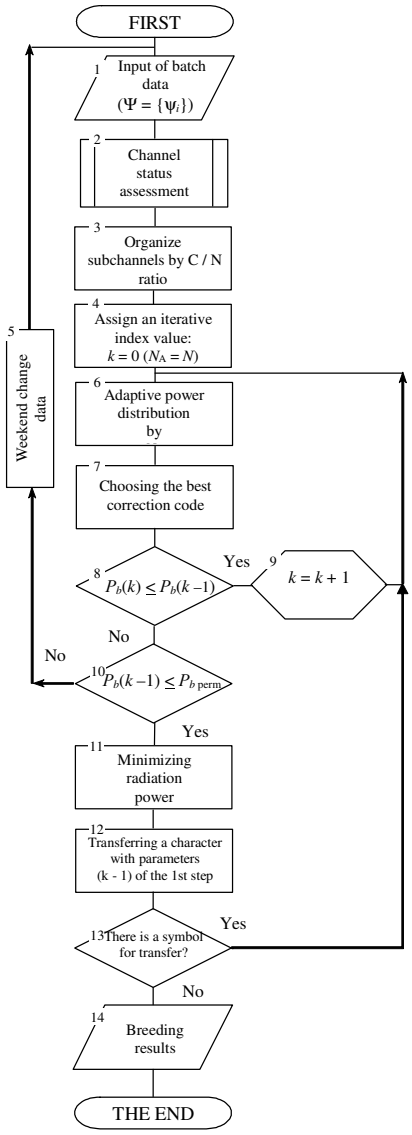

Fig. 1. The block diagram of the algorithm for implementing the selection method of optimal values of the OFDM signal, depending on the status of the link

Input of input data. The parameters of the transmitter and communication channel $\Psi = \{\psi_i\}$, are entered, as well as the admissible value of the probability of false signal $P_{\mathrm{b\,parm}}$ reception and the minimum required information transmission rate $v_{\mathrm{i\,parm}}$.

Assessment of the transmission characteristics of the communication channel. At this stage, the state of the multi-channel communication channel is evaluated and its transfer characteristic is determined.

Arranging subchannels in order of decreasing ratio of signal/noise at the receiver input. At this stage, the results of evaluation of the transfer characteristics of the channel are an assignment of sequence numbers to each subchannel in the order of decreasing ratio of signal/noise (worse subchannels have larger sequence numbers): $Q_1^2 \geq Q_2^2 \geq ... \geq Q_N^2$

Assigning the value of the iteration index. The choice of the optimal values of the OFDM signal parameters is an iterative procedure for identifying the step numbers from which the iteration index k is entered. The maximum possible number of active subcarriers ($N_A = N$) corresponds to $k = 0$. At each subsequent step of the iterative procedure ($k = k + 1$), the worst-case subcarrier signal/noise ratio ($N_A = N–1$) is disconnected. Disconnecting subcarriers with low signal/noise ratio reduces the harmful effects of interference and frequency-selective fading on the probability of false reception.

Adaptive power distribution between active subcarriers. At this stage, in the first place, the average value for all active Q_{mid}^2 subcarriers is determined:

$$Q_{\text{mid}}^2(k) = \frac{1}{N_A}\sum_{i=1}^{N_A} Q_i^2$$

Then, the coefficient of power distribution is determined as follows:

$$K_i(k) = \frac{Q_{\text{mid}}^2(k)}{Q_i^2}$$

Choosing the best correction code. At this stage, from the finite number of correction codes determined by the initial data, those that meet the information rate requirements are selected first and for them the average signal/noise ratio in the channel exceeds the limit value Q_{bor}^2 at which the code begins to gain. Then, by sequential scanning, the code is determined which provides the best noise immunity of the acceptance:

$$\begin{cases} v_i(k) \geq v_{i\ parm},\ Q_{\text{bor}}^2 < Q_{\text{mid}}^2(k) \\ P_b(k) = \min \end{cases}$$

If no code satisfies the condition, then at this stage the mode is selected without the use of interference-free encoding.

Checking the conditions for the iteration procedure. At this stage, the condition is checked

$$P_b(k) \leq P_b(k-1)$$

Under condition, the value of the iteration index ($k = k+1$) is increased, the next subcarrier with the lowest signal/noise ratio is disconnected, and the repeat of paragraphs 4-7 is performed. If the condition is not met, the iterative procedure stops and the condition is checked

$$P_b(k-1) \leq P_{b\ parm}$$

Minimization of radiation power. At this stage, if the condition is fulfilled, the total radiation power of the transmitter is reduced to a certain threshold, at which the probability of error becomes equal to the maximum allowable:

$$P_b \leq P_{\text{b parm}}$$

Consequently, the optimal values of the parameters of the next OFDM symbol are determined: N_A, K_i, n, k, d, P_s, the information about the values that is transmitted as a part of the service information for the counter station.

2. An algorithm for implementing a method of selecting optimal OFDM signal values

It is obvious that the proposed iteration procedure consists, in the gradual disconnection, of subcarriers with small gain factors (high power of effective noise), adaptive power distribution between active subcarriers for equalizing the transmission characteristics of the channel and the choice of correction code, which ensures the least probability of erroneous reception. After this, the reserve for noise immunity is exchanged to reduce the total radiation power of the transmitter (that is, the power decreases until the probability of error becomes equal to the allowable value

$$P_b \leq P_{\text{b parm}}$$

The sub-carrier disconnection procedure continues until the disconnection of another subcarrier results in an increase of the probability of false acceptance in the system.

After that, one needs to find the value at which, in an explicit form, it is impossible to solve equation (5) with respect to the variable. Therefore, for solution (5), it is expedient to apply the half-division method.

The proposed iteration procedure is the gradual disconnection of subcarriers with small gain factors (high power of effective noise), adaptive power distribution between active subcarriers in order to equalize the transmission characteristics of the channel and the choice of the correction code, which ensures the least probability of erroneous reception [7–8]. After this, the reserve for noise immunity is exchanged to reduce the total radiation power of the transmitter (that is, the power decreases until the probability of error becomes equal to the allowable value

$$P_b \leq P_{\text{b parm}}\ .$$

To evaluate the effectiveness of the proposed methodology, using the recommendations, an imitation model was developed in the MathCad programming environment.

The program that implements the developed model simulates the work of the radio line for the following cases:

1) without adaptation in radio traffic (system 1);
2) with the adaptation of the radiation power, that is, the ARP algorithm (system 2).
3) using the developed method of selecting the optimal values of the OFDM signal parameters, depending on the state of the communication channel (system 3).

Systems 1 and 2 operate using the least speed code from a given set (R = 0.5) and do not use the sub-carrier disconnection algorithm. It can be assumed that system 1 reproduces the algorithm of the IEEE 802.11a standard using OFDM modulation. However, it should be noted that the evaluation of efficiency compared with this system is rather conditional, since in the case of deterioration of the connection quality to the inadmissible level the IEEE 802.11a system passes to another operating frequency [9].

The assessment of the effectiveness of the developed methodology was carried out by comparing the energy efficiency indicators for systems 1, 2 and 3 with given identical output data. Fig. 2 shows the dependence of the power gain of the transmitter ΔP_c for the three systems from the average signal/noise ratio in the channel at a given depth of frequency-selective fade.

The abscissa line corresponds to the use of the maximum possible transmitter power, that is, in principle, it is impossible to implement positive values in the axis (under such conditions the system cannot provide the exchange of information with a given quality), and calculations for this area were conducted to compare the efficiency of systems 1 to 3 to each other. From the charts it is clear that the system 3 allows to increase the energy efficiency index, depending on the depth of selective fading, by a value of 5–7.5 dB in comparison to system 1 and by 2–3 dB in comparison to system 2.

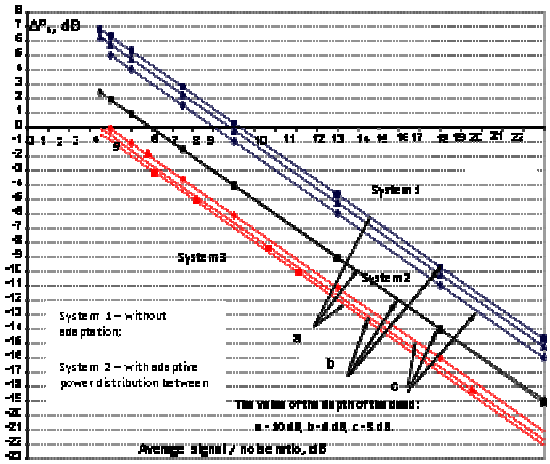

Fig. 2. Dependence of the growth of the transmitter power from the average signal/noise ratio in the channel for different values of the fading depth

Fig. 3 shows the dependence of the transmitter power gain on the target bandwidth for a channel with an average signal-to-noise ratio of 10 dB and a dead-end depth of 6 dB.

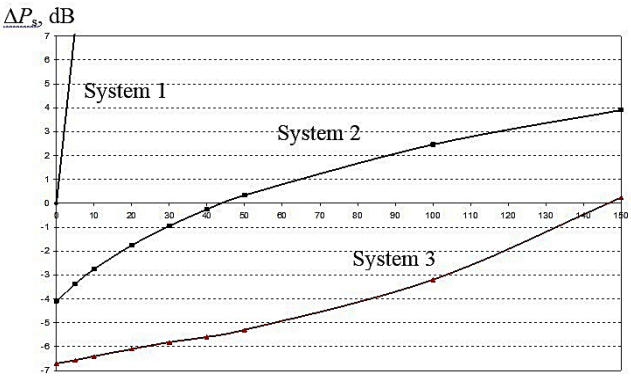

Fig. 3. Dependence of the power gain of the transmitter on the width of intentional bandwidth for a medium-sized channel, 10 dB signal and noise, and 6 dB fading depth.

The noise power is selected to produce a 0 dB signal/noise ratio in the subchannel of the system 1. It can be seen that system 3 in such conditions is capable of transmitting information at a bandwidth of a powerful interference that overlaps about 50% of the signal spectrum. For system 2, it is sufficient to diminish the noise of the signal to less than 20% of the signal spectrum, to disable it, and system 1 stops functioning with the given quality when overcoming the interruption of at least one subcarrier.

The estimation of the computational complexity of the implementation of the developed method showed that for the given output data and when using the ADSP-21261 processor, the formation of a signal with optimal parameter values can be carried out in real time with a delay required for the transmission of information about these values through the service feedback channel.

3. Conclusion

The optimal values of the signal parameters for a particular state of the communication channel are determined from the finite number of valid variants, which simplifies the practical implementation of the modem equipment of adaptive radio communication systems. The difference of the proposed methodology is that the optimal values of the OFDM parameters are determined by the criterion of the maximum of the energy efficiency in the conditions of frequency-selective fade and the effect of intentional noise, and the signal parameters the values of which are determined when solving the optimization problem are: the number of active subcarriers, the type of correction code, the transmitter power and the amplification frequencies of the frequency subchannels.

A positive effect of the implementation of the developed methodology is provided by the following interconnected factors: the maximization of energy efficiency; the minimization of transmitter power; the improvement of electromagnetic compatibility of radio-electronic means; the increase of the secret of the information transfer; the minimization of energy consumption.

References

[1] Coleri S., Ergen M., Puri A., Bahai A. : Channel estimation techniques based on pilot arrangement in OFDM systems. IEEE Trans. Broadcast 48(3)/2002, 223–229.

[2] Morelli M.: A Comparison of Pilot-Aided Channel Estimation Methods for OFDM Systems. IEEE Trans. on Signal Processing 49(12)/2001, 3065–3073.

[3] Kuvshinov O. V.: OFDM technology: an overview of problems and ways of solving them. Communication 1/2008, 42–46.40.

[4] Pickholtz R. L.: Theory of Spread-Spectrum Communications. IEEE Trans. Commun. Com-30(5)/1982, 855–884.

[5] Edfors O., SandellM., van de Beek J. J. et al.: OFDM channel estimation by singular value decomposition. IEEE Trans. Commun. 46(7)/1998, 931–939.

[6] Li Y.: Robust channel estimation for OFDM systems with rapid dispersive fading channels. IEEE Trans. Commun. 46/1998, 902–915.

[7] Toliupa S., Gursky T. G., Voskolovich A. I.: An analysis of the method of evaluating the parameters of the channel's channels in the link. News of the Sovereign to the University of Information Technology 9(3)/2011, 194–204.

[8] Toliupa S., Babenko T., Parhomenko I.: The method of forming and signal processing aimed at improving stealth and energy efficiency. 2nd International Conference Advanced Information and Communication Technologies (AICT), 2017, 304–308.

[9] Gursky T.G.: Mathematical model of radio line using OFDM technology in the conditions of influence of intentional interference. Proceedings of VITI NTU "KPI" 2/2008, 9–16.

Prof. Sergey Toliupa
e-mail: tolupa@i.ua

His scientific and practical interests are related to areas such as intelligent control systems, the direction of improving the efficiency of information technology, information security systems, cybersecurity and cyber defense. He is the author of 5 monographs and over 150 scientific and methodological works, 16 textbooks and manuals.

http://orcid.org/0000-0002-1919-9174

Prof. Vladimir Nakonechnyi
e-mail: nvc2006@i.ua

His scientific and practical interests are related to areas such as intelligent control systems, the direction of improving the efficiency of information technology, information security systems, cybersecurity and cyber defense. He is the author of 4 monographs and over 80 scientific and methodological works, 7 textbooks and manuals.

http://orcid.org/0000-0002-0247-5400

Ph.D. Alexander Trush
e-mail: trush.viti@gmail.com

His scientific and practical interests are related to areas such as information and communication systems and networks, systems of technical protection of information, cyber defense. He is the author of over 35 scientific and methodological works, 2 textbooks.

http://orcid.org/0000-0001-8473-9387

otrzymano/received: 15.11.2019 *przyjęto do druku/accepted: 15.02.2020*

http://doi.org/10.35784/iapgos.913

SYNTHESIS OF SAFE BEHAVIOR ALGORITHMS OF RADIOELECTRONIC SYSTEMS FOR CRITICAL APPLICATIONS

Leonid Ozirkovskyy, Bohdan Volochiy, Mykhailo Zmysnyi, Oleksandr Shkiliuk
Lviv Polytechnic National University, Department of Theoretical Radio Engineering and Radio Measurement, Lviv, Ukraine

Abstract. *The safety of radio electronic systems for critical applications is traditionally ensured by inducing structural redundancy. This paper shows a developed technique for ensuring a required level of safety of such systems by inducing time and functional redundancy into its behavior algorithm. The defined safety characteristic is proposed for quantitative efficiency estimation of the induced redundancy. Presented in the article is the synthesis technique of safe behavior algorithms on the basis of safety characteristic minimization of increased values. The developed technique was tested through solving the synthesis problem of the behavior algorithm of the target detection radio electronic complex system.*

Keywords: safety, safety engineering, behavior algorithm, system design

SYNTEZA ALGORYTMÓW BEZPIECZNEGO POSTĘPOWANIA W SYSTEMACH RADIOELEKTRONICZNYCH DO ZASTOSOWAŃ W SYTUACJACH KRYTYCZNYCH

Streszczenie. *Bezpieczeństwo radiowych systemów elektronicznych używanych w sytuacjach krytycznych jest tradycyjnie zapewnione przez wprowadzenie redundancji strukturalnej. W pracy zaproponowano sposób zapewnienia określonego poziomu bezpieczeństwa radiowych systemów elektronicznych poprzez wprowadzenie redundancji czasowej i funkcjonalnej do algorytmu postępowania. Aby zmierzyć wydajność wprowadzonej redundancji, zaproponowano określone cechy bezpieczeństwa. Artykuł przedstawia metodę syntezy algorytmów bezpiecznego postępowania na podstawie minimalizacji wzrostu wartości określonych cech bezpieczeństwa. Opracowana metoda została przetestowana podczas rozwiązywania problemu syntezy algorytmu postępowania dla złożonego systemu radioelektronicznego przeznaczonego do wykrywania celów.*

Słowa kluczowe: bezpieczeństwo, inżynieria bezpieczeństwa, algorytm postępowania, projekt systemu

Introduction

This paper represents a problem of behavior algorithm design which is developed for a radio-electronic system and should provide a high level of functional safety. The radio electronic system, as a part of a complex technical system, performs a task of organizing control actions. As an example of such complex technical system there can be mentioned a nuclear power plant, and a radio electronic system as its information driven system [8].

The exploitation safety of a complex technical system depends on several factors which include the functional safety and reliability of the radio electronic system [9]. That is why we use in this paper the definition "radio electronic system for critical applications" – RESCA.

An effect of the disability of a complex technical system is an emergency, and one of the reasons of failure is a non-execution of the RESCA task.

Therefore, the RESCA is designed as hardware and software system with fault tolerance structure [6, 11]. It consists of different subsystems and each of them performs its objective function. A spare subsystem should be provided for each subsystem to ensure the fault tolerance of the RESCA. The spare subsystem performs its function in a different way than the main one.

The safety of the RESCA is determined by its fault-tolerant structure and robust behavior, as well as its functional behavior [5, 10]. Functional behavior is defined by an algorithm that specifies the conditions and sequence of actions performed by the RESCA subsystems and modules when performing its functions. The behavior algorithm (BA) is being developed at the stage of the RESCA system design [1, 14]. Synthesis methods of different types of algorithms are discussed in details in monographs [3, 7, 12]. However, the synthesis problem concerning safe algorithms in these works is not solved.

There are more peculiarities of the RESCA behavior algorithms– they are characterized both by a successful and an unsuccessful execution [16]. Examples of such BAs are algorithms of target searching and detection, algorithms of receiving, recording and transmitting telemetry data, algorithms of obtaining navigation data, and others. An unsuccessful execution of such BAs leads to emergencies.

Failures of BA performance are caused by operator errors, hardware and software faults, inaccurate input data, a malfunction of control and diagnostics, etc. To minimize the number of unsuccessful executions of the RESCA and, accordingly, to ensure the required level of exploitation safety, the RESCA is provided with some means of time [2] and functional redundancy [15].

Verification of the feasibility of inducing each type of redundancy should take place at the stage of the RESCA system design. A lack of such ability in modern design means forced safety testing only at the testing stage of a complex technical system [13]. However, such approach is not always acceptable due to presence of errors in the RESCA behavior algorithm, when the complex technical system falls into an emergency. Such cases can be often seen in recent years after the launches of Soyuz rocket with spacecraft Progress (2011, 2015, 2016, 2017, 2018), SpaceX spacecraft Dragon (2015), military missiles Bulava (2017) and Burevestnik (2019). The main reason, for almost all emergencies, were errors in the BA of the launcher units, control systems, navigation systems. And it is important to detect these errors at the system design stage. Fortunately, these accidents happened only with the cargo spacecrafts.

Nevertheless, all consequences of such accidents can be very significant – these are a potential death of the crew, a contamination of large areas with hazardous substances (rocket fuel, radioactive substances etc.), a risk of potential fall of explosive objects on residential buildings, etc.

Therefore, a lot of attention should be paid to the problem of synthesizing the safe behavior algorithms of the RESCA. For qualitative solving of such a problem, it is necessary to operate tools (models, methods, techniques and software) which adequately take into account all the features of the behavior algorithm of the RESCA. So, all of it allows to carry out the synthesis of BA via multivariate analysis for short period of time. It should be noted that in order to confirm the accuracy of the obtained results at the stage of system design, it is necessary to operate not one, but two methods (or more) of solving the problem of BA analysis, since fulfilled reliability simulation results will allow to reduce the volume and, accordingly, the development cost of the RESCA field tests.

1. Problem statement

In order to provide a required level of safety for the RESCA exploitation, it is necessary to minimize the probability of failure of its behavior algorithm (unsuccessful execution). This necessity demands the re-execution of critical functions in case of hardware failures, software malfunctions, or operator errors. The re-execution of certain functions within the execution time period of

the BA requires a time redundancy, which implies the re-execution of some set of the BA operational blocks [2]. Accordingly, additional cycles are induced in the BA, which should contain blocks for checking stochastic and deterministic conditions [16]. In the case of a stochastic condition, it is not possible to predict in advance how many times the cycle will be executed and, accordingly, the duration of the cycle. If the execution of a certain function in certain conditions does not lead to a positive result, then the BA should provide the possibility of transferring the execution of mentioned function from one subsystem to the other, which performs this function in a different way. It means that the successful execution of the BA is ensured by functional redundancy.

A characteristic feature of the RESCA is the limit value of the duration of each BA objective function. If this value exceeds the allowable maximum, the algorithm fails to complete its operation and the RESCA falls into a critical failure. Thus, the induction of time redundancy in the BA may not be acceptable by certain requirements of the duration. To minimize the probability of unsuccessful execution of the BA, and accordingly, an emergency of a complex technical system, it is necessary to determine the maximum number of repetitions of each cycle.

Switching to another operating block means switching the function execution to another RESCA subsystem, which performs this function in another way. If, after several repetitive cycles the RESCA fails to complete the task and the average cycle time exceeded the limit, then switching to another RESCA subsystem is done. If this subsystem is not able to perform its function, it switches to the next one. If all the functions provided in the AP are completed, then we have a successful execution. Otherwise, we have an unsuccessful execution so, accordingly, the complex technical system falls into an emergency.

Checking the induction efficiency of each of the redundancy varieties should be done at the stage of the RESCA system design and the following questions should be answered:

- for which BA functions should a repeatable cycle be induced?
- how many times should each cycle be executed?
- will the average duration of the behavior algorithm exceed the limit value?
- should another RESCA subsystem to perform a non-executed function be switched to?
- how will the induction of redundancy impact the safety of the RESCA exploitation?

Therefore, at the system design stage, designers should have some set of models, methods and techniques that will provide the efficiency estimation of the RESCA, depending on the tactical and technical characteristics of hardware, indexes of reliability, different number of repeatable cycles of behavior algorithm, an operator's reaction rate, etc.

2. Method of synthesis of safe behavior algorithms

As it was mentioned above, for the synthesis of the safe BA, it is necessary to induce time and functional redundancies, and to determine their effect on the performance of the algorithm, since the efficiency and safety indexes of the BA are closely linked. This is explained by the fact that during unsuccessful completion, the BA includes successful executions and unsuccessful executions (emergency states).

Let's consider a model of all possible options for the implementation of BA while the RESCA operation is in the form of a graph of states and transitions. To do this, one has to assume that the RESCA is supposedly monitored, and the same BA is run many times. As a result of the BA execution, the RESCA gets into different states. States of current execution are defined by determined factors that operate the BA execution process (number of operating blocks, duration of operation, number of cycles, number of paths, etc.), and the states of successful execution and the emergency states are determined by random factors that lead to the failure (failure of subsystems, operator errors) or stoppage of the BA (average duration (T_{avg}) of BA exceeds the limit value of duration (T_{lim}), external interference, etc.).

Thus, there are three groups of states:

- the states from the first group reflect the process of transition from one operating unit of the BA to another in the process of performing the objective function;
- the states from the second group are the successful completion of the BA;
- the states from the third group are the unsuccessful completion of the BA.

2.1. Characteristics of behavior algorithm exploitation safety

As a result of the execution of the behavior algorithm, the RESCA is in the first group of states for a certain period of time, the average value of which (T_{avg}) should not exceed the limit of the execution duration (T_{lim}) of the objective function. Then, depending on the external and internal factors, the RESCA changes its state to the second group or to the third group. If the RESCA stays in the first group of states over the limit value (T_{lim}), it cannot perform its task and the complex technical system falls into an emergency. If, under the $T_{avg} \leq T_{lim}$, the RESCA enters the second group of states, and it completes successfully its objective function. If the RESCA falls into the third group of states, there are two consequences for them:

- for $t \leq T_{lim}$, the RESCA can return to the first group of states as a result of re-execution of some part of the AP. Moreover, there are several transmissions into the third group of states from the first state group and back.
- for $t > T_{lim}$, the RESCA remains in the third state group because the BA falls into the state of unsuccessful execution of the task, so the RESCA causes no emergency at all.

The changes of the RESCA state to the first and the second groups are characterized by the probability of successful execution of the BA – $P_{sp}(t)$. This is the probability that the RESCA completes its task as a result of the execution of the BA. This probability is the sum of probabilities of being in k states of successful execution – $P_j(t)$:

$$P_{sp}(t) = \sum_{j=1}^{k} P_j\,(t), \tag{1}$$

The changes of the RESCA state to the third state group characterized by the probability of unsuccessful (emergency) execution of the BA – Q(t). This is the probability of an unsuccessful completion of the BA, so as a result RESCA does not perform its task.

$$Q(t) = \sum_{i=q}^{v} P_i\,(t), \tag{2}$$

where $q, \ldots, v$ – numbers of unsuccessful execution states.

However, the probability of unsuccessful completion of the task is an integral characteristic of the BA and does not allow to estimate how many times during T_{avg} time the RESCA falls into emergency state. Therefore, we propose to define a new feature of BA exploitation safety – frequency of falling into the emergency state:

$$w(t) = \frac{dQ(t)}{dt} = \sum_{q=0}^{z-1} \lambda_{z,z-q} \cdot P_{z-q}(t), \tag{3}$$

where $\lambda_{z,z-q}$ – intensity of transition to the z state of unsuccessful execution of the BA from the z-q state,

$P_{z-q}(t)$ – the probability that the RESCA stays in the z-q state,

Q(t) – the probability that the RESCA gets in critical failure state.

Obtained characteristics of BA exploitation safety have the following variants (Fig. 1).

If the RESCA does not have functional and structural redundancy, then the maximum of the safety characteristic w (t) will be at time t = 0 and the characteristic will decrease exponentially.

When redundancy is presented then frequency of falling into emergency state *w(t)* at time *t* = 0 can take the value ≥ 0 and further increase to some maximum value, and later decrease

exponentially to zero. The more redundancy (temporal and / or functional) is induced into the BA, the lower is the value of the w(t) maximum and the further to the right it moves. In other words, with an increase of redundancy, the frequency of falling into an emergency state decreases.

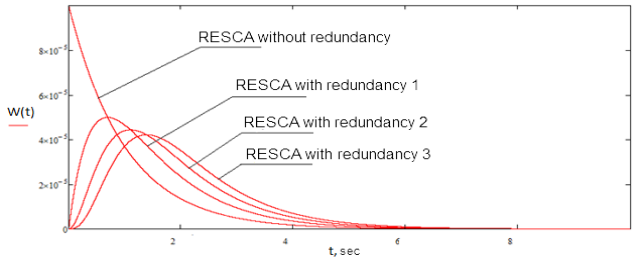

Fig. 1. Characteristics of BA exploitation safety

Figure 2 shows the relationship between safety characteristics and the RESCA efficiency.

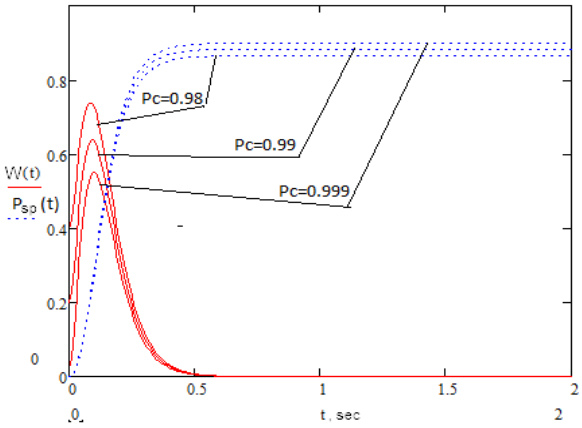

Fig. 2. Relationship between safety characteristics and the RESCA efficiency

Thus, the essence of the procedure for the synthesis of safe behavior algorithms for the RESCA is to minimize the maximum value of the frequency of falling into emergency state under the following restrictive conditions:

- a minimum permissible threshold for the probability of successful execution of the BA – $P_{lim}(t)$,
- a limited value of probability of unsuccessful execution of BA – Q(t),
- a limited value of the permissible average value of the execution duration of the BA – T_{lim}.

2.2. Technique of safe behavior algorithm synthesis

The technique of safe behavior algorithm synthesis consists of a set of methods and models presented by the scheme in Fig. 3. This technique consists of nine stages. Its essence is that at the first stage time redundancy is heuristically introduced into critical function of the BA of the RESCA to achieve successful completion. Practically its use is realized in a cyclic re-execution of certain operating blocks (functions). Such cycles of repetition of certain functions in the AP can be several dozens. Moreover, there is a certain contradiction: on the one hand it is impossible to determine the required number of repetitions, and on the other hand it is impossible to allow a loop on a certain function (causes too long cycle duration). If, after a certain number of repetitions, the subsystem is unable to complete the task, then its task is performed with some probability of successful execution by another subsystem, if it is possible. This case induces functional redundancy.

Functional redundancy is displayed in the BA by the induction of stochastic check blocks. If, under certain conditions of application, the BA with the induction of time and functional redundancy in the RESCA cannot complete the task with a given probability for a given time, the BA fails. Thus, in the first step, additional re-execution cycles (time redundancy) and stochastic checking blocks of functional redundancy need to be induced in the initial version of the RESCA behavior algorithm to provide a given level of safety for the RESCA exploitation. As a result, we get a new version of the BA for which it is necessary to select the parameters of time and functional redundancy, and operating modes of equipment and hardware to provide the necessary value of probability of execution and the average value of the execution duration of the RESCA task.

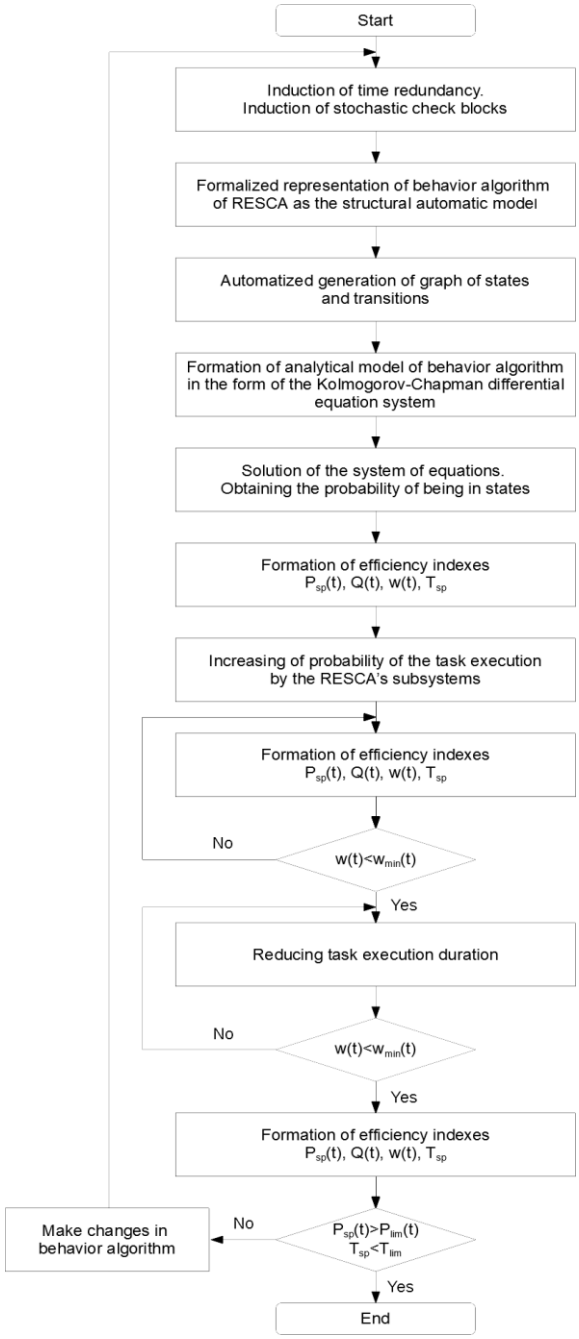

Fig. 3. Flowchart of the method of safe behavior algorithms synthesis

The second and the third steps of the technique provide a representation of the BA model in the form of a graph of states and transitions. An effective tool for such representation is improved space state method [4]. This method allows to obtain a complete state space, which includes all three of the mentioned above groups of states, it gives an ability to adequately reflect all variants of application of the RESCA behavior algorithm during the task execution.

In the second stage it is necessary to develop a structural-automatic model (SAM) [4] of the behavior algorithm. The peculiarity of such SAM is the presence of two types of check blocks (stochastic and deterministic) and one base event – the current execution of the operating block. At the third stage the model is automatically built in the form of a graph of states and transitions using the ASNA software [17].

At the fourth stage, an analytical model is formed in the form of Kolmogorov – Chapman differential equation system. This equation system is formed automatically using ASNA software. The solution of the differential equation system in the fifth stage will result in the distribution of probabilities of being in each state. From the resulting distribution, formulas are composed to determine the efficiency indexes of the BA as the sum of the probabilities of being in the respective states (the sixth step).

The obtained indexes depend on the parameters of the BA (the probability of performing the RESCA subsystems function, the average performance time of the RESCA subsystems function the probability of failure-free performance of the RESCA subsystem, the number of re-execution cycles of the BA operational units, the probability of switching to an alternative subsystem, etc.). Changing these parameters, one need to find the minimum value of the frequency of falling into emergency state – $w_{min}(t)$ in the state of unsuccessful completion of the BA (steps 7, 8 and 9).

The limiting conditions in this case are the minimum permissible limit of the task execution probability– $P_{lim}(t)$, and the maximum permissible limit value of task execution duration – $T_{lim}(t)$. If the safety characteristic w(t) takes the minimum value, and the $P_{sp}(t) \geq P_{lim}(t)$ (t) and $T_{sp} \leq T_{lim}$, then the obtained BA is safe. If this condition is not fulfilled, it is necessary to make changes in the BA and repeat all the above steps. Thus, the problem of finding the minimum value of the characteristics maximum of the BA is solved through a repeated change of the input data, which depends on the probability of the BA successful completion and its average duration.

This problem is solved with the help of ASNA software [17], which constructs new graphs of states and transitions, forms the systems of Kolmogorov – Chapman differential equations, and solves them on the basis of the BA automatic structural model. Based on these solutions, the BA exploitation safety characteristics are calculated. The technique was tested through the algorithm for searching, detecting and capturing targets of the air monitoring radio electronic system.

3. Conclusion

The application of the exploitation safety characteristics w(t) of the behavior algorithm made it possible to assess the impact of the induced time redundancy on the efficiency indexes of the radio electronic systems for critical applications.

We can estimate the frequency of behavior algorithm falling into the states of unsuccessful execution. The developed technique, then, allows system designers to minimize the frequency of behavior algorithm failures performing multivariate analysis considering both the configuration of the behavior algorithm and the hardware parameters of subsystems of complex technical system.

References

[1] Alexander R., Alexander-Bown R., Kelly T.: Engineering Safety-Critical Complex Systems. Proceedings CoSMoS 2008: Workshop on Complex Systems Modelling and Simulation. Luniver Press, 2008, 33–62.

[2] Ayoob M.; Adi W.: Fault Detection and Correction in Processing AES Encryption Algorithm. Proceedings Sixth International Conference on Emerging Security Technologies (EST), Braunschweig, Germany, 2015, 7–12.

[3] Benoit A., Robert Y., Vivien F.: A Guide to Algorithm Design. Paradigms, Methods, and Complexity Analysis. CRC Press Published, 2013.

[4] Bobalo Yu., Volochiy B., Lozinsky O., Mandziy B., Ozirkovsky L., Fedasyuk D., Scherbovskikh S., Yakovina V.: Mathematical Models and Methods for Reliability Analysis of Radio. Electronic and Software Systems. Lviv Polytechnic National University, 2013. (in Ukrainian).

[5] Dubrova E.: Fault-Tolerant Design. Springer, New York 2013.

[6] Hobbs C.: Embedded Software Development for Safety-Critical Systems. Second edition. Routledge, 2019.

[7] Kleinberg, J., Tardos E.: Algorithm design. First edition, Pearson, 2005.

[8] Pietrantuono R., Russo S.: Introduction to Safety Critical Systems. Innovative Technologies for Dependable OTS-Based Critical Systems. Challenges and Achievements of the CRITICAL STEP Project, Springer, 2013.

[9] Rausand M.: Reliability of Safety-Critical Systems: Theory and Applications. Wiley-Blackwell, 2014.

[10] Saha S., Sadi M. S.: Synthesizing fault tolerant safety critical systems. Journal of Computers 9(8)/2014, 1809–1816.

[11] Shafei E., Moawad I., Sallam H., Mostafa A.: A Methodology for Safety Critical Software Systems Planning. Proceedings 7th WSEAS European Computing Conference (ECC '13), Dubrovnik, Croatia, 2013.

[12] Skiena S.: The Algorithm Design Manual. 2 ed., Springer, 2009.

[13] Trukhanov V. M.: Reliability of Technical Systems of Mobile Units Types at the Stage of Prototypes Design and Testing. Mashynostroenie, 2003. (In Russian).

[14] Van Beek T., Tomiyama T.: Requirements for Complex Systems Modeling. Proceedings 18th CIRP Design Conference - Design Synthesis. Enschede, Netherlands, 2008.

[15] Viktorov D.: Algorithm Providing Fault Tolerance of Onboard Computing Systems with Structural and Time Redundancy. Information and Control Systems 6(2011), 30–35. (in Russian).

[16] Volochiy B., Ozirkovskyi L., Shkiliuk O. Mashchak A.: Technique of Construction Models of Behavior Algorithms of Radio Electronic Complex System using the Scheme of Paths Method. International Journal of Computing 13(3)/2014, 183–190.

[17] Volochiy B., Mandziy B., Ozirkovskyi L.: Extending the features of software for reliability analysis of fault-tolerant systems. Computational Problems of Electrical Engineering 2(2)/2012, 113–121.

Ph.D. Leonid Ozirkovskyy
e-mail: l.ozirkovsky@gmail.com

Ph.D., Associate Professor of Theoretical Radio Engineering and Radio Measuring Department of Lviv Polytechnic National University.
Experience of teaching in higher education for is over 19 years. Author of 140 scientific publications including 2 monographs, 5 textbooks. He has prepared 3 Doctors of philosophy (PhD). Research interests include the development of methods and tools for modeling functional and reliability behavior of information systems, safety engineering, reliability engineering.

http://orcid.org/0000-0003-0012-2908

D.Sc. Bohdan Volochiy
e-mail: bvolochiy@ukr.net

D.Sc., Professor of Theoretical Radio Engineering and Radio Measuring Department of Lviv Polytechnic National University
Experience of teaching in higher education for is over 40 years. Author of 280 publications, including 4 monographs, 3 textbooks, 5 inventions. He has prepared 4 Doctors of philosophy (Ph.D.). Research interests are: theory and practice of system design of radio electronic information systems.

http://orcid.org/0000-0001-5230-9921

Ph.D. Mykhailo Zmysnyi
e-mail: zmysnyim@gmail.com

Ph.D., Senior Lecturer of Theoretical Radio Engineering and Radio Measuring Department of Lviv Polytechnic National University
He has been teaching in higher educational establishments for over 5 years. The author of over 30 scientific publications. Research interests include the development of methods and tools for modeling functional and reliability behavior of fault-tolerant systems with majority structure.

http://orcid.org/0000-0002-3384-6139

Ph.D. Oleksandr Shkiliuk
e-mail: oleksandr.p.shkiliuk@lpnu.ua

Ph.D., Senior Lecturer of Theoretical Radio Engineering and Radio Measuring Department of Lviv Polytechnic National University
He has been teaching in higher educational establishments for 5 years. The author of over 30 scientific publications. Research interests include the development of methods and tools for modeling functional and reliability behavior of algorithms of radio electronic critical systems.

http://orcid.org/0000-0001-9237-4808

otrzymano/received: 15.11.2019 *przyjęto do druku/accepted: 15.02.2020*

http://doi.org/10.35784/iapgos.911

METHOD FOR ASSESSING THE STRUCTURAL RELIABILITY OF NETWORKS WITH UNDETERMINED TOPOLOGY

Nina Kniazieva, Alexey Nenov, Irina Kolumba

Odessa National Academy of Food Technologies, Faculty of Computer Engineering, Programming and Cyber Security, Odessa, Ukraine

Abstract. *This paper shows the relevance of the task of assessing the structural reliability of networks with undetermined topology. Proposed is a method for assessing the structural reliability of networks of undetermined topology based on taking into account the basic structural characteristics of the network (the number of nodes and branches, the degree of network connectivity, the maximum allowable rank of paths, and others). To obtain an estimate of the structural reliability for a network of any dimension and any topology, expressions are proposed in the scientific research to determine the number of paths of various ranks, which must be taken into account when calculating the structural reliability index by the upper and lower bounds method.*

Keywords: network of undetermined topology, structural reliability, route rank, number of routes of a certain rank, upper and lower bounds

METODA OCENY STRUKTURALNEJ NIEZAWODNOŚCI SIECI O NIEOKREŚLONEJ TOPOLOGII

Streszczenie. *Ten artykuł pokazuje znaczenie zadania polegającego na ocenie niezawodności strukturalnej sieci o nieokreślonej topologii. Proponowana jest metoda oceny niezawodności strukturalnej sieci o nieokreślonej topologii, która oparta jest na uwzględnieniu podstawowych cech strukturalnych sieci (liczba węzłów i rozgałęzień, stopień połączenia z siecią, maksymalna dopuszczalna ranga ścieżek itp.). Aby oszacować strukturalną niezawodność sieci o dowolnej wielkości i dowolnej topologii, badania naukowe proponują wyrażenia algebraiczne, które określają liczbę ścieżek o różnych rangach, które należy wziąć pod uwagę przy obliczaniu wskaźnika niezawodności strukturalnej, używając do tego metody opartej na kresach górnych i dolnych wskaźnika.*

Słowa kluczowe: sieć o nieokreślonej topologii, niezawodność strukturalna, ranga ścieżki, liczba ścieżek o określonej randze, górne i dolne kresy

Introduction

The development strategy of modern communication networks is currently aimed at meeting the growing needs of users and ensuring the required quality of the services. In this regard, there is a tendency to a constant increase in the volume of transmitted data and the complexity of the network structure. The characteristic features of modern networks are the priority use of wireless access and the introduction of self-organization mechanisms into the network. Communication networks are increasingly becoming decentralized, wireless, do not have a constant structure, and the number of nodes and connections between nodes are random variables in time. Each node of such a network can forward data destined to other nodes. The data transfer route is determined dynamically, based on the connectivity of the network at a certain point in time [10]. Moreover, in networks with an undetermined topology, multi-path routing is often used, the aim of which is to provide the source node with the ability to select one of several possible routes to a specific destination node. This approach allows one to optimally use the capacity of the communication channel and increase the overall network bandwidth [8]. Additionally, network fault tolerance and transmission reliability are provided.

A number of scientific papers by A. Ye. Kucheryavy [10], A. V. Roslyakov [15], A. V. Prokopyev, Ye. A. Kucheryavy [9], A. Goldsmith [3], Neha Rathi and others are devoted to the study of modern communication networks with an undetermined topology and elements of self-organization. Most researches note that the use of networks with an undetermined topology has several advantages over networks of a traditional (certain) topology due to the possibility of self-configuration, self-optimization and self-healing. Such network characteristics allow the adaptation of devices when changing network parameters (for example, the number of users, signal level, level of external interference, etc.) and provide redistribution of functions between devices in the event of failure of any network nodes to increase its reliability and fault tolerance [7]. The introduction of self-organization mechanisms can significantly expand the client base and the range of services provided to network users [10].

Reliability remains one of the network requirements presented in the recommendations of the International Telecommunication Union (ITU-T). So, according to ITU-T Recommendation X.120, the network must be safe, reliable and accessible at any time [16]. The issue of reliability is especially relevant for networks with an undetermined topology. Due to the dynamically changing structure and the lack of centralized management, this type of network is more vulnerable in comparison with fixed topology networks.

The term “network reliability” is understood to mean the property of the network to keep in time within the established limits the values of all parameters characterizing the ability to perform the required functions in the given modes and conditions of use [17]. Network reliability characteristics should provide users with the opportunity to continuously receive services in the conditions of technical failures, operational errors, and also take into account possible threats and risks.

Reliability of networks is ensured by the use of reliable equipment and the introduction of redundancy in the network structure to increase its fault tolerance. Since communication networks with an undetermined topology and elements of self-organization belong to complex structural systems, issues of assessing structural reliability are of particular importance for such networks.

Currently, there are works devoted to the problem of reliability of complex communication systems. These are the works of V. A. Netes [12], N. N. Egunov and V. P. Shuvalov [5], A. V. Kharybin. The structural reliability of self-organized networks is the subject of a number of works by Rudenko and D. A. Migov [11]. In these works, the object of reliability assessment are networks of an initially given structure described by adjacency matrices and other network characteristics. The goal of the classical network analysis problem of a certain topology is to determine the structural reliability of a functioning network or the resulting design solution, presented in the form of some structure [6]. However, in the case where the scale of the network is known, however, the network topology has not yet been determined (at the design stage, for example) or is constantly changing (at the operation stage), for a given (known) set of nodes, the set of branches is unknown. In this case, the network is characterized only by the number of nodes and branches. Therefore, the existing methods for assessing structural reliability, focused on applications for networks with a previously known topology, in cases of networks with an undetermined topology, are of little use.

When considering problems related to the analysis of the structural reliability of communication networks, a random graph is usually used as a network model [1, 2, 11, 13]. Among these models classical are, first of all, the Erdős–Rényi (*ER*) model

(G (n, p)), proposed and studied by the authors at the turn of the 50–60s of the XX century [2], and also its generalization – the model G (Hn, p) [13].

In addition, various restrictions and refinements of this model are introduced and studied: communications or nodes can be unreliable, the presence of dedicated network nodes, restrictions on the diameter of the network, and others. A large number of studies are carried out in the field where the nodes are considered completely reliable and do not fail. However, a number of works are devoted to the study of the structural reliability of networks where it is nodes that are unreliable, for example, [13].

As a reliability indicator, usually taken are the connectivity probability of the corresponding random graph [13], the average connectivity probability of pairs of vertices [14], or the expected size of the connected component [4]. For networks with a certain topology, a method for obtaining a structural reliability indicator based on taking into account the basic structural characteristics – the number of nodes and branches of the network – was proposed in [6]. However, in the indicated papers [1, 2, 4, 6, 11, 13, 14], the issues related to obtaining an estimate of structural reliability for networks of a given dimension (with a given number of nodes and branches) of an undetermined topology are not resolved. Thus, the topic of this work, devoted to the development of a method for obtaining an estimate of structural reliability for a network with a constantly changing structure, is of particular importance and is relevant at present.

1. Statement of the problem and the methodical basis of research

The structure of the analyzed generalized network of the undetermined topology is described by a random *ER*-graph (model $G(N, p)$, ER-network). The set of vertices $\boldsymbol{N}$ of the graph corresponds to points (nodes) of the network, $|\boldsymbol{N}| = N$. The set of edges $\boldsymbol{L}$ corresponds to the branches of the network – direct connections connecting pairs of nodes, $|\boldsymbol{L}| = L$. Considered an undirected connected network.

The connectivity between pairs of nodes is provided by routes in the form of chains of branches without cycles and loops. The degree of connectivity of a pair of nodes is determined by the number of routes (in the general case, dependent) connecting these nodes. The rank R of the route corresponds to the number of branches included in the route. In a network of undetermined topology, the set $\boldsymbol{L}$ is not defined, but its cardinality is known L. The reliability index of all branches (the probability of failure-free operation of the branch β_{xy} – (p_{xy})) is given (x, $y = \overline{1,n}$, n – number of network nodes, $x \neq y$). Network nodes are considered absolutely reliable.

The basis of this paper was the work [7], proposing an approach that provides for the estimation of the structural reliability of a network of undetermined topology, based on taking into account basic structural characteristics. In this paper, to determine the upper and lower boundaries of structural reliability, proposes a method that allows one to determine the number of routes of given ranks that can be used to organize connections (i-j). This makes it possible to obtain an assessment of the structural reliability of both individual connections and the network as a whole.

The indicator of the structural reliability – P_{ISR} for a network is defined as the weighted average value according to the indicators of the structural reliability– $P_{ISR\,ij}$ of all connections [7]:

$$P_{ISR} = \frac{\sum_{i=1}^{n}\sum_{j=1}^{n} P_{ISRij} w_{ij}}{\sum_{i=1}^{n}\sum_{j=1}^{n} w_{ij}}, \tag{1}$$

here w_{ij} is the weight characteristics of individual connections that determine the priority of each connection;

P_{ISRij} is an indicator of the structural reliability of a single connection (i-j) in the network;

$i, j = \overline{1,n}$, n is a number of network nodes, $i \neq j$.

Coefficients w_{ij} are not normalized and can be represented in points, for example, in 10- or 100-point rating systems.

To assess the structural reliability of an individual connection (i-j) P_{ISRij} in the network, presented is the calculation of the indicator of structural reliability as the weighted average of the values of the upper boundary P_{UBSRij} and the lower boundary P_{LBSRij} of the structural reliability for a separate connection (i-j) [6]:

$$P_{ISRij} = P_{UBSRij} \cdot k_U + P_{LBSRij} \cdot k_L, \tag{2}$$

here k_U and k_L is the weighted normalized characteristics ($k_U + k_L = 1$), that determine the importance (significance) for finding P_{ISRij} indicators P_{UBSRij} and P_{LBSRij}, respectively.

Thus, the set of defined routes of rank no more than R, realizing communication in the (i-j) direction, and considering them as independent for a given communication, gives an upper bound on the reliability of communication between nodes. Calculation of the upper boundary of the structural reliability P_{UBSRij} for communication (i-j) in a network with an undetermined topology is carried out in accordance with expression (3) [7]:

$$P_{UBSRij} = 1 - \prod_{\mu_{ij}^{k} \in M_{ij}} \left(1 - \prod_{\beta_{xy} \in \mu_{ij}^{k}} p_{xy}\right), \tag{3}$$

here β_{xy} is a section of track μ_{ij}^{k};

k is a number of the set routes M_{ij};

p_{xy} is the probability of failure-free operation of the β_{xy}.

The calculation of the lower boundary of the structural reliability of P_{LBSRij} of an individual connection (i-j) in a network with an undetermined topology is performed in accordance with expression (4) [7]:

$$P_{LBSRij} = 1 - \prod_{\gamma_{ij}^{l} \in \gamma_{ij}} \left(1 - \prod_{\beta_{xy} \in \gamma_{ij}^{l}} p_{xy}\right), \tag{4}$$

here γ_{ij} is a set of separating cross sections,

l is a number of cross section set γ_{ij};

β_{xy} is a branch in a cross section with the corresponding p_{xy} value – the probability of failure-free operation.

The set of dividing sections γ_{ij} is formed on the basis of a specific, proposed method using routes between i and j, for each l–th section $\gamma_{ij}^{l} \in \gamma_{ij}$, the number of section β_{xy} is determined using the value p_{xy}.

As follows from the presented expressions (3, 4), one of the basic structural characteristics used in this method is the number of routes of a certain rank.

In a network with L branches, the number of routes of rank R (more precisely, the mathematical expectation of this number) can be obtained according to the following recursive expression proposed in [6]:

$$M_{R,L} = M_{R,L+1}\left(1 - \frac{R}{L+1}\right), \tag{5}$$

Since, to determine the number of routes of rank R in a network with L branches, one first needs to calculate the number of routes of rank R in a network with (L + 1) branches, recursive calculation begins with calculating the number of routes in a fully connected network with $L_{all} = \frac{n(n-1)}{2}$ branches (n is the number of network nodes) [6]:

$$M_{R,L_{all}} = \frac{n(n-1)!}{2(n-R-1)!}. \tag{6}$$

It is important to note that this method assumes uniformly random saturation of many nodes with branches and, thus, does not take into account the requirements for the formation of a fully connected network. As a result of this, it is possible to obtain the number of routes $M_L < 1$ for small L and large R. This result is consistent with the probabilistic nature of the number of routes in *ER*-networks (as a mathematical expectation) and means that paths with given parameters will not be present in all implementations of a random graph.

The number of routes of rank R per one connection is calculated as the ratio of the total number of M_R routes to the known number t of connections:

$$m_{Rij} = \frac{M_R}{t}. \quad (7)$$

The number t of connections can be determined in accordance with expressions (8, 9) or it can be a given constant indicator for a particular network.

In an oriented network, the total number t_o of connections is determined on the basis of expression (8):

$$t_o = n(n-1). \quad (8)$$

If the network is non-oriented, then the total number of t_n connections is defined as:

$$t_n = \frac{n(n-1)}{2}. \quad (9)$$

The above analytical method is not the only one route to obtain the structural characteristics of the network. The number of routes in *ER* networks of a relatively small dimension can be determined by the simulation of *ER* graphs.

2. Research results

In this research, using the proposed expressions (5–6), a series of experiments was carried out for *ER* networks of dimensions 20, 50, and 100 nodes with a different number of branches: from close to minimum L_{tree}, in which the network is connected (tree), to close to maximum based on expressions (5–6), in which the network is fully connected. To record large numbers, the decimal exponential notation of the form mEn = $m \cdot 10^n$, standard for computer programs, is used.

The experimental results of determining the number of routes of different ranks by the analytical method are presented in tables. Table 1 shows the results of a study for an *ER* network with a dimension of 20 nodes with a different number of branches (20, 70, 120, and 170 branches).

Table 1. The number of routes of rank R in an ER-network with N = 20 nodes and L branches

L	M_a (N = 20)					
	R = 1	R = 2	R = 3	R = 4	. . .	R = 19
20	20	36	59	86		3.79E–07
70	70	460	2829	1.62E+04		1.20E+09
120	120	1360	14511	1.45E+05		1.11E+14
170	170	2736	41567	5.94E+05		1.31E+17

The number of routes M_a of the rank R=1 corresponds to a given number of branches L. The number of routes of a rank higher than 1 increases with the number of branches and the value of the route rank. In real networks, for the implementation of a single connection, routes of maximum ranks are practically not used for a reason of network performance. Constraints are usually fulfilled at the level of the third or fourth rank. According to this rule, the table shows the calculations of M_a for routes for rank R <= 4.

Tables 2 and 3 show the results of similar calculations for an *ER* network with N = 50 and N = 100 nodes.

Table 2. The number of routes of rank R in an ER network with N = 50 nodes and L branches

L	M_a (N = 50)					
	R = 1	R = 2	R = 3	R = 4	...	R = 49
50	50	96	177	314		5.87E-23
300	300	3518	40285	450384		7.29E+32
550	550	11841	249371	5134767		4.04E+46
800	800	25067	768725	2.31E+07		7.68E+54

Table 3. The number of routes of rank R in an ER network with N = 100 nodes and L branches

L	M_a (N = 100)					
	R = 1	R = 2	R = 3	R = 4	...	R = 99
100	100	196	377	709		2.00E–50
350	350	2419	16501	111117		3.27E+37
600	600	7117	83431	966571		4.44E+63
850	850	14290	237560	3.90E+06		5.80E+79

The above tables can be used in practical calculations of the reliability of networks of undetermined topology. Using the obtained values of the number of routes M_a, given in Table 1, will provide an example of calculating indicator of the structural reliability for a non-oriented communication network with the number of nodes N = 20 and the number of branches L = 20.

Based on expressions (7) and (9), we determined the average number of routes of each rank (R = 1, ..., 4) per one bond (i-j):

$$m_{1\,ij} = 2 \cdot 20 / (20 \cdot (20-1)) = 0.105,$$
$$m_{2\,ij} = 0.189,$$
$$m_{3\,ij} = 0.311,$$
$$m_{4\,ij} = 0.453. \quad (10)$$

In real systems, devices with a low reliability value are not used. According to statistics, the probability of uptime is usually in the range of 0.96 – 0.99. Basing on this, in this example, we take the probability of failure-free operation of the network branches p = 0.98.

The upper boundary of the structural reliability P_{UBSRij} is determined by expression (4). Transforming it, according to the source data, obtains the following expression:

$$P_{UBSRij} = 1 - ((1-p)^{m1ij} \cdot (1-p^2)^{m2ij} \cdot (1-p^3)^{m3ij} \cdot (1-p^4)^{m4ij}). \quad (11)$$

Using the given probabilities p of the failure-free operation of network sections and the number of routes m_{Rij} of each rank (R = 1, ..., 4) per one connection (i-j), obtains:

$$P_{UBSR_{ij}} = 1 - ((1-0.98^1)^{0.105} \cdot (1-0.98^2)^{0.189} \cdot (1-0.98^3)^{0.311} \cdot (1-0.98^4)^{0.453}) = 0.99999639.$$

To obtain the value of the lower boundary of the structural reliability P_{LBSRij}, based on the set of routes M_{ij}, one should obtain the set of dividing cross sections γ_{ij}. In order to be able to record the set of cross sections in disjunctive normal form, the values obtained in (10) of the number of routes of each rank per one bond to the nearest larger integer should be rounded off. The result values are:

$$m_{1\,ij} = 1,\ m_{2\,ij} = 1,\ m_{3\,ij} = 1,\ m_{4\,ij} = 1.$$

Represented a set of paths M_{ij} in disjunctive normal form:

$$M_{ij} = k_1 + k_2k_3 + k_4k_5k_6 + k_7k_8k_9k_{10}. \quad (12)$$

Further, for expression (12), it obtains the dual Boolean function in conjunctive normal form:

$$\gamma_{ij} = k_1(k_2+k_3)(k_4+k_5+k_6)(k_7+k_8+k_9+k_{10}). \quad (13)$$

Performing the conversion of conjunctive normal form (13) to disjunctive normal form obtains a set of cross sections (14):

$$\gamma_{ij} = k_1k_2k_4k_7 + k_1k_2k_4k_8 + k_1k_2k_4k_9 + k_1k_2k_4k_{10} + k_1k_2k_5k_7 + \cdots + k_1k_3k_6k_{10}. \quad (14)$$

According to (4), we it obtain the expression for calculating P_{LBSRij}:

$$P_{LBSR_{ij}} = \big(1-(1-p_1)(1-p_2)(1-p_4)(1-p_7)\big) \cdot \ldots \cdot \big(1-(1-p_1)(1-p_2)(1-p_4)(1-p_8)\big) \cdot \ldots \cdot \big(1-(1-p_1)(1-p_2)(1-p_4)(1-p_9)\big) \cdot \ldots \cdot \big(1-(1-p_1)(1-p_3)(1-p_6)(1-p_{10})\big). \quad (15)$$

Transforming (15) according to the initial data we obtain the following expression:

$$P_{LBSR_{ij}} = (1-(1-p)^4)^q \,, \tag{16}$$

here q defined as:

$$q = \prod_{R=1}^{4} R^{m_{Rij}}.$$

Using the given values of the number of routes m_{Rij} of each rank (R = 1, ..., 4) per one connection and the probabilities p_{xy} of the network branches to fail we obtain:

$$q = \prod_{R=1}^{4} R^{m_{Rij}} = 1^1 \cdot 2^1 \cdot 3^1 \cdot 4^1 = 24.$$

$$P_{LBSR_{ij}} = (1-(1-0.98)^4)^{24} = 0.99999616.$$

Based on expression (2) for the values accepted for this example, k_U = 0.55 and k_L = 0.45, the value of the indicator P_{ISRij} for communication (i-j) is determined:

$$\begin{aligned} P_{ISRj} &= P_{UBSRij} \cdot 0.55 + P_{LBSRij} \cdot 0.45 \\ &= 0.99999639 \cdot 0.55 + 0.99999616 \cdot 0.45 \\ &= 0.99999629. \end{aligned}$$

Performing calculations for all connections (i-j) makes it possible to determine the value of the indicator P_{ISR} of the structural reliability of the entire network (based on expression (1), taking into account the values of weighting coefficients w_{ij}).

3. Conclusion

The paper shows the relevance of the task of assessing the structural reliability of networks of undetermined topology. A method for obtaining such an estimate based on the basic structural characteristics of the network – the number of nodes and branches, the maximum allowable rank of routes, and others – is presented. Presented is also a method for determining the number of routes of each rank per one connection. Calculations were carried out for *ER* networks of dimensions of 20, 50 and 100 nodes with different number of branches: from close to the minimum L_{tree}, at which the network is connected (tree), to close to the maximum L_{all} (fully connected network).

The proposed method for assessing the structural reliability of networks with an undetermined topology is based on the formation of indicator P_{ISR} of the structural reliability, which is determined using the lower and upper boundaries of structural reliability. Expressions are presented for determining the number of routes of different ranks that can be used to service applications that enter the network of the undetermined topology. Based on the upper and lower boundaries of the structural reliability of individual links, presented is an approach that allows one to obtain a weighted average estimate of the structural reliability of the entire network of the undetermined topology.

An example of the implementation of the method for determining the structural reliability indicator of a network of undetermined topology is performed.

Further development of this work is the solution of issues related to the development of approaches to determining the values of the probabilities of failure-free operation of network branches, as well as the values of weighting coefficients for determining the upper and lower boundaries of the structural reliability of both individual connections and the entire network of the undetermined topology.

References

[1] Bollobás B.: Random Graphs. Cambridge University Press, 2001.
[2] Erdos P. Rényi A.: On random graphs I. Publicationes Mathematicae Debrecen 6/1959, 290–297.
[3] Effros M., Goldsmith A., Médard M.: The Rise of Instant wireless Networks. Scientific American 72/2010, [http://doi.org/10.1038/scientificamerican0410-72].
[4] Youssef M., Khorramzadeh Y., Eubank S.: Network reliability: The effect of local network structure on diffusive processes. Physical Review 88(5)/2013, 052810.
[5] Egunov M., Shuvalov V. P.: Structural Reliability Analysis of Transport Network. Vestnik SibGUTI 1/2012, 54–60.
[6] Kniazieva N. A., Nenov A. L.: A method for assessing the structural reliability of a network when its structure changes. Visnik DUIKT 9(4)/2011, 318−325.
[7] Kniazieva N., Kolumba I.: The Use of the Basic Structural Characteristics of the Network of Uncertain Topology to Assess Its Structural Reliability. Control, Navigation and Communication Systems. Academic Journal 6(52)/2018, 130–134, [http://doi.org/10.26906/SUNZ.2018.6.130].
[8] Kolumba I. V.: Characteristic of Multiple-Way Protocols in Wireless Self-Organized Communication Networks. Visnyk Universyteta "Ukrayina" 21/2/2018, 70–80.
[9] Kucheryavyy A. Ye. et al.: Self-organizing networks. Lyubavich, Sankt-Peterburg 2011.
[10] Kucheryavyy A. Ye.: Internet of Things and self-organizing networks. Proc. of "Infocommunication technologies in the digital world", SPB GEU LETI, 2012, 3–5.
[11] Migov D.: New network reliability model for wirelles ad hoc networks. Vestnik SibGUTI 3/2014, 3–12.
[12] Netes V. A., Tarasyev Y. I., Shper V. L.: Current issues of terminology standardization in dependability. Dependability 2/2014, 116–123.
[13] Raygorodskiy A. M.: Random graph models and their application. Trudy MFTI 4/2011, 130–140.
[14] Rodionov A. S., Rodionova O. K.: Cumulative estimates of the average probability of connectivity of a random graph pair of vertices. Informatics problems 2(19)/2013, 3–12.
[15] Roslyakov A.: Communication networks: manual for the discipline "Communication Networks and Switching Systems", PGUTI, Samara 2017.
[16] Data networks, open system communications and security, ITU-T Recommendations – X series, 04/2008.
[17] Dependability of Technics. Terms and definitions. DSTU 2860-94, Kiev, 1996.

Prof. Nina Kniazieva
e-mail: knyazeva@ukr.net

Doctor of Technical Sciences (specialty – Telecommunication theory), Professor, Academician of the Ukrainian Academy of Communications (Department of International Informatization Academy, associate member of the UN)
Honorary Telecommunications Worker of Ukraine, Professor at the Department of Computer Engineering at Odessa National Academy of Food Technologies.
Nina Kniazieva has written over 250 scientific papers.

http://orcid.org/0000-0002-1523-6775

Ph.D. Alexey Nenov
e-mail: anotnew@gmail.com

Alexey Nenov was born in 1976 in Odessa. He graduated from Odessa State Polytechnic University with a degree in Robotic Systems and Complexes. In 2014 he defended his thesis with a degree in Telecommunication Systems and Networks. He works as a senior teacher at the Department of Computer Engineering at the Odessa National Academy of Food Technologies.

http://orcid.org/0000-0002-8774-7793

Postgraduate student Irina Kolumba
e-mail: iryna.kolumba@ukr.net

Irina Kolumba graduated from the Odessa State Academy of Refrigeration in the specialty "Information systems and technology management" in 2002. Currently she is a postgraduate student and a teacher at the Department of Computer Engineering at Odessa National Academy of Food Technologies.

http://orcid.org/0000-0002-5903-6193

otrzymano/received: 15.11.2019 *przyjęto do druku/accepted: 15.02.2020*

http://doi.org/10.35784/iapgos.910

PHOTODIODE BASED ON THE EPITAXIAL PHOSPHIDE GALLIUM WITH INCREASED SENSITIVITY AT A WAVELENGTH OF 254 nm

Yurii G. Dobrovolsky[1], Volodymyr M. Lipka[2], Volodymyr V. Strebezhev[1], Yurii O. Sorokatyi[1], Mykola O. Sorokatyi[1], Olga P. Andreeva[2]
[1]Yuriy Fedkovych Chernivtsi National University, Chernivtsy, Ukraine, [2]PJC "CDB" Rhythm", Chernivtsy, Ukraine

Abstract. *The paper shows the results of the development of a photodiode technology based on gallium phosphide structure n^+-n-GaP-Au with high sensitivity. It provides the ion etching of the surface of the gallium phosphide before an application of a leading electrode of gold. The barrier layer of a 20 nm thick gold is applied to the substrate in the magnetic field of GaP. When forming the contact with the reverse side of the indium substrate at 600°C, there occurs the annealing of the gold barrier layer. At the maximum of the spectral characteristics obtained by the photodiode, it has a sensitivity of 0.13 A/W, and at a wavelength of 254 nm – about 0.06 A/W. The dynamic range of the photodiode is not less than 10^7.*

Keywords. photodiode, gallium phosphide, sensitive, 254 nm, Schottky barrier

FOTODIODA OPARTA NA EPITAKSJALNYM FOSFORKU GALU O ZWIĘKSZONEJ WRAŻLIWOŚCI PRZY DŁUGOŚCI FALI 254 nm

Streszczenie. *Artykuł pokazuje rezultaty rozwoju technologicznego fotodiody opartej na fosforku galu o strukturze n^+-n-GaP-Au o wysokiej czułości. Umożliwia to wytrawianie jonowe powierzchni fosforku galu, zanim zastosowana zostanie elektroda przewodząca wykonana ze złota. Złota warstwa barierowa o grubości 20 nm jest nakładana na podłoże GaP w polu magnetycznym. Gdy powstaje styk z tyłu podłoża indowego w temperaturze 600°C, złota warstwa barierowa jest wyżarzana. Przy maksymalnej charakterystyce spektralnej uzyskanej przez fotodiodę, ma ona czułość 0,13 A/W, a przy długości fali 254 nm – około 0,06 A / W. Zakres dynamiczny fotodiody wynosi co najmniej 10^7.*

Słowa kluczowe: fotodioda, fosforek galu, czułość, 254 nm, bariera Schottky'ego

Introduction

Gallium phosphide (GaP) is an effective material for photodiodes with Schottky barrier, sensitive in the ultraviolet region of the spectrum, which is now being actively developed in the branch of optoelectronics. This material is substantially transparent to optical radiation, because it has a wavelength of about 0.5 microns. As such, the photodiodes made of a gallium phosphide do not require complex filters to "cut" the visible and infrared radiation. In comparison to the more effective material in terms of sensitivity – gallium nitride (GaN), gallium phosphide has a substantially lower cost, which allows it to remain relevant in the market of the photodiodes that are sensitive in the ultraviolet region of the spectrum.

Such photodiodes are used, in particular, for the creation of the UV radiation radiometer because they have, in this case, the photovoltaic mode. As such, the most effective photodiodes are based on epitaxial n^+-n^- structures with a carrier concentration in the epitaxial layer of about 10^{16} cm^{-3} [7]. As the active electrode, there is used a metal film (mostly – semi-transparent layer of gold) [1, 7], or a thin conductive ITO layer (a mixture of SnO_2 and In_2O_3), and also FTO (SnO_2 layer, fluorine-doped) [8], which may be made by pulverization [2]. It provides high sensitivity (0.2 A/W at 450 nm – a peak of spectral sensitivity characteristic). The disadvantages of this technology are that it provide high sensitivity unevenness on the surface of the photosensitive member (over 10%) even in the case of a film deposition by magnetron sputtering of metal oxides. The cause of this phenomenon lies in the fact that the film begins to grow islets. And it is not possible to obtain uniformly thick layer at a film thickness smaller than 30 nm [4]. For the same reason, up to 30% of films made by the photodiodes in each cycle are defective. The sensitivity at a wavelength of ~250 nm is not pains 0.05 A/W.

To increase the value of the current monochromatic sensitivity, authors of [6], found that the structure formation based on AlGaN with a gold transparent contact, as in the case of gallium phosphide, exhibits the highest sensitivity among photodiodes, in a Schottky barrier, and the structure of the heat treatment showed that the contact annealing increases the photosensitivity three times. This effect is illustrated by authors [6] and they show the fact that a layer of oxide is on the AlGaN surface after chemical cleaning. In total, after the deposition of the gold contact, there is obtained a metal structure – a dielectric (thin oxide film) – semiconductor. The process of annealing of the formed structure, according to the authors of [6], partially diffuses through the oxide layer closer to the semiconductor surface, which reduces the resistance of the whole structure and, as a consequence.

Obviously, such a situation occurs and the photodiode is based on the second compound semiconductor including gallium phosphide.

A view of this work is based on the optimization technique of photodiodes n^+-n-GaP-Au to increase the current monochromatic sensitivity at a wavelength of 254 nm.

1. Results of research

Preliminary assessment of the design and technology of the new photodiode was carried out in accordance with [5]. This software is designed to find ways to increase the sensitivity of photodiodes operating in the photodiode regime. An analysis and calculation results compared with the results of the current measurement of sensitivity to monochromatic 450 nm showed that, despite the effectiveness of the propsed optimization method, it does not fully fit the situation, when the photodiode operates in the photovoltaic mode.

The known algorithm is also not provided for the calculation of the optical properties of the photodiode surface by the amount of its sensitivity. The surface consists of at least three media: air – AR coating – the semiconductor surface.

In our case, in the operating wavelength range (200–500 nm), there is almost a complete absorption of the optical radiation (up to 86% is caught in a semiconductor layer of radiation) that takes place in a layer that is 1.5 microns thick [5]. This is why the most effective is a photodiode structure based on the epitaxial structure of n^+-n^- type in which a working layer – the layer in which optical radiation is absorbed is n-type high-resistance layer – was disposed on the low-resistance substrate.

To determine the maximum possible value of the sensitivity that can be obtained in this case, the inventors have used the approach described in [4], which suggested to maximize the sensitivity of the photodiode structure, ensuring the system of inequalities (1), which contain the basic parameters of the photodiode structure and the physical parameters of the material.

$$\begin{cases} x_0 < h_{эс} \le \left(L_p + x_0 + h\right) \\ L_p < \left(h_{эс} - x_0\right) \\ \alpha_к < x_0 \le L_p \\ d = \lambda\left(2n+1\right)/4 \\ I_F S \cong S_{\text{int}}\, p \end{cases} \quad (1)$$

where: x_0 – the width of the space charge region in the epitaxial layer, h_{es} – thickness of the epitaxial layer, L_p – the diffusion length of holes, h – the depth of field propagation due to the impurity concentration distribution profile, α_k – absorption depth shortwave (UV) radiation in gallium phosphide, d – thickness of the metal oxide layer, λ – wave length, n – the refractive index of the metal oxide film, R – the value of the optical flux, S_{Iint} – the integral sensitivity due to optical radiation incident on the photodiode, I_F – the specific value of the photocurrent generated in that unit area which provides sensitivity S_{int}, S – the area of the photosensitive element illuminated by the incident optical radiation to the photodiode.

The first expression defines a region collecting photogenerated carriers that generate a long-wavelength component of the spectral sensitivity range of the photodiode, the second component – a high-resistivity isolation protects the epitaxial layer from the influence of the charge carriers generated in the low-resistance substrate, and the epitaxial structure, the third component, provides a short-range contribution. The fourth reflection phenomenon takes into account the flow of optical radiation from the surface of an optical transparent conductive metal oxide electrode and the surface of the metal oxide film section – semiconductor (gallium phosphide). The fifth considers a photosensitive member area, which may depend on the magnitude of the photocurrent when the photodiode is illuminated by the entire marketplace stream R.

An analysis of equations and inequalities (7) conducted in the MS Office Excel 2003 showed that the maximum sensitivity in the wavelength range 250–450 nm can reach 0.1 – 0.17 A/W.

2. Technology of the photodiode

To create the structure of a photodetector there was used an epitaxial n^+-n-type conductivity with a total thickness of 300–370 microns. Orientation GaP substrate [11], the concentration of charge carriers in the substrate was $(1–4)\times10^{17}$ cm^{-3}. The thickness of the epitaxial n-type layer does not exceed 15 microns, and the concentration of charge carriers does not exceed $(0.9–2)\times10^{16}$ cm^{-3}.

Proposed was the technology of obtaining a structure of n^+-n-GaP-Au, which provides ionic surface etching of gallium phosphide before the application of a leading electrode of gold. Such operation helps to maximize the purification of the wafer surface, which in turn prevents the formation of chaotic, uncontrolled Au film growth centres during its application. Further, AuGaP layer is applied to the plate in a magnetic field. Experiments have shown that it promotes a more uniform distribution of the Au layer on the surface of the wafer of gallium phosphide and provides a more reliable adhesion. Before applying the gold film, the gallium phosphide surface was treated with a solution of bromine in dimethylformamide followed by rinsing in alcohol.

Then, after the ion etching the surface of the wafer, by thermal evaporation under vacuum, deposited is a barrier layer of gold. A layer of gold is deposited at a temperature of 370 ± 10°C. In this case, the substrate temperature was controlled not to fall below 100°C. The thickness of the barrier layer was 20 nm.

Ohmic contact with the gold layer of the barrier was also created by thermal evaporation under vacuum at a temperature of 370 ± 10°C and a substrate temperature of at least 100°C. The thickness of the contact layer was 0.7 microns.

The magnetic field in the area of application of the barrier layer of gold was formed using gyrotropic cylindrical capacitor which consists of a ring-based material with an external ferrodielectric R_1 and inner radius R_2, and a thickness D. The magnetic field of the ring is oriented in such a way that the south and north poles are located on the opposite sides of area $\pi\left(R_1^2 - R_2^2\right)$. On the outer and inner sides of the metal cylinder there is a ring electrode, and all these parts constitute a capacitor.

With the use of the electrodes there were made applications to the DC voltage U cylindrical capacitor cover that led to the interaction of electric and magnetic fields and the appearance of both the radial and axial components of the electric field. This, together with the geometrical factor – annular shape magnet – LED to the total concentration of the electric field in the capacitor region of space which is at a distance from the center of the device and is located at its center line. The density of the electric field at this point is several orders of magnitude greater than the density of the electric field that arises between the annular covers.

An ohmic contact was created on the back-side annealing of an In-Ni alloy in a vacuum (or under a hydrogen atmosphere) at a temperature of about 600°C. To avoid undesired contamination, the plates were annealed on a flat surface. This was accompanied by the annealing process of the gold barrier layer, contributing to the decrease of the surface conduction channels formed by the surface states and an improvement of the sensitivity of the final structure.

As is known, the physical nature consists of four basic types of surface states [9, 10] which are somehow related to the presence of additional charge that is present on the semiconductor surface or on the full screen in the vicinity of the surface. A feature of the epitaxial structure is that it is generated in a natural growth area of the semiconductor film. Therefore, the surface states of Tamm and Shockley provided therein little probability that this surface is not broken prior to the application of the barrier layer. Two other types of surface states are associated with practical and processing quality of epitaxial layer surface prior to the application of the barrier layer. Thus, in this case, the annealing process takes place in order to reduce the density of the available surface states.

The isolation of photosensitive elements and contact layers is performed by standard techniques of photolithography. Connection conductors are carried by soldered tinned copper conductors to the contact layers. When using the ultrasonic welding, there is used a variant structure where the contact metallization layer of the barrier layer is made out of gold.

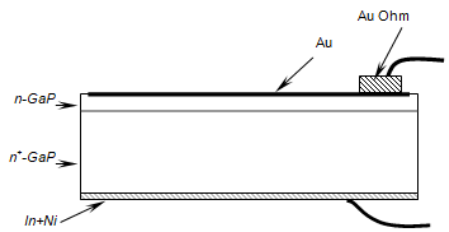

Fig. 1. Construction of the photosensitive member on the basis of the photodiode n^+n-GaP-Au

Photodiode crystal construction is shown in Figure 1. Shown here is an n^+ conductivity type of gallium phosphide substrate (n^+-GaP). An epitaxial (n-GaP) layer of n-type conductivity is formed on it. A Schottky barrier is formed on the surface of the epitaxial layer. The material of the barrier layer is gold (Au). Its thickness is 20 nm. On the barrier layer of gold, there is also formed a gold ohmic contact (AuOhm). An ohmic contact of indium with a nickel layer (In+Ni) is formed on the reverse side of an n+ type of gallium phosphide substrate.

3. A study of the photodiode

Fig. 2 shows the difference values of ionized donors and acceptors ND concentration in the surface layer of gallium phosphide before and after the annealing process, calculated according to the measuring capacity of the photosensitive member (PSM) before and after the annealing process.

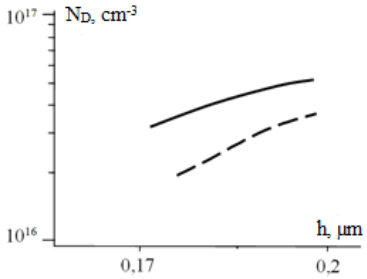

Fig. 2. N_D concentration distribution profile in the surface region of the epitaxial layer of gallium phosphide {dashed line – after annealing, solid – before annealing)

Calculation was performed according to [11], in accordance with the formula:

$$N_D = \frac{2}{q\varepsilon_s}\frac{(-dU)}{d\left(\frac{1}{C^2}\right)}, \tag{2}$$

where $\varepsilon_s = \varepsilon_o\varepsilon$, $\varepsilon_o = 8.85\cdot10^{-12}$ F/m – the dielectric constant, $\varepsilon = 10$ – dielectric constant of gallium phosphide, dU – change in the bias voltage, q – the electron charge, C – specific capacity of the photodiode.

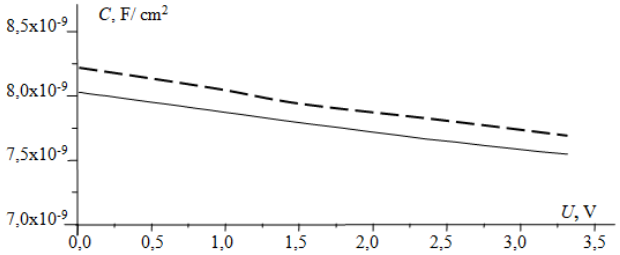

Fig. 3. The capacitance-voltage characteristic of the PSMs (as can be seen, the dependence hardly changes in the operating voltages)

An investigation of the spectral characteristics of the selected photodetectors is conducted with the help of the spectral complex type KSVU-23 by comparing the working standard (photodiode PD 288V, certified sensitivity to 440 nm wavelength). The radiation source is used in the respective ranges: in the spectral range from 200 to 400 nm, it was a deuterium lamp with DSA-30; in the spectral range from 400 to 1200 nm – an incandescent lamp KGM24-150. Used was also a preamplifier precision converter "current-voltage" PPTN-03.

The measured current values of a monochromatic sensitivity and the absolute values are shown in Figure 4.

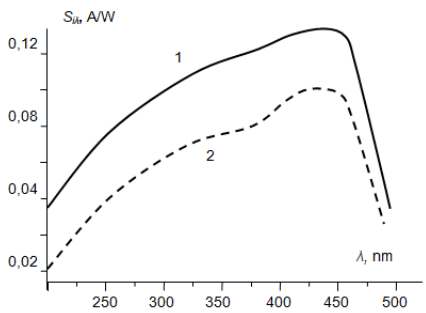

Fig. 4. The absolute spectral sensitivity characteristics of the photodiode of gallium phosphide (1 – spectral response of the photodiode with the annealed layer of gold, 2 – spectral characteristic photodiode without the annealing)

We can see that at the maximum of the spectral sensitivity characteristics of the photodiode, which was subjected to annealing process, the gold layer has better sensitivity over the entire spectral range.

In particular, at the maximum of spectral characteristics of the proposed photodiode, it has a sensitivity of 0.13 A/W, and at a wavelength of 254 nm (wavelength emitted by a germicidal lamp) – about 0.06 A/W.

Measurements of the dark current (IT) are conducted via a precision transducer "current-voltage" PPTN-03 at an operating voltage for the photodiode (UP) 10 mV. The voltage U is measured with a voltmeter. The dark current is calculated by the formula:

$$I_T = \frac{U}{K} \tag{3}$$

where K – conversion gain PPTN-03 B/A.

According to measurements, the dark current value is not more than 10^{-9} A.

Measurement of sensitivity nonlinearity (δ_S) and dynamic range of the photodiodes are conducted in a suitable machine and the method of the luminance increase is calculated with the use of the formula:

$$\delta_S = \frac{|(U_1+U_2)-U_3|}{U_1+U_2} \tag{4}$$

wherein U_1 and U_2 – video output of the photodiode when alternately illuminated with PSM, U_3 – video output while the photodiode is illuminated by both light fluxes PSM channel settings.

Nonlinearity of the energy generated in the photodiode characteristics oscillates in the range from 10^{-4} to 10^3 W/m^2, according to the formula for measurement and calculation of (4) that does not exceed 1%. Thus, the dynamic range of the photodiode is not less than 10^7.

Conducted was a comparison of a photodiode based on a gallium phosphide, manufactured by a new technology (new UVD), with previously known photodiodes – analogues. Comparison was made with the following photodiodes:

- UV1 based on GaP-Au
- G1962 based on GaP-Au

Table 1 shows the technical specifications of the above photodiodes.

Table 1. Technical characteristics of ultraviolet photodiodes – analogues of the proposed photodiode

Name of the parameter	New UVD	G1962	UV1
The spectral region sensitivity, nm	200–480 (λ_{max}=440)	200–480 (λ_{max}=440)	200–450 (λ_{max}=370)
Dark current, no more (Ur = 10 mV), A	$1\cdot10^{-9}$	$5\cdot10^{-12}$	$1\cdot10^{-10}$
Monochromatic sensitivity (λ= 400 nm), not less than A/W	0.13	0.12	0.11
Dynamic range, times (with nonlinearity of energy characteristic δE = ± 1%)	$1\cdot10^7$	$1\cdot10^7$	$1\cdot10^7$
Area of PSM, mm^2	49	5.2	10.0

The analysis given in Table 1 shows the following:

1) The proposed photodiode (new UVD) has the same spectral sensitivity range as that of analogues.
2) The level of dark current of the new UVD corresponds to the level of analogues, taking into account the area of the photosensitive element.
3) In terms of sensitivity, the new UVD is superior to analogues having a Schottky barrier contact made of gold.
4) The dynamic range of the new UVD corresponds to its analogues.

Thus, it can be seen that the new UVD, in terms of its technical characteristics, is not inferior to the analogues with the Schottky barrier, but it exceeds them in the area of sensitivity.

4. Findings

Presented is a technology-based structure of gallium phosphide n^+-n-GaP-Au photodiode with high sensitivity, which is constructed in particular with ionic gallium phosphide. Ion etching surface before the application of the gold barrier layer is formed on the GaP substrate in a magnetic field, and is subjected to the annealing process at 600ºC to form contact with the reverse side of the substrate of indium. The thickness of the barrier of the burning gold is 20 nm.

The maximum spectral sensitivity characteristics obtained by the photodiode is a sensitivity of 0.13 A/W, and at a wavelength of 254 nm – about 0.06 A/W. The dynamic range of the photodiode is not less than 10^7.

References

[1] Anisimov I. D., Stafeev V. I.: Ultraviolet photodetectors based on wideband compounds. Applied physics 2/1999, 41–44.
[2] Bix M. P., Dobrovolsky Y. G., Shabashkevich B.: UV Photodetectors based on gallium phosphide. Applied physics 4/2005, 97–100.
[3] Dobrovolsky Y. G.: Photodiode, resistant to ambient lighting. Sensor Electronics and Microsystem Technologies 4/2006, 33–37.
[4] Dobrovolsky Y. G., Pidkamin L., Prokhorov G.: Photodiodes on the basis of gallium phosphate with increased sensitivity at a wavelength of 254 nm. Proceedings SPIE 8338/2011, 83380N [http://doi.org/10.1117/12.920931].
[5] Dobrovolsky Y. G.: Based on GaP photodiode with high sensitivity in the short-wave UV region of the spectrum. TKEA 5/2012, 31–34.
[6] Lamkin I. A., Menkovich E. A., Tarasov S. A.: Ultraviolet photodiodes based metal contacts – solid solutions of gallium nitride and aluminum. Scientific and technical statements STU. Physics and mathematics 3/2012, 28–31.
[7] Malik A. I.: Optoelectronic properties of heteroijunctions metal oxide-gallium phosphide. Semiconductor Physics and Technology 25(10)/1991, 1891–1695.
[8] Malik A. I., Seco A., Fortunator E., Martins R., Shabashkevich B., Piroszenko S.: A new high ultraviolet sensivity FTO-GaP Schottky photodiode fabricated by spray pyrolysis. Semicond. Sci. Technol. 13/1998, 102–107.
[9] Nicollian E. H., Brews J. R.: MOS (Metal Oxide Semiconductor) Physics and Technology. Wiley, New York 1982.
[10] Sah C. T.: Fundamentals of solid-state electronics. World Scientific, 1991.
[11] Sze S. M., Ng K. K.: Physics of Semiconductor Devices. 3rd Edition. John Wiley & Sons Inc., New Jersey 2006.

D.Sc. Yuri Dobrovolsky
e-mail: y.dobrovolsky@chnu.edu.ua

Associate Professor at the Department of Physics of Semiconductors and Nanostructures (DPSN). Author of 150 scientific articles and 50 patents. The author of 23 developments of measuring equipment.

http://orcid.org/0000-0002-1248-3615

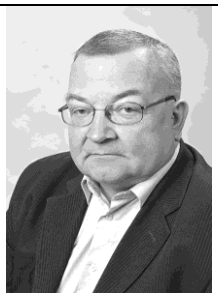

Volodymyr Lipka
e-mail: olodymyrlipka9@gmail.com

PJC "CDB "Rhythm". Chairman of the Board
The author of 2 scientific articles.

http://orcid.org/0000-0002-5899-6213

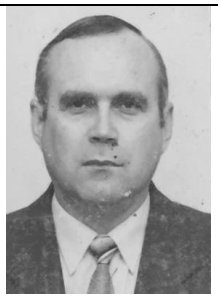

Ph.D. Vladimir Strebezhev
e-mail: v.strebezhev@chnu.edu.ua

Assistant at DPSN. Author of 10 scientific articles and 2 patents.

http://orcid.org/0000-0001-8962-647X

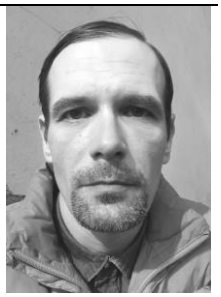

Yurii Sorokatyi
e-mail: yra.sorokatiy@gmail.com

Graduate Student at DPSN. The author of 2 scientific articles.

http://orcid.org/0000-0001-9462-775X

Mykola Sorokatyi
e-mail: sorokatijmikola@gmail.com

Graduate Student at DPSN. The author of 2 scientific articles.

http://orcid.org/0000-0001-6602-5698

Olga Andreeva
e-mail: Andreevd190779@gmail.com

PJC "CDB" Rhythm". The author of 2 scientific articles.

http://orcid.org/0000-0002-9437-1931

otrzymano/received: 15.11.2019 *przyjęto do druku/accepted: 15.02.2020*

http://doi.org/10.35784/iapgos.918

DETERMINATION OF THE STRUCTURAL STATE AND STABILITY OF THE LASER CRYSTALLIZED $Cd_{1-x}Mn_xTe$ CRYSTAL SURFACE

Victor Strebezhev[1], Ivan Yuriychuk[1], Petro Fochuk[2], Sergiy Nichyi[1], Yuriy Dobrovolsky[1], Victoria Tkachuk[1], Mykola Sorokatyi[1], Yurii Sorokatyi[1]

[1]Yuriy Fedkovych Chernivtsi National University, Physical, Technical and Computer Sciences Institute/Department of Physics of Semiconductors and Nanostructures, Chernivtsi, Ukraine,

[2]Yuriy Fedkovych Chernivtsi National University, Institute of Biology, Chemistry and Bioresources/Department of General Chemistry and Chemical Material Science, Chernivtsi, Ukraine

Abstract. *The modified surface layers of the $Cd_{1-x}Mn_xTe$ crystals were obtained by the laser recrystallization of the crystal surface with the use of millisecond and nanosecond impulse ruby lasers. The determination and diagnostics of the layer structural state were performed by the study of the electron channeling patterns in the SEM. The AFM studies showed that mechanically stable contact regions within the CdTe crystal – Cu film system can be formed, depending on the laser energy density and beam defocusing. On the base of the ellipsometric studies, it was found that while irradiating the $Cd_{1-x}Mn_xTe$ crystal surface, the refractive index of the oxide film on the modified surface changes depending on the laser beam energy density, which can be interpreted as the formation of the oxides of the different chemical composition.*

Keywords: $Cd_{1-x}Mn_xTe$ crystal, surface, laser, thin film

OKREŚLENIE POSTACI STRUKTURALNEJ ORAZ STABILNOŚCI POWIERZCHNI KRYSZTAŁU $Cd_{1-x}Mn_xTe$ KRYSTALIZOWANEJ LASEREM

Streszczenie*. Zmodyfikowane warstwy wierzchnie kryształów $Cd_{1-x}Mn_xTe$ zostały uzyskane metodą laserowej rekrystalizacji powierzchni kryształu przy wykorzystaniu impulsów milisekundowych i nanosekundowych laserów rubinowych. Określenie i diagnostyka strukturalnej postaci powierzchni zostały wykonane metodą badania struktury kanałów elektronu SEM. Badania AFM wykazały, że mogą zostać wytworzone obszary mechanicznie stabilnego obszaru kontaktowego kryształ CdTe – powłoka Cu, w zależności od skupienia energii laserowej oraz zdekoncentrowania wiązki. Na podstawie pomiarów elipsometrycznych odkryto, że podczas napromieniowywania powierzchni kryształu $Cd_{1-x}Mn_xTe$, wskaźnik refrakcyjny powłoki tlenku na powierzchni zmodyfikowanej ulega zmianie w zależności od skupienia energii wiązki laserowej, co może być interpretowane, jako powstawanie tlenków o różnym składzie chemicznym.*

Słowa kluczowe: kryształ $Cd_{1-x}Mn_xTe$, powierzchnia, laser, cienka powłoka

Introduction

Development and optimization of non-cooled X- and gamma-ray detectors based on the wide band gap $Cd_{1-x}Mn_xTe$ crystals is an important problem of micro- and nanoelectronics [1, 4, 10]. For this purpose, the method of photonic correction of crystallographic and electrophysical characteristics using a laser is used to modify and nanostructure the surface of semiconductors [3, 9]. Laser recrystallization of the $Cd_{1-x}Mn_xTe$ crystal surface with the formation of a laser-modified layer can be used to form active structures and contact places. It is known that the introduction of the Mn atoms into the CdTe crystal stabilizes the $Cd_{1-x}Mn_xTe$ alloy lattice [5, 8]. In this case, the homogeneous and structurally stable alloys are formed with the Mn concentrations up to x = 0.4.

Laser treatment of the $Cd_{1-x}Mn_xTe$ crystals is accompanied by the structural changes in the modified surface layer, which are determined by the laser radiation absorption processes depending on the composition x [2, 6]. When the crystal is transparent for a given laser wavelength, the deposition of a metal film over the surface is very effective for laser melting [2]. An important question here is the degree of structural perfection of the laser-modified layer undergoing the action of the laser irradiation of different intensity and wavelength. The control of the laser recrystallized $Cd_{1-x}Mn_xTe$ crystal surface can be carried out by the scanning atomic force and electron microscopy. Great possibilities of the scanning electron microscopy to determine the structural imperfections of semiconductor crystals are more clearly recognized in the case of the correlation of the electron probe characteristics and the crystal lattice parameters. In the scanning electron microscope at high beam current values and optimal scanning angles, crystal contrast patterns are observed, which contain information about the crystal surface inhomogeneities.

Structure diagnostics of the laser crystallized $Cd_{1-x}Mn_xTe$ crystal surface can be performed by using complex studies in the atomic force and in scanning electron microscopes. The high resolution of the vertical dimensions of the structural imperfections and the statistics in the AFM are complemented by the better lateral resolution in the SEM. It is natural to add the ellipsometric study of the surface films to the AFM and SEM results. Ellipsometry is characterized by the non-destructive action, high sensitivity and a variety of informative features for determination of the optical characteristics and composition of the films [7]. The structural and morphological transformations of the recrystallized surface as a result of the laser treatment are correlated with the change of the ellipsometric parameters. In this paper we propose the method for study the structural state and stability of the modified $Cd_{1-x}Mn_xTe$ crystal surface by using the AFM, SEM and ellipsometric data. The relevance of these studies is related to the search of new opportunities for the development of high-sensitivity radiation sensors based on this material.

1. Research methods

To study the laser modification of the surface, the samples were made in the form of the plates with a thickness ~ (1–1.3 mm) from the CdTe and $Cd_{1-x}Mn_xTe$ crystals grown by the Bridgman method. The final stage of the surface treatment was the polishing on the diamond pastes and washing in benzene and alcohol. The laser treatment of the samples was carried out by a defocused beam of the millisecond optical generator on the ruby (wavelength $\lambda = 0.694$ μm, pulse duration $\tau = 1.2$ ms), as well as using the nanosecond ruby laser (pulse duration $\tau = 70$ ns). The laser radiation was directed to the diaphragm, which selects the most homogeneous part of the beam. By using projection lens, an image of the diaphragm in the form of the laser spot with a diameter ~3–4 mm was formed on the sample. The studies of the morphology and surface structure of the CdTe and $Cd_{1-x}Mn_xTe$ crystals, before and after the laser treatment, were carried out by application of ~~using~~ TESCAN VEGA-3 scanning electron microscope with the EDS block for the microanalysis of the chemical composition. The SEM data on the morphology of the laser-modified epitaxial layers were complemented with the atomic force microscopy studies using the NT-206 setup. The scans were obtained in the contact mode by using the CSC38/AL probe. In the scan area, the number of points per matrix was 256×256, the load on the probe was 10–12 units. The optical characteristics of the films on the CdTe and $Cd_{1-x}Mn_xTe$ crystal surface were determined by using the laser ellipsometer (wavelength $\lambda = 632.8$ nm) with the

incidence angle of the beam within 45–85°. The parameters of the surface films were calculated using the model of "a transparent dielectric thin film – an absorbing substrate".

2. Experimental results and discussion

The processes of laser recrystallization of the $Cd_{1-x}Mn_xTe$ crystal surface were studied using the nanosecond ruby laser with the wavelength $\lambda = 0.694$ μm and pulse duration $\tau = 70$ ns. The laser-induced melting of the crystal surface, followed by the rapid crystallization, leads to the structural transformations in the nonequilibrium $Cd_{1-x}Mn_xTe$ solid phase system. At the same time, within the area of the laser exposure, a variety of defects is generated, some of which can be relaxed, and the rest are fixed in the solid laser-epitaxial layer. The determination and control of the structural imperfections in the $Cd_{1-x}Mn_xTe$ after the laser treatment was performed by the SEM in order to the carried out photonic correction of the recrystallized epitaxial layer properties. It was found that the CdTe and $Cd_{1-x}Mn_xTe$ crystals show structural features that promote observation of the electron channeling pattern in the crystal contrast mode. The pictures of the crossed strips and lines arising during the anomalous absorption of electrons contain information about the state and stability of the crystalline structure of the layers (Fig. 1). The local fields of the thermoelastic stresses and deformations are observed in the form of the curved lines and a number of bands in the visual area of the raster (Fig. 1a).

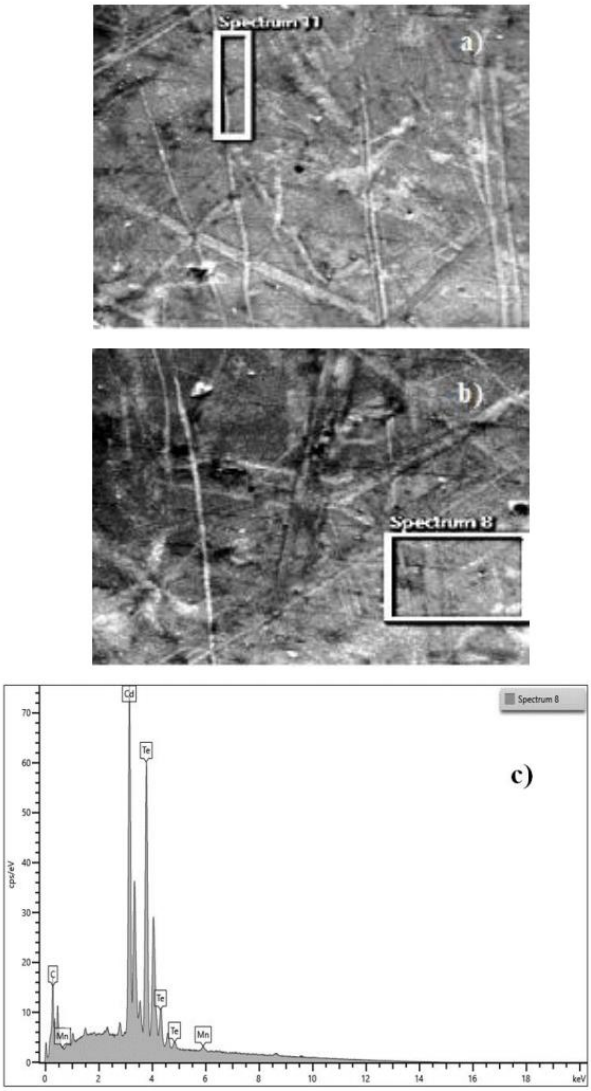

Fig. 1. Electron channeling patterns and EDS spectra (c) in the $Cd_{0.96}Mn_{0.04}Te$ crystals after irradiation by a ruby laser with the energy density: a) E = 0.15 J/cm^2; b) E = 0.21 J/cm^2 (study in SEM)

The optimal modes of the laser treatment made it possible to obtain a better pattern of electron channeling with a large number of straight stripes and lines, which indicates the perfection of the laser epitaxial $Cd_{0.96}Mn_{0.04}Te$ layer (Fig. 1a). It should be noted that the electron channeling patterns for the laser-modified layers do not appear to be as symmetrical and geometrically correct as compared to the bulk single crystals. Further studies of the crystalline contrast on the films and layers, which are significantly non-equilibrium systems, are need to be compared to the single crystals. In our study, the shape of the channeling patterns (typical patterns are presented in Fig. 1) for the $Cd_{1-x}Mn_xTe$ layers was used to determine the optimal laser treatment modes. The EDS chemical composition analysis of the most perfect $Cd_{0.96}Mn_{0.04}Te$ layers showed the accordance of the spectra to the chemical composition of the $Cd_{0.96}Mn_{0.04}Te$ base crystal (Fig. 1c), which indicates that there is no significant evaporation of the components at the optimal laser treatment mode.

The presence of the carbon in the EDS spectrum can be explained by the fact, that on the surface of the base $Cd_{0.96}Mn_{0.04}Te$ crystal after mechanical treatment and washing with organic solvents the organic films remain, which decompose under the action of the laser beam. It is possible to get rid of these residues by the ion-plasma etching of the crystal surface in an argon atmosphere just before laser treatment.

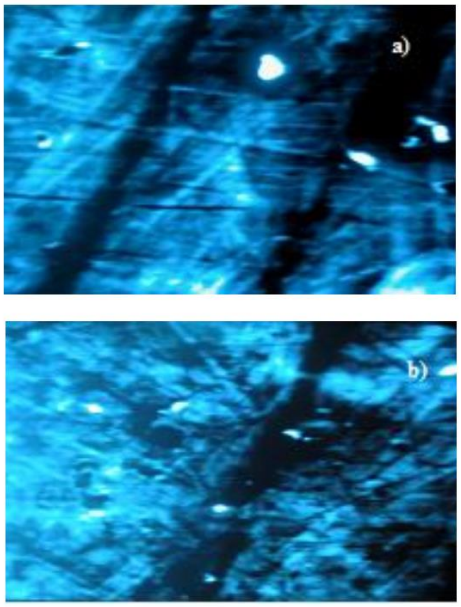

Fig. 2. Electron channeling patterns in the $Cd_{0.9}Mn_{0.1}Te$ crystals after irradiation by a ruby laser with the energy density: a) E = 7 J/cm^2; b) E = 12 J/cm^2 (study in SEM)

We also present the electron channeling patterns of the $Cd_{1-x}Mn_xTe$ (x = 0.1–0.45) crystal irradiated by the millisecond ruby laser ($\tau = 1.2$ ms, $\lambda = 0.694$ μm). For the compositions $x \leq 0.2$ the depth of the surface melting, depending on the energy density, is $h = 5$–14 μm. The correlation of the structure perfection of the laser-epitaxial layer with the crystal contrast patterns is observed for the millisecond laser irradiation as well as for the nanosecond laser irradiation (Fig. 2).

For example, the laser-modified $Cd_{0.9}Mn_{0.1}Te$ layer after the irradiation of the laser with the energy density $E = 7$ J/cm^2 gives a better symmetrical and clear picture of the lines and bands (Fig. 2a) than in the case of more destructive energy $E = 12$ J/cm^2 (Fig. 2b). In both cases, the inclusions of the light and dark contrast regions, depending on the chemical composition, are detected in the electron channeling pictures (Fig. 2). Accordingly, they can be identified as the inclusions of Te and Cd, since the atomic number contrast in the SEM is brighter for the heavy element and darker for the relatively light element.

We also studied the action of the lased on the CdTe crystals with the Cu films deposited from the $CuSO_4$ salt solutions. The melting of the sample surface and formation of the layers with different morphology are observed within the pulse area at laser

treatment. This is a result of the redistribution of the energy between the environment, Cu film and CdTe crystal. It was experimentally found that, depending on the energy density and the corresponding defocusing of the laser beam, the relief and surface structure of the CdTe crystal change in different ways.

The surface presents the concentric angular morphology with the radial step-wave formations at irradiation by the laser beam with the density $E = 15$ J/cm^2 (Fig. 3a). Such morphology can be explained by the geometry of the surface wave dissemination in the liquid phase of the melt, which are formed as closed concentric circles. The wave pattern which is formed in the melt is fixed in the solid film after the crystallization process. The processes of copper ablation are observed at the maximum temperature in the center of the light spot of the laser. This leads to the formation of the craters of unequal shape (Fig. 3a).

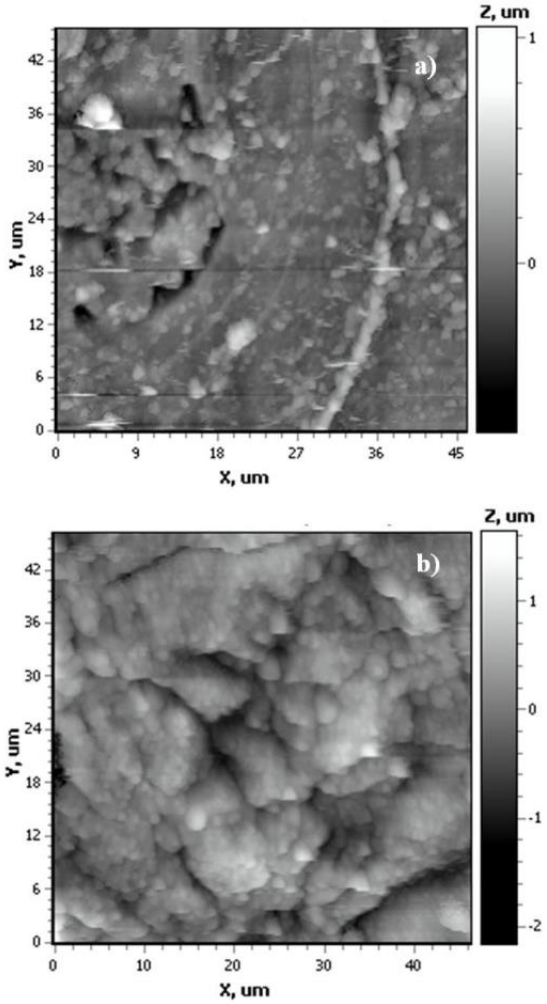

Fig. 3. Morphology of the CdTe crystal surface with the Cu film after the laser irradiation: a) focused beam with the energy density E = 15 J/cm^2 (at the center of the laser spot); b) defocused beam with the energy density E = 9 J/cm^2 (study in AFM)

In the case of the defocused laser beam, the irradiated surface presents humpy morphology (Fig. 3b). Here the Cu film does not contain craters, areas of evaporation of the material, microcracks and other defects. When soldering the electrodes to the regions of the samples with such humpy morphology, good adhesion and hardness at the point of the contact is ensured.

The structure of the grains (crystallites) that formed the Cu film was analyzed. The direction of crystallite growth is determined by the intensity of heat dissipation in the area of the laser spot. The crystallites are preferably in the form of rounded triangles, the size of which decreases slightly from 1–1.3 μm in the middle of the laser spot to 0.5–0.8 μm on the periphery of the laser spot. More elongated crystallites, oriented along the axis of the heat dissipation of the grain, are observed on the periphery of the laser spot. One can visually identify areas of the initial crystallization and recrystallization, which form larger grains, as well as areas of recrystallization with smaller grains of secondary structure. To evaluate the microroughness of the Cu film surface, the parameters R_a and R_q were used, which characterize the surface roughness and are calculated by the AFM software of the NT-206 microscope for each scan image.

In order to diagnose the structural state of the laser-modified $Cd_xMn_{1-x}Te$ crystals, it is necessary to determine the presence of the surface films formed after the crystallization of the molten regions. For this purpose, the ellipsometry method is used, the interpretation of which requires the selection of adequate models of the laser beam reflection process and the simulation of the corresponding nomograms.

To find the solution of the ellipsometric problem for the system consisting of a transparent dielectric thin film on a substrate we applied the graphical-analytical method [7]. The nomograms in the Ψ-Δ ellipsometric parameters were calculated to determine the refractive index of the film and its thickness for the different incidence angles of the laser beam with 632.8 nm wavelength. In Fig. 4, as an example, we present the nomogram calculated for the thin film on the $Cd_xMn_{1-x}Te$ substrate for the incidence angle $\varphi = 50^o$. The solid lines correspond to the constant value of the refractive index of the film and the less bold lines correspond to the constant value of its thickness in nanometers. The input data for the calculations are the refractive index and the absorption coefficient of $Cd_xMn_{1-x}Te$, the wavelength of the radiation, and the refractive index of the environment (air).

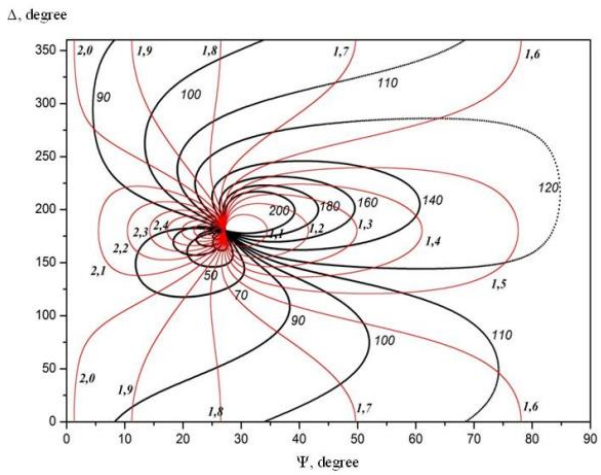

Fig. 4. Calculated nomogram for the determination of the refractive index and thickness of the thin film on the $Cd_xMn_{1-x}Te$ substrate for the incidence angle $\varphi = 50^o$

The refractive index and the thickness of the films were determined using an ellipsometer by measuring the compensation angle of the polarizer and the analyzer at the zero value of the intensity of the reflected laser beam. The main ellipsometric parameters Ψ and Δ were calculated using the experimental values of these angles. It was found that while irradiating the $Cd_{0.9}Mn_{0.1}Te$ surface the different values of the laser beam energy density correspond to the different values of the refractive index of the oxide film on the modified surface (Table 1).

Table 1. The dependence of the refractive index and the corresponding chemical composition of the film on the energy density of the laser

N	Energy density of the laser, J/cm^2	Refractive index	Composition of the film
1	2.5	2.43	CdO
2	5.2	2.45	CdO
3	7.3	2.2	$CdTeO_3$
4	8.4	2.15	$CdTeO_3$
5	9.0	2.1	$CdTeO_3$
6	10.3	1.9	TeO_2
7	11.5	1.8	TeO_2

These changes in the refractive index can be interpreted as the formation of the oxides of different chemical composition. The TeO_2 oxide is unstable among these oxides. The mechanism of

formation and growth of the oxide film changes depending on the intensity of the laser action. The formation of the oxides, which are mainly formed from the Cd or Te component, is affected by the evaporation of the volatile component from the region of rapid melting in the $Cd_{0.9}Mn_{0.1}Te$ crystal.

The thickness of the oxide film according to the Ψ-Δ nomograms increase with increasing laser energy density and is within 35–56 nm. Since the oxide films can act as dielectrics or passivators, especially for submicron- and nanoelectronics, the obtained experimental data can be used for the laser correction of the structural phase state of the film layers in the radiation detectors on the base of the $Cd_{1-x}Mn_xTe$ crystals.

3. Conclusion

The processes of the laser recrystallization of the $Cd_{1-x}Mn_xTe$ crystal surface with the use of both millisecond and nanosecondlaser lead to the structural transformations in the $Cd_{1-x}Mn_xTe$ laser epitaxial layer. The analysis of the channeling patterns, which still needs further development with respect to the $Cd_{1-x}Mn_xTe$, can be used as a criterion for the selection of the optimal laser treatment modes. The complex studies using the SEM, AFM, and ellipsometry methods of the laser-modified surface are promising for the determination, diagnostics, and correction of the surface structural phase state in the $Cd_{1-x}Mn_xTe$ based devices.

References

[1] Cui Y., Bolotnikov A., Hossain A., Camarda G., Mycielski A., Yang G., Kochanowska D., Witkowska-Baran M. James R.B.: CdMnTe in X-ray and gamma-ray detection: potential applications. Proc. SPIE 7079/2008.

[2] Dremlyuzhenko S.G., Zakharuk Z. I., Savchuk A. I., Fochuk P. M.: Effect of treatment on the CdTe, $Cd_{1-x}Mn_xTe$ and $Cd_{1-x}Zn_xTe$ surface stoichiometry. Phys. Stat. Sol. (b) 244/2007, 1650–1654.

[3] Gatskevich E., Ivlev G., Prikryl P., Cerny R., Chab, V., Cibulka, O.: Pulsed laser-induced phase transformations in CdTe single crystals. Appl. Surf. Sci. 248/2005, 259–263.

[4] Mycielski A., Kowalczyk L., Galazka R. R., Sobolewski R., Wang D., Burger A., Sowinska M., Groza M., Siffert P., Szadkowski A., Witkowska B., Kaliszek W.: Applicaions of II–VI semimagnetic Semiconductors. J. Alloys Compd. 423/2006, 163–168.

[5] Nikonyuk E. S., Zakharuk Z. I., Kuchma M. I., Rarenko A. I., Shlyakhovyi V. L., Yuriychuk I. M.: Relaxation processes in conductivity of $Cd_{1-x}Mn_xTe$ crystals (0.02<x<0.55). Semiconductors 42(9)/2008, 1012–1015.

[6] Savchuk A. I., Fochuk P. M., Strebezhev V. V., Kleto G. I., Yuriychuk I. M., Khalavka Y. B., Obedzynskyi Y. K., Strebezhev V. M.: The effect of laser treatment on the morphology and structure of CdSb-$Cd_{1-x}Mn_xTe$ and CdSb-$In_4(Se_3)_{1-x}Te_{3x}$ thin film heterojunctions: Appl. Sur. Sci. 418/2017, 536–541.

[7] Tompkins H. G., Hilfiker J. N.: Spectroscopic Ellipsometry: Practical Application to Thin Film Characterization. Momentum Press, New York 2016.

[8] Triboulet R., Siffert P.: CdTe and Related Compounds; Physics, Defects, Hetero-and Nano-structures, Crystal Growth, Surfaces and Applications. Elsevier, Amsterdam 2010.

[9] Vorobets G. I., Vorobets O. I., Strebegev V. N.: Laser manipulation of clasters, structural defects and nanoaggregates in barrier structures on silicon and binary semiconductors. Appl. Surf. Sci. 247/2005, 590–601.

[10] Yuriychuk I. M., Fochuk P. M., Bolotnikov A. E., James R. B.: Ab initio GGA+U investigations of the structural, electronic, and magnetic properties of $Cd_{1-x}Mn_xTe$ alloy. Proc. SPIE 11114/ 2019.

Ph.D. Victor Strebezhev
e-mail: v.strebezhev@chnu.edu.ua

The head of the Department of Physics of Semiconductors and Nanostructures of Yuriy Fedkovych Chernivtsi National University. Research interests: technology and physics of semiconductor epitaxial layers and thin films; optical and photoelectric properties of semiconductors quantum structures; submicron technologies.

http://orcid.org/0000-0001-6127-656X

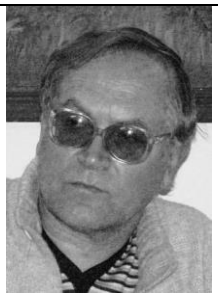

Ph.D. Ivan Yuriychuk
e-mail: i.yuriychuk@chnu.edu.ua

Associate Professor of the Department of Physics of Semiconductors and Nanostructures of Yuriy Fedkovych Chernivtsi National University. Research interests: electronic spectra of A(II)B(VI) semiconductor compounds and low-dimensional structures on their basis.

http://orcid.org/0000-0001-6475-8337

Prof. Petro Fochuk
e-mail: p.fochuk@chnu.edu.ua

Vice-chairman of Yuriy Fedkovych Chernivtsi National University. Research interests: technology of crystal growth, properties of point defects in CdTe and other A(II)B(VI) compounds.

http://orcid.org/0000-0002-4149-4882

Ph.D. Sergiy Nichyi
e-mail: s.nichyi@chnu.edu.ua

Associate Professor of the Department of Physics of Semiconductors and Nanostructures of Yuriy Fedkovych Chernivtsi National University. Research interests: technology of thin semiconductor films, automation of the measurements of their electrophysical properties.

http://orcid.org/0000-0003-2662-9694

D.Sc. Yuriy Dobrovolsky
e-mail: y.dobrovolsky@chnu.edu.ua

Associate Professor of the Department of Physics of Semiconductors and Nanostructures of Yuriy Fedkovych Chernivtsi National University. Research interests: semiconductor converter of the ultraviolet, visible and near-infrared radiation.

http://orcid.org/0000-0002-1248-3615

M.Sc. Victoria Tkachuk
e-mail: v.tkachuk@chnu.edu.ua

Assistant of the Department of Physics of Semiconductors and Nanostructures of Yuriy Fedkovych Chernivtsi National University. Research interests: stadu of physical and technological characteristics of high-perfect CdTe crystals.

http://orcid.org/0000-0002-4265-194X

M.Sc. Mykola Sorokatyi
e-mail: m.sorokatyi@chnu.edu.ua

Graduate student of the Department of Physics of Semiconductors and Nanostructures of Yuriy Fedkovych Chernivtsi National University. Research interests: technology and physics of semiconductor thin films.

http://orcid.org/0000-0001-6602-5698

M.Sc. Yurii Sorokatyi
e-mail: m.sorokatyi@chnu.edu.ua

Graduate student of the Department of Physics of Semiconductors and Nanostructures of Yuriy Fedkovych Chernivtsi National University. Research interests: technology and physics of semiconductor converter of the ultraviolet radiation.

http://orcid.org/0000-0001-9462-775X

otrzymano/received: 15.11.2019 *przyjęto do druku/accepted: 15.02.2020*

http://doi.org/10.35784/iapgos.896

TECHNOLOGY AND MEASUREMENTS OF MAGNETORESISTANCE IN THIN-LAYERED FERROMAGNETIC STRUCTURES

Jakub Kisała[1], Karolina Czarnacka[2], Mateusz Gęca[1], Andrzej Kociubiński[1]
[1]Lublin University of Technology, Lublin, Poland, [2]University of Life Sciences, Lublin, Poland

Abstract. *The paper presents the technology for obtaining NiFe/Ti/NiFe layer structures in MEMS technology using magnetron purge with the assumption of being used as semi-magnetic sensors. A series of samples was made on a glass substrate with a sandwich structure, where the individual layers were 100 nm NiFe, 10 nm Ti and on top again NiFe with a thickness of 100 nm. Measurements of DC resistance of the obtained structures in a constant magnetic field, which was produced by neodymium magnets and an electromagnet, were carried out. The obtained results confirm the occurrence of phenomena known as the magnetoresistance effect. The influence of the spatial arrangement of structures relative to the constant magnetic field vector was checked and proved.*

Keywords: static magnetic field, magnetron sputtering, MEMS, magnetoresistance

TECHNOLOGIA I POMIARY MAGNETOOPORU W CIENKOWARSTWOWYCH STRUKTURACH FERROMAGNETYCZNYCH

Streszczenie. *W pracy przedstawiono technologię otrzymywania struktur warstwowych NiFe/Ti/NiFe w technologii MEMS metodą rozpylania magnetronowego w założeniu mających służyć jako czujniki pól magnetycznych. Wykonano serię próbek na szklanym podłożu o budowie kanapkowej, gdzie poszczególne warstwy stanowiły 100 nm NiFe,10 nm Ti oraz na wierzchu ponownie NiFe o grubości 100 nm. Przeprowadzono pomiary rezystancji stałoprądowej otrzymanych struktur w stałym polu magnetycznym, które było wytwarzane przez magnesy neodymowe oraz elektromagnes. Otrzymane wyniki potwierdzają występowanie zjawisk określanych jako efekt magnetooporowy. Sprawdzony oraz udowodniony został wpływ ułożenia przestrzennego struktur względem wektora stałego pola magnetycznego.*

Słowa kluczowe: statyczne pole magnetyczne, rozpylanie magnetronowe, MEMS, magnetoopór

Introduction

The phenomenon of magnetoresistance is defined as the change in the resistance of a material or device under the influence of a magnetic field [4]. One of the first applications of devices operating based on this effect were magnetic field sensors and hard disk read heads [5]. Currently, magnetoresistive sensors are widely used in many industries due to the low production cost, temperature stability, simplicity of implementation and the possibility of integration with CMOS systems [12, 19]. One of the most popular applications of this type of sensors is their use for current measurement, because they ensure high sensitivity and linearity of measurements without interfering with the integrity of the measured circuit [4]. In the automotive industry, magneto-resistive sensors are used to measure distance, angle, speed and rotational speed due to the convenience of their use in contactless position registration [4]. They are also used in the biotechnology industry, where they are used, among others in tests for proteins and microfluidic systems [9, 11].

Besides widely used sensors working based on the Hall effect, an attractive option for determining the intensity of the magnetic field seems to be microscopic structures whose work is based on the phenomenon of magnetoresistance. Their advantages are low weight and dimensions, high sensitivity and stability [1, 2, 13]. A good example of the material for the production of such structures is the NiFe alloy, which is used in the vast majority of sensors working on the principle of magnetoresistance [21, 22]. It is a popular material used in spintronics due to the appropriate magnetic parameters and is characterized by sufficiently large magnetoresistance changes [22]. However, the use of layered structures significantly increases the intensity of magnetoresistive phenomena [1, 2]. A simple three-layer structure consisting of two external ferromagnetic layers and an internal diamagnetic or para-magnetic layer, with a much higher conductivity, provides large changes in resistance under the influence of a constant magnetic field. As ferromagnetic layers, NiFe alloy [20] or pure metals such as cobalt or iron [14] are usually used, because they have low magnetostriction and are magnetically soft. As an internal non-magnetic layer, precious metals or copper are used, which ensures good electrical conductivity [8, 16]. In such systems, several parameters can be manipulated, for example, layer thickness, surface roughness, and even crystal structure, which can strongly affect the magnetic properties of the product [6].

A wide spectrum of deposition techniques appear in the process of obtaining ferromagnetic layered structures, which include spin coating, chemical vapor deposition (CVD), ion sputtering, vacuum deposition, or pulse electroplating [3, 7, 10]. It is worth emphasizing that the spin coating method cannot guarantee a uniform coating thickness [15], and the layers obtained by CVD methods have low purity [18]. On the other hand, thin ferromagnetic layers produced by means of vacuum deposition can be coarse-grained, in the range of 200–500 nm, which negatively affects the magnetic properties. Therefore, ion sputtering is a method that is often used, which ensures even coverage and high sample purity [17].

The purpose of the work was to develop a technology for the production of MEMS NiFe/Ti/NiFe structures and to conduct measurements of DC resistance depending on the magnetic field in terms of determining the occurrence of the phenomenon of magnetoresistance.

1. Technology of thin-film resistor

Designed structures were developed in the Department of Electronics and Information Technology of Lublin University of Technology using magnetron sputtering. A Kurt J. Lesker Company® NANO 36 sputtering system was used to develop thin film layers. Microscope slides were used as substrates for structures.

Figure 1. shows the sequence of technological steps performed to develop designed structures. The first and the third layer of the device were deposited using a NiFeCuMo alloy target. Due to a low content of copper and molybdenum in the alloy, it will be further on referred to as NiFe.

Process parameters for a 100 nm thick NiFe layer deposition in a vacuum of 10^{-7} Torr were as follows: plasma power density – 180 W/cm^{-2}, argon flow rate – 100 sccm, deposition rate – 0.3 Å/s, deposition time – 57 min. In the next step, a 10 nm thick layer of titanium was deposited. Purity of a used target was equal to 98.4%. Process parameters in a vacuum of 10^{-7} Torr were: plasma power density – 80 W/cm^{-2}, argon flow rate – 100 sccm, deposition rate – 0.1 Å/s, deposition time – approx 15 min.

Following the deposition of a second layer, at both ends of developed structures, electrical contacts to titanium layer with dimensions of 1×1 mm^2 were provided using kapton tape as a mask.

The second layer of NiFe was deposited with the same process parameters as previously mentioned. Finally, copper wires were glued to electrical contacts using Anders Products Wire Glue. The resulting structures have dimensions of 10 mm × 1 mm × 210 nm.

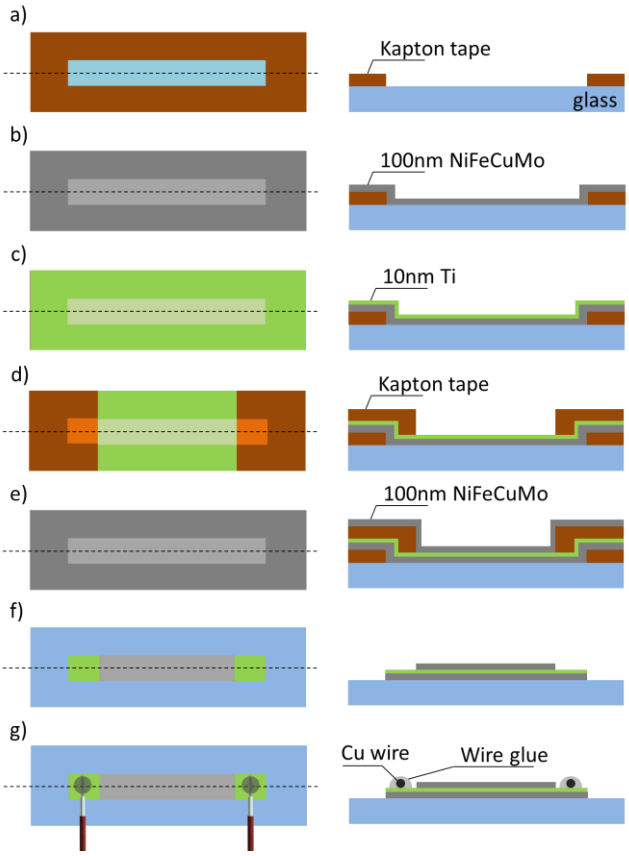

Fig. 1. The fabrication steps of the ferromagnetic resistor process: (a) sticking a kapton tape with exposed space for the structure, (b) deposition of a 100 nm NiFe layer, (c) deposition of a 10 nm Ti layer, (d) covering titanium contact fields with a kapton tape, (e) deposition of a second 100 nm NiFe layer, (f) removal of the kapton tape, (g) the final device.

2. Experimental procedure

The research carried out on the prepared NiFe/Ti/NiFe structure was aimed to confirming the occurrence of magnetoresistance effects. First, a pair of neodymium magnets mounted in a vice were used as the source of the permament magnetic field. The measurements of the constant current of the sample were carried out using a KeySight 34410A multimeter cooperating with LabView software, where the measurement values were stored. The measurements were carried out for three positions of the sample relative to the magnetic field as shown schematically in figure 2. The value of magnetic flux density between neodymium magnets was about 0.5 T. The intervals between individual measurements were 5 seconds.

The next stage was measurements carried out in a magnetic field created by an electromagnet whose coil was connected to a DC power supply. A schematic of the measuring system for this configuration is shown in figure 3.

The structure resistance values were measured for the increasing magnetic flux density value, which was obtained by stepwise changing the voltage value applied to the coil from 0 V to 400 V, with a 10 V step, for two variants of voltage coil polarization. Changes in voltage directly affected into changes in the coil current, and thus the value of magnetic flux density. This values were measured using a GM08 teslometer from Hirst Magnetics and the characteristics of the magnetic flux density *B* depended on the coil current *I* was developed, Fig. 4.

The number of resistance measurements for each value of the magnetic flux density was 100, between changes in the magnetic flux density was 5 seconds gap in the resistance measurement. The value of sample resistance for a given coil current was statistically developed from 100 measurements. The measurements were carried out in three positions of the sample in the magnetic field as shown in figure 2.

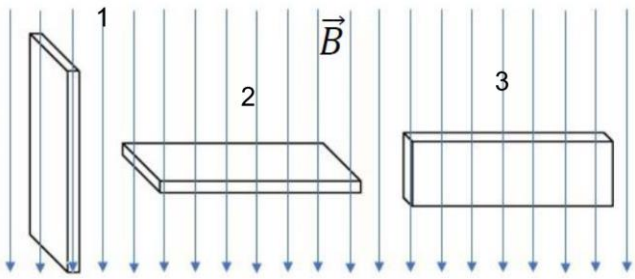

Fig. 2. Positions of the sample in the magnetic field

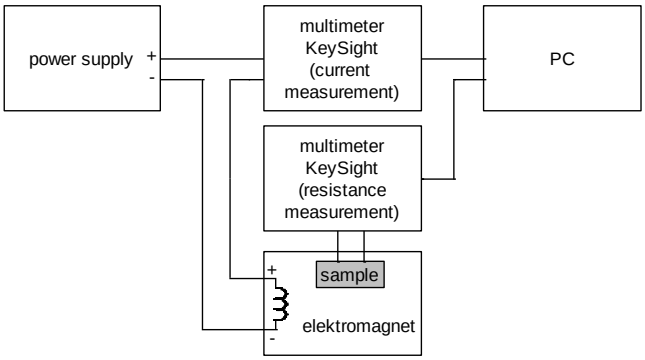

Fig. 3. The scheme of measurement station

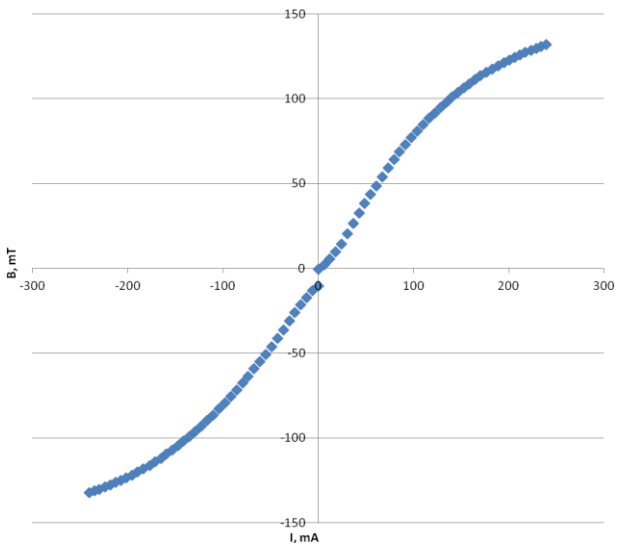

Fig. 4. Electromagnet characteristics

3. Results and discussion

Measurements of a change in resistance of the tested NiFe/Ti/NiFe sample under the influence of a static magnetic field with a flux density of approximately 0.5 T show evident changes in sample's resistance, as shown in figure 5. In both cases, the sample's resistance decreases when placed in the magnetic field and returns to its initial value after removing it from neodymium magnets. For the position 2, a resistance change of approximately 0.5 Ω is visible, while for the position 1 – approx. 1 Ω. Small fluctuations in the resistance value of about 0.2 Ω do not seem to affect its change resulting from magnetoresistive properties.

Further measurements verifying presence of the magneto-resistance phenomenon in the designed structures were conducted using an electromagnet providing magnetic flux densities of significantly smaller magnitude (approx. 0.13 T) (Fig. 6).

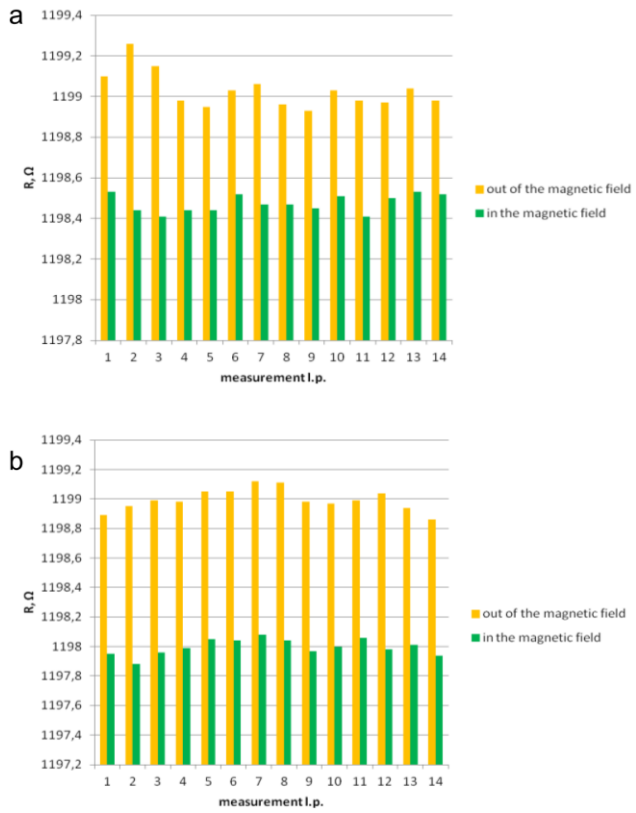

Fig. 5. Measurements of resistance in the magnetic field of a neodymium magnet in the position: a) 2, b) 1

For a sample in position 2, it is difficult to clearly state the nature of the changes; the sample's resistance values in and outside the field do not differ significantly from each other. Position 1 of the structure gives the expected results. Changes in resistance induced by a presence of a magnetic field are clearly visible and reach value of approx. 0.6 Ω. As in previous cases, fluctuations in resistance during measurements do not seem to significantly affect the differences in structure's resistance in and outside of the magnetic field.

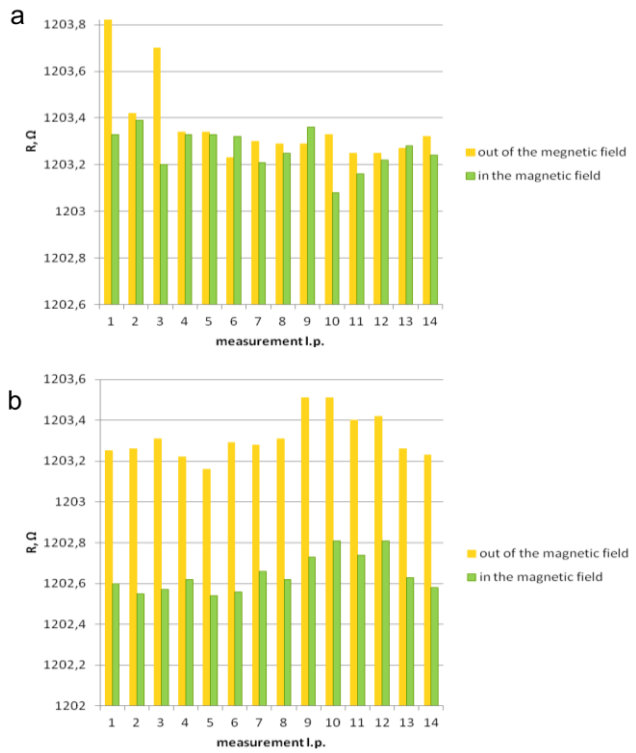

Fig. 6. Measurements of resistance in the magnetic field of the electromagnet in position: a) 2, b) 1

The first series of measurements was conducted for the position 1 of the NiFe/Ti/NiFe structure. Obtained results are presented in figure 5. Further experiments were run for the structures positions 2 and 1, as presented in figures 7 and 8 respectively. The difference between an initial resistance of a sample for the current of the solenoid coil equal to 0 A and the sample's resistance measured at a given solenoid coil's current is denoted as ΔR.

For all structure arrangements, a decrease in resistance due to an increase in magnetic flux density is observed. The smallest difference in resistance ΔR between extreme values of the magnetic flux density for a given polarization occurs in the case of a position 2 of the sample and is about -0.6 Ω. The largest difference in resistance ΔR reaches approx. -1.4 Ω. For a structure in position 2, relatively large differences between adjacent measurement points are visible. In the position 3, where the ΔR value is more than twice as large compared to other sample's arrangements, ΔR fluctuations are also less noticeable. The magnetoresistance effect is clearly visible and its intensity depends on the arrangement of the structure relative to the direction of the magnetic field vector. Despite the differences in the characteristics determined for both current polarities, it can be stated that the effect of magnetic resistance occurs regardless of the sense of the magnetic field vector.

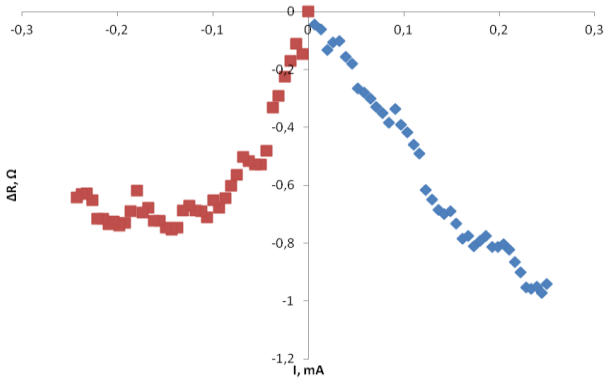

Fig. 7. The decrease in resistance depending on the magnetic flux density (the diagram shows as the coil current) – position 1

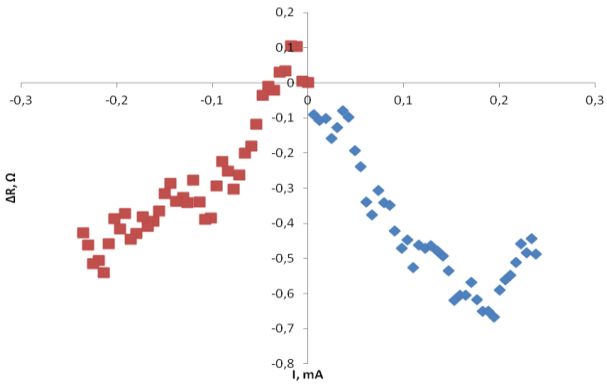

Fig. 8. The decrease in resistance depending on the magnetic flux density (the diagram shows as the coil current) – position 2

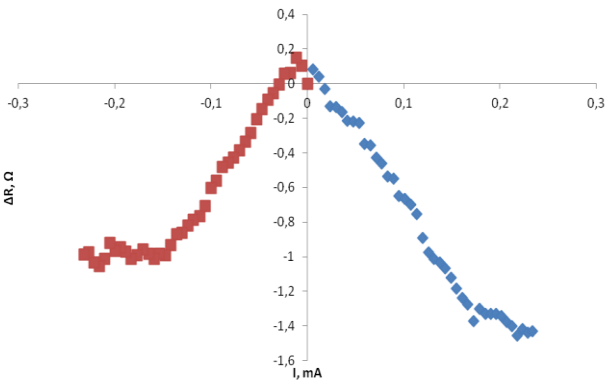

Fig. 9. The decrease in resistance depending on the magnetic flux density (the diagram shows as the coil current) – position 3

4. Conclusion

The measurements of the resistance of the obtained NiFe/Ti/NiFe structures confirm the assumptions about the presence of magneto-resistance effects in them. Structure production technology therefore brings the expected results. The studied effect of the spatial arrangement of the sample relative to the magnetic field allows to determine its impact on the intensity of magnetoresistive phenomena occurring.

References

[1] Chen L., Zhou Y., Lei C., Zhou Z. M., Ding W.: Giant magnetoimpedance effect in sputtered single layered NiFe film and meander NiFe/Cu/NiFe film. Journal of Magnetism and Magnetic Materials 322(19)/2010, 2834–2839, [http://doi.org/10.1016/j.jmmm.2010.04.038].

[2] Chen L., Zhou Y., Lei C., Zhou Z. M.: Effect of sputtering parameters and sample size on giant magnetoimpedance effect in NiFe and NiFe/Cu/NiFe films. Materials Science and Engineering B: Solid-State Materials for Advanced Technology 172(2)/2010, 101–107, [http://doi.org/10.1016/j.mseb.2010.04.026].

[3] Dixit G., Singh J. P., Srivastava R. C., Agrawal H. M., Choudhary R. J., Ajay G.: Structural and magnetic behaviour of $NiFe_2O_4$ thin film grown by pulsed laser deposition. Indian Journal of Pure & Applied Physics 48(4)/2010, 287–291.

[4] Djamal M., Ramli: Development of sensors based on giant magnetoresistance material. Procedia Engineering 32/2012, 60–68, [http://doi.org/10.1016/j.proeng.2012.01.1237].

[5] Ennen I., Kappe D., Rempel T., Glenske C., Hütten A.: Giant Magnetoresistance: Basic concepts, microstructure, magnetic interactions and applications. Sensors 16/2016, [http://doi.org/10.3390/s16060904].

[6] Esmaili S., Bahrololoom M. E., Zamani C.: Electrodeposition of NiFe/Cu multilayers from a single bath. Surface Engineering and Applied Electrochemistry 47(2)/2011, 107–111, [http://doi.org/10.3103/S1068375511020049].

[7] Fernandez G. V., Grundy P. J., Vopson M. M.: Control and Analysis of Grain Size in Sputtered NiFe Thin Films. Journal of Condensed Matter Physics 1(1)/2013, 6–9.

[8] García-Arribas A., Fernández E., Svalov A., Kurlyandskaya G. V., Barandiaran J. M.: Thin-film magneto-impedance structures with very large sensitivity. Journal of Magnetism and Magnetic Materials 400/2016, 321–326, [http://doi.org/10.1016/j.jmmm.2015.07.107].

[9] Gijs M. A. M.: Magnetic bead handling on-chip: New opportunities for analytical applications. Microfluidics and Nanofluidics 1/2004, 22–40, [http://doi.org/10.1007/s10404-004-0010-y].

[10] Gupta N., Verma A., Kashyap S. C., Dube D. C.: Dielectric behavior of spin-deposited nanocrystalline nickel-zinc ferrite thin films processed by citrate-route. Solid State Communications 134(10)/2005, 689–694, [http://doi.org/10.1016/j.ssc.2005.02.037].

[11] Hall D. A., Gaster R. S., Lin T., Osterfeld S. J., Han S., Murmann B., Wang S. X.: GMR biosensor arrays: A system perspective. Biosensors and Bioelectronics 25(9)/2010, 2051–2057, [http://doi.org/10.1016/j.bios.2010.01.038].

[12] Jogschies L., Klaas D., Kruppe R., Rittinger J., Taptimthong P., Wienecke A., Wurz M. C.: Recent developments of magnetoresistive sensors for industrial applications. Sensors 15/2015, 28665–28689, [http://doi.org/10.3390/s151128665].

[13] Kurlyandskaya G. V., Fernández E., Svalov A., Burgoa Beitia A., García-Arribas A., Larranaga A.: Flexible thin film magnetoimpedance sensors. Journal of Magnetism and Magnetic Materials 415/2016, 91–96, [http://doi.org/10.1016/j.jmmm.2016.02.004].

[14] Kuru H., Kockar H., Alper M.: Giant magnetoresistance (GMR) behavior of electrodeposited NiFe/Cu multilayers: Dependence of non-magnetic and magnetic layer thicknesses. Journal of Magnetism and Magnetic Materials 444/2017, 132–139, [http://doi.org/10.1016/j.jmmm.2017.08.019].

[15] Lai C. H., Matsuyama H., White R. L., Anthony T. C., Matsuyama H.: Anisotropic Exchange for NiFe Films Grown on Epitaxial NiO. IEEE Transactions on Magnetics 31(6)/1995, 2609–2611, [http://doi.org/10.1109/20.490068].

[16] Makhnovskiy D. P., Panina L. V., Fry N., Mapps D. J.: Magneto-impedance in NiFe/Au/NiFe sandwich films with different types of anisotropy. Journal of Magnetism and Magnetic Materials 272–276(III)/2004, 1866–1867, [http://doi.org/10.1016/j.jmmm.2003.12.833].

[17] Motomura Y., Tatsumi T., Urai H., Aoyama M.: Soft Magnetic Properties and Heat Stability for Fe/NiFe Superlattices. IEEE Transactions on Magnetics 26(5)/1990, 2327–2331, [http://doi.org/10.1109/20.104714].

[18] Phani A. R., Santucci S.: Structural characterization of nickel titanium oxide synthesized by sol-gel spin coating technique. Thin Solid Films 396/2001, 1–4, [http://doi.org/10.1016/S0040-6090(01)01131-2].

[19] Reig C., Cubells-Beltrán M.-D., Ramírez Munoz D.: Magnetic Field Sensors Based on Giant Magnetoresistance (GMR) Technology: Applications in Electrical Current Sensing. Sensors 9(10)/2009, 7919–7942, [http://doi.org/10.3390/s91007919].

[20] Svalov A. V., Larranaga A., Kurlyandskaya G. V.: Effect of Ti seed and spacer layers on structure and magnetic properties of FeNi thin films and FeNi-based multilayers. Materials Science and Engineering B: Solid-State Materials for Advanced Technology 188/2014, 102–105, [http://doi.org/10.1016/j.mseb.2014.06.006].

[21] Zhao C. J., Wu Z. L., Zhao Z. D., Ding L., Lu X. A., Li X. J., Yu G. H.: Influence on the transport behaviors of spin-polarized electrons exerted by MgO/NiFe and NiFe/MgO heterointerfaces. Journal of Magnetism and Magnetic Materials 368/2014, 59–63, [http://doi.org/10.1016/j.jmmm.2014.05.013].

[22] Zhao Z. D., Li M. H., Zhao C. J., Yang G., Zhang J. Y., Jiang S. L., Yu G. H.: Large enhancement of magnetoresistance in NiFe film with MgO layers sandwiched after annealing. Applied Surface Science 321/2014, 554–559, [http://doi.org/10.1016/j.apsusc.2014.10.047].

Eng. Jakub Kisała
e-mail: jakub.kisala@pollub.edu.pl

Master student at the Lublin University of Technology
Faculty Electrical Engineering and Computer Science
Branch of study: Mechatronics
Speciality: Mobile system in mechatronics

http://orcid.org/0000-0002-4898-3670

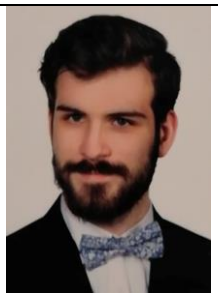

M. Sc. Eng. Karolina Czarnacka
e-mail: karolina.czarnacka@up.lublin.pl

An employee as an assistant in the Department of Fundamentals of Technology at the University of Life Sciences in Lublin. Ph.D. student at the Lublin University of Technology in the discipline of Electrical Engineering.

http://orcid.org/0000-0003-1434-734X

M. Sc. Eng. Mateusz Gęca
e-mail: mati.geca@gmail.com

An employee in the Department of Electronics and Information Technology, Lublin University of Technology (LUT). He received the M.Sc. degree in mechatronics from LUT. Research area concerns diagnostics and characterization of semiconductor devices.

http://orcid.org/0000-0002-0519-7389

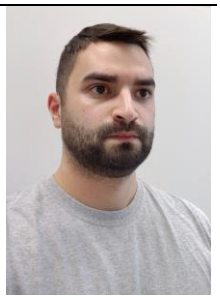

Ph.D. Andrzej Kociubiński
e-mail: akociub@semiconductor.pl

He received the M.Sc. and Ph.D. degrees in electronic engineering from Warsaw University of Technology, Poland. In 2007 he joined the Lublin University of Technology, where he was involved in research on semiconductor technology. His research interest is concentrated on semiconductor devices and technology. His recent activities are related to microsystems for biomedical applications.

http://orcid.org/0000-0002-0377-8243

otrzymano/received: 14.12.2019 *przyjęto do druku/accepted: 15.02.2020*

http://doi.org/10.35784/iapgos.907

STUDYING THE PROPERTIES OF PIXELS PERMUTATIONS BASED ON DISCRETIZED STANDARD MAP

Serhii Haliuk, Oleh Krulikovskyi, Vitalii Vlasenko
Chernivtsi National University, Department of radio engineering and information security, Chernivtsi, Ukraine

Abstract. *In this article, we described specifics of pixels permutations based on the discretized, two-dimensional Chirikov standard map. Some properties of the discretized Chirikov map can be used by an attacker to recover the original images that are studied. For images with dimensions $N \times N$ the vulnerability of permutations allows for brute force attacks, and shown is the ability of an intruder to restore the original image without setting the value of keys permutations. Presented is also, successful cryptographic attack on the encrypted image through permutation of pixels. It is found that for images with dimension $N \times N$ the maximum number of combinations is equal to N^{N-1}. A modified Chirikov map was proposed with improved permutation properties, due to the use of two nonlinearities, that increase the keys space to $N^2!$.*

Keywords: discretized standard map, permutation of pixels, key space, precision of computing

BADANIE WŁAŚCIWOŚCI PERMUTACJI PIKSELI W OPARCIU O ZDYSKRETYZOWANĄ MAPĘ STANDARDOWĄ

Streszczenie. *W tym artykule opisana została specyfika permutacji pikseli w oparciu o zdyskretyzowaną, dwuwymiarową mapę standardową Czirikowa. Niektóre właściwości tej mapy mogą zostać użyte przez napastnika, aby odzyskać oryginalne obrazy, które są badane. Jeśli chodzi o obrazy o wymiarach $N \times N$, permutacje są podatne na agresywne ataki. Pokazana jest również możliwość odzyskania przez intruza oryginalnego obrazu bez ustawienia wartości permutacyjnych. Przedstawiony został również udany atak kryptograficzny na zaszyfrowany obraz za pomocą permutacji pikseli. Stwierdzono, że w przypadku obrazów o wymiarach $N \times N$, maksymalna liczba kombinacji jest równa N^{N-1}. Zaproponowano zmodyfikowaną mapę Czirikowa z ulepszonymi właściwościami permutacji, dzięki wprowadzeniu dwóch nieliniowości, które zwiększyły zestaw możliwych kombinacji do $N^2!$.*

Słowa kluczowe: zdyskretyzowana mapa standardowa, permutacja pikselowa, możliwe kombinacje, precyzja obliczeń

Introduction

Over the last two decades the application of deterministic chaos for information security became an active field of research [2, 6, 8]. Among chaos–based cryptography algorithms, a significant part is designed for image encryption. The most commonly used design is cipher with two mean stages: pixels permutation and diffusion which can be repeated several times [5]. Permutations of pixels are needed to break relations between adjacent pixels and prevent correlation attacks. The goal of diffusion is to transform the uneven distribution of color pixels into uniform, thereby concealing the statistical properties of the original image. Typically for pixels permutations, used are discretized versions of Standard, Baker or Cat map [5] or their modifications. For the diffusion step typically is used PRNG based on one, two or multi-dimensional maps. Along with the new encryption algorithms based on deterministic chaos, the works dedicated to cryptanalysis have been presented [1, 3, 10, 12]. In [10] was proposed one of the earliest chaotic image encryption algorithms which uses discretized version of Chirikov standard map for pixels permutations [4]. It was later shown in [9] that in this map, the first pixel does not change its position after any number of permutation cycles. To eliminate this vulnerability, it was suggested to use mechanism, which essence is to shift first pixel into any position in the image. Also, there were given [9] recommendations for minimum size images for encryption and minimum number of permutation cycles.

In this paper we focus on cryptographic security of pixels permutations based on the discretized two-dimensional Chirikov standard map considering its geometric properties. We explore the resistance of permutations to brute force attack and we find property that greatly reduces the key space of permutations compared to the known assessment of key space made in [9]. To eliminate the identified vulnerabilities, we propose to modify the discretized standard map by entering additional nonlinearity. Also, we estimate the key space of permutations for double-precision arithmetic and we show that the key space is very small compared to the theoretically possible maximum. Please note that we consider changes as only one stage of the chaotic algorithms.

In section 1 specifics of pixels permutations based on discretized standard map and power of key space are described. In section 2 shown is a cryptographic attack on the encrypted image by permutation of pixels and reduced key space.

1. Specifics of permutations based on discretized standard map

As noted above, in [5] was introduced discretized standard map for pixels permutations, that is given by the following iterative equations:

$$\begin{aligned} x_{i+1} &= (x_i + y_i) \bmod N \\ y_{i+1} &= \left(y_i + K \sin\left(\frac{x_{i+1} N}{2\pi} \right) \right) \bmod N \end{aligned} \tag{1}$$

where x_i and y_i are coordinates, $i \in [0;\ N-1]$, K – a control parameter which is a positive integer, N is the number of pixels in width or height of the original image. As we can see, (1) is suitable only for bitmaps with $N \times N$ dimensions.

Properties of the discretized map (1) are not as perfect as the original [3], but it can be implemented in the integer x_i and y_i values of intervals, which reduce the computational complexity and are more convenient to encryption data applications [5].

The procedure of one cycle of pixels permutation for bitmap with dimension $N \times N$ in RGB format is as follows:

a) For each pixel x_i and y_i there is a calculation of (1) made to form its new coordinates x_{i+1} and y_{i+1} in encrypted image.
b) Coordinates x_{i+1} and y_{i+1} in encrypted image record pixel color values (RGB) of the original image.
c) These operations (1 and 2) are carried out sequentially for each pixel.

Let's analyze features of pixels permutations based on map (1), considering its geometric properties for bitmaps with $N \times N$ dimensions.

1.1. Features of permutations

Any picture with dimension $N \times N$ has $2N-1$ diagonals (see Fig. 1). The first and the last diagonals are composed of one element. Number of elements in the diagonal varies from 1 to N. The first element of the diagonal is the pixel with the lowest x_i. Permutations based on discretized standard map have following properties:

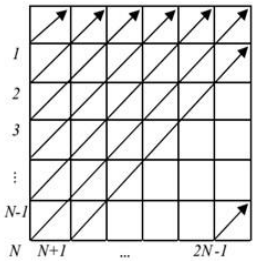

Fig. 1. Diagonals of any image with N × N dimensions

a) The first pixel in coordinates $(0;\ 0)$ does not change its position at any number of permutation cycles, it can be used by cryptanalyst to crack the encrypted images [9]. When $x_i = 0$, $y_i = 0$ we use (1) and calculate that $x_{i+1} = 0$, $y_{i+1} = 0$.

b) Each column after one cycle of permutation consists of two diagonals with numbers n and $N + n$, $n \in [2; N-1]$ except the diagonal N. It is because the diagonal N consists of N elements. This property of the permutation is shown in Fig. 2b, where each column of the image after one permutation cycle contains pixels with two colors. Each square is a pixel in an image sized 10×10 (see Fig. 2a). All pixels in the diagonal after the permutation will always be placed in one column. Consistently placed diagonal elements (see Fig. 2b) for which the original image:

$$(x_i + y_i) \bmod N = C = const \tag{2}$$

where $C \in 0...N-1$ corresponding column element of the encrypted image (Fig. 2*b*), according to (1) $x_{i+1} = C = const$. When the equation for calculation of coordinate line y_{i+1} can be written as:

$$y_{i+1} = (y_i + KC) \bmod N \tag{3}$$

where

$$C_1 = \sin\left(\frac{x_{i+1}N}{2\pi}\right) = \sin\left(\frac{CN}{2\pi}\right) = const$$

it means that after permutation, pixels coordinates which satisfy (2) are placed in one column consecutively, but are shifted in relation to the initial position, which depends on the parameters K and C_1.

c) Pixels for which coordinates the equation is true:

$$x_{i+1} = (x_i + y_i) \bmod N = 0 \tag{4}$$

always after the permutation will be in the first column. By doing so, the coordinates of the rows will not change because of (1). Let's take into account (4) $x_{i+1} = 0$, $y_{i+1} = y_i$ (Fig. 2b).

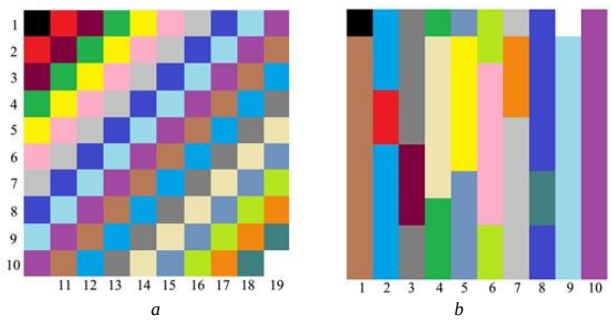

Fig. 2. Image (10×10) – original (a), after one cycle of permutation by K = 123 (b)

Each pixel diagonal can be uniquely identified by a column number that forms this diagonal. Using properties (2–4), a cryptanalyst can try to reproduce the original image by moving the pixels in columns to the place of pixels in diagonals.

1.2. Analysis of key space

The row number where a pixel may be moved after the permutation by $x_i + y_i \neq N$, $x_i + y_i \neq 0$ depends on the value of the parameter K and term KC_1 in (3). Thus, for pixels that are in the first column, their position in the original image is uniquely known. Two consecutive columns contain the pixels of two neighboring diagonals.

Therefore, there are possible only N variants to shift elements of the second column in relation to the first. Given the fact that the pixels of adjacent diagonals slightly differ among themselves, shift between them can be determined by the maximum of the correlation function.

Given the map properties (2) and (3), the number of combinations of a brute force attack that is needed to restore the original image after one permutation cycle equals to N^{N-1} which is much less than $N^2!$ as was considered in the evaluated key space for this map in [9, 12].

1.3. Subkeys properties

Let's consider another property of the standard map (1) that can be used to break pixels permutations. Let's assume that:

$$K_i = K \sin\left(\frac{x_{i+1}N}{2\pi}\right).$$

Then, if $x_{i+1} = const$ then number K_i is a key of permutation in the diagonal in a column. In total, there are N subkeys, while some of them may be the same.

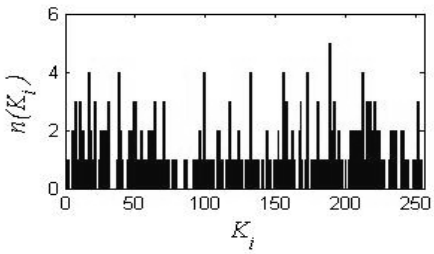

Fig. 3. Histogram of subkeys distribution for image sized 256×256 pixels at K = 1000003

From Fig. 3 one can understand that each subkey was found a limited number of times $m \leq N$, which reduces the key space of permutation in comparison with N^{N-1}. Setting a limit on the number of appearances of permutation subkeys is possible to estimate the key space for a brute force attack as the number of permutations of N different elements of N, provided that each element of it occurred fewer than m times [11]:

$$K = \sum_{\substack{n_1+n_2+...+n_N=N \\ n_i \leq m,\ i=1...N}} \frac{N!}{n_1!n_2!...n_N!} = \\ = \sum_{r_1=N-m}^{N} \sum_{r_2=r_1-m}^{r_1} \sum_{r_3=r_2-m}^{r_2} ... \sum_{r_k=r_{k-1}-m}^{r_{k-1}} C_N^{r_1} C_{r_1}^{r_2} C_{r_2}^{r_3} ... C_{r_{k-1}}^{r_1} \tag{5}$$

However, these properties of subkeys can be used by an attacker to select the most likely key at the beginning of attacks, and thus increase their chances of success. Reducing key space of (1) through dependence between the N and m according to (5) is shown in Table 1.

Table 1. Reducing the key space, %

N	$m = 3$	$m = 5$	$m = 7$
64	72.6	3.2	0.046
128	93.1	6.81	0.11
256	99.6	13.7	0.11

In Tab. 1 it can be seen that at $m \leq 5$ the key space is greatly reduced. For $m \geq 5$ the key space is weakly reduced.

1.4. The effect of limiting precision of calculations

As it is known, a set of different states of chaotic system is defined by precision of calculations [9] and increases with increased precision. For permutations using (1), this effect is also true. We estimate the key space using system (1), provided that the parameter K is a positive integer. In calculations of double precision, the mantissa is 52 bits. The range of integers that can be accurately represented in the form of double precision is $1...2^{53}$ [14]. Given the possible steps 2, the number of different positive integer values of K is $2^{61.9}$. In [9] it is recommended to use for permutations an image which size is of at least $N \geq 128$. Thus we can say that the most appropriate break permutations based on the standard map are the brute force of a possible key values, because:

$$N^{N-1} = 128^{127} \cong 2^{894.6} \gg 2^{61.9} \tag{6}$$

The real key space for modern computing systems is small compared to theoretically possible. Please note that we have established a number of options of the brute force in various possible methods of attack, without considering time complexity of their implementation.

2. Cryptographic attack based on the correlation between adjacent pixels

Considering the facts that there are possible only N variants of shifting elements of the second column in relation to the first and that pixels in adjacent diagonals differ slightly from each other, we can find a shift between pixels of adjacent columns by the maximum of the correlation function.

2.1. Cryptographic attack based on the correlation between adjacent pixels

We organized our cryptographic attack on permutations based on (1) as follows:

a) For two adjacent columns we calculated the value of cross-correlation function:

$$c_k = \sum_{k=0}^{N-1} \left(x_{i,n} - m_i\right)\left(x_{i+1,n+k} - m_{i+1}\right) \tag{7}$$

where $m_i = \frac{1}{N}\sum_{N=0}^{N-1} x_{i,n}$.

b) Defined k for which

$$c_k = \max\{c_0, c_1, ..., c_{n-1}\} \tag{8}$$

c) Column $i+1$ shifted to the K positions down, i.e.

$$x_{i+1,n} = x_{i+1,n+K} \bmod N \tag{9}$$

d) Repeated steps a, b and c for remaining columns in the image. The algorithm has been tested on the image in Fig. 4.

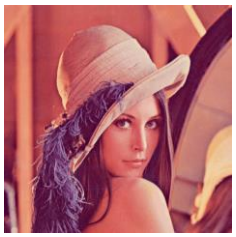

Fig. 4. Original test image

After the first and second permutation cycles, the original image is successfully restored (see Fig. 5). However, there is a slight distortion. After three permutation cycles, the correlation between adjacent pixels is lost and the restoration of the original image by this method is impossible. Thus, considering the correlation, image properties can be broken by 2 cycles of permutations.

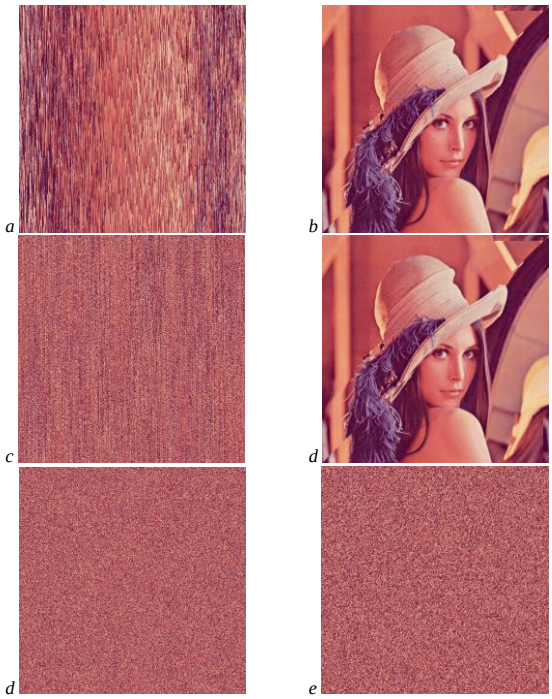

Fig. 5 a; c; e – encrypted test image after one, two and three cycles of permutation, respectively; b; d; f – recovered image

2.2. Modified standard map with a maximum key space for permutations

In order to get the maximum size of the key space of permutation for the system (1), it is necessary to introduce non-linearity in the variable x_{i+1}. Our proposed map in the discretized form is described by the following recurrent system of equations:

$$\begin{cases} x_{i+1} = \left(x_i + K_x \sin\left(\frac{y_i N}{2\pi}\right)\right) \bmod N \\ y_{i+1} = \left(y_i + K_y \sin\left(\frac{x_{i+1} N}{2\pi}\right)\right) \bmod N \end{cases} \tag{10}$$

where K_x, K_y – parameters (keys). Jacobian system (10):

$$D = \begin{vmatrix} \frac{\partial x}{\partial x} & \frac{\partial x}{\partial y} \\ \frac{\partial y}{\partial x} & \frac{\partial y}{\partial y} \end{vmatrix} = \begin{vmatrix} 1 & \frac{K_x N}{2\pi}\cos\left(\frac{yN}{2\pi}\right) \\ \frac{K_y N}{2\pi} a & 1 + \frac{K_y K_x N^2}{(2\pi)^2} a \cos\left(\frac{yN}{2\pi}\right) \end{vmatrix} = 1 \tag{11}$$

where $a = \cos\left(\left(x + K_x \sin\left(\frac{yN}{2\pi}\right) N\right) / 2\pi\right)$, i.e., map saves the area and is potentially useful for permutations in encryption algorithms. The drawback of the map (10) is the need to have two sinus functions computed. Considering that value of trigonometric functions in digital means are calculated using the Taylor series of desired functions, the number of mathematical operations in system (1) is less complex in comparison to (10).

Let us consider the effectiveness of permutations based on (10). The encrypted image after one cycle of permutations is shown in Fig. 6.

Fig. 6. Permutation of pixels of a test image using (10)

In the encrypted image contours are not observed and pixels of different colors are uniformly distributed within its size. To evaluate the similarity of two images, we use the correlation coefficient [7]. Correlation coefficient close to zero means that two images are independent and use the map characterized by good mixing properties.

The calculation results for different number of permutation cycles using (1) and (10) are presented in the Table 2.

Table 2. Correlation of image pixels depending on the number of cycles n in permutations N = 512, K = K_x = K_y = 10000

n	Correlation of pixels	Standard map	
		with one nonlinearity (1)	with two nonlinearity (10)
0	horizontal	0.9753	0.9753
	vertical	0.9853	0.9853
1	horizontal	0.0972	-0.0011
	vertical	0.9699	0.0375
2	horizontal	-0.0040	0.00006
	vertical	0.0969	0.00063
3	horizontal	-0.00075	-0.0015
	vertical	-0.0070	-0.0034
4	horizontal	0.0011	-0.0026
	vertical	-0.00025	-0.0029

Systems (1) and (10) are explored with the parameters $K = K_x = K_y = 10000$ For the original image (Fig. 4) the correlation coefficient between the adjacent pixels in columns and rows equals to 0.9759 and 0.9857 respectively. One cycle of permutations with a standard map does not lead to uniform dissemination of pixels (Fig. 5 a), because preserved was a strong correlation between pixels in columns.

From Tab. 2 it can be deduced that system (10) compared to (1) has better correlation properties. Efficiency of permutations with (1) and (10) is seen in Fig 7.

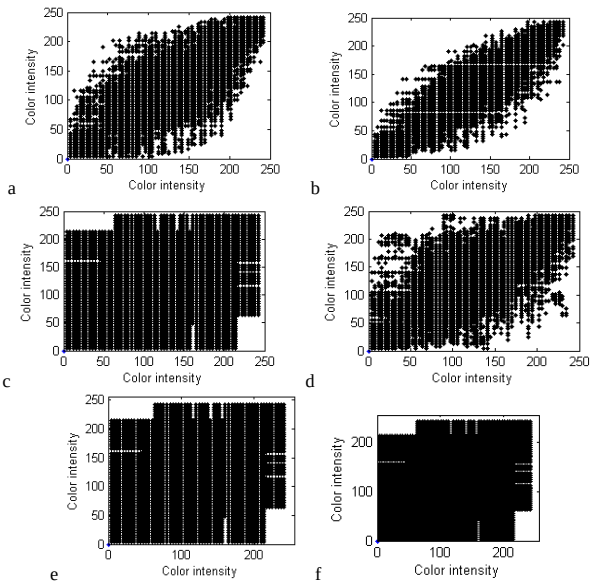

Fig. 7. The relationship between the adjacent pixels: a; b – in the horizontal and vertical for test image (Fig. 4); c; d – after one cycle of permutations using the map (1); e; f – after one cycle of permutations using the map (10)

For one cycle permutations performed by system (1), pixels are grouped along the diagonal (see Fig. 7 c, d). After one cycle permutations (10), relationships between adjacent pixels in rows (Fig. 7 e) and columns (Fig. 7 f) have the form of a square, which means no statistical relationship between them.

3. Conclusion

We analyzed permutations of pixels based on discretized Chirikov standard map considering its geometric features. We discovered specific properties of a map that can be used by an attacker to recover the original image. It is shown that the permutations are much weaker before brute force attacks, and it is possible to recover the original image without setting the key value (key) permutations. For images with dimension $N \times N$ the number of combinations is N^{N-1} for one permutation cycle instead of $N^2!$ as was previously thought. In order to get the maximum size of key space of permutation for the discretized standard map, we proposed to introduce additional nonlinearity. Please note that the evaluation of key space of permutations is received on the condition that calculations are made with absolute precision.

References

[1] Alvarez, G., Li, S. J.: Some Basic Cryptographic Requirements for Chaos-Based Cryptosystems. Inter. Journal of Bif. and Chaos 16(8)/2006, 2129–2151.
[2] Argyris A., Syvridis D., Larger L., Annovazzi-Lodi V., Colet P., Fischer I., García-Ojalvo J., Mirasso C.R., Pesquera L., Shore K.A.: Chaos-based communications at high bit rates using commercial fibre-optic links. Nature 438(7066)/2005, 343–346.
[3] Arroyo D., Alvarez G., Fernandez V.: A basic framework for the cryptanalysis of digital chaos-based cryptography. Proc. of the 6th International Multi-Conference on Systems, Signals and Devices, Djerba 2009, 58–63.
[4] Chirikov B. V.: Research concerning the theory of nonlinear resonance and stochasticity Preprint 267, Institute of Nuclear Physics, Novosibirsk, 1969, (Engl. Trans., CERN Trans. 1971, 71–40).
[5] Fridrich J.: Symmetric Ciphers Based on Two-Dimensional Chaotic Maps. Inter. Journal of Bif. and Chaos 8(6)/1998, 1259–284.
[6] Hussain I., Shah T.: Literature survey on nonlinear components and chaotic nonlinear components of block ciphers. Nonlinear Dynamics 74/2013, 869–904.
[7] Jolfaei A., Mirghadri A.: An image encryption approach using chaos and stream cipher. Journal of Theoretical and Applied Information Technology 19(2)/2010, 117–125.
[8] Kocarev L., Lian S. (Eds.): Chaos-Based Cryptography Theory, Algorithms and Applications. Springer-Verlag Berlin Heidelberg, 2011.
[9] Lian S. G., Sun J., Wang Z.: A block cipher based on a suitable use of chaotic standard map. Chaos, Solitons and Fractals 26(1)/2005, 117–29.
[10] Lian S., Sun J., Wang Z.: Security analysis of a chaos-based image encryption algorithm. Phisyca A 351(2)/2005, 645–661.
[11] National Institute of Standards and Technology (May 11, 2010). NIST Digital Library of Mathematical Functions. Section 26.4. Retrieved August 30, 2010.
[12] Solak, E., Cokal, C., Yildiz, O.T., Biyikoglu, T.: Cryptanalysis of fridrich's chaotic image encryption. Int. J. Bifurcation Chaos 20(5), 1405–1413.
[13] von Bremen H. F., Udwadia F. E., Proskurowski W.: An efficient QR based method for the computation of Lyapunov exponents. Physica D 101/1997, 1–16.
[14] Warren H. S. .: Hacker's Delight. Addison-Wesley Professional. 2012.
[15] Yuan G., Yorke J. A.: Collapsing of chaos in one dimensional maps. Physica D: Nonlinear Phenomena 136/2000, 18–30.

Ph.D. Serhii Haliuk
e-mail: s.haliuk@chnu.edu.ua

Assistant of professor at Radio Engineering and Information Security Department of Yuriy Fedkovych Chernivtsi National University. His research field covers the development of the different components of hidden communication systems. Author of more than 20 publications.

http://orcid.org/0000-0003-3836-2675

Ph.D. Oleh Krulikovskyi
e-mail: o.krulikovskyi@chnu.edu.ua

Assistant of professor at Radio Engineering and Information Security Department of Yuriy Fedkovych Chernivtsi National University. His research field covers digital signal processing, FPGA and cryptography. Author of more than 20 publications.

http://orcid.org/0000-0001-5995-6857

Vitalii Vlasenko
e-mail: vetalvlasenko98@gmail.com

A graduate student. Winner of Ukrainian national student contests on the topic of cybersecurity in 2017 and 2019.

http://orcid.org/0000-0002-9085-5787

otrzymano/received: 15.11.2019 *przyjęto do druku/accepted: 15.02.2020*

http://doi.org/10.35784/iapgos.922

FACE RECOGNITION TECHNIQUES

Olexandr N. Romanyuk[1], Sergey I. Vyatkin[2], Sergii V. Pavlov[1], Pavlo I. Mykhaylov[3], Roman Y. Chekhmestruk[4], Ivan V. Perun[4]

[1]Vinnytsia National Technical University, Vinnitsa, Ukraine, [2]Institute of Automation and Electrometry SB RAS, Novosibirsk, Russia, [3]3D GNERATION GmbH, Dortmund, Germany, [4]3D GENERATION UA, Vinnitsa, Ukraine

Abstract. *The problem of face recognition is discussed. The main methods of recognition are considered. The calibrated stereo pair for the face and calculating the depth map by the correlation algorithm are used. As a result, a 3D mask of the face is obtained. Using three anthropomorphic points, then constructed a coordinate system that ensures a possibility of superposition of the tested mask.*

Keywords: methods of recognition stereo pair, depth map, correlation algorithm, perturbation functions, operation of subtraction

TECHNIKI ROZPOZNAWANIA TWARZY

Streszczenie. *Omawiany jest problem rozpoznawania twarzy. Rozważane są główne metody rozpoznawania. Użyta zostaje skalibrowana para stereo dla twarzy oraz obliczanie mapy głębokości poprzez algorytm korelacji. W wyniku takiego, uzyskiwana jest maska twarzy w wymiarze 3D. Użycie trzech antropomorficznych punktów, a następnie skonstruowany systemu współrzędnych zapewnia możliwość nakładania się przetestowanej maski.*

Słowa kluczowe: metody rozpoznawania pary stereo, mapa głębi, algorytm korelacji, funkcje perturbacji, działanie odejmowania

Introduction

Work on the identification of persons has been going on for a long time. Previously, this problem was based on two-dimensional (2D) images: their acquisition and comparison with the existing set. However, in most cases, small changes in the position of the object of observation made the system ineffective. The test samples could not be matched to any of the databases and the error rate was too high.

Known methods of identification of individuals. In the video, the face of a man is captured by a video camera and a special filter processes the image. Next, the task of selecting special points (FFE – Face Feature Extraction) on the image is automatically solved, after which these points (and the distances between them) form a standard by which the comparison is made.

The advantages of the method include the ability to carry out continuous identification covertly. The disadvantages of the method – dependence on the rotation of the head, and external characteristics of the face.

An alternative to video is a thermogram – the heat emitted by the human body, which can be registered by an infrared camera and this image can be processed. The method is convenient because a person can be registered in complete darkness, which increases the secrecy of registration. However, at the same time there is a dependence on external sources of thermal noise. The disadvantage can also be attributed to the use of special equipment.

Three-dimensional recognition (3D) is one of the most advanced methods. The head is highlighted with a special slide consisting of lines. By distorting the lines on the surface of the head three-dimensional model of the head is restored. In this model, special points are allocated, which form a feature vector. Advantages of the method - continuous identification of the object and the possibility of hidden identification. The system can also operate in an invisible range. Three-dimensional recognition lacks a number of drawbacks. It is almost impossible to fake a fake. Twins are different. Small dependence on the rotation of the head (the deviation range is significantly increased). With the right choice of light range small dependence on ambient light, from the hair. Reduced dependence on facial tumors (because there are anthropomorphic points on the face, almost not susceptible to swelling). The quality of recognition competes with most of other methods. 3D identification can be used in a dark environment; it remains effective even when the face is rotated, up to 90 degrees (up to the "profile" position). Disadvantages of the method – special equipment, high computational power requirements (often requiring hardware implementation of algorithms, which, accordingly, increases the cost of the system). The recognition system performs the identification process by performing a number of actions.

1. General face image processing in recognition

It is possible to identify a common pattern of the face recognition process. The first step is the detection and localization of faces on the image. At the recognition stage, the alignment of the face image (geometric and brightness), the calculation of features and directly recognition is performed-comparison of the calculated features with the standards incorporated in the database. The main difference of all presented algorithms will be the calculation of features and comparison of their sets among themselves.

1.1. Elastic graph matching

The essence of the method is reduced to elastic comparison of graphs describing images of faces [24]. Faces are represented as graphs with weighted vertices and edges. At the recognition stage, one of the graphs – the reference graph – remains unchanged, while the other is deformed to best fit the first one. In such recognition systems, graphs can be either a rectangular lattice or a structure formed by characteristic (anthropometric) points of the face.

Feature values are calculated at the vertices of the graph, most often using complex values of the Gabor filters or their ordered sets-Gabor wavelets, which are calculated in some local area of the graph vertex locally by convolution of pixel brightness values with the Gabor filters.

Graph structure for face recognition: a) regular lattice b) graph based on anthropometric points of the face (Fig. 1).

The edges of the graph are weighted by the distances between adjacent vertices. The difference (distance, discrimination characteristic) between two graphs is calculated using some deformation price function, which takes into account both the difference between the feature values calculated at the vertices and the degree of deformation of the edges of the graph.

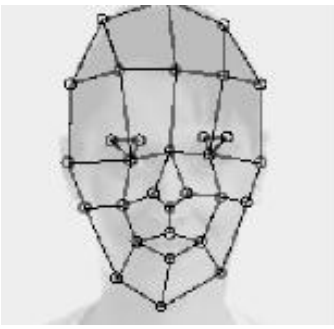

Fig. 1. The graph based on anthropometric points of the face

Deformation of a graph occurs by shifting each of its vertices by some distance in certain directions relative to its original location and choosing such a position that the difference between the values of the features (responses of the Gabor filters) at the vertex of the deformable graph and the corresponding vertex of the reference graph is minimal. This operation is performed alternately for all vertices of the graph until the smallest total difference between the features of the deformable and the reference graphs is reached. The value of the deformation price function at this position of the deformable graph will be a measure of the difference between the input face image and the reference graph. This "relaxation" deformation procedure must be performed for all reference persons included in the system database. The result of the system recognition is the standard with the best value of the deformation price function.

Some publications indicate 95–97% recognition efficiency even in the presence of different emotional expressions and changing the angle of the face to 15 degrees. However, the developers of elastic comparison systems on graphs refer to the high computational cost of this approach. For example, for comparison of the input image of the person with 87 reference approximately 25 seconds were spent at work on the parallel computer with 23 transputers [8] (note: the publication is dated 1993). Other publications on the subject either do not indicate the time or say that it is long.

Disadvantages: high computational complexity of the recognition procedure. Low-tech when memorizing the new standards. Linear time dependence on the size of the database.

1.2. Neural-networks

Currently, there are about a dozen varieties of neural networks (NN). One of the most widely used options is a network built on a multilayer perceptron, which allows you to classify the input image/signal in accordance with the pre-setup/training of the network.

NN are trained on a set of training examples. The essence of the training is to adjust the weights of interneuron connections in the process of solving the optimization problem by gradient descent. In the process of NN training, there is an automatic extraction of key features, determination of their importance and building relationships between them. It is assumed that the trained NN will be able to apply the experience gained in the learning process to unknown images due to generalizing abilities.

Convolutional Neural Network (hereinafter – CNN) showed the best results in the field of facial recognition (based on the results of the analysis of publications) [9], which is a logical development of the ideas of such NN architectures as cognitron and neocognitron. The success is due to the possibility of taking into account the two-dimensional topology of the image, in contrast to the multilayer perceptron.

Distinctive features of CNN are the local receptor fields (provide local two-dimensional connectivity of neurons), common weights (provide detection of some traits anywhere in the image) and hierarchical organization with spatial sampling (spatial subsampling). With these innovations, the CNN provides partial resistance to changes in the scale, offsets, rotations, changes in the angle and other distortions.

CNN testing on the ORL database, which contains images of faces with small changes in lighting, scale, spatial rotations, position and various emotions, showed 96% recognition accuracy.

CNN received its development in the development of Deep Face [18] (Fig. 2), which was acquired by Facebook for facial recognition of the users of its social network. All features of the architecture are closed.

Disadvantages ofNN: adding a new reference person to the database requires a complete retraining of the network on all available set (quite a long procedure, depending on the sample size from 1 hour to several days). Problems of mathematical nature related to training: getting into a local optimum, choosing the optimal optimization step, retraining, etc. Difficult to normalize the stage of choosing the network architecture (number of neurons, layers, nature of connections). Summarizing all the above, we can conclude that the NN is a "black box" with hard-to-interpret results.

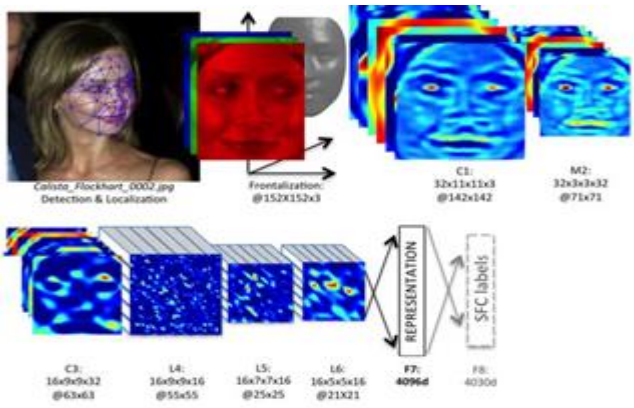

Fig. 2. Principle of operation of Deep Face

1.3. Hidden Markov's models

One of the statistical methods of face recognition is the hidden Markov models (HMM) with discrete time [12]. HMM uses statistical properties of signals and takes into account directly their spatial characteristics. The elements of the model are the set of hidden states, the set of observed states, the matrix of transition probabilities, the initial probability of states. Each has its own HMM. When recognizing an object, HMM generated for a given object database are checked and the maximum observed probability that the corresponding model generates the sequence of observations for a given object is searched.

To date, no example of commercial use of HMM for facial recognition has been found.

Disadvantages:

- It is necessary to select model parameters for each database.
- The HMM has no discriminating ability, i.e. the learning algorithm only maximizes the response of each image to its model, but does not minimize the response to other models.

1.4. Principal component analysis

One of the most well known and developed is the principal component analysis (PCA) method based on the transformation [7].

Initially, the principal component analysis was used in statistics to reduce feature space without significant loss of information. In the problem of face recognition it is used mainly to represent the image of the face by a vector of small dimension (principal components), which is then compared with the reference vectors embedded in the database.

Main purpose of the method of PCA is a significant reduction of dimensionality of the feature space so as better described the "typical" images, owned by many persons. Using this method it is possible to identify the different variability in the training set of facial images and describe this variation in a few orthogonal basis vectors, called own (eigenface).

The set of eigenvectors obtained once in the training sample of face images is used to encode all other face images, which are represented by a weighted combination of these eigenvectors. Using a limited number of eigenvectors, a compressed approximation of the input face image can be obtained, which then can be stored in the database as a coefficient vector that serves as a search key in the face database at the same time.

The essence of the PCA is as follows. Initially, the entire training set of faces is converted into one common data matrix, where each row is a single instance of the face image decomposed into a row. All faces of the training set should be reduced to the same size and with normalized histograms.

Then the data is normalized and the rows are reduced to the 0-th mean and 1-th variance, the covariance matrix is calculated. The problem of determining eigenvalues and corresponding eigenvectors (eigenvalues) is solved for the obtained covariance matrix. Then the eigenvectors are sorted in descending order of eigenvalues and only the first k vectors are left according to the rule:

$$\frac{\sum_{i=1}^{k} l_i}{\sum_{i=1}^{n} l_i} \rangle Threshold \ (0.9 \ or \ 0.95)$$

where l_i are ordered eigenvalues.

1) Zero mean:

$$x_{ij} = x_{ij} - \rho_i \quad \rho_i = \frac{1}{n}\sum_{j=1}^{n} x_{ij}$$

2) Unit variance:

$$x_{ij} = \frac{x_{ij}}{\xi_j} \quad \xi_i = \frac{1}{n-1}\sum_{j=1}^{n}(x_{ij} - \rho_i)^2$$

3) Covariance matrix: $\Sigma = XX^T$

4) Compute eigenvectors of $\Sigma : W^T$

5) Project X onto the k principal components (Fig. 3).

Fig. 3. An example of building (synthesis) of a human face using a combination of Eigen-faces and principal components

The PCA is well established in practical applications. However, in cases where the image of the face presents significant changes in light or facial expression, the effectiveness of the method decreases significantly. The point is that the PCA chooses a subspace with the goal of approximating the input dataset as closely as possible, rather than discriminating between classes of individuals. In [2] it was proposed to solve this problem with the use of linear discriminant Fisher (in the literature there is a name ″Eigen-Fisher″, ″Fisherface″, LDA). LDA looks for a data projection in which classes are as linearly separable as possible. For comparison, the PCA looks for a projection of the data that maximizes the spread across the person database (excluding classes). According to the results of experiments [2] in conditions of strong tank and lower shading of face images, Fisherface showed 95% efficiency compared to 53% of Eigenface.

1.5. Active appearance models

Active Appearance Models (AAM) are statistical image models that can be adjusted to the real image by means of various deformations. Tim Cootes and Chris Taylor proposed this type of two-dimensional model in 1998 [5]. Initially, AAM were used to evaluate face image parameters.

The AAM contains two types of parameters: shape-related parameters (shape parameters) and image pixel statistical model or texture-related parameters (appearance parameters). Before use, the model must be trained on a set of pre-labelled images. Marking of images is done manually. Each label has its own number and defines a characteristic point that the model will have to find during adaptation to the new image.

The layout of the face image of 68 points forms the shape of AAM. The AAM training procedure begins by normalizing the shapes on the labelled images to compensate for differences in scale, slope, and offset. The so-called generalized analysis is used for this purpose. From the entire set of normalized points, the principal components are then distinguished using the PCA method. The AAM shape model consists of a triangulation lattice s_0 and a linear combination of displacements s_i with respect to s_0 (Fig. 4).

Next, a matrix is formed from the pixels inside the triangles formed by the points of the shape, in such a way that each column contains the pixel values of the corresponding texture. It is worth noting that the textures used for training can be both single-channel (grayscale) and multi-channel (for example, RGB color space or other). In the case of multichannel textures, pixel vectors are formed separately for each of the bands, and then their concatenation is performed. After finding the principal components of the texture matrix, the AAM model is considered trained. The AAM consists of a base view A0 defined by the pixels inside the base lattice s0 and a linear combination of offsets Ai relative to A0.

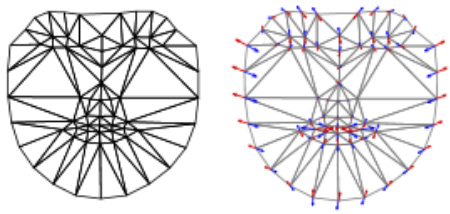

Fig. 4. AAM shape and displacement model

Fitting the model to a specific image of the face is performed in the process of solving the optimization problem, the essence of which is to minimize the functionality gradient descent method. The parameters of the model found in this case will reflect the position of the model in a particular image.

With AAM, you can model images of objects that are subject to both rigid and non-rigid deformation. AAM consists of a set of parameters, some of which represent the shape of the face; the rest set its texture. Deformations are generally understood as geometric transformations in the form of transport, rotation, and scaling compositions. When solving the problem of face localization in the image, the search for parameters (location, shape, texture) of AAM, which represent the synthesized image closest to the observed one, is performed. According to the degree of proximity AAM customized image is decided-there is a person or not.

2. Active Shape Models (ASM)

The essence of the ASM method [14] is to take into account the statistical relationships between the locations of anthropometric points on the available sample of full-face images. In the image, the expert marks the location of anthropometric points. In each image, the dots are numbered in the same order.

In order to bring the coordinates on all images to a single system, the so-called generalized Procrustean analysis is usually performed, because of which all points are brought to the same scale and centered. Then the average shape and covariance matrix are calculated for the whole set of images. Based on the covariance matrix, eigenvectors are computed and then sorted in descending order of their corresponding eigenvalues. The ASM model is defined by the matrix F and the mean vector s.

Localization of the ASM model on a new image that is not included in the training sample is carried out in the process of solving the optimization problem.

However, the main purpose of AAM and ASM is not a facial recognition, but the precise localization of the face and anthropometric points in the image for further processing.

In almost all algorithms, the mandatory step that precedes classification is alignment, which means alignment of the face image to the frontal position relative to the camera or bringing a set of faces (for example, in the training sample for training the classifier) to a single coordinate system. To implement this stage, it is necessary to localize anthropometric points typical for all faces on the image – most often; these are the centers of the pupils or the corners of the eyes. Different researchers distinguish different groups of such points. In order to reduce computational costs for real-time systems, developers allocate no more than 10 such points.

The AAM and ASM models are just intended to accurately localize these anthropometric points on the face image.

The main problems associated with the development of facial recognition systems

1) Illumination Problem,
2) Head Position Problem (face is a 3D object).

In order to evaluate the effectiveness of the proposed facial recognition algorithms, DARPA and the U.S. army research laboratory developed the FERET (face recognition technology) program.

The large-scale tests of the FERET program involved algorithms based on flexible comparison on graphs and various modifications of the PCA. The efficiency of all algorithms was approximately the same. In this regard, it is difficult or even impossible to make clear distinctions between them (especially if the test data are agreed). For frontal images taken on the same day, the acceptable recognition accuracy is typically 95%. For images taken by different devices and in different lighting conditions, the accuracy usually drops to 80%. For images taken with a difference of a year, the recognition accuracy was approximately 50%. It is worth noting that even 50 percent-is more than acceptable accuracy of the system of this kind.

Every year FERET publishes a report on a comparative test of modern facial recognition systems based on more than one million faces. Unfortunately, the latest reports do not disclose the principles of construction of recognition systems, and only the results of commercial systems are published. Today the leading system is NeoFace developed by NEC.

2.1. Method recognition based on scalar perturbation functions

The method of face recognition with the use of perturbation functions and the set-theoretic operation of subtraction was presented in [21, 23].

A calibrated stereo pair is used for calculating 3D points on the face. Let us assume that we have two projective matrices M_i

$$\begin{pmatrix} u_i s_i \\ v_i s_i \\ s_i \end{pmatrix} = M_i \begin{pmatrix} X \\ Y \\ Z \\ 1 \end{pmatrix}$$

where x, y, z are three-dimensional coordinates of the point, u_i and v_i are their projections in the image i, and s_i is the scale factor. The stereo pair is characterized by the following parameters: the points of the image planes $E_1 = (u_1, v_1)$ and $E_2 = (u_2, v_2)$, and the point of the world coordinate system $P = (x, y, z)$.

Using the calibrated stereo pair for the face, we calculate the depth map by the correlation algorithm. In this work, we use an area-based algorithm with correlation of image intensity levels.

$$s = \frac{\sum_{i,j}\left((I1(x+i,y+j)-\vec{I}1)-(I2(x+dx+i,y+dy+j)-\vec{I}2)\right)^2}{\sqrt{\left(\sum_{i,j}(I1(x+i,y+j)-\vec{I}1)^2\right)\left(\sum_{i,j}(I2(x+dx+i,y+dy+j)-\vec{I}2)^2\right)}}$$

Here $I1$ and $I2$ are the intensities of the left and right images, $\vec{I}1$ and $\vec{I}2$ are their mean values, dx and dy are the displacements along the epipolal line, and $s = \max(0.1 - c)$ is the correlation estimate.

There are two images of the stereo pair; scanning of these images provides information about the depth buffer (depth map).

In finding the perturbation peak, we calculate the characteristic size of the projection of the current interval, which is used as a basis for determining the detail level. For a larger interval, a rough approximation of the original function is taken. If a more detailed presentation is needed, then bilinear or bicubic interpolation of heights at the last detail level is performed. As a result, we obtain a 3D mask of the face (Fig. 5). Using three anthropomorphic masks, we construct a coordinate system that ensures a possibility of superposition of the tested masks; finally, a clipping plane for equalization of the volumes cuts off certain parts. Applying the set-theoretic operation of subtraction

$$F3 = F1 \backslash F2$$

We determine the set of 3D points (voxels) belonging to the object f3 = **F**i (f1(x, y, z), f2(x, y, z)), **F**1: f1(x, y, z) ≥ 0, **F**2: f2(x, y, z) ≥ 0. To find 3D points, voxelization of the remaining part of the volume after the subtraction is needed.

The smaller the number of voxels left, the greater the similarity of the tested objects.

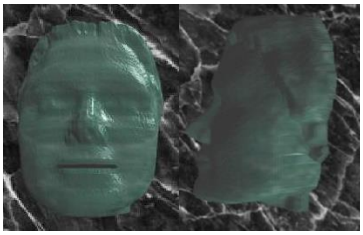

Fig. 5. 3D masks

2.2. Scanning technology

Computing three-dimensional (3D) data and information range is an important task in a variety of applications including computer graphics, medicine, multimedia, machine vision, navigation, automotive safety, computer interaction, tracking, image recognition, and more. Obtaining three-dimensional geometric data from a real and complex environment has been the subject of research for many years. Computer graphics and image analysis are the two methods of processing visual information. Computer graphics operate with formal descriptions of objects to create their visual images. Image analysis systems work with images to produce formalized models of objects. Recently, there has been a trend towards convergence and mutual integration of computer graphics and image analysis. This is primarily due to the development of virtual reality systems.

Scanning technologies are divided into contact and contactless. The first implies the presence of a mechanical device by means of which the coordinates of the selected points are transmitted to the computer.

Contactless three-dimensional scanners are much more complex devices, which have complex algorithms for creating objects. Some devices combine laser sensors and a digital camera, which is used for greater scanning accuracy.

New technologies are researched and developed with improved accuracy and reduced cost. In addition, systems, as well as methods suit for object perception, data acquisition and depth in three-dimensional space. These systems and technologies use various resources, including electromagnetic waves, sound waves, ultrasound, laser, light rays, etc. They have been used in various systems, including lasers, radars, sonars, ultrasonoscopes, imaging systems, etc. Among these systems the laser detection and rangefinder (LADAR) can be distinguished – a system of transmission, detection, processing and reception of electromagnetic waves reflected from targets. The laser sensors of these systems provide range information constructed from a set of point measurements from a single point of view. The laser rangefinder (LRF), working on the principle of transmitting a laser pulse to the surface of an object and receiving a reflected pulse, measures the time between sending and receiving a pulse [1]. On a 3D laser scanner, the concept is similar to LADAR. However, the system was created for the purpose of 3D digital measurement, visualization and documentation, it is able to capture 3D digital information and obtain images with high accuracy and speed [6]. Another typical system is the light detection and ranging system (LIDAR), a system for mapping terrain, measuring forests and vegetation. Lidar has the ability to detect different reflections from only one laser pulse [15]. Radio frequency identification (RFID) is an automatic tracking and identification technology that uses small tags (transponders) that are attached to a physical object where the

tags contain store information. Radar detection and range (Radar) is a detection technology that uses radio waves transmitted and reflected back by objects to obtain the angle, speed, range, and properties of targets [26]. Thermal imagers are another technology for sensing objects based on the difference in temperature scales, these technologies are able to detect the heat given off by the desired targets. Global positioning systems (GPS and GLONASS), space systems that determine the exact location and provide timely information about the desired location anywhere on Earth and in all weather conditions.

There are also three-dimensional scanning systems based on ultrasonic installations [10].

Ultrasonic technology based on sound wave is an approach to measuring distances and detecting objects. They transmit high-frequency pulses by using a sensor probe. Then the reflected waves are received back by the same sensor probe [16]. Another type of systems is the use of magnetic scanners, which use to determine the spatial coordinates of the object change its spatial magnetic field. However, ultrasonic and magnetic scanners are very sensitive to various kinds of noise.

Optical scanners are divided into active and passive. Passive devices are devices based on two cameras, devices used for reconstruction of silhouettes of objects, etc. In [3] an overview of passive scanning methods is given. Active systems have a matched light source and image receiver [11]. There are a number of methods of scanning the object: the method of structured light, time-of-flight cameras and methods of accumulation of information about the object (the method of assessing the shape of the movement). The essence of the methods of scanning the object is reduced to its illumination, for example, a template in the form of a grid, a projector can be used, projecting a regular grid of light lines on the surface of objects. The camera, when forming images, transmits the result of distortion of the grid due to the shape and orientation of the surface. As follows from the above, the method of object scanning requires specialized equipment (projectors, 3D scanners, radars, time-of-flight cameras, sonars or lidars [15]), whereas the proposed method of binocular stereo vision works with conventional web cameras. Methods of accumulation of information, in turn, analyze the local movement of parts of the scene over time. When the camera or object is moved, or both, the system receives a sequence of changing images. Surfaces and angles can be reconstructed from optical flow vectors or corresponding points in three-dimensional scenes. Identifying objects from motion presents a task similar to that of binocular stereo vision; only the images to be processed will be obtained at different times. This leads to the complexity and greater resource intensity of the problem of finding the corresponding points, which makes the method of binocular stereo vision more advantageous.

Modeling the shape of real-world objects from a series of images has been investigated in the recent years. One well-known approach to three-dimensional modeling is to create a shape from a silhouette that restores the shape of objects along their contours. This approach is popular due to its fast calculations and reliability. The first work on the construction of three-dimensional models from several points of view was described in [4]. The method [13] uses orthogonal projection to construct three-dimensional models. Numerous studies have been devoted to the creation of shapes from silhouettes to transform visible contours into visual form [17, 19].

3. Conclusions

During the experiments it was found, that the effective size of the comparison window in the construction of the search space is determined by the resolution and size of the objects depicted on it.

Quality testing of several criteria was carried out as the sum of modules of differences, sum of squared differences, and the criterion of the census. The first was discarded immediately, because its quality was almost the same as the second, but it is impossible to calculate a linear algorithm.

It was tested with a different set of permissions, using the SSD criterion. It is established that: on average, it takes approximately equal time to fill the search space with its values and search for the optimal path, the operating time depends linearly on the difference between the maximum and minimum disparities, the time depends linearly on the image area. While maintaining the width-to-height ratio.

The results of testing the method are encouraging. Both virtual objects from available databases and real persons were used. The 3D technology of face recognition provides effective operation; more than 98% of test objects were successfully recognized by using this method. Nevertheless, some factors result in failure of verification. These factors can be classified into two groups: incorrect position ahead of the camera and interferences in data readout. The first class includes situations where only some part of the face is visible for the camera. The face is not directed toward the camera, the head is turned downward or to the left or right from the camera, the person is located too close to the camera, or the person goes away from the camera too fast after the beginning of verification (less than one second). The method operates successfully if the recognized object moves uniformly, but the camera fails to capture the observed object exactly in the case of its sudden acceleration.

It should be noted that observation of only some part of the face in the camera is not completely unacceptable because fragments can be successfully verified by using the geometric operation of intersection. The proposed method allows for selective testing with the use of the geometric operation of intersection of a transparent cylinder or any other geometric shape with the surface.

Interferences of data readout occur if the facial expression is not neutral as required or if the headwear, mirror shades, or hair covers a major part of the face [22, 25].

Advanced methods are capable of recognition based on different facial expressions. Three-dimensional morphing is used for recognition in the proposed method.

If we compare 2D systems and the proposed 3D method of recognition, we can see that the false response probability in the first case is 0.12% and the false rejection probability is 9.8% for the recognition threshold being set at 70%. In the second case, the recognition threshold was set at 90%, and the method provided the false response probability of 0.004% and the false rejection probability of 0.1%.

In all tests performed simultaneously for both technologies with the use of the same images, the 3D technology of face recognition turned out to be more efficient than the 2D technology.

An example of 3D recognition methods is the well-known method of fitting for reconstructing the shape and parameters of the texture. This method is based on a system of linear equations. Recognition is performed based on comparisons of the reconstructed shapes and texture of the image.

However, manual initialization is needed in the Face Identification by fitting a 3D Morphable Models method. The recognition time (approximately 1 minute on the Pentium III processor with a frequency of 800 MHz) does not satisfy the requirements of most real systems.

As compared to previously available methods, the proposed method offers the following advantages. 3D morphing allows recognition of faces with different facial expressions. Face identification based on some part of the image is possible. Texturing of the face surface is not needed; the method is completely automatic and fast (about 200 ms for one face image with a resolution of 640×480 pixels with the use of the Intel Core i7-2700K processor (8 MB cache memory, 3.90 GHz)), which is faster than the fitting method approximately by two orders of magnitude. The measurement error is no more than 0.8 mm (for each point of the 3D surface).

For real-time visualization, a binary method of searching for image elements with the use of graphics processing units adapted for calculating perturbation functions can be used. Therefore, a method of face recognition based on perturbation functions and

the set-theoretic operation of subtraction is proposed. Three-dimensional masks were used for face recognition. This method differs from available 3D methods by the fact that it involves not only all points of the surface in the recognition procedure, but also the volume of the tested mask. The method offers the following advantages: manual initialization of the process is not needed; three-dimensional morphing solves the problem of face recognition based on different facial expressions; face recognition based on only some part of the image is possible; face reconstruction is completely automated. The computation time is approximately 200 ms with a resolution of 640×480 pixels.

The method can be used in various situations where intellectual video monitoring of specially protected objects is needed: defense complex enterprises, heavily crowded areas, etc.

References

[1] Amann M. C., Bosch T. M., Lescure M., Myllylae R. A., Rioux M.:Laser ranging: a critical review of unusual techniques for distance measurement. Optical Engineering 40(1)/2001, 10–19, [http://doi.org/10.1117/1.1330700].

[2] Belhumeur P. N., Hespanha J. P., Kriegman D. J.: Eigen faces vs. Fisher faces: Recognition using Class Specific Linear Projection. IEEE Transactions on pattern analysis and machine intelligence 19(7)/1997, 711–720, [http://doi.org/10.1109/34.598228].

[3] Butime J., Gutierrez I., GaloCorzo L., Flores C.: Espronceda. 3D reconstruction methods, a survey. Proceedings of the First International Conference on Computer Vision Theory and Applications, 2006, 457–463, [http://doi.org/0.5220/0001369704570463].

[4] Chien C. H., Aggarwal J. K.: Identification of 3D Objects from Multiple Silhouettes Using Quadtrees / Octrees. Computer Vision Graphics And Image Processing 36(2–3)/1986, 256–273.

[5] Edwards G. J., Cootes T. F., Taylor C. J.: Face recognition using active appearance models. European Conference on Computer Vision, 1998, 581-595. [http://doi.org/10.1007/BFb0054766].

[6] Jecić S., Drvar N.: 3D Shape Measurement Influencing Factors. NDT – Competence & Safety, Zagreb 2004, 109–116.

[7] Jolliffe I. T.: Principal component analysis, second edition. Springer, New York 2002.

[8] Lades M., Vorbruggen J.C., Buhmann J., et al.: Distortion Invariant Object Recognition in the Dynamic Link Architecture. IEEE Transactions on Computers 42(3)/1993 300–311, [http://doi.org/10.1109/12.210173].

[9] Lawrence S., Giles C.L., et al.: Back. Face Recognition: A Convolutional Neural-Network Approach. IEEE Transactions on Neural Networks 8(1)/1997, 98–113, [http://doi.org/10.1109/72.554195].

[10] Lipton L.: Foundations of the Stereoscopic Cinema – A Study in Depth. Van Nostrand Reinhold, New York 1982.

[11] Martin W. N., Aggarwal J. K.: Volumetric Descriptions of Objects from Multiple Views. IEEE Transactions on Pattern Analysis and Machine Intelligence 5(2)/1983, 150–158.

[12] Nefian A. V.: A hidden Markov model-based approach for face detection and recognition. A Proposal for a Doctoral Dissertation. Georgia Institute of Technology 1998.

[13] Niem W.: Robust and Fast Modeling of 3D Natural Objects from Multiple Views. Proceedings Image and Video Processing II 2182/1994, 388–397.

[14] Prabhu U., Seshadri K.: Facial Recognition Using Active Shape Models, Local Patches and Support Vector Machines, 2009.

[15] Reutebuch S. E., Andersen H., Mcgaughey R. J., Forest L.: Light Detection and Ranging (LIDAR): An Emerging Tool for Multiple Resource Inventory. J. For. 103(6)/2005, 286–292.

[16] Siudak M., Rokita P.: A survey of passive 3D reconstruction methods on the basis of more than one image. Machine Graphics & Vision 23(3/4)/2014, 57–11.

[17] Szeliski R.: Shape from rotation. IEEE Computer Society Conference on Computer Vision and Pattern Recognition (CVPR'91), 1991, 625–630.

[18] Taigman Y., Yang M., et al.: Deep Face: Closing the gap to human level performance in face verification. IEEE Conference on Computer Vision and Pattern Recognition, 2014, 1701–1708.

[19] Vedula S., Rander P., Saito H., Kanade T.: Modeling, Combining, and Rendering Dynamic Real-World Events From Image Sequences. Proc. 4th Conference on Virtual Systems and Multimedia (VSMM98), 1998, 326–332.

[20] Vyatkin S. I., Romanyuk A. N., Gotra Z. Y., et al.: Offsetting, relations and blending with perturbation functions. Proc. of SPIE 10445/2017, 104452B.

[21] Vyatkin S. I., Romanyuk S. A., Pavlov S. V., Necheporyk M. L.: Face Identification Algorithms and its using. Modern Engineering and Innovative Technologies 5/2018, 111–115.

[22] Vyatkin S. I.: Complex surface modeling using perturbation functions. Optoelectronics, instrumentation and data processing 43/2007, 226–231.

[23] Vyatkin S. I.: Method of face recognition using of scalar perturbation functions and set-theoretic operation of subtraction. Optoelectronics, instrumentation and data processing 52(1)/2016, 1–7.

[24] Wiskott L., Fellous J. M., Kruger N., et al.: Face Recognition by Elastic Bunch Graph Matching. Proc. of International Conference on Image Processing 1/1997, 129–132, [http://doi.org/10.1109/ICIP.1997.647401].

[25] Wójcik W., Pavlov S., Kalimoldayev M.: Information Technology in Medical Diagnostics II. Taylor & Francis Group, London 2019.

[26] Rawal R., Yadav V., Sharma S.: Radar – a brief study. International Journal of Innovative Research and Technology 1(12)/2015, 1017–1020.

Prof. Olexandr N. Romanyuk
E-mail: rom8591@gmail.com

Doctor of Technical Sciences, Professor, Department of Software. Work of Vinnytsia National Technical University, head of Software Department
Research field: formation and processing of graphic images

http://orcid.org/0000-0002-2245-3364

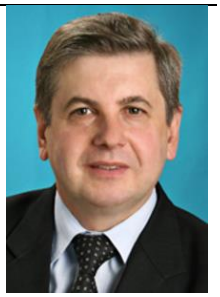

Ph.D. Sergey I. Vyatkin
E-mail: sivser@mail.ru

Candidate of Technical Sciences, senior scientific researcher. Research field: formation and processing of graphic images

http://orcid.org/0000-0002-1591-3588

Prof. Sergii Pavlov
e-mail: psv@vntu.edu.ua

Doctor of Technical Sciences, Professor, Academician of the International Academy of Applied Radioelectronic.Vice-rector of for Scientific Work of Vinnytsia National Technical University, professor of biomedical Engineering, Scientific direction – biomedical information optoelectronic and laser technologies for diagnostics and physiotherapy influence. Deals with issues of improving the distribution of optical radiation theory in biological objects, particularly through the use of electro-optical systems, and the development of intelligent biomedical optoelectronic diagnostic systems and standardized methods for reliably determining the main hemodynamic cardiovascular system of comprehensive into account scattering effects.

http://orcid.org/0000-0002-0051-5560

M.Sc. Pavlo I. Mykhaylov
E-mail:pm@3dgeneration.com

General director CEO 3D GNERATION GmbH (Germany). Research field: formation and processing of graphic images

http://orcid.org/0000-0001-5861-5970

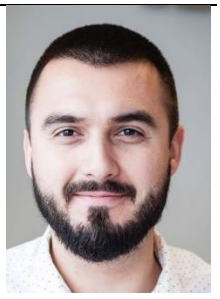

Ph.D. Roman Y. Chekhmestruk
E-mail: Rc.ua@3dgeneration.com

Candidate of Technical Sciences. Technical Director 3D GENERATION UA, researchfield: formation and processing of graphic images.

http://orcid.org/0000-0002-5362-8796

M.Sc. Ivan V. Perun
E-mail: ip.ua@3dgeneration.com

Project manager 3D GENERATION UA, researchfield: formation and processing of graphic images.

http://orcid.org/0000-0001-7402-4417

otrzymano/received: 15.11.2019 *przyjęto do druku/accepted: 15.02.2020*

http://doi.org/10.35784/iapgos.912

INVESTIGATION OF THE KOLMOGOROV-WIENER FILTER FOR CONTINUOUS FRACTAL PROCESSES ON THE BASIS OF THE CHEBYSHEV POLYNOMIALS OF THE FIRST KIND

Vyacheslav Gorev, Alexander Gusev, Valerii Korniienko
Dnipro University of Technology, Department of Information Security and Telecommunications, Dnipro, Ukraine

Abstract. *This paper is devoted to the investigation of the Kolmogorov-Wiener filter weight function for continuous fractal processes with a power-law structure function. The corresponding weight function is sought as an approximate solution to the Wiener-Hopf integral equation. The truncated polynomial expansion method is used. The solution is obtained on the basis of the Chebyshev polynomials of the first kind. The results are compared with the results of the authors' previous investigations devoted to the same problem where other polynomial sets were used. It is shown that different polynomial sets present almost the same behaviour of the solution convergence.*

Keywords: continuous fractal processes, Kolmogorov-Wiener filter weight function, Chebyshev polynomials of the first kind

BADANIE FILTRU KOŁMOGOROWA-WIENERA DLA CIĄGŁYCH PROCESÓW FRAKTALNYCH W OPARCIU O WIELOMIANY CZYBYSZEWA PIERWSZEGO RODZAJU

Streszczenie. *Praca ta jest poświęcona badaniu wagi filtra Kołmogorowa-Wienera dla ciągłych procesów fraktalnych w oparciu o funkcję gęstości prawdopodobieństwa. Głównym zamierzeniem jest znalezienie odpowiedniej wagi będącej przybliżonym rozwiązaniem równania całkowego Wienera-Hopfa. W tym celu wykorzystano metodę rozwinięcia ograniczonego wielomianu. Rozwiązanie oparte jest na wielomianach Czybyszewa pierwszego rodzaju. Wyniki są porównywane z wcześniejszymi badaniami autora dotyczącymi tego samego problemu, w których to użyte zostały inne układy wielomianów. Udowodniono, że różne układy wielomianów zachowują się podobnie a ich rozwiązania są zbieżne.*

Słowa kluczowe: ciągłe procesy fraktalne, waga filtru Kołmogorowa-Wienera, wielomiany Czybyszewa pierwszego rodzaju

Introduction

Nowadays fractal processes are widely used in different fields of knowledge, see, for example, [7] and references therein. We investigate the Kolmogorov-Wiener filter weight function for continuous fractal processes with a power-law structure function. The observation interval of the filter input signal is considered to be finite. The importance of the problem under consideration for the traffic forecast in telecommunications is stressed in [1].

As is known (see, for example, [6]), the Kolmogorov-Wiener filter weight function for continuous processes is the solution of the Wiener-Hopf integral equation, which, in fact, is the Fredholm integral equation of the first kind. In [1] it is proposed to use the Volterra integral equation rather than the Fredlolm one. The corresponding Volterra integral equation is exactly solvable (see [2]), but in the general case it may be not applicable, so we need to seek the solution of the Fredholm integral equation of the first kind.

The explicit analytical solution of the corresponding Wiener-Hopf integral equation meets difficulties, so an approximate solution may be found. As is known [8], such a solution may be sought in the form of a truncated expansion in a complete system of functions. Such a system is often chosen as a polynomial set.

Our previous investigations were devoted to the above-mentioned truncated polynomial expansion method on the basis of a polynomial set orthogonal on the observation interval without weight [3] and on the basis of the Chebyshev polynomials of the second kind [4]. The convergence behaviour of the solutions in [3] and [4] is, in fact, the same; some approximations fail, but some approximations give reliable results. Therefore, two interesting questions arise. First of all, is the behaviour of the solution convergence identical only for the sets in [3] and [4], or also for other polynomial sets? May the use of another polynomial set refine such behaviour? It is interesting then to investigate the problem under consideration on the basis of another polynomial set.

The aim of this work is to obtain the corresponding Kolmogorov-Wiener filter weight function on the basis of the Chebyshev polynomials of the first kind and to compare the results with papers [3, 4].

1. Truncated polynomial expansion method

We investigate the Kolmogorov-Wiener filter for a continuous stationary fractal process $x(t)$ with a power-law structure function $c(\tau)$:

$$c(\tau) \equiv \left\langle \left(x(t) - x(t-\tau) \right)^2 \right\rangle_t = \alpha \cdot |\tau|^{2H} \tag{1}$$

where α is a constant and $H \in (0,5;1)$ is the Hurst exponent. The correlation function of such a process is as follows [1]:

$$R(t) = \sigma^2 - \frac{\alpha}{2}|t|^{2H} \tag{2}$$

where σ^2 is the process variance.

Let the filter input signal be observed for a time interval $t \in [0,T]$, and let us denote the time interval for which the forecast is made as k. Then, as is known, the Kolmogorov-Wiener filter weight function $h(\tau)$ obeys the Wiener-Hopf integral equation

$$R(t+k) = \int_0^T d\tau h(\tau) R(t-\tau) \tag{3}$$

which, in fact, is the Fredholm integral equation of the first kind. In this paper we investigate the truncated polynomial expansion method based on the Chebychev polynomials of the first kind.

As is known [5], the Chebychev polynomials of the first kind are given by the expression

$$T_n(x) = \sum_{k=0}^{[n/2]} C_n^{2k} \left(x^2 - 1 \right)^k x^{n-2k} \tag{4}$$

where $[y]$ is the integer part of y. These polynomials obey the orthogonality property

$$\int_{-1}^{1} \frac{T_n(x) T_m(x)}{\sqrt{1-x^2}} dx = A_n \delta_{nm}, \; A_n = \begin{cases} \pi, n = 0 \\ \pi/2, n \neq 0 \end{cases}. \tag{5}$$

As is known [8], according to (3) we need polynomials orthogonal on the interval $t \in [0,T]$ rather than on $[-1,1]$.

Changing the variable in (5) yields

$$\int_0^T T_n\left(\frac{2y}{T}-1\right)T_m\left(\frac{2y}{T}-1\right)w(y)dy=\frac{T}{2}A_n\delta_{mn} \tag{6}$$

where

$$w(y)=\left(1-\left(\frac{2y}{T}-1\right)^2\right)^{-1/2}. \tag{7}$$

So the polynomials

$$S_n(t)=T_n\left(\frac{2t}{T}-1\right), \tag{8}$$

are orthogonal on $t\in[0,T]$ with the weight $w(y)$, and the solution $h(\tau)$ may be sought as

$$h(\tau)=\sum_{n\geq 0}g_nS_n(\tau). \tag{9}$$

Substituting (8) into (3) one can obtain

$$R(t+k)=\sum_{n\geq 0}g_n\int_0^T d\tau h(\tau)S_n(\tau), \tag{10}$$

which after multiplying by $S_m(\tau)$ and integrating leads to

$$\sum_n g_n\int_0^T\int_0^T d\tau dt S_n(\tau)S_m(t)R(t-\tau)=\int_0^T dt S_m(t)R(t+k) \tag{11}$$

The quantities

$$G_{nm}=\int_0^T\int_0^T d\tau dt S_n(\tau)S_m(t)R(t-\tau) \tag{12}$$

are called the integral brackets, so (11) may be rewritten as

$$\sum_n g_nG_{nm}=b_m \tag{13}$$

where

$$b_m=\int_0^T dt S_m(t)R(t+k) \tag{14}$$

Expression (13) is an infinite set of linear algebraic equations in g_n. This set can hardly be treated, so the sum (9) should be artificially truncated:

$$h^{[l]}(\tau)=\sum_{n=0}^{l-1}g_n^{[l]}S_n(\tau). \tag{15}$$

where $h^{[l]}(\tau)$ is the Kolmogorov-Wiener filter weight function in the l-polynomial approximation and $g_n^{[l]}$ are the corresponding coefficients multiplying the polynomials. These coefficients are the solutions of the following set of linear algebraic equations:

$$\sum_{n=0}^{l-1}g_n^{[l]}G_{nm}=b_m. \tag{16}$$

So one should obtain the values of the coefficients $g_n^{[l]}$ from (16) and substitute them into (15) to obtain the Kolmogorov-Wiener filter weight function in the l-polynomial approximation.

It should be explained why the Chebyshev polynomials of the first kind are convenient for the problem under consideration. On the basis of (4), (8), (12) and the fact that the correlation function $R(t)$ is an even one, it can be shown that

$$G_{nm}=0 \text{ if } m,n \text{ are of different parity} \tag{17}$$

Also, on the basis of the fact that $R(t)$ is an even function, from (12) it is evident that

$$G_{nm}=G_{mn}. \tag{18}$$

The calculation of the integral brackets takes the most part of the computing time. On the basis of (17) and (18) it can be seen that G_{nm} should be computed by a straightforward calculation only for $n\geq m$ and n,m of the same parity. This fact significantly reduces the computing time.

2. Investigation of the method convergence

This section is devoted to the investigation of the convergence behavior of the obtained solutions. First of all, as is known (see, for example, [9]), the convergence is guaranteed if the kernel of an integral equation is a positively defined function. In our case $R(t)$ is not a positively defined function, so the method convergence is not guaranteed.

In order to check the obtained solutions for different numbers of polynomials, we calculate the weight function on the basis of the Wolfram Mathematica 11.0 package and compare left-hand and right-hand sides of eq. (3) with each other.

In other words, the functions

$$\text{Left}(t)=\sum_{n=0}^{l-1}g_n^{[l]}\int_0^T d\tau S_n(\tau)R(t-\tau) \tag{19}$$

and

$$\text{Right}(t)=R(t+k) \tag{20}$$

are numerically compared with each other, the coefficients $g_n^{[l]}$ are calculated on the basis of (16). It should be stressed that the substitution of (2) into (19) gives

$$\text{Left}(t)=\sum_{n=0}^{l-1}g_n^{[l]}\int_0^T d\tau S_n(\tau)\left(\sigma^2-\frac{\alpha}{2}|t-\tau|^{2H}\right), \tag{21}$$

and on the basis of the Wolfram Mathematica package this function is treated as

$$\text{Left}(t)=\sum_{n=0}^{l-1}g_n^{[l]}\int_0^t d\tau S_n(\tau)\left(\sigma^2-\frac{\alpha}{2}(t-\tau)^{2H}\right)+$$
$$+\sum_{n=0}^{l-1}g_n^{[l]}\int_t^T d\tau S_n(\tau)\left(\sigma^2-\frac{\alpha}{2}(\tau-t)^{2H}\right) \tag{22}$$

The following set of parameters is investigated:

$$T=100,\ \sigma=1.2,\ H=0.8,\ \alpha=3\cdot 10^{-3}. \tag{23}$$

This set of parameters is also investigated in [3, 4]. It should be stressed that the well-known inequality

$$|R(t)|\leq R(0), \tag{24}$$

holds for the set (23) on the observation interval $t\in[0,T]$.

The investigation is made up to the 18-polynomial approximation, the corresponding coefficients multiplying the polynomials in the l-polynomial approximation are given in Table 1. The coefficients in Table 1 are rounded off to three significant digits.

Table 1. Coefficients multiplying polynomials for the set (23)

l	Coefficients multiplying the polynomials
1	$g_0^{[1]}=4,86\cdot 10^{-3}$
2	$g_0^{[2]}=4,86\cdot 10^{-3}$, $g_1^{[2]}=-2,91\cdot 10^{-2}$
3	$g_0^{[3]}=-8,8\cdot 10^{-2}$, $g_1^{[3]}=-2,91\cdot 10^{-2}$, $g_2^{[3]}=-2,06\cdot 10^{-1}$
4	$g_0^{[4]}=-8,8\cdot 10^{-2}$, $g_1^{[4]}=-5,01\cdot 10^{-2}$, $g_2^{[4]}=-2,06\cdot 10^{-1}$, $g_3^{[4]}=-3,24\cdot 10^{-2}$
5	$g_0^{[5]}=6,61\cdot 10^{-2}$, $g_1^{[5]}=-5,01\cdot 10^{-2}$, $g_2^{[5]}=1,36\cdot 10^{-1}$, $g_3^{[5]}=-3,24\cdot 10^{-2}$, $g_4^{[5]}=8,56\cdot 10^{-2}$
6	$g_0^{[6]}=6,61\cdot 10^{-2}$, $g_1^{[6]}=-7,19\cdot 10^{-2}$, $g_2^{[6]}=1,36\cdot 10^{-1}$, $g_3^{[6]}=-6,02\cdot 10^{-2}$, $g_4^{[6]}=8,56\cdot 10^{-2}$, $g_5^{[6]}=-3,28\cdot 10^{-2}$
7	$g_0^{[7]}=6,68\cdot 10^{-2}$, $g_1^{[7]}=-7,19\cdot 10^{-2}$, $g_2^{[7]}=1,39\cdot 10^{-1}$, $g_3^{[7]}=-6,02\cdot 10^{-2}$, $g_4^{[7]}=1,15\cdot 10^{-1}$, $g_5^{[7]}=-3,28\cdot 10^{-2}$, $g_6^{[7]}=6,11\cdot 10^{-2}$
8	$g_0^{[8]}=6,68\cdot 10^{-2}$, $g_1^{[8]}=-9,51\cdot 10^{-2}$, $g_2^{[8]}=1,39\cdot 10^{-1}$, $g_3^{[8]}=-8,71\cdot 10^{-2}$, $g_4^{[8]}=1,15\cdot 10^{-1}$, $g_5^{[8]}=-6,59\cdot 10^{-2}$, $g_6^{[8]}=6,11\cdot 10^{-2}$, $g_7^{[8]}=-3,27\cdot 10^{-2}$
9	$g_0^{[9]}=8,02\cdot 10^{-2}$, $g_1^{[9]}=-9,51\cdot 10^{-2}$, $g_2^{[9]}=1,64\cdot 10^{-1}$, $g_3^{[9]}=-8,71\cdot 10^{-2}$, $g_4^{[9]}=1,49\cdot 10^{-1}$, $g_5^{[9]}=-6,59\cdot 10^{-2}$, $g_6^{[9]}=1,11\cdot 10^{-1}$, $g_7^{[9]}=-3,27\cdot 10^{-2}$, $g_8^{[9]}=5,37\cdot 10^{-2}$

Table 1 (cont.). Coefficients multiplying polynomials for the set (23)

l	Coefficients multiplying the polynomials
10	$g_0^{[10]} = 8,02 \cdot 10^{-2}$, $g_1^{[10]} = -1,20 \cdot 10^{-1}$, $g_2^{[10]} = 1,64 \cdot 10^{-1}$, $g_3^{[10]} = -1,15 \cdot 10^{-1}$, $g_4^{[10]} = 1,49 \cdot 10^{-1}$, $g_5^{[10]} = -9,86 \cdot 10^{-2}$, $g_6^{[10]} = 1,11 \cdot 10^{-1}$, $g_7^{[10]} = -6,97 \cdot 10^{-2}$, $g_8^{[10]} = 5,37 \cdot 10^{-2}$, $g_9^{[10]} = -3,26 \cdot 10^{-2}$
11	$g_0^{[11]} = 9,53 \cdot 10^{-2}$, $g_1^{[11]} = -1,20 \cdot 10^{-1}$, $g_2^{[11]} = 1,94 \cdot 10^{-1}$, $g_3^{[11]} = -1,15 \cdot 10^{-1}$, $g_4^{[11]} = 1,86 \cdot 10^{-1}$, $g_5^{[11]} = -9,86 \cdot 10^{-2}$, $g_6^{[11]} = 1,57 \cdot 10^{-1}$, $g_7^{[11]} = -6,97 \cdot 10^{-2}$, $g_8^{[11]} = 1,09 \cdot 10^{-1}$, $g_9^{[11]} = -3,26 \cdot 10^{-2}$, $g_{10}^{[11]} = 5,03 \cdot 10^{-2}$
12	$g_0^{[12]} = 9,53 \cdot 10^{-2}$, $g_1^{[12]} = -1,47 \cdot 10^{-1}$, $g_2^{[12]} = 1,94 \cdot 10^{-1}$, $g_3^{[12]} = -1,44 \cdot 10^{-1}$, $g_4^{[12]} = 1,86 \cdot 10^{-1}$, $g_5^{[12]} = -1,32 \cdot 10^{-1}$, $g_6^{[12]} = 1,57 \cdot 10^{-1}$, $g_7^{[12]} = -1,07 \cdot 10^{-1}$, $g_8^{[12]} = 1,09 \cdot 10^{-1}$, $g_9^{[12]} = -7,24 \cdot 10^{-2}$, $g_{10}^{[12]} = 5,03 \cdot 10^{-2}$, $g_{11}^{[12]} = -3,25 \cdot 10^{-2}$
13	$g_0^{[13]} = 1,13 \cdot 10^{-1}$, $g_1^{[13]} = -1,47 \cdot 10^{-1}$, $g_2^{[13]} = 2,29 \cdot 10^{-1}$, $g_3^{[13]} = -1,44 \cdot 10^{-1}$, $g_4^{[13]} = 2,25 \cdot 10^{-1}$, $g_5^{[13]} = -1,32 \cdot 10^{-1}$, $g_6^{[13]} = 2,03 \cdot 10^{-1}$, $g_7^{[13]} = -1,07 \cdot 10^{-1}$, $g_8^{[13]} = 1,64 \cdot 10^{-1}$, $g_9^{[13]} = -7,24 \cdot 10^{-2}$, $g_{10}^{[13]} = 1,09 \cdot 10^{-1}$, $g_{11}^{[13]} = -3,25 \cdot 10^{-2}$, $g_{12}^{[13]} = 4,82 \cdot 10^{-2}$
14	$g_0^{[14]} = 1,13 \cdot 10^{-1}$, $g_1^{[14]} = -1,76 \cdot 10^{-1}$, $g_2^{[14]} = 2,29 \cdot 10^{-1}$, $g_3^{[14]} = -1,74 \cdot 10^{-1}$, $g_4^{[14]} = 2,25 \cdot 10^{-1}$, $g_5^{[14]} = -1,65 \cdot 10^{-1}$, $g_6^{[14]} = 2,03 \cdot 10^{-1}$, $g_7^{[14]} = -1,45 \cdot 10^{-1}$, $g_8^{[14]} = 1,64 \cdot 10^{-1}$, $g_9^{[14]} = -1,14 \cdot 10^{-1}$, $g_{10}^{[14]} = 1,09 \cdot 10^{-1}$, $g_{11}^{[14]} = -7,44 \cdot 10^{-2}$, $g_{12}^{[14]} = 4,82 \cdot 10^{-2}$, $g_{13}^{[14]} = -3,24 \cdot 10^{-2}$.
15	$g_0^{[15]} = 1,31 \cdot 10^{-1}$, $g_1^{[15]} = -1,76 \cdot 10^{-1}$, $g_2^{[15]} = 2,68 \cdot 10^{-1}$, $g_3^{[15]} = -1,74 \cdot 10^{-1}$, $g_4^{[15]} = 2,66 \cdot 10^{-1}$, $g_5^{[15]} = -1,65 \cdot 10^{-1}$, $g_6^{[15]} = 2,50 \cdot 10^{-1}$, $g_7^{[15]} = -1,45 \cdot 10^{-1}$, $g_8^{[15]} = 2,18 \cdot 10^{-1}$, $g_9^{[15]} = -1,14 \cdot 10^{-1}$, $g_{10}^{[15]} = 1,69 \cdot 10^{-1}$, $g_{11}^{[15]} = -7,44 \cdot 10^{-2}$, $g_{12}^{[15]} = 1,09 \cdot 10^{-1}$, $g_{13}^{[15]} = -3,24 \cdot 10^{-2}$, $g_{14}^{[15]} = 4,69 \cdot 10^{-2}$.
16	$g_0^{[16]} = 1,31 \cdot 10^{-1}$, $g_1^{[16]} = -2,07 \cdot 10^{-1}$, $g_2^{[16]} = 2,68 \cdot 10^{-1}$, $g_3^{[16]} = -2,07 \cdot 10^{-1}$, $g_4^{[16]} = 2,66 \cdot 10^{-1}$, $g_5^{[16]} = -2,00 \cdot 10^{-1}$, $g_6^{[16]} = 2,50 \cdot 10^{-1}$, $g_7^{[16]} = -1,84 \cdot 10^{-1}$, $g_8^{[16]} = 2,18 \cdot 10^{-1}$, $g_9^{[16]} = -1,57 \cdot 10^{-1}$, $g_{10}^{[16]} = 1,69 \cdot 10^{-1}$, $g_{11}^{[16]} = -1,20 \cdot 10^{-1}$, $g_{12}^{[16]} = 1,09 \cdot 10^{-1}$, $g_{13}^{[16]} = -7,56 \cdot 10^{-2}$, $g_{14}^{[16]} = 4,69 \cdot 10^{-2}$, $g_{15}^{[16]} = -3,22 \cdot 10^{-2}$
17	$g_0^{[17]} = 1,52 \cdot 10^{-1}$, $g_1^{[17]} = -2,07 \cdot 10^{-1}$, $g_2^{[17]} = 3,09 \cdot 10^{-1}$, $g_3^{[17]} = -2,07 \cdot 10^{-1}$, $g_4^{[17]} = 3,10 \cdot 10^{-1}$, $g_5^{[17]} = -2,00 \cdot 10^{-1}$, $g_6^{[17]} = 2,99 \cdot 10^{-1}$, $g_7^{[17]} = -1,84 \cdot 10^{-1}$, $g_8^{[17]} = 2,72 \cdot 10^{-1}$, $g_9^{[17]} = -1,57 \cdot 10^{-1}$, $g_{10}^{[17]} = 2,30 \cdot 10^{-1}$, $g_{11}^{[17[} = -1,20 \cdot 10^{-1}$, $g_{12}^{[17]} = 1,74 \cdot 10^{-1}$, $g_{13}^{[17]} = -7,56 \cdot 10^{-2}$, $g_{14}^{[17]} = 1,09 \cdot 10^{-1}$, $g_{15}^{[17]} = -3,22 \cdot 10^{-2}$, $g_{16}^{[17]} = 4,59 \cdot 10^{-2}$
18	$g_0^{[18]} = 1,52 \cdot 10^{-1}$, $g_1^{[18]} = -2,40 \cdot 10^{-1}$, $g_2^{[18]} = 3,09 \cdot 10^{-1}$, $g_3^{[18]} = -2,41 \cdot 10^{-1}$, $g_4^{[18]} = 3,10 \cdot 10^{-1}$, $g_5^{[18]} = -2,36 \cdot 10^{-1}$, $g_6^{[18]} = 2,99 \cdot 10^{-1}$, $g_7^{[18]} = -2,23 \cdot 10^{-1}$, $g_8^{[18]} = 2,72 \cdot 10^{-1}$, $g_9^{[18]} = -2,00 \cdot 10^{-1}$, $g_{10}^{[18]} = 2,30 \cdot 10^{-1}$, $g_{11}^{[18]} = -1,66 \cdot 10^{-1}$, $g_{12}^{[18]} = 1,74 \cdot 10^{-1}$, $g_{13}^{[18]} = -1,24 \cdot 10^{-1}$, $g_{14}^{[18]} = 1,09 \cdot 10^{-1}$, $g_{15}^{[18]} = -7,70 \cdot 10^{-2}$, $g_{16}^{[18]} = 4,59 \cdot 10^{-2}$, $g_{17}^{[18]} = -3,21 \cdot 10^{-2}$

The obtained comparison of Left(t) and Right(t) is illustrated on the following graphs. The function Right(t) is shown as a solid line, and the functions Left(t) are shown as dotted lines.

The corresponding comparison for the one-polynomial approximation is shown in Fig. 1. As can be seen, the one-polynomial approximation is not accurate enough.

For the two-polynomial approximation we have (see Fig. 2).

As can be seen, the two-polynomial approximation is rather accurate: the functions Left(t) and Right(t) are rather close to each other.

The graphs for the three-polynomial and the four-polynomial approximations are approximately the same. As can be seen, they are less accurate than the two-polynomial one, but more accurate than the one-polynomial one.

As can also be seen from Fig. 2 and Fig. 3, the approximation accuracy may not increase with the number of polynomials. Such behavior of the approximations may take place because the correlation function $R(t)$, which is the kernel of the integral equation (3), is not positively defined.

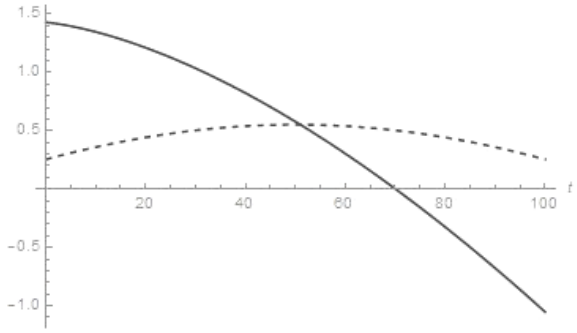

Fig. 1. Comparison of Left(t) and Right(t) for the one-polynomial approximation for parameters (23)

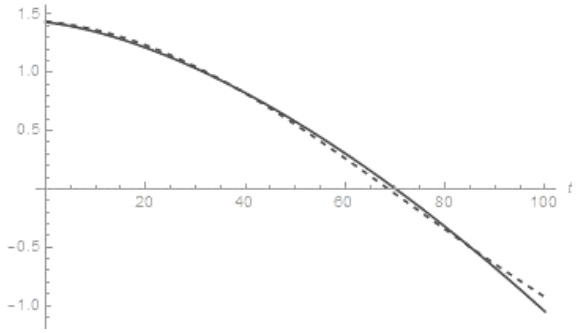

Fig. 2. Comparison of Left(t) and Right(t) for the two-polynomial approximation for parameters (23)

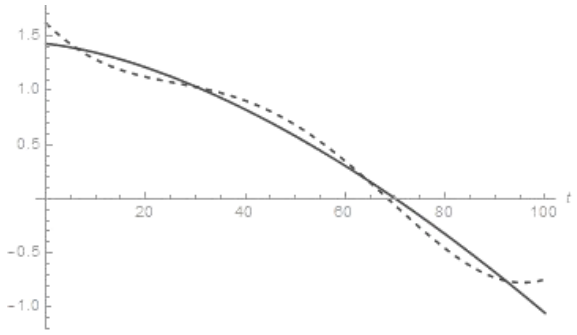

Fig. 3. Comparison of Left(t) and Right(t) for the three-polynomial approximation for parameters (23)

As can be seen from Fig. 4, the five-polynomial approximation is accurate: the graphs of Left(t) and Right(t) almost coincide.

The investigation of the number of polynomials from 5 to 8 shows that the accuracy of the corresponding approximations increases with the number of polynomials. For example, the comparison for the eight-polynomial approximation is given in Fig. 5.

As can be seen from Fig. 4 and Fig. 5, the eight-polynomial approximation is more accurate than the five-polynomial one.

But, unfortunately, the investigation of the numbers of polynomials from 9 to 15 shows that the corresponding approximations completely fail. Such behavior of the solutions is rather strange. In our opinion, it may be explained as follows. The convergence of the method is not guaranteed because the kernel of the integral equation (3) is not a positively defined function. So, not only may the accuracy not increase with the number of polynomials, but some approximations may also completely fail.

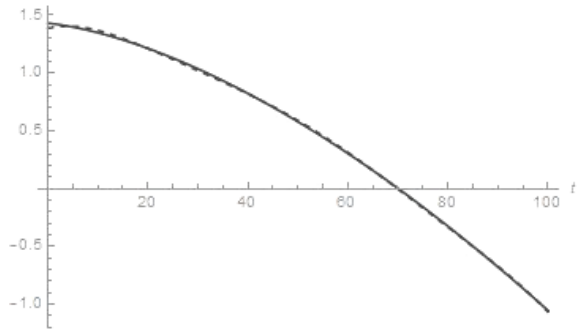

Fig. 4. Comparison of Left(t) and Right(t) for the five-polynomial approximation for parameters (23)

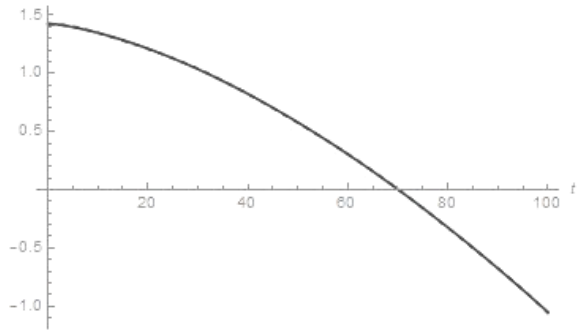

Fig. 5. Comparison of Left(t) and Right(t) for the eight-polynomial approximation for parameters (23)

But the investigation of the number of polynomials from 16 to 18 shows that the corresponding approximations give almost ideal results. Approximations of more than 18 polynomials are not investigated because the "unphysical ripple" takes place on the graphs in such a case. In our opinion, such a situation occurs because Wolfram Mathematica has not enough recourses to build corresponding graphs adequately.

The same behavior of Left(t) and Right(t) is also observed for other polynomial sets in papers [3, 4].

The following parameter sets are also investigated for the same reason as the set (23):

$$T = 10,\ \sigma = 1.2,\ H = 0.8,\ \alpha = 10^{-1}. \tag{24}$$

and

$$T = 1000,\ \sigma = 1.2,\ H = 0.8,\ \alpha = 8 \cdot 10^{-5}. \tag{25}$$

It is obtained that the behavior of Left(t) and Right(t) for these sets is also the same as for the other polynomial sets described in [3, 4].

3. Conclusion

This paper is devoted to the investigation of the Kolmogorov-Wiener weight function for continuous fractal processes with a power-law structure function. As an exact analytical solution to the corresponding integral equation (2) can hardly be found, we use the truncated polynomial expansion method in order to obtain an approximate solution to this equation. In this paper the weight function is expanded in a truncated series of the Chebyshev polynomials of the first kind.

It is shown that the accuracy of polynomial approximations may not increase with the number of polynomials. Moreover, some of the approximations may totally fail. In our opinion, it takes place because the kernel of the integral equation (2) is not a positively defined function.

However, it is shown that some approximations give reliable results, so the method under consideration may lead to good results. It should be stressed, however, that each approximation should be checked numerically.

The results are compared with the corresponding results of papers [3, 4] where other polynomial sets were used. In paper [3] the same problem is investigated on the basis of polynomials orthogonal on the observation interval without weight. In paper [4] the corresponding investigation is made on the basis of the Chebyshev polynomials of the second kind. It is shown that the convergence behavior of the solutions is the same for all the above-mentioned polynomial sets. So, the hypothesis may be made that the convergence behavior of the solutions is independent of the polynomial set used in the framework of the truncated polynomial expansion method.

The obtained results may be applied to the investigation of the fractal process forecast in different systems of practical interest, for example, for telecommunication traffic forecast.

References

[1] Bagmanov V. Kh., Komissarov A. M., Sultanov A. Kh.: Teletraffic forecast on the basis of fractal fliters. Bulletin of Ufa State Aviation Technical University 9(6(24))/2007, 217–222 (in Russian).
[2] Gorev V. N., Gusev A. Yu., Korniienko V. I.: On the analytical solution of a Volterra integral equation for investigation of fractal processes. Radio Electronics, Computer Science, Control 4/2018, 42–50.
[3] Gorev V. N., Gusev A. Yu., Korniienko V. I.: Polynomial solutions for the Kolmogorov-Wiener filter weight function for fractal processes. Radio Electronics, Computer Science, Control 2/2019, 44–52.
[4] Gorev V. N., Gusev A. Yu., Korniienko V. I.: Investigation of the Kolmogorov-Wiener filter for treatment of fractal processes on the basis of the Chebyshev polynomials of the second kind, CEUR Workshop Proceedings 2353/2019, 596–606.
[5] Gradshteyn I. S., Ryzhik I. M.: Table of Integrals, Series, and Products, Eighth edition, Zwillinger D., Moll V. (Ed.) Elsevier, Amsterdam 2015.
[6] Miller S., Childers D.: Probability and Random Processes With Applications to Signal Processing and Communications, Second edition. Elseiver, Amsterdam 2012.
[7] Pipiras V., Taqqu M.: Long-Range Dependence and Self-Similarity. Cambridge University Press, 2017.
[8] Polyanin A. D., Manzhirov A. V.: Handbook of the integral equations., Second edition. Boca Raton, Chapman & Hall/CRC Press 2008.
[9] Ziman J. M.: Electrons and Phonons. The Theory of Transport Phenomena in Solids. Oxford University Press, 2001.

Ph.D. Vyacheslav Gorev
e-mail: lordjainor@gmail.com

In 2012 graduated from the Department of Theoretical Physics of Oles Honchar Dnipro National University. In 2016 defended a Ph.D. thesis in theoretical physics. Since 2017 has been working at the Department of Information Security and Telecommunications of Dnipro University of Technology.

http://orcid.org/0000-0002-9528-9497

Prof. Alexander Gusev
e-mail: gusev1950@ukr.net

In 1972 graduated from the Department of Automation and Telemechanics of the Novosibirsk Electrotechnical Institute. From 1972 worked in the Siberian branch of the USSR Academy of Sciences. In 1982 defended a Ph.D thesis. From 1983 worked at the Dnepropetrovsk Scientific Institute of Automation. Since 2005 works as a professor of Dnipro University of Technology.

http://orcid.org/0000-0002-0548-728X

Prof. Valerii Korniienko
e-mail: vikor7@ukr.net

Doctor of Engineering Science (2010), Professor (2011). In 1979 graduated from Dnipropetrovsk Mining Institute in the specialty of "Automation and Telemechanics". He is the Head of the Department of Information Security and Telecommunication since 2016. He has 130 scientific publications. His inventions were introduced in the Ukrainian-Russian space vehicle 'Ocean-O'.

http://orcid.org/0000-0002-0800-3359

otrzymano/received: 15.11.2019 *przyjęto do druku/accepted: 15.02.2020*

http://doi.org/10.35784/iapgos.915

MODELLING OF SPINTRONIC DEVICES FOR APPLICATION IN RANDOM ACCESS MEMORY

Ruslan Politanskyi[1], Maria Vistak[2], Andriy Veryga[1], Tetyana Ruda[1]
[1]Yuriy Fedkovych Chernivtsi National University, Physical, Technical and Computer Sciences Institute, Department of Radio Engineering and Information Security, Chernivtsi, Ukraine, [2]Danylo Halytsky Lviv National Medical University, Faculty of Pharmacy, Department of Biophysics, Lviv, Ukraine

Abstract. *The article analyzes the physical processes that occur in spin-valve structures during recording process which occurs in high-speed magnetic memory devices. Considered are devices using magnetization of the ferromagnetic layer through transmitting magnetic moment by polarized spin (STT-MRAM). Basic equations are derived to model the information recording process in the model of symmetric binary channel. Because the error probability arises from the magnetization process, a model of the magnetization process is formed, which is derived from the Landau-Lifshitz-Gilbert equations under the assumption of a single-domain magnet. The choice of a single-domain model is due to the nanometer size of the flat magnetic layer. The developed method of modeling the recording process determines the dependence of such characteristics as the bit error probability and the rate of recording on two important technological characteristics of the recording process: the value of the current and its duration. The end result and the aim of the simulation is to determine the optimal values of the current and its duration at which the speed of the recording process is the highest for a given level of error probability. The numerical values of the transmission rate and error probability were obtained for a wide range of current values (10–1500 μA) and recording time of one bit (1–70 ns), and generally correctly describe the process of information transmission. The calculated data were compared with the technical characteristics of existing industrial devices and devices which are the object of the scientific research. The resulting model can be used to simulate devices using different values of recording currents: STT-MRAM series chips using low current values (500-100 μA), devices in the stage of technological design and using medium current values (100–500 μA) and devices that are the object of experimental scientific research and use high currents (500–1000 μA). The model can also be applied to simulate devices with different data rates, which have different requirements for both transmission speed and bit error probability. In this way, the model can be applied to both high-speed memory devices in computer systems and signal sensors, which are connected to sensor networks or connected to the IoT.*

Keywords: STT-MRAM, spin-polarized current, binary symmetric channel

MODELOWANIE URZĄDZEŃ SPINTRONICZNYCH DO ZASTOSOWANIA W PAMIĘCI O DOSTĘPIE SWOBODNYM RAM

Streszczenie. *W tym artykule analizowane są procesy fizyczne zachodzące w strukturach zaworów spinowych podczas procesu rejestrowania informacji, który występuje w urządzeniach z szybką pamięcią magnetyczną. Obiektem badań są urządzenia wykorzystujące magnetyzację warstwy ferromagnetycznej poprzez przenoszenie momentu magnetycznego za pomocą spolaryzowanego spinu (STT-MRAM). Wyprowadzono podstawowe równania potrzebne do modelowania procesu rejestrowania informacji w modelu symetrycznego kanału binarnego. W związku z tym, że prawdopodobieństwo błędu wynika z procesu magnesowania, stworzony jest model procesu magnesowania, który został wyprowadzony z równań Landaua-Lifshitza-Hilberta przy założeniu magnesu jednodomenowego. Wybór modelu jednodomenowego wynika z nanometrycznej wielkości płaskiej warstwy magnetycznej. Opracowana metoda modelowania procesu rejestrowania informacji określa zależność wskaźników, takich jak prawdopodobieństwo błędnego bitu i szybkość transmisji informacji, od dwóch ważnych właściwości procesu rejestrowania: natężenia prądu i czasu jego trwania. Końcowym rezultatem i zarazem celem symulacji jest określenie optymalnych wartości natężenia prądu i czasu trwania rejestracji informacji, przy których prędkość procesu zapisu będzie najwyższa dla danego stopnia prawdopodobieństwa błędu. Uzyskano wartości liczbowe dla szybkości transmisji i prawdopodobieństwa błędu dla szerokiego zakresu natężenia prądu (10–1500 μA) i czasu rejestracji jednego bitu (1–70 ns), które ogólnie poprawnie opisują proces transmisji informacji. Wyniki obliczeń zostały porównane ze specyfikacją techniczną istniejących urządzeń przemysłowych i urządzeń będących obiektami badań naukowych. Powstały model można wykorzystać do symulacji urządzeń wykorzystujących różne wartości natężenia prądu: układy szeregowe STT-MRAM wykorzystujące niskie natężenie prądu (500–100 μA), urządzenia na etapie projektowania technologicznego, które wykorzystują średnie natężenie prądu (100–500 μA) oraz urządzenia będące obiektami eksperymentalnych badań naukowych, które wykorzystują wysokie natężenie prądu (500–1000 μA). Model można również zastosować w symulacjach urządzeń o różnych szybkościach transmisji danych, które mają różne wymagania dotyczące zarówno szybkości transmisji, jak i prawdopodobieństwa błędu w jednym bicie informacji. W ten sposób model ten można wykorzystać zarówno w urządzeniach z szybką pamięcią w systemach komputerowych, jak i w czujnikach sygnałów, które są podłączone do sieci czujników lub podłączone do Internetu rzeczy.*

Słowa kluczowe: STT-MRAM, prąd spolaryzowany spinowo, symetryczny kanał binarny

Introduction

There are three development stages of the devices used for the processing of digital data, which use different states of magnetization and differ in physical mechanisms of magnetization reversal of active cells (MRAM). In the first generation of devices for magnetization reversal there is used the interaction with an external magnetic field. Devices of the second generation are based on the interaction mechanism of electron spins and magnetized layer with a small coercive force (STT-MRAM). STT-MRAM devices have two different topological implementations that differ in the direction of magnetization: perpendicular-to-plane and in-plane implementations [3]. To ensure two stable states, it is necessary that the thickness of the magnetic layer is much smaller than its transverse dimensions. Devices with parallel orientation have already been introduced into serial production of small memory modules with 64 Mb (2015) and 256 Mb (2016) [2]. Research is being conducted in the direction of constructing MRAM modules up to 4 GB [6].

STT-MRAM technologies are potentially attractive because they enable high-speed performance in the absence of device degradation (compared to FLASH modules) [2] and the refusal of uninterrupted power supply to memory chips (compared to SRAM modules). The theoretical basis for further speed increase of MRAM devices is that the transfer of the magnetization state of a magnetic field can occur much faster than the transport of charge carriers in classical semiconductor devices. This means that the switching time of the STT-MRAM can be further reduced. Therefore, according to the statements of some authors [3], in the future, magnetic memory devices will be able to conquer most of the RAM market.

The processes of magnetization reversal in STT-MRAM devices are of a statistical nature [9]. Therefore, methods of combating errors and the study of statistical patterns of their formation have great importance.

STT-MRAM devices are used in the embedded memory applications [10] for automotive industry [4] and the Internet [1, 8], which do not require the use of powerful computing systems. There are also studies on the use of these technologies in non-volatile operating computer memory, along with flash-memory technologies [7]. There are also projects in which MRAM devices are used for file systems [14].

In addition to that, STT-MRAM devices are used in the manufacture of relatively cheap authentication devices and the generation of secret keys [13], and the generation of cryptographic primitives (so-called software non-repetitive methods).

The ability of STT-MRAM devices to operate in the temperature range (-40°C to 125°C) [10] without the use of additional power sources makes it possible to use these devices in the IoT technologies and in sensor networks.

STT-MRAM devices are considered to be resistant to external interference. What is more, it is noted that there is a probability that there can occur the transition of the magnetization vector from one state to another. This is due to thermal fluctuations of the energy values of thermal fluctuations comparable with the values of the magnetization reversal energy. In [4], it is foretold that three types of errors may occur in STT-MRAM:

1) errors caused by higher values of current than technological standards;
2) errors caused by lower values of the recording current than technological standards;
3) errors caused by random magnetization.

The object of the study is a process of writing information in magnetic memory devices with a change in the state of magnetization of a free layer in a spin-valve, which is described by Landau-Lifshitz-Gilbert equation:

$$\frac{d\vec{M}}{dt} = -\gamma \cdot \left[\vec{M} \times \vec{H}_{eff}\right] - \frac{\alpha}{M_s} \cdot \left[\vec{M} \times \frac{d\vec{M}}{dt}\right] + \vec{T}_{s.t.} \quad (1)$$

or after simplification:

$$\frac{d\vec{M}}{dt} \approx -\gamma \cdot \left[\vec{M} \times \vec{H}_{eff}\right] - \frac{\alpha \cdot \gamma}{M_s} \cdot \left[\vec{M} \times \left[\vec{M} \times \vec{H}_{eff}\right]\right] + \vec{T}_{s.t.} \quad (2)$$

where $\vec{M}$ is a magnetization of a free layer; γ is is the gyromagnetic ratio; $\vec{H}_{eff}$ is a sum of all external magnetic fields; α is the phenomenological LLG damping constant; M_s is a saturation value of a free layer magnetization; $\vec{T}_{s.t.}$ is the moment of interaction between magnetic moment $\vec{M}$ and spin moment of the polarized current (s.t. – spin torque).

The investigation of information writing processes in memory devices is carried out on the basis of discrete channel models with a given bit error writing probability.

The object of the study is the dependence of the probability of magnetization flipping of ferromagnetic layer with two stable states of magnetization on the value of writing current and its duration.

The purpose of the work is to determine the optimum current value and its duration in the process of one–bit writing, at which the highest rate of information recording is observed at the smallest probability of a bit error.

1. Mathematical models of physical processes in spin-valves

Let's consider a model of flipping magnetization that occurs in the writing process and limits the speed of the device, since the read-out processes tend to have more stable characteristics. We simulate the operation of the STT-MRAM device, in which the magnetization vector is directed along the plane of the magnetic layer. The geometry of the device, as well as the direction of the electron flux, is shown in Fig. 1.

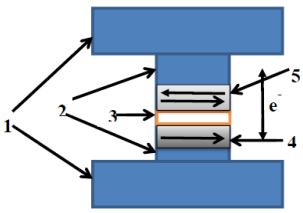

Fig. 1. Spin-valve structure: 1, 2 – contacts of a non-magnetic material, 3 – laye of a non-magnetic metal separating ferromagnets, 4 – ferromagnet with high coercive force (fixed layer), 5 – a ferromagnet with low coercive force (free layer, magnetic soft ferromagnet)

We construct a model of the error that occurs in the process of writing binary data. To do this, one must consider a device with STT-MRAM technology, in which the magnetization vector is directed along the plane of the magnetic layer. The geometry of the device as well as the direction of the electron flux is shown in Fig. 1.

The simulation of magnetization reversal in flat spin-valve structures with two possible stable states of magnetization is carried out on the basis of the LLG equation (macro-spin model) [11], which takes into account the interaction with the spin-polarized current $\vec{T}_{s.t.}$. The expression for the term $\vec{T}_{s.t.}$ in (2) has the following form [5]:

$$\vec{T}_{s.t.} = \left(\frac{I_S}{M_S^2}\right) \cdot \left[\vec{M} \times \left[\vec{M} \times \vec{n}_{ref}\right]\right] \quad (3)$$

The final form of the equation based on the macro-spin model that uses the amplitude value of the spin current, derived from the quantum-mechanical model of the electron flow, can be written as follows:

$$\frac{d\vec{M}}{dt} = -\gamma \cdot \left[\vec{M} \times \vec{H}_{eff}\right] - \\ -\frac{\alpha \cdot \gamma}{M_s} \cdot \left[\vec{M} \times \left[\vec{M} \times \left(\vec{H}_{eff} - \frac{I_s}{\alpha \cdot \gamma \cdot M_s} \cdot \vec{n}_{ref}\right)\right]\right] \quad (4)$$

where I_s is the spin current.

The mathematical model (4) of a single-domain magnet interacting with spin current allows us to establish the existence of two stable states of magnetization and to estimate the probability of transition from one state to another, depending on the value of write current. In the work, the probabilities of such flipping were determined for a wide range of values of write current.

Not taking into account the action of an external magnetic field in addition to the field of a fixed layer (the so-called field of anisotropy), the equation describing the precession of the magnetization vector of the free layer can be written as follows:

$$\frac{d\vec{M}}{dt} = -\gamma \cdot \left[\vec{M} \times \vec{H}_{eff}\right] - \frac{\beta \cdot \gamma}{M_s} \cdot \left[\vec{M} \times \left[\vec{M} \times \vec{n}_{ref}\right]\right] \quad (5)$$

where

$$\beta = \alpha - \frac{I_S}{\left|\vec{H}_{eff}\right| \cdot \gamma \cdot M_S} \quad (6)$$

The equation (5) in the form is a classical equation of LLG. Oppositely, however, the coefficient β can take both positive and negative values.

As can be seen in (6), the coefficient β changes the sign at a certain threshold value of the spin current. Given [5] that the spin current (7) is directly proportional to the usual current, it is possible to find the threshold value of the current below where no magnetization flipping occurs:

$$I_s = \hbar/2e \cdot (I \cdot \eta) = (I \cdot \eta) \cdot 10^{-16}\ J/s^2 \quad (7)$$

where $\hbar$ is the Planck's constant; η is the spin polarization; e is the electron's charge.

The probability of returning the spin-valve to the previous state is determined by the following expression [5]:

$$p(\tau, I) = 1 - \exp\left\{-\frac{\pi^2 \cdot \xi}{4} \cdot \exp\left[-\frac{2\tau}{\tau_0} \cdot \left(\frac{I}{I_c} - 1\right)\right]\right\} \quad (8)$$

where τ is the time of a one-bit recording; I is a current; ξ is the ratio between the energy of thermal fluctuations and the energy barrier for magnetization reversal; τ_0 is the time constant; I_c is a value of the threshold current.

The model of the symmetric binary channel is used to determine the writing speed depending on the probability of error.

The capacity of the binary symmetric channel depends on the bit error and bit generation rate:

$$C = R \cdot \left[1 + p_e \cdot \log_2\left(p_e\right) + \left(1 - p_e\right) \cdot \log_2\left(1 - p_e\right)\right] \quad (9)$$

where C is a speed of recording, p_e is the bit error probability defined by expression (9), R is a bit rate.

Let's assume that the recording speed is the same as the capacity of channel C. What is more, we suppose that the generation rate of the bit stream depends inversely on proportion to the time of one-bit writing.

$$R = 1/\tau \quad (10)$$

where τ is a duration of one pulse.

2. Experiments

Let us consider in detail the physical values τ_0, I_c and ξ, which determine the probability of error of bit writing (9).

The parameter ξ is determined by the relation between the energy of the thermal vibrations which is $k_b \cdot T$ and the energetic barrier of the magnetization reversal in a one-domain approximation:

$$E_b = 1/2 \cdot M_S \cdot H_{eff}\,, \quad (11)$$

which is approximately $60 \cdot k_b \cdot T$ [11, 12].

Then, at room temperature (T = 300 K), the dimensionless multiplier for an exponent in equation (7) is equal to:

$$\frac{\pi^2 \cdot \xi}{4} = \frac{\pi^2}{4} \cdot 60 \approx 148 \quad (12)$$

In the absence of the action of an external magnetic field, the threshold value of the current, at which the conversion process is possible, is determined by the Gilbert damping constant α, the energetic barrier E_b, and the degree of spin polarization η [11]:

$$I_c = \left(2e/\hbar\right) \cdot \left(\alpha/\eta\right) \cdot E_b \quad (13)$$

We consider the value of the degree of current polarization to be 0.5.

Consequently, the value of the critical current is:

$$I_c = \frac{2 \cdot 1.9 \cdot 10^{-19}}{6.62 \cdot 10^{-34}} \cdot \frac{0.1}{0.5} \cdot 2.5 \cdot 10^{-19} \approx 22\mu A \quad (14)$$

Constant τ_0, which has the dimension of time, characterizes the return frequency of the magnetization vector to its previous state and is determined by the following relation [11]:

$$\tau_0 = \left(m_e/\mu_B\right)/\eta \cdot \left(I_s/e\right) \approx 8ns \quad (15)$$

where m_e is the mass of the electron; μ_B is the Bohr magneton, I_s is a spin current.

Then the dependence of the probability of the bit error writing on the current and its duration will be of the following form:

$$p\left(\tau, I\right) = 1 - \exp\left\{-148 \cdot \exp\left[-\frac{\tau}{4} \cdot \left(\frac{I}{22} - 1\right)\right]\right\} \quad (16)$$

Expressions (8) and (16) are basic for mathematical model of the writing digital information process in STT-MRAM. We have investigated the capacity of a channel and bit error probability for current values in the range of 50–200 μA and the time of a single bit writing in the range of 1–70 ns. It should be noted that the read current is 1–5 μA, which is due to another physical mechanism for reading based on the dependence of the logic gate resistance on the direction of current flow.

3. Results

The research was carried out for low (50–90 μA), medium (100–500 μA) and high values of write currents (500–1500 μA).

At low current values, the value of recording speed is 80 Mbps, and the optimum duration value of a one-bit writing varies from 25 ns (for a write current of 50 μA) to 13 ns (for a write current of 90 μA). For average currents, the maximum recording speed was 500 Mbps, and the optimal duration of a one bit ranged from 9 ns (for 100 μA) to 1.8 ns (for 500 μA). The high value of write currents makes it possible to achieve write speeds up to 1 Tbit/s, for currents of 1000 μA with the duration of a one bit of 1.1 ns. For a current of 600 μA, the speed is almost twice as low – 600 Mbps.

Table 1 summarizes the result of the one-bit duration simulation, the recording speed and the one-bit error probability at different current values requirements, and the bit error level and the recording speed.

The investigated range of current values was 50–1500 μA, covering various areas of possible application of the model, what are the devices of industrial production, design developments and experimental researches.

Table 1. Optimal values of simulated parameters

Modes	Write current, μA	The requirement for the highest recording speed			The requirement for equality of bit error probability to 10^{-4}		The requirement for the lowest error probability		
		Duration of a single bit writing, ns	The recording speed, Tb/s	The bit error probability	Duration of a single bit writing, ns	The recording speed, Tb/s	Duration of a single bit writing, ns	The bit error probability	The recording speed, Tb/s
Low current (industrial devices)	50	27.8–29.4	0.0307	0.0211–0.0127	37.6	0.0263	65	$1.5 \cdot 10^{-7}$	0.0154
	60	20.6–21.4	0.0417	0.0201–0.0143	32.8–33	0.0304	65	$9.6 \cdot 10^{-11}$	0.0154
	70	16.4–16.8	0.0527	0.0191–0.0154	26–26.2	0.0384–0.0381	65	$5.9 \cdot 10^{-14}$	0.0154
	80	13.8	0.0637	0.0165	21.4	0.0467	63	$1.1 \cdot 10^{-16}$	0.0157–0.016
	90	11.8	0.0747	0.0161	18.2–18.4	0.0549	53.6–54.8	$1.1 \cdot 10^{-16}$	0.0184–0.0187
Average current (research work with expected implementation)	100	10.2–10.4	0.0856	0.0146–0.0174	16	0.0624	46.6–47.6	$1.1 \cdot 10^{-16}$	0.0209–0.0224
	200	4.4–4.6	0.1951	0.0134–0.02	7	0.1426	20.6–20.8	$1.1 \cdot 10^{-16}$	0.0481–0.0485
	300	2.8	0.3045	0.0211	4.4	0.2268	13.3	$1.1 \cdot 10^{-16}$	0.0746–0.0758
	400	2	0.4101	0.0271	3.2	0.3118	9.8	$1.1 \cdot 10^{-16}$	0.1
	500	1.6	0.521	0.0246	2.6	0.384	7.8	$1.1 \cdot 10^{-16}$	0.1282
High current (experimental and scientific research)	600	1.4	0.6344	0.0149	2.2	0.454	6.4	$1.1 \cdot 10^{-16}$	0.1562
	800	1.1	0.8519	0.0212	1.6	0.624	4.6	$3.3 \cdot 10^{-16}$	0.2174
	1000	1.1	0.9774	0.0022	1.1	0.8307	3.8	$1.1 \cdot 10^{-16}$	0.2632
	1200	1.1	0.9969	$2.3 \cdot 10^{-4}$	1.1	0.9969	3	$5.6 \cdot 10^{-16}$	0.3333
	1400	1.1	0.9996	$2.3 \cdot 10^{-5}$	–	–	2.6	$3.3 \cdot 10^{-16}$	0.3846

4. Conclusions

The important problem of modeling the information recording speed based on the model of error of magnetization flipping in STT-MRAM devices is solved.

The scientific novelty of obtained results is a combination of the probability model of error in the process of magnetization reversal, based on the fundamental theory, and the binary channel model. Based on the model, the recording speed of information in STT-MRAM devices was studied in a wide range of write current values.

The practical significance of the model developed is that it enables a prediction of the probability of error of a single bit writing depending on the value of write current and its duration. the model also allows to determine the value of the write current and its duration at the permissible values of the probability of single bit writing.

A prospect for further research is an improvement of the bit error model, taking into account the asymmetry of the binary transmission channel.

References

[1] Alioto M.: STT-MRAM memories for IoT applications. Challenges and opportunities at circuit level and above International Symposium on VLSI Technology, Systems and Application VLSI-TS, Hsinchu, 2017, [http://doi.org/10.1109/VLSI-TSA.2017.7942448].

[2] Apalkov D., Dieny B., Slaughter J.: Magnetoresistive Random Access memory. Proc. of the IEEE 109/2017, 1796–1830, [http://doi.org/10.1109/JPROC.2016.2590142].

[3] Bhatti S. et al.: Spintronic based random access memory: a review. Materials Today 6(9)/2017, 530–548, [http://doi.org/10.1016/j.mattod.2017.07.007].

[4] Cai K., Immink K. A. S.: Cascaded channel modeling, analysis, and hybrid decoding for spin-torque transfer magnetic random access memory. IEEE Transactions on Magnetics 53(11)/2017, 1–11, [http://doi.org/10.1109/TMAG.2017.2711245].

[5] Cai H.: High performance MRAM with spin-transfer-torque and voltage-controlled magnetic anisotropy effects. Applied Sciences 7(9)/2017, 929–943, [http://doi.org/10.3390/app7090929].

[6] Chung S. et al.: 4Gbit Density STT-MRAM using Perpendicular MTJ Realized with Compact Cell Structure IEEE International Electron Devices Meeting IEDM, San Francisco 2016, [http://doi.org/10.1109/IEDM.2016.7838490].

[7] Greenan K., Miller E.: Reliability mechanisms for file systems using non-volatile memory as a metadata store. International conference on Embedded software EMSOFT, Seoul 2006, [http://doi.org/10.1145/1176887.1176913].

[8] Lai H. et al.: STT-MRAM application on IoT data privacy protection system. IEEE International Conference on Consumer Electronics ICCE-TW, Taichung 2018, [http://doi.org/10.1109/ICCE-China.2018.8448476].

[9] Lee K.: Bit error rate engineering for spin-transfer-torque MRAM. International Integrated Reliability Workshop. International IEEE Conference, South Lake Tahoe 2014, [http://doi.org/10.1109/IIRW.2014.7049540].

[10] Lee Y. et al.: Embedded STT-MRAM in28-nm FDSOI Logic Process for Industrial MCU/IoT Application. IEEE Symposium on VLSI Technology, Honolulu 2018, [http://doi.org/10.1109/VLSIT.2018.8510623].

[11] Sun J.Z., Xu, Y.: Handbook of Spintronics. Springer, Chicago 2016.

[12] Sverdlov V., Makarov A.,Selberherr S.: Switching current reduction in advanced spin-orbit torque MRAM. Joint International EUROSOI Workshop and International Conference on Ultimate Integration on Silicon EUROSOL-ULIS, 2018, [http://doi.org/10.1109/ULIS.2018.8354759].

[13] Vatajelu E. et al.: STT MRAM-Based PUF's. Design, Automation & Test in Europe Conference & Exhibition DATE, Grenoble 2015, [http://doi.org/10.7873/DATE.2015.0505].

[14] Wang P. et al.: Development of STT-MRAM for embedded memory applications. IEEE International Magnetic Conference INTERMAG, Dublin 2017, [http://doi.org/10.1109/INTMAG.2017.8007930].

[15] Yamauchi T.: Prospect of embedded non-volatile memory in the smart society. VLSI Technology, System and Application: International Symposium, Hsinchu 2015, [http://doi.org/10.1109/VLSI-TSA.2015.7117541].

D.Sc. Ruslan Politanskyi
e-mail: polrusl@i.ua

He received M.S. degrees in applied mathematics and physics/qualification of an engineer-physicist from Moscow Institute Physics and Technologies, Russia, in 1994. He received a Ph.D. in solid state physics at Yuriy Fedkovych Chernivtsi National University. He received a Dr Science in telecommunication at the Institute of Telecommunications, of Lviv Polytechnic National University. His research interests include signal processing, coding theory, pseudorandom sequence systems with chaotic dynamics (differential equations and circuits, including his own invention), modelling of STT-MRAM and thin films for anti-reflecting coatings, artificial intelligence in cognitive radio et cetera.

http://orcid.org/0000-0003-0015-7123

D.Sc. Maria Vistak
e-mail: vistak_maria@ukr.net

Maria Vistak is an Associate Professor in Biophysics Department of Danylo Halytsky Lviv National Medical University. She is a Physics graduate of Lviv National University, Ukraine, in 1977. She received her Ph.D. Degree in Physics of Liquid Crystals in 1986. Since 1987, she works as an Assistant Professor and Associate Professor in Biophysics Department of Danylo Halytsky Lviv National Medical University. Since 2017 she is a Professor in the Biophysics Department of Danylo Halytsky Lviv National Medical University. She has published over 150 journal and conference papers. Her scientific interest is focused on modification of liquid crystal electronic structures to control physical quantities.

http://orcid.org/0000-0001-5192-4017

Ph.D. Andriy Veryga
e-mail: veriga@ukr.net

He received B.S. and M.S. degrees in Radio Engineering at Yuriy Fedkovych Chernivtsi National University, Ukraine. He received a Ph.D. in Radio Engineering at Yuriy Fedkovych Chernivtsi National University. He is currently an assistant of the Radio Engineering Department at Yuriy Fedkovych Chernivtsi National University. His research interests include signal processing, development of electronic circuits.

http://orcid.org/0000-0002-2616-3057

Student Tetyana Ruda
e-mail: tetianaruda1998@gmail.com

She is a student at Yuriy Fedkovych Chernivtsi National University. She is currently a student in the Radio Engineering and Information Security Department. Her interests include coding theory, computer discrete mathematics and C++ programming. She is also keen on studying English language, she has a diploma certifying her upper intermediate level of English (B2).

http://orcid.org/0000-0002-0008-9362

otrzymano/received:15.11.2019 *przyjęto do druku/accepted: 15.02.2020*

http://doi.org/10.35784/iapgos.1513

HARDWARE AND SOFTWARE MEANS FOR ELECTRONIC COMPONENTS AND SENSORS RESEARCH

Gryhoriy Barylo[1], Oksana Boyko[2], Ihor Gelzynskyy[1], Roman Holyaka[2,3], Zenon Hotra[1], Tetyana Marusenkova[4], Mykola Khilchuk[3], Magdalena Michalska[5]

[1]Lviv Polytechnic National University, Department of Electronics Devices, Lviv, Ukraine, [2]Danylo Halytsky Lviv National Medical University, Department of Medical Informatics, Lviv, Ukraine, [3]Lviv Polytechnic National University, Department of Electronics and Information Technology, Lviv, Ukraine, [4]Lviv Polytechnic National University, Department of Software, Lviv, Ukraine, [5]Lublin University of Technology, Department of Electronics and Information Technology, Lublin, Poland

Abstract. *The main results of RETwix development are presented in the paper. RETwix is an universal hardware and software means for laboratory research, which can be used for investigation both electronic components and arbitrary electrical, thermal, chemical or biochemical processes. Sensors, actuators and signal transducers of the Analog Front-End are used for this purpose. The RETwix means includes two CV-LAB devices (Capacitance & Voltage LABoratory) and UA-LAB (Universal Analog LABoratory). The peculiarities of construction and examples of RETwix using are described.*

Keywords: embedded system, electronic components, sensor, laboratory research

SPRZĘT I OPROGRAMOWANIE DO BADAŃ ELEMENTÓW ELEKTRONICZNYCH I CZUJNIKÓW

Streszczenie. *Główne wyniki opracowania RETwix zostały przedstawione w artykule. RETwix jest uniwersalnym sprzętem i oprogramowaniem do badań laboratoryjnych, które można wykorzystać do badania zarówno komponentów elektronicznych, jak i dowolnych procesów elektrycznych, termicznych, chemicznych lub biochemicznych. W tym celu zostały wykorzystane czujniki, aktuatory i przetworniki sygnału Analog Front-End. RETwix zawiera dwa urządzenia CV-LAB (Capacitance & Voltage LABoratory) oraz UA-LAB (Universal Analog LABoratory). Zostały opisane osobliwości budowy oraz przykłady zastosowania RETwix.*

Słowa kluczowe: system wbudowany, elementy elektroniczne, czujnik, badania laboratoryjne

Introduction

Electronic information technology is currently one of the most dominant engines of modern society technological development. In addition to the traditionally electronic fields of technology – radio, telecommunications, information-measuring and computing, electronics and devices based on them have become important tools for the development of industry, biology, medicine, ecology, entertainment, etc [7–9]. The implementation of modern electronic devices in these industries is based on the concept of Embedded system [11]. Sensors, actuators, and signal transducers, called Analog Front-End (AFE), are the basis for the interaction of electronics with the physical world [10]. The relevance of the development and usage of Analog Front-End is due to the modern concept of the Internet of Things (IoT) [12]. Examples of IoT AFE are the Capacitive MEMS Accelerometer Analog Front-End for Ultra-Low-Power IoT Applications [1], Low-Power Low-Noise Inductorless Front-End for IoT Applications [19], Analog-to-Digital Acquisition Channel for an IoT Water Management Sensor Node [17].

The implementation of modern information technologies, including IoT, into various fields of science and technology requires intensification and further increase of education levels. The basis of education and science at all levels is experimental research. Modern publications on the development and implementation of hardware and software systems in training laboratories (Labs instrumentation for education) are connected with: e-Learning program [18], virtual hands-on Lab platform for computer science education [5], improving online higher education with virtual and remote Labs [15], virtual labs in engineering education [6], integrating remote labs in dotLRN [16], Internet of Things (IoT) remote labs for students education [13].

In accordance with the aforementioned problem, this paper presents the main results of the development of the RETwix – universal hardware and software tools for laboratory research, which solve the problems of educational and scientific laboratories of the broadest profile.

1. General characteristics of the RETwix

The elaborated RETwix includes two devices (Fig. 1) CV-LAB (Capacitance & Voltage LABoratory) and UA-LAB (Universal Analog LABoratory). The versatility of RETwix is that electronics components can be objects of research, as well as arbitrary electrical, thermal, chemical or biochemical processes. Measurements of the aforementioned processes are carried out with the help of the primary transducers or sensors – converters of the energy of investigated processes into an electrical signal. The shape and power of the primary transducer signal is, mainly, not optimal for the measurement process. Therefore, majority of the measuring devices use secondary (signal) transducers that amplify and normalize the signal. Considering the increasing demands on modern equipment, the importance of secondary transducers has increased significantly in the recent period. In some tasks, appropriate excitation is applied to obtain certain information about the investigated environment (process). Such excitations are formed by actuators.

Fig. 1. RETwix Devices

The RETwix provides the ability to perform laboratory tests in static and dynamic modes. In static mode, the measurement result is the monitoring of a certain value or DC (Direct Current) characteristics. For dynamic studies, a certain process is activated and the time dependencies of the parameters of this process are measured. Examples of dynamic objects of investigation are: charge and discharge of the capacitor; charge and discharge of chemical power sources; thermal relaxation; generation of charges in piezoelectric elements; chemical (biochemical) exo- and endothermic reactions.

The object of the investigation may be the RETwix itself. In the fields of measurement engineering, metrology and computer engineering, the investigation of the functionality and parameters of the complex allows to study the basics of information-measuring systems, digital-to-analog and digital-to-digital conversion, theory of measurement errors and more.

2. Signal transducers of capacitive sensors

The vast majority of signal transducers of modern capacitive sensors are based on two basic methods of measuring conversion. The first method is for SCM (Self Capacitance Measure) sensors, in which the capacitance C_X between the active sensor electrode and the interaction object that forms the passive electrode is an informative signal. In particular, it can be a person's finger or any other object with significant own capacity. It is obvious that in the process of measuring conversion, the change of potential or the measurement of current through a passive electrode is not possible. In terms of signal measurement, electrical interaction occurs only with the active electrode, and the passive electrode potential is considered quasi-constant or zero. The second method is for sensors of the MCM (Mutual Capacitance Measure) type, in which the informative signal of the measuring conversion is the mutual capacity between two active electrodes – transmitter (T_x – Transmit electrode) and receiver (R_x – Receive electrode). In such sensors, a voltage pulse is formed on the transmit electrode, which causes the charge of the measuring capacitor C_X to be induced, and the accumulated charge enters the measuring circuit through the receive electrode.

In modern capacitance sensors with microprocessor control, both conversion methods are implemented by two-stage switching of the measuring capacitor C_X. Consider the basic principles for implementing the circuit that perform the above-mention concepts, and the results of their model analysis.

Typically, sensors of the SCM type in the first phase charge the measuring capacitor C_X, and in the second – transfer this charge into the measuring circuit. Only the active electrode is used in both phases. The elementary signal circuit of such measurement is shown in Fig. 2a. In the first phase (Ph_1), the measuring capacitor C_X of the primary transducer is charged from the voltage source VS, and in the second (Ph_2), the charge obtained by the measuring capacitor $Q_X = C_X V_S$ is transmitted to the integrating capacitor C_{INT}. The voltage on this capacitor is the information signal of the transducer $V_{OUT} = V_{CINT}$. The charge of the C_X capacitor is carried out by the switch S_1, and the switch S_2 is used to transfer of the accumulated charge into the circuit of the integrating capacitor C_{INT}.

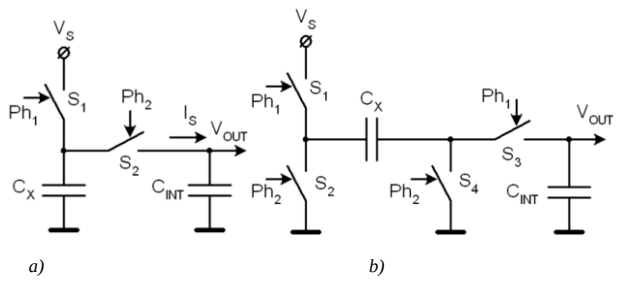

Fig. 2. The elementary signal circuit for capacitance measurement of SCM (a) and MCM (b) types

The elementary signal circuit that implements the principle of measuring conversion of MCM sensors is shown in Fig. 2b. The measurement conversion cycle contains the phase charge of the circuit of the sequentially connected measuring C_X and the integrating capacitor C_{INT} and the discharge phase of the measuring capacitor, during which the charge of the integrating capacitor remains unchanged. During the charge phase, the transmit electrode of the capacitor C_X is connected (switch S_1) to the positive voltage of the power source V_S, and the receive electrode to the integrating capacitor C_{INT} (switch S_3). Instead, in the discharge phase, the transmit and receive electrodes of the C_X capacitor are connected to negative (zero) voltage (switches S_2, S_3) and the C_{INT} capacitor remains open.

In the vast majority of laboratory research tasks the capacitive sensors are used. Their informative quantity is the reciprocal capacitance between two active electrodes. Therefore, consider only the circuit of measuring transducer of sensors MCM type. The scheme of such transducer (Fig. 3) corresponds to the above-mentioned in Fig. 2b elementary signal circuit. The measuring transducer circuit contains an X_{OA} operational amplifier, the switches S_1, S_2, S_3, S_4 and the control signals sources VP_{11}, VP_{12}, VP_{21}, VP_{21} that control these switches.

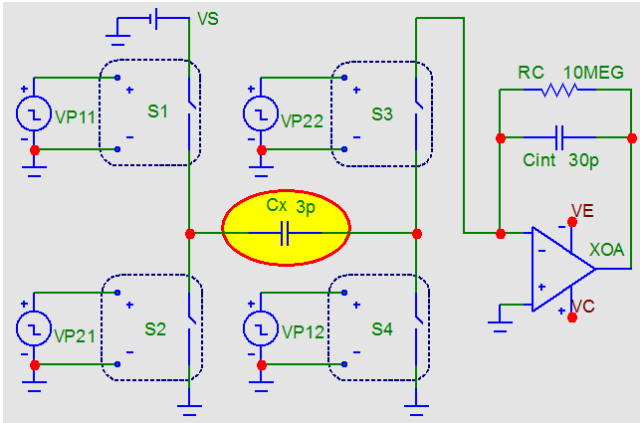

Fig. 3. Circuit of measuring transducer of MCM type

An integrated capacitor C_{INT} is connected into the negative feedback loop of the amplifier. Unlike the elementary circuit, such connection of the capacitor C_{INT} ensures high linearity of the transfer function. In parallel with the C_{INT}, a shunt resistor RC is switched on, which stabilizes the DC feedback circuit. In the first phase Ph1 of measurement transformation: VP_{11} = HIGH, VP_{12} = HIGH, VP_{21} = LOW, VP_{21} = LOW, where Low and HIGH are logical levels. At the logical level LOW switches are open (OFF) and at level High – closed (ON). Instead, in the second phase of Ph_2: VP_{11} = LOW, VP_{12} = LOW, VP_{21} = HIGH, VP_{21} = HIGH.

The result of a model study of the measurement transducer circuit in a Micro-Cap environment using SPICE models is shown in Fig. 4. Control signals, the voltages V [Ph_1] and V [Ph_2], are represented on the upper plot, and the output voltage V_{OUT} – on the lower plot.

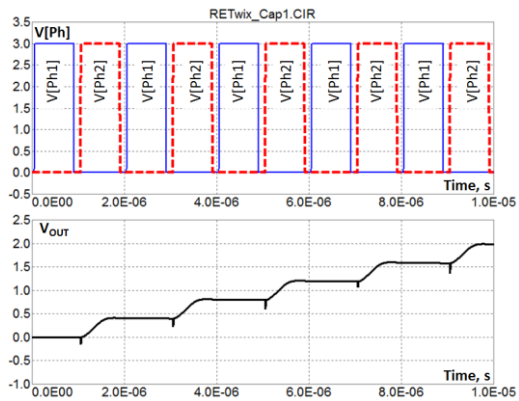

Fig. 4. Control signals V [Ph] and output voltage VOUT of the measuring transducer

The output voltage is formed over several switching cycles (typically from 10 to 100), depending on the required speed and accuracy of the measurement conversion. Moreover, the higher speed, the lower accuracy, and vice versa. The diagrams depict 5 measurement conversion cycles.

It can be seen that in each of these cycles, there are three processes – voltage rise, voltage is kept at the constant level and spurious transitions. These spurious transitions are caused by transfer processes of switching and they are the subject for further optimization of the switching modes and output signal filtering.

The informative value of the measured capacitance is the increase in output voltage V_{OUT}, which is equal to approximately 0.4 V in each cycle.

3. CV-LAB device

The CV-LAB (Capacitance & Voltage LABoratory) device (Fig. 5) is designed to implement a wide range of capacitive sensors and created on their base integrated sensors of physical quantities.

Fig. 5. CV-LAB device

The CV-LAB includes (Fig. 6):

- MCM& MUX module – measuring transducer of MCM type sensors (Fig. 2) and analog multiplexer;
- AD7747 – module on high-precision ΣΔ24-Bit Capacitance-to-Digital Converter and Voltage-to-Digital Converter;
- ATMEGA329P – microcontroller (the use of other microcontrollers or systems on crystal, including ESP32 with integrated Wi-Fi and Bluetooth radio standards is possible);
- Cross unit – digital line switching module, which, in particular, provides serial I2C / SPI communication interfaces to external modules – ADXRS453 (Digital Output Gyroscope), ADIS16334 (6 Degrees of Freedom Inertial Sensor), GY-80 (10 Degree of Freedom IMU board), etc.

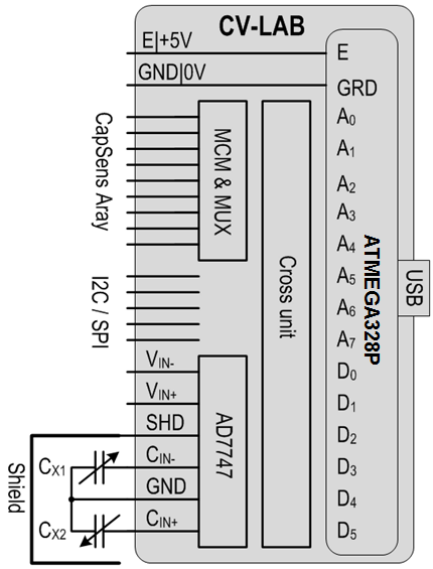

Fig. 6. CV-LAB scheme

The use of two modules for capacitance measurement is due to the specific of the tasks of wide profile capacitive sensors constructing. The part of the capacitive sensors, such as matrix touch panels or vibration sensors, require high speed conversion and multichannel. These parameters are provided by the MCM & MUX module with a rate of at least 3000 measurements per second. Instead, other capacitive sensors, such as biochemical or deformation sensors, require high resolution and accuracy of measurement transformations. These parameters are provided by a module based on the AD7747 Separator Converter, an electrical capacity measurement resolution is 10^{-16} F (the speed does not exceed 10 measurements per second).

In addition to the high-precision 24-bit capacity difference measurement (outputs – CIN1 (+), CIN1 (-)), the converter provides also other important functions. Firstly, it is the active shielding of the input circuits (output – SHLD), which is extremely important during the measurement of very small capacitance changes. Such shielding is performed by auxiliary electrodes or shielding surfaces on which excitation pulses are formed. The amplitude of such impulses is adapted to the specific conditions of the investigated object. Secondly, the converter allows to synthesize auxiliary capacities, which, being included in the measurement circuit, allow to compensate the parasite capacities of this circuit. Such synthesis is performed by CAP DAC1, CAP DAC2 converters of "digital code – capacity" type. And thirdly, the converter allows to measure the difference of voltages at auxiliary leads VIN (+), VIN (-) with 24-bit resolution.

4. UA-LAB device

The UA-LAB (Universal Analog LABoratory) device (Fig. 7) is designed for laboratory researches with a wide range of functionalities. The UA-LAB hardware consists of digital module and analog front-end. The digital module implements the UA-LAB program management code, provides USB interface, analog-to-digital conversion, pulse-width modulation and some other features. Analog front-end units perform the functions of digital-to-analog conversion, amplification, and current-to-voltage conversion. The simplified functional diagram of UA-LAB is shown in Fig. 8. The following leads of the microcontroller are used: E and GND – supply voltage and ground, respectively; A_0, …, A_7 – analog inputs of eight-channel ADC; D_0, …, D_5 – digital outputs.

Fig. 7. UA-LAB device

Analog front-end units are implemented on OA_1, OA_2 AD8544 (CMOS Rail-to-Rail General-Purpose Amplifiers) operational amplifiers and R_{A1}, R_{A2} negative feedback resistors. The leads VIN1 +, VIN1-, VIN2 +, VIN2- are used to form the input circuits of the analog front-end. The output voltages of the V_{AMP1}, V_{AMP2} amplifiers are applied to the inputs A_6, A_7 ADC and form circuits $A_6|V_{AMP1}$ and $A_7|V_{AMP2}$, respectively.

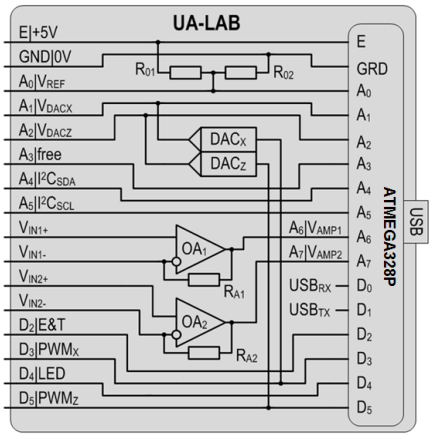

Fig. 8. UA-LAB scheme

The DAC_X and DAC_Z units provide the formation of two program-controlled analog voltages V_{DACX} and V_{DACZ}. The function of digital-to-analog conversion is implemented by the method of pulse-width modulation, followed by averaging using second order active filters. For simplification of the UA-LAB

scheme, the components of these filters, in particular operational amplifiers and corresponding RC circuits, are not given in Fig. 8. PWM_X and PWM_Z pulse width modulation control signals are generated at D_3 and D_5 digital outputs – D_3 | PWM_X and D_5| PWM_Z circuits, respectively. Measurements of the formed voltages V_{DACX} and V_{DACZ} are carried out using the inputs A_1 and A_2 ADC – A_1 | V_{DACX} and A_2 | V_{DACZ} circuits, respectively. A_3 ADC input is not connected with other circuits – A_3 | free. The A_4 and A_5 ADC inputs, can be used for voltage measurement and implementation the I^2C interface (SDA and SCL buses) with external modules – $A_4|I^2C_{SDA}$ and $A_5|I_2C_{SCL}$.

The D_0 and D_1 digital outputs are used to implement signal circuits USB interface USB_{RX}, USB_{TX}. The digital output D_2 – circuit D_2 | E&T – is used to form the polarity of the voltages (E or 0) of the circuits under consideration when measuring current-voltage characteristics or time parameters of transition processes. As it was noted, digital outputs D_3 and D_5 optionally can be used for tasks requiring pulse-width modulation – $D_3|PWM_X$ and $D_5|$ PWM_Z circuit. The D4 digital output optionally can be used to control the light-emitting diode – D_4 | LED circuit.

5. Approbation

The approbation of the RETwix has been carried out in numerous laboratory research of microelectronic sensors based on resistive, capacitive, inductive, diode and transistor structures. The following modes are used in these tasks:

- formation of output voltages and their changes in accordance with the given algorithm of research;
- single measurement of one or more input voltages;
- measurements of the input voltage arrays in accordance with the output voltage change;
- multiple measurements of input voltages with activation of a certain process and selected delay between measurements.

There are three basic algorithms for informative signals generating:

- periodic eight-channel measurement for monitoring the investigated parameters;
- scanning eight-channel measurement, which determines the dependences of the studied parameters on the change (modulation) of the activating voltages;
- two-channel oscilloscope measurement with formation of arrays of the investigated parameters with fixed time parameters.

According to the basic parameters of the primary transducer the structures of capacitive sensors can be divided by the change of:

- the area of the inter-electrode overlap;
- the distance between electrodes;
- the parameters of the inter-electrode dielectric;
- the impact of environmental objects.

On the basis of these structures sensors of spatial displacement; pressure sensors and matrices; accelerometers; tactile matrices; humidity sensors; devices for chemical and biological research; electrode scanners; ultrasonic tomographs; condenser microphones; fingerprint scanners; non-contact control devices are realized.

An example of capacitance measuring by a sensor that demonstrates the ability to achieve resolution 10^{-16} F is shown in Fig. 9. In this example, a CV-LAB module based on a high-precision ΣΔ 24-Bit converter AD7747 is used. In accordance with current trends in the development of sensor electronics, the use of RETwix has significant relevance in the concept of Data fusion and Sensor fusion[14]. In this concept, we have implemented integrated devices for combining thermal measurement methods with capacitive [2], magnetic [4] and optical [3] sensors. Such integrated devices are the basis of IoT sensors for chemical and biological analysis in the concept of Lab-on-Chip.

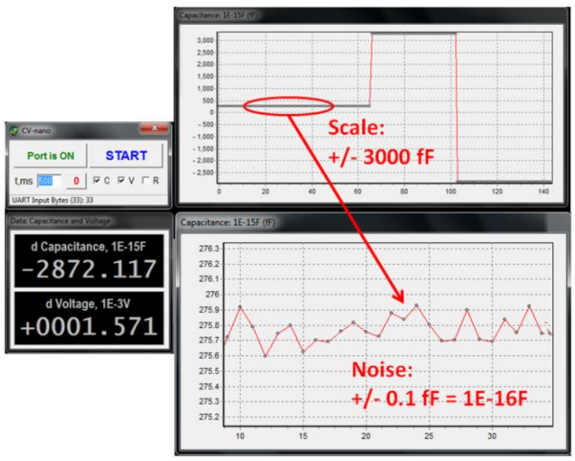

Fig. 9. Example of capacitance measuring by a sensor based on AD774 converter

Analog front-end configuration and measurement results of the UA-LAB are presented in the following examples:

- Fig. 10 – measurement of current-voltage characteristics of the transistor structure T_X;
- Fig. 11 – implementation of sensors based on primary transdusers of the bridge type R_B;
- Fig. 12 – implementation of sensors based on differential optocouples LED – D_{PH1}, D_{PH1};
- Fig. 13 – implementation of an integrated device based on the coil L of magnetic field forming and Hall sensor HG for its measurement;
- Fig. 14 – the result of the scanning measurement of the current-voltage characteristics of the transistor structure;
- Fig. 15 is the result of a two-channel oscilloscope measurement of transients in an RC circle.

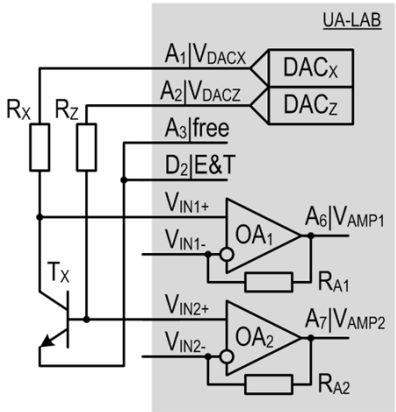

Fig. 10. Analog front-end of the transistor structure

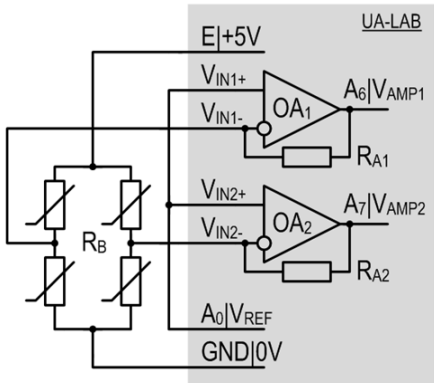

Fig. 11. Analog front-end of the bridge type sensor

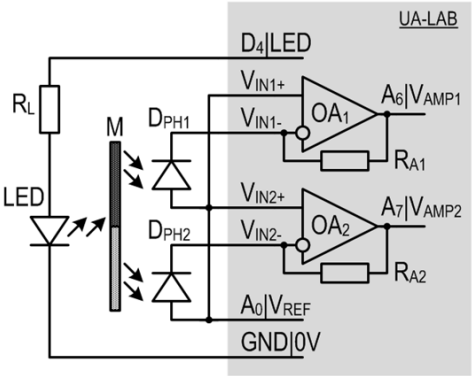

Fig. 12. Analog front-end of the differential optocoupler

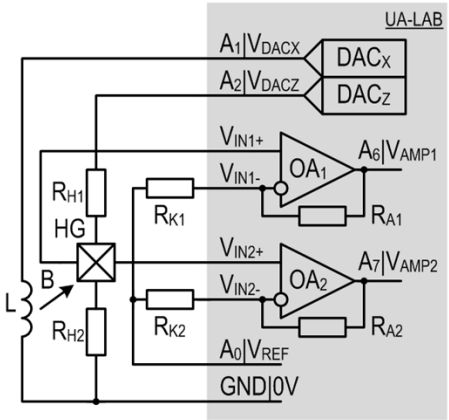

Fig. 13. Analog front-end of magnetic field formation and measurement

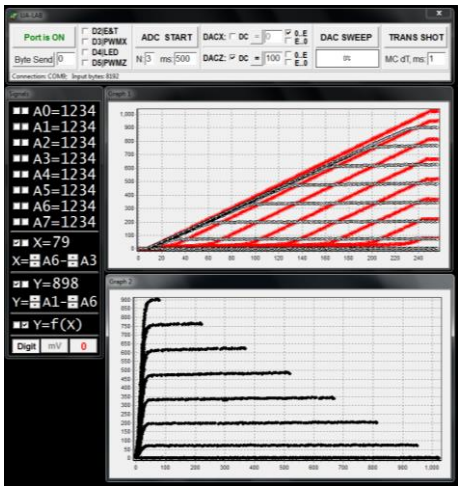

Fig. 14. The result of the scanning measurement of the current-voltage characteristics of the transistor structure

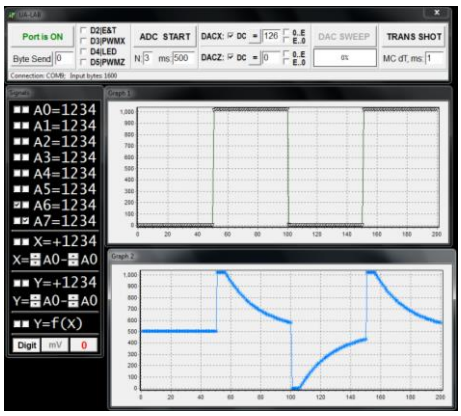

Fig. 15. The result of two-channel oscilloscope measurement of transition processes in the RC circuit

In accordance with current trends in the development of sensor electronics, the use of RETwix has significant relevance in the concept of Data fusion and Sensor fusion [13]. In this concept, we have implemented integrated devices for combining thermal measurement methods with capacitive [14], magnetic [15] and optical [16] sensors. Such integrated devices are the basis of IoT sensors for chemical and biological analysis in the concept of Lab-on-Chip

6. Conclusions

The main results of development and examples of using the RETwix hardware and software for laboratory research are presented. RETwix includes two devices – CV-LAB (Capacitance & Voltage LABoratory) and UA-LAB (Universal Analog LABoratory).

The principles of measuring conversion in capacitive sensors of two types SCM – Self Capacitance Measure and MCM – Mutual Capacitance Measure are analyzed. An informative signal for the conversion of SCM type sensors is the capacitance C_X between the active electrode of the sensor and the object which is the passive electrode. In particular, it can be a person's finger or any third-party object with significant own capacity. An informative signal for the conversion of MCM type sensors is the mutual capacity between two active electrodes, a transmitter (Tx – Transmit electrode) and a receiver (Rx – Receive electrode). In such sensors, a voltage pulse is formed on the transmit electrode, which causes the charge of the measuring capacitor CX, and the accumulated charge comes to the measuring circuit through the receive electrode.

The main modules of the CV-LAB are the MCM (MCM & MUX) type measuring transducer and the high-precision ΣΔ 24-Bit Capacitance-to-Digital and Voltage-to-Digital Converter AD7747. The UA-LAB includes digital and analog modules. The digital module implements the control code, provides USB interface, analog-to-digital conversion, pulse-width modulation, etc.

In accordance with current trends in the development of sensor electronics, the use of RETwix has significant relevance in the concept of data fusion and sensor fusion (Sensor fusion). In this concept, we have implemented integrated devices for combining thermal measurement methods with capacitive, magnetic and optical sensors

References

[1] Akita I., Okazawa T., Kurui Y., Fujimoto A., Asano T.: A Feedforward Noise Reduction Technique in Capacitive MEMS Accelerometer Analog Front-End for Ultra-Low-Power IoT Applications. IEEE Journal of Solid-State Circuits 2019, 1–11, [http://doi.org/10.1109/JSSC.2019.2952837].

[2] Boyko O., Barylo G., Holyaka R., Hotra Z., Ilkanych K.: Development of signal converter of thermal sensors based on combination of thermal and capacity research methods. Eastern-European Journal of Enterprise Technologies, 4/9(94)/2018, 36–42, [http://doi.org/10.15587/1729-4061.2018.139763].

[3] Boyko O., Holyaka R. Hotra Z., Fechan A., Ivanyuk H., Chaban O., Zyska T., Shedreyeva I.: Functionally integrated sensors of thermal quantities based on optocoupler. Proc. of SPIE 10808/2018, 1080812, [http://doi.org/10.1117/12.2501632].

[4] Boyko O., Holyaka R., Hotra Z.: Functionally integrated sensors on magnetic and thermal methods combination basis. Proc. IEEE 14th Int. Conf. on Advanced Trends in Radioelectronics, Telecommunications and Computer Engineering (TCSET'2018), 2018, 697–701.

[5] Deng Y., Lu D., Chung C. J., Huang D., Zeng Z.: Personalized Learning in a Virtual Hands-on Lab Platform for Computer Science Education. Proc. IEEE Frontiers in Education Conference (FIE), 2018, 1–8, [http://doi.org/10.1109/FIE.2018.8659291].

[6] Diwakar A., Poojary S., Noronha S. B.: Virtual labs in engineering education: Implementation using free and open source resources. Proc. IEEE International Conference on Technology Enhanced Education (ICTEE), 2012, 1–4, [http://doi.org/10.1109/ICTEE.2012.6208670].

[7] Hotra O.: Microprocessor temperature meter for dentistry investigation. Przegląd Elektrotechniczny 86/2010, 63–65.

[8] Hotra O., Boyko O., Zyska T.: Improvement of the operation rate of medical temperature measuring devices. Proc. of SPIE 9291/2014, 92910A, [http://doi.org/10.1117/12.2070167].

[9] Hotra O., Boyko O.: Compensation bridge circuit with temperature-dependent voltage divider. Przegląd Electrotechniczny 88(4A)/2012, 169–171.

[10] Hu H., Islam T., Kostyukova A., Ha S., Gupta S.: From Battery Enabled to Natural Harvesting: Enzymatic BioFuel Cell Assisted Integrated Analog Front-End in 130 nm CMOS for Long-Term Monitoring. IEEE Transactions on Circuits and Systems I: Regular Papers 66(2)/2019, 534–545, [http://doi.org/10.1109/TCSI.2018.2869343].
[11] Huang J., Li R., An J., Ntalasha D., Yang F., Li K.: Energy-Efficient Resource Utilization for Heterogeneous Embedded Computing Systems. IEEE Transactions on Computers 66(9)/2017, 1518–1531, [http://doi.org/10.1109/TC.2017. 2693186].
[12] Jo D., Kim G. J.: ARIoT: scalable augmented reality framework for interacting with Internet of Things appliances everywhere. IEEE Transactions on Consumer Electronics 62(3)/2016, 334–340, [http://doi.org/10.1109/TCE.2016.7613201].
[13] Leisenberg M., Stepponat M.: Internet of Things Remote Labs: Experiences with Data Analysis Experiments for Students Education. Proc. IEEE Global Engineering Education Conference – EDUCON 2019, 22–27, [http://doi.org/10.1109/EDUCON.2019.8725070].
[14] Moore S. I., Omidbeike M., Fleming A., Yong Y. K.: Capacitive Instrumentation and Sensor Fusion for High-Bandwidth Nanopositioning. IEEE Sensors Letters 3(8)/2019, 2475–1472.
[15] Perales M., Pedraza L., Moreno-Ger P.: Work-In-Progress: Improving Online Higher Education with Virtual and Remote Labs. Proc. IEEE Global Engineering Education Conference – EDUCON 2019, 1136–1139.
[16] Pesquera A., Morales R., Pastor R., Ros S., Hernandez R., Sancristobal E., Castro M.: DotLAB: Integrating remote labs in dotLRN. Proc. IEEE Global Engineering Education Conference – EDUCON 2011, 111–117, [http://doi.org/10.1109/EDUCON.2011.5773123].
[17] Serra H., Bastos I., de Melo J. L., Oliveira J. P., Paulino, N., Nefzaoui E., Bourouina T.: A 0.9-V Analog-to-Digital Acquisition Channel for an IoT Water Management Sensor Node. IEEE Transactions on Circuits and Systems II: Express Briefs 66(10)/2019, 1678–1682, [http://doi.org/10.1109/TCSII.2019.2933276].
[18] Shambhavi B. R., Babu K. M., Vijaykumar A.: Enhanced e-Learning with Quality Enhancement in Engineering Education (QEEE) Program. Proc. 5th IEEE International Conference on MOOCs, Innovation and Technology in Education (MITE) 2017, 67–71, [http://doi.org/10.1109/MITE.2017.00018].
[19] Yang Y. C., Yang J.: Low-power low-noise inductorless front-end for IoT applications. Proc. 6th International Symposium on Next Generation Electronics (ISNE) 2017, [http://doi.org/10.1109/ISNE.2017.7968711].

D.Sc. (Tech.) Gryhoriy Barylo
e-mail: gbarylo@polynet.lviv.ua

Gryhoriy Barylo graduated from Lviv Polytechnic University with a degree in radio engineering. He has worked for many companies and institutes. He was the head of the Microprylad production enterprise in Lviv. Since 2008 he has been working at the Department of Electronic Devices of Lviv Polytechnic National University. His research activity is focused on the problem of the use of impedance spectrometry in sensor technology, materials science, biological and medical research. His scientific approaches are based on the results of mathematical modelling, elements of artificial intelligence, systems and achievements of Internet technologies.

http://orcid.org/0000-0001-5749-9242

Ph.D. Oksana Boyko
e-mail: oxana_bojko@ukr.net

Oksana Boyko graduated from Lviv Polytechnic State University with a master's degree in Applied Mathematics. Since 2011 she is the Head of the Medical Informatics Department of Danylo Halytsky Lviv National Medical University.
Her research interests include mathematical modelling, biomedical sensors and embedded systems, medical information systems. She is the author of over 200 scientific and methodological works.

http://orcid.org/0000-0002-8810-8969

Ph.D. Ihor Gelzynskyy
e-mail: iigorg@ukr.net

Ihor Gelzynskyy He graduated from Lviv Polytechnic Institute Faculty of Electrophysics. He is a doctor of solid-state electronics, lecturer at Department of Electronic Devices of Lviv Polytechnic National University. He has worked in a number of ukrainian and international projects related to materials science, engineering and characteresating organic and gibrid light-emitting devices for organic electronics. His research area focuses on WOLED, PhOLED, QLED and electronics. Total number of citations of his works are 153 in 124 documents.

http://orcid.org/0000-0002-1931-6991

Prof. Roman Holyaka
e-mail: holyaka@yahoo.com

Roman Holyaka is a doctor of solid-state electronics, professor at Department of Electronics and Information Technology of Lviv Polytechnic National University. He has worked in a number of international projects related to diagnostic systems and electronic solutions for augmented reality. His research area focuses on electronics, sensors and embedded systems.

http://orcid.org/0000-0002-7720-0372

Prof. Zenon Hotra
e-mail: zhotra@polynet.lviv.ua

Zenon Hotra is the Head of the Electronic Devices Department of Lviv Polytechnic National University. Research interests: physical processes in semiconductor devices, radio engineering devices and means of telecommunications. Author of nearly 800 publications in this research area.

http://orcid.org/0000-0002-6566-6706

Ph.D. Tetyana Marusenkova
e-mail: tetyana.marus@gmail.com

Tetyana Marusenkova is an Associate Professor at Software Department of Lviv Polytechnic National University. She works on projects of Dinamica Generale S.p.A., a company that specializes on innovative electronic solutions and sensors for agriculture. Her main interests are mathematical modeling, MEMS inertial sensors, data fusion algorithms and embedded systems.

http://orcid.org/0000-0003-4508-5725

M.Sc. Mykola Khilchuk
e-mail: mykola.o.khilchuk@lpnu.ua

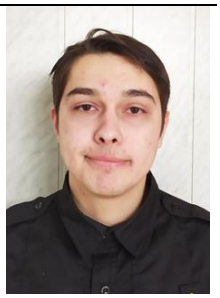

Mykola Khilchuk graduated from Lviv Polytechnic National University with a master's degree in radio engineering. Since 2019 he is a Ph.D. student. His research activity is focused on the problem of embedded systems in sensor technology, biological and medical research.

http://orcid.org/0000-0001-8579-9234

M.Sc. Magdalena Michalska
e-mail: magdalena.michalska@pollub.edu.pl

Ph.D. student at Lublin University of Technology. Recent graduate Warsaw University of Technology The Faculty Electronics and Information Technology. Her research interests include medical image processing, 3D modelling, optoelectronics, spectrophotometry. Author of more than 10 publications.

http://orcid.org/0000-0002-0874-3285

otrzymano/received: 15.01.2020 *przyjęto do druku/accepted: 25.02.2020*

http://doi.org/10.35784/iapgos.934

WAYS TO PRODUCE RENEWABLE ENERGY FROM CARBON DIOXIDE

Natalia Grigorieva[1], Viktor Shabaykovich[2], Larysa Gumeniuk[2], Pavlo Humeniuk[2], Lubov Dobrovolska[3], Dmitry Sobchuk[3]

[1]Lutsk National Technical University, Department of Instrumentation, Lutsk Ukraine, [2]Lutsk National Technical University, Department of Automation and Computer-Integrated Technologies, Lutsk Ukraine, [3]Lutsk National Technical University, Department of Electric Power Supply, Lutsk Ukraine

Abstract. *The interrelated problems of using renewable energy from carbon dioxide are considered. Particular attention was paid to the fact that on the one hand there is the possibility of obtaining renewable energy from carbon dioxide using new devices. At the same time, on the other hand, the Earth's atmosphere is cleared of such a gas and the greenhouse effect is also eliminated. To implement this approach, the current factors and their interaction, as well as examples of such installations with devices, are described. Their positive and negative aspects were emphasized.*

Keywords: renewable electricity, carbon dioxide, technology

ODNAWIALNA ENERGIA ELEKTRYCZNA Z DWUTLENKU WĘGLA

Streszczenie. *Opisano technologię i szereg problemów wykorzystania odnawialnej energii elektrycznej otrzymywanej z dwutlenku węgla. Zauważono, że z jednej strony możliwe jest pozyskiwanie odnawialnej energii elektrycznej z dwutlenku węgla za pomocą nowych urządzeń. Z drugiej strony – jednocześnie oczyszcza się atmosferę Ziemi z tego gazu i eliminuje efekt cieplarniany. Aby umożliwić wdrożenie prezentowanej technologii, opisano czynniki operacyjne i ich interakcje oraz podano przykłady takich instalacji z urządzeniami. Odnotowano pozytywne i negatywne strony prezentowanej technologii.*

Słowa kluczowe: odnawialna energia elektryczna, dwutlenek węgla, technologia

Introduction

Renewable energy is the production and use of energy from renewable sources, which include various energy flows in nature, such as water, wind, sun, thermal groundwater, biofuel, cold, etc. Their use was determined by the development of science and technology at individual stages. Modern development makes it possible to obtain renewable energy from carbon dioxide (CO_2). The use of renewable energy is becoming increasingly popular, especially in the context of energy-saving technologies and equipment. Renewable energy from CO_2, which is additional to the main source of energy, releases consumers from acute dependence on centralized energy networks. The consumption of other types of expensive energy is reduced. The issues of energy conservation and energy efficiency of renewable energy using CO_2 are also related to environmental safety issues, since it helps to reduce the amount of hazardous gas in the Earth's atmosphere.

In Ukraine, the Institute of Renewable Energy of the National Academy of Sciences of Ukraine, the Intersectoral Scientific and Technical Centre, the Bioenergy Association of Ukraine, as well as other research institutions and private organizations, deal with the problems of renewable energy depending on their financing. Irrational use of funds does not contribute to success. This paper presents a new way to capture greenhouse gases and convert them into electricity. In most modern methods, carbon capture is achieved by absorbing it with liquid or solid substances, which are heated or bled to release carbon dioxide. The concentrated gas can then be compressed and further used for combustion. All these things require improvement.

The total economically viable potential of renewable energy sources in Ukraine is approximately 454.4 billion kW·h. As of 2012, renewable energy sources had only 2% of energy consumption. Ukraine joined the European Energy Community and undertook unreasonable commitments to produce 11% of electricity from renewable sources by 2020 and the right to use the green tariff from 2009. In 2013, the share of renewable energy in the EU was 15%. However, by 2020, they suggest its increase to 20%. In Denmark, Sweden, Lithuania, and other countries this share is already equivalent to 42% and it is constantly growing. Carbon dioxide, which enters the atmosphere as a product of fuel combustion, should be beneficial. Such projects of more or less successful equipment and devices have been known for a long time. Nevertheless, they just indicate the beginning of serious developments. These are the first steps that should be maximized.

We can assume that it takes only 200 dollars to convert the tone of CO_2 into useful electricity [6, 17]. In this work, a well-known innovative method for producing cheap reducing energy and pure hydrogen from water, CO_2 dissolved in it, and two catalysts is described. This use is double, since the Earth's atmosphere will be simultaneously cleaned for the same expenses, which is of great importance, as, according to statistics, every minute 32 thousand tons of CO_2 are released into the Earth's atmosphere. Practically carbon dioxide reserves are inexhaustible. Experts estimate the strategic volume of the capture, processing, and storage market at 22.5 billion euros per year. This combination of benefits is extremely important. According to the International Energy Agency, by 2019, the world plans to increase renewable energy by 40% in five years. At the same time, they warn of the complexity of the further development of this area due to a decrease in funding for renewal of energy, the use of green tariffs, etc.

By analysing this sequence of using energy sources, we can confidently predict that the next step will be the generation of electricity from space. However, science and technology are still preparing for this to happen.

Based on a critical review and comparison with known solutions to the problem, the relevance of the article is to cover the primary issues of obtaining renewable energy from carbon dioxide, both in theory and, especially, in practice. Therefore, for a comprehensive increase in the organization of obtaining cheap renewable energy from carbon dioxide, the creation and implementation of scientific and practical developments of such processes, as well as efficient equipment and tools, is relevant.

1. Literature data analysis and problem statement

The use of carbon dioxide to generate electricity is a new modern efficient direction, about which there are not so many publications. Most publications [5, 11] describe a general approach to the topic. Since specifics are still very few, nobody is focusing on it. In subsequent works [1, 4], the authors also cite general factors that influence the production of renewable energy, describe the history, the beginning of work and the future, comparison with other methods of producing renewable energy (such as nuclear energy, wind energy, hydroelectricity, solar power, geothermal energy, etc.), which is confirmed by various digital data. Some materials are devoted to well-known installations and devices that implement this new direction. Hence, in the device for converting CO_2 into carbon fuel [3], hot and cold chambers are used on each side. In the centre, there is a row of 14 rings rotating at a speed of one revolution per minute. The outer edge of each ring contains iron oxide with a support compound of a zirconium matrix. A sunlight concentrator is installed inside one chamber to reach a temperature of 1500ºC, which leads to the reaction of an oxygen molecule with iron oxide on one side of the ring. In the opposite chamber, the reacting side of the ring rotates,

gradually loses heat, and the amount of CO_2 decreases. This cooling allows iron oxide to remove oxygen molecules from CO_2 leaving carbon monoxide behind.

There is also a device for absorbing CO_2 with the production of electricity [7], which is based on the technology of converting water into an electrolyte by transmitting gases formed during the combustion of organic fuel through it. They installed membranes around the electrodes of this device, each of which transmits only one type of ion. As a result, ions accumulate on the electrodes. Thus, the battery separates the electric charges and generates an electric voltage. There is a device for generating electric current due to the flow of gas or air on piezoelectric elements in the form of wave-shaped plates located with a gap in the generator housing [12]. The air stream enters the generator housing through a bell-slot device, drives the materials of the piezoelectric elements (vibration, deformation), which produce electric current removed by current collectors.

According to the results of publications of periodical scientific publications, especially the Internet, which reflects the latest data, it can be considered that the "niche" of this problem for further developments is their diversity, which gives rise to structural complexity, a difference in their indicators, insufficient coefficient of conversion of air gas energy into electrical energy associated with the selection of part of the heat from the gases. It is also possible to note insufficient environmental friendliness, which is explained by the fact that flue gases contain 93% carbon dioxide and 7% sulphur dioxide, nitrogen oxides, carbon monoxide, soot, powder particles, and possible radioactive elements. Also, there is little initial performance associated with the instability and relatively long formation time of the plasma energy core. Therefore, the problem statement for future research can be considered both the development of the theoretical part of the processes of renewable energy from CO_2 and the selection of the best options for technological equipment, their unification, and the development of improvement methods.

2. The purpose and objectives of the research

The purpose of the article is to determine the prerequisites for the development of renewable energy sources (in particular from CO_2), to generalize the development trends in the field of alternative energy, to study methods for producing renewable energy from CO_2 (both modern and efficient). To achieve this goal it is necessary to meet the following objectives:
to determine the features of processes as well as equipment and tools for energy recovery using CO_2;
to establish all factors affecting the effectiveness of such processes and the relationship between them;
to give examples of the most modern efficient devices and equipment for generating energy from CO_2.

3. The basics of getting energy from carbon dioxide

During energy generation [10], CO_2 is absorbed by liquid or solid substances, which are heated or bled to release carbon dioxide. Then they compress, transport, and use concentrated carbon dioxide. One of the disadvantages of the method is that for the capture of carbon dioxide it is necessary to use about 25% of the generated electricity. The electrochemical cell generates 13 ampere-hours per gram of porous carbon at a discharge potential of 1.4 V, which is comparable to the generation of current by a battery. In addition, the disadvantage is that the electrolyte is a liquid that connects the anode to the cathode, and which is very sensitive to water and has low productivity.

There are three main schemes for CO_2 capture: removal of carbon dioxide after burning fossil fuels, until combustion and oxygen-fuel combustion. In a first gas capture scheme, CO_2 is separated from flue gases. A promising absorption method is used. The absorbent is an aqueous solution of monoethanolamine, as a result of which a mixture of bound CO_2 (which enters the regenerator) is formed. It heats up regenerating the absorbent and releasing pure concentrated CO_2 (up to 99.9%). The efficiency of gas capture is up to 95%, while the disadvantages are significant energy costs for the restoration of absorbent and compression of CO_2 for transportation. In the second scheme, the primary fuel is processed in a reactor to produce a mixture of carbon monoxide, dioxide, and hydrogen, from which CO_2 and a mixture of H_2 and CO_2 are obtained, which are used as fuel for generating electricity. Oxygen-fuel combustion is based on the use of an oxidizer enriched with atmospheric oxygen with the release of nitrogen from it. After burning, they receive flue gases with a high concentration of CO_2 greatly facilitating the capture of gas.

By way of innovation, a new porous CO_2-absorbing material [2], which uses the structure of the new NOTT-202a material with cellular ordering, was invented. The material structure is used for selective adsorption of CO_2. While other gases (nitrogen, methane, and hydrogen) come back, CO_2 remains trapped in the material nanopores. There is also an innovative device [16] which uses modern Fischer-Tromp technology. The installation combines CO_2 absorption with electricity production. This technology is based on the conversion of water or an ethanolamine solution to an electrolyte when burning fossil fuels, where CO_2 reacts with water to H_2CO_3 form carbonic acid. Around the electrodes are installed such membranes that pass only one type of ion, which leads to the accumulation of ions, separation of electric charges, and the formation of electric current.

However, the story gets better. The well-known plant, which is considered economically inefficient [14], produces aviation fuel with CO_2. With the help of catalysts, gas is purified from atmospheric air in a reactor; under pressure, it turns into a liquid that is used for industry. The most difficult and responsible is the capture of CO_2. For this, various devices, the disadvantage of which is the irrational use of funds and low productivity, are used.

The capture process consists in obtaining pure gaseous CO_2 from a mixture of gases. To do this, they use the following methods: absorption, membrane application, distillation, mineralization, heat treatment, thermochemical treatment, etc. For example, thermochemical treatment combines the absorption of CO_2 with the production of electricity.

The choice of CO_2 capture technology depends on many factors, such as sophistication, practical application, operating costs, etc. The most promising technology is post-combustion capture technology. As an example, one of these settings is shown in Fig. 1. The scheme uses a straightforward method in which smoke from the atmosphere enters a treatment tank, to which a liquid solvent, which reacts only with CO_2 without reacting with other components, is attached. Typical solvents are ammonia or its solutions in water.

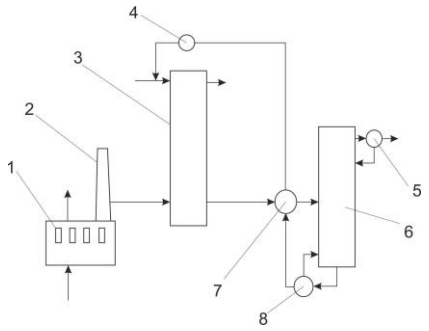

Fig. 1. Scheme of the installation for collecting CO_2 after fuel combustion: 1 — power station, 2 — exhaust gases with CO_2, 3 — gas scrubber column, 4, 5 — cooler, 6 — regeneration column, 7 — heat exchanger, 8 — heating element

In the tank, gaseous nitrogen remains at the top while liquid solvent remains at the bottom. Then the mixture of solvent and CO_2 is heated in the heat exchanger and the compound decomposes, after which CO_2 is released rising up the tank. Pure ammonia remains at the bottom of the tank and returns back to the treatment tank. Such capture technologies can produce up to 90% of CO_2. The disadvantages of this method include large volumes

of gas that are processed and require bulky equipment, additional energy, and significant costs.

One approach is carbon dioxide capture technology. To do this, oxygen-containing aluminium, which uses electrochemical reactions to both capture CO_2 and to generate electricity, has been developed. To do this, aluminium is used as the anode while mixed flows of CO_2 and oxygen as the active ingredients of the cathode. Electrochemical reactions between the anode and cathode bind CO_2 to carbon-rich compounds. In most devices, when carbon is captured, it is absorbed by liquid or solid substances, which are then heated or bled to release carbon dioxide. Concentrated gas can be compressed and transported for industrial use or stored. In addition, the process is able to turn CO_2 into more reaction molecules, such as oxalate, which contains two carbon atoms and represents new reaction processes that can be used to synthesize various products. Therefore, to increase the performance of electrochemical systems, it is necessary to use electrolytes that are less sensitive to water.

Particular attention should be paid to the device for generating electrical energy, which contains a gas reactor 1 with a pump source 2, a pipe 3 for supplying gas to the cavity of the reactor 1 and a nozzle 4 for removing plasma from the reaction zone (Fig. 2) [9].

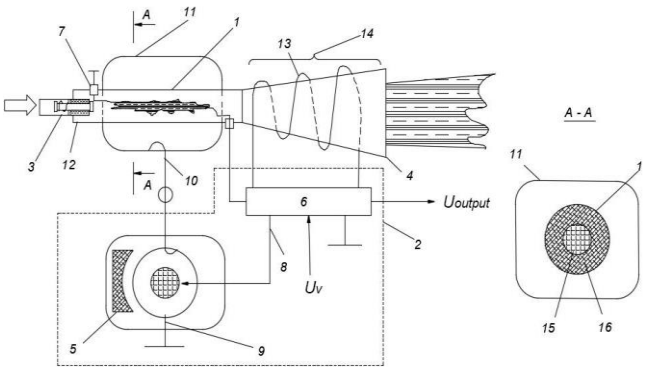

Fig. 2. Design of a device for generating energy from flue gases

The pumping source 2 of the reactor 1 contains an EMW generator, for example, a magnetron 5 and a high voltage arrester 6, the electrodes 7 of which are brought into the cavity of the reactor, and the modulating output 8 is connected to the cathode 9 of the magnetron 5. The EMW output of the magnetron 5 is connected by a waveguide 10 with a resonator 11 through the cavity of which a gas reactor 1 passes. The reactor vessel 1 has a cylindrical shape. It is made of a refractory dielectric material (for example, porcelain or ceramic). An inlet pipe 3 for supplying a gas reagent is installed on one end side of the reactor 1 while a nozzle 4 is installed on the other end side. The pipe 3 contains a check valve 12 while the nozzle 4 contains an inductive winding 13, forming a source of electrical energy 14 connected to the power input of the pump source 2 and external consumers of electricity. The high-voltage spark gap 6 is made in the form of an inductive or capacitive energy storage device with an adjustable pulse repetition rate (modulated by the magnetron 5) and beams of discharge pulses, which are supplied to the electrodes 7. The frequency f_{os} of high-frequency electromagnetic oscillations in each pulse of the magnetron 5 and the frequency f_{dp} of discharge pulses in the packet are selected corresponding to one or more resonant frequencies f_0 of absorption of electromagnetic waves by flue gas (CO_2 reagent and its impurities) introduced into the cavity of reactor 1. The volume of the inner chamber of the gas reactor 1 is selected from the condition of sufficiency of energy for injection sources for the resonant activation of flue gas and to exclude the rupture of chamber 1 during the explosion of the mass of the gas reagent enclosed in it.

The operation of the device is as follows. The energy storage device 6 is supplied with a supply voltage U_v. At the same time, flue gases fill the cavity of the gas reactor 1 through the valve 12, which is open in the normal state. When the high-voltage spark gap 6 enters the operating mode, the latter (with a transit period T) produces high-voltage modulation pulses of negative polarity of duration τ to the cathode 9 of magnetron 5. Simultaneously with the same repetition period, beams of discharge pulses of duration τ and pump frequency f_p, which corresponds to or is a multiple of the resonant frequency f_0 of the absorption of the gas reagent, are emitted to the electrodes 7 of the gas reactor. Under the influence of a potential difference > 30 kV/cm between the electrodes 7 of the gas reactor 1, an electrical breakdown of the gas reagent and the formation of a streamer – path from the current carriers – ions and electrons with a charge density of the order of 10^{-7} cm^{-3} occurs. At the same time, magnetron 5, under the influence of high-voltage pump pulses, produces high-frequency EMW injection beams with a frequency of $f_p = f_0$ and with an energy density of at least 1 J/cm^2 and transmits them through waveguide 10 to resonator 11 for electromagnetic pumping of an ionized gas reagent in the chamber of gas reactor 1. At the same time, due to resonant absorption of EMW energy and impact ionization, molecular bonds and CO_2 molecules are broken into constituent elements that are released as a result of the reaction. The generated heat (which is unstable to steady ionization of CO_2 formation), as well as the resonant effect on the medium, which is ionized by EMW energy and sources of electric discharge injection, contribute to the development of the further process of ionization and destruction of oxygen atoms and ions with the formation of a deficit in their mass. An increase in the density of charge carriers to 10^{14} cm^{-3} in reactor 1 leads to the initiation of oxygen reactions, which is accompanied by explosive destruction of oxygen molecules, the release of a free electron of their bond and the quantum energy of the secondary ionizing radiation from the ultraviolet to soft X-ray range of electromagnetic waves leading to avalanche ionization of gas reagent in the reactor 1 and to the complete separation of electrons from positively charged nuclei of oxygen atoms as well as other components of the flue gas. The presence of a small percentage of nitrogen, which binds part of the oxygen in reactor 1, in flue gases slightly reduces the reaction rate due to the fact that nitrogen molecules (having a negative excess charge) surround parts of oxygen molecules, which have a positive excess charge, forming aggregates of oxygen shielded by nitrogen from the action of ionizing effects.

The disadvantages of this method include an insufficient coefficient of conversion of flue gas energy into electrical energy, low environmental friendliness, etc. These shortcomings were eliminated in the device [15] due to the introduction of a tank with CO_2, a reactor with a device for acting on a gas, ultraviolet radiation, pulsed activation of a gas reagent, and regulation of average outgoing power.

4. The results of a study of renewable energy processes from carbon dioxide

As of today, one of the promising areas is the generation of electricity from CO_2. However, work in this direction is at the beginning stage. Therefore, there is little material both on the recovery processes of electricity and on equipment (that is also imperfect and quite diverse), which in turn leads to the irrational use of working time and financing. Therefore, an important task for all complexes is the selection of the best theory of renewable energy and related technical equipment and tools as well as their partial unification at the outset.

The results were obtained on the most difficult generation of electricity from CO_2. Since there were few such studies due to lack of purpose (they were engaged in other methods of restoring electricity, for example, wind, solar, etc.), now we use well-known physical and chemical processes that still need to be adapted to this method. These are devices for capturing CO_2 from air or liquids. In the study of such CO_2 capture schemes, it was found that CO_2 removal is best done after fuel combustion and oxygen-fuel combustion. To implement this scheme, some rare original samples of technological equipment and tools are known that can be used right now to produce renewable energy from CO_2 by

installing them directly on the exhaust pipes. Despite the fact that they are slow, such devices capture up to 90% of CO_2 and are considered the best. When burning oxygen-enriched fuel, CO_2 capture occurs due to an increase in oxygen (rather than air), which in turn reduces the cost of energy recovery from CO_2. Less interesting are the schemes for CO_2 separation using solvents, membranes, mineralization, etc. However, in most cases, these are experimental samples that require structural refinement.

This work presents equipment for producing renewable energy from flue gases CO_2, which so far is also experimental and needs some changes. The above equipment is also quite complex, since it contains a gas generator, a pump source, an electromagnetic wave generator, etc. according to old technology for generating electricity (for example, they use a plasma to electric energy converter). That is, a well-known but rather complex and expensive design, which also requires additional refinement and reduction of technological costs for industrial use, is presented here.

Based on an analysis of studies of known and proprietary material, a universal installation for generating energy from CO_2 (for which a patent application was filed) was developed. The design consists of CO_2 traps that are placed above the environment with CO_2 (for example, pipes of power plants, boiler houses, thermal stations, plants, etc.). Captured CO_2 is converted to liquid fuel using new optimal catalysts. Thus, it is possible to solve the problem of global climate change through the purification of the Earth's atmosphere. The fuel cell consists of sodium alkali metal, a cathode, a separator, and anode catalyst. Known devices that are part of this installation are selected according to the criterion of modern design and high technical and economic indicators. Then a reservoir and devices for using liquid fuel are used. The novelty in such an installation is the interconnection of individual devices, the use of two sources of energy reserves (both a reservoir and a battery), the location of CO_2 traps and mechanical energy use devices. The technical and economic efficiency of the developed installation is justified by a new quality, which is obtained through the use of these devices.

5. Discussion of the results of a study on the production of renewable energy from carbon dioxide

The advantages of the study of obtaining renewable energy from CO_2 are in the comprehensive disclosure of the problem of CO_2 capture from air or water, the manufacture of carbon dioxide, its storage and transportation to the place of consumption. As a rule, well-known publications disclose certain elements of recovery technologies, known imperfect equipment and tools. Since such comprehensive studies are at the beginning stage, so far the technologies and equipment are at the initial level (that is, they are fragmented). At the same time, the whole complex requires significant improvement using the modern development of science and technology. So far, the basis of their functioning is the old physical and chemical principles that require additional changes and coordination. Their main disadvantages are low technical indicators and significant costs, which are stipulated by the lack of a coherent and effective theory as well as practice of recovering electricity from CO_2.

The studies performed are very important because they provide the double benefit: obtaining cheap renewable energy from inexhaustible reserves of CO_2 and cleaning the atmosphere from harmful gases. Provided that the well-known technological equipment and tools are improved to ensure its industrial use, it can be argued that it is natural to identify the influence of the main factors on these processes, in particular the relationship and technical and economic indicators. It is necessary to highlight their actions according to the impacts established. It is with the help of such a mechanism of influence of factors that it is possible to increase the efficiency of energy recovery from CO_2.

To study and obtain a rational technical solution for designing equipment and tools for obtaining renewable energy from CO_2, it is first necessary to select the best prototypes among analogues and to skilfully improve them in the future using computerization and preferably virtual design [13] with an innovative approach. Thus, you can quickly get the desired design for use in industry and other sectors of the economy, including energy-saving technologies and equipment. This is a continuation of previous studies (however, this time it is about the highest industrial level) in specialized research centres, which must be organized taking care of their staffing and financial support. It is possible to do this in private firms with the help of highly qualified specialists who have no signs of overt or covert enrichment.

The continuation of relevant studies on the production of renewable energy from CO_2 in the near future would be very appropriate since it would make it possible to obtain cheap electricity and clean the atmosphere from harmful greenhouse gases. In addition, the presence of additional sources in electric networks helps to increase the reliability of power supply [8].

6. Summary

As a result of studies on the production of renewable energy from CO_2 using energy-saving technologies and equipment, the following things were proved:

- the greatest promise of obtaining renewable energy from CO_2, which is confirmed by the dual benefits, is to obtain cheap electricity from inexhaustible reserves of CO_2 sources, as well as to cleanse the Earth's atmosphere of harmful gas;
- the effectiveness of technological processes for obtaining renewable energy from CO_2 and components of energy-saving technologies is influenced by a number of external and internal interrelated factors, such as: the level of the general scientific and technical basis for such restoration, the basis for the development and production of renewable energy from CO_2, as well as the availability of technological equipment;
- despite the previous various well-known theories, technical equipment and tools retain their individual characteristics and remain separate; their existence in the general scientific and technical basis for obtaining cheap electricity from CO_2 is difficult and can be widely used both at the beginning of theoretical and practical developments;
- in most cases, the literature provides fragmentary multifaceted descriptions of both the theory as well as devices and equipment, which are distinguished by a variety of designs, technical characteristics, which hinder their professional design in specialized scientific and technical centres provided decent centralized funding;
- the various characteristics of such multifaceted equipment and tools are explained by individual (and not always qualified) approaches in the development, outdated organization of work, unstable supply, and lack of funding;
- the most efficient approach, which is responsible for the CO_2 capture cycle, uses post-combustion technology that can be applied to existing sources of air pollution from power plants, enterprises, metallurgical plants, and other organizations polluting the environment;
- in connection with the actual start of CO_2 capture technology development, most of the technological equipment and tools are distinguished by structural imperfection and low performance;
- a typical structure of technological equipment for generating electricity from CO_2 is devices for capturing CO_2 from a medium saturated with it (air, water), storage and transportation for use, as well as processing it into fuel;
- to increase the development efficiency, it is necessary to single out both typical best examples of the technology for producing carbon fuel and technological equipment and tools with their subsequent unification, which can only be better provided with innovative solutions of narrow specialists in the field of energy supply of renewable energy from CO_2;
- significant development improvements are provided by the use of computerization, that is, when you can quickly make the

necessary changes (especially with a modular concept and virtual development) without any loss;

- first, obtaining rational layouts of technological equipment and equipment for renewable energy from CO_2 involves the development of a recovery technology, the selection of the best samples, as well as the search for innovative solutions and design;
- the research is of great importance for operations to further develop energy-supplying technologies and equipment by reducing the traditional fuel base in transport and the economy in general;
- the negative side of this problem is the complete lack of preparedness and possible misunderstanding of the importance of implementation in resource-saving technologies and equipment, since now completely different tasks dominate (in most cases, they are political) and the general situation is also unfavourable. Subject to a change in the situation in the near future for the better, we can assume that such work will be in demand and used.

References

[1] Bazeiev Y., Varlamov H. B., Volchyn I. A., Kazanskyi S. V., Kesova L. O., Kryzhanivskyi A. L., Shyliaiev B. A.: Energy: history, present and future. Book 2: Knowledge and Experience – The Road to Modern Energy, Kyiv 2013.

[2] Boute A.: Promoting renewable energy through capacity markets: An analysis of the Russian support scheme. Energy Policy 46/2012, 68–77, [http://doi.org/10.1016/j.enpol.2012.03.026].

[3] Diver R., Miller J., Allendorf M., Siegel N., Hogan R.: Solar Thermochemical Water-Splitting Ferrite-Cycle Heat Engines. Journal of Solar Energy Engineering 130(4)/2008, 041001, [http://doi.org/10.1115/1.2969781].

[4] Dobrovolska L., Volynets V., Sobchuk D., Cherkashyna V.: Electricity networks with renewable energy sources. Lutsk National Technical University, Lutsk 2019.

[5] Jacobson M. Z., Delucchi M. A.: A Path to Sustainable Energy by 2030. Scientific American 301(5)/2009, 58–65, [http://doi.org/10.1038/scientificamerican1109-58].

[6] Janssen R.: Renewable energy ... into the mainstream. Sittard, Netherlands: IEA Renewable Energy Working Party, 2002.

[7] Hamelers H. V. M., Schaetzle O., Paz-García J., Biesheuvel M., Buisman C.: Harvesting Energy from CO_2 Emissions. Environmental Science and Technology Letters 1/2014, 31–35, [http://doi.org/10.1021/ez4000059].

[8] Lezhnyuk P., Komar V., Kravchuk S., Sobchuk D.: Mathematical modeling of operation quality of electric grid with renewable sources of electric energy. Proceedings of the International Conference on Modern Electrical and Energy Systems MEES 2017, 2018, 324–327, [http://doi.org/10.1109/MEES.2017.8248923].

[9] Lypets A., Dyryna L., Budniatskyi D., Benenson E., Usov A., Dehtiarev V. et al.: Russian Federation patent no. SU 1824510 A1. State Patent Office of the USSR, 1993.

[10] Matveev V. A., Zvonov A. A.: Russian Federation patent no. PCT/RU2009/000216. Federal servicefor intellectual property, patents and trademarks, 2009.

[11] McCrone A., Moslener U., Grüning C., d'Estais F.: Global Trends in Renewable Energy Investment 2019. Frankfurt School-UNEP Centre/BNEF, 2019.

[12] Rogovik V. I.: Russian Federation patent no. RU 2253938c2. Federal servicefor intellectual property, patents and trademarks, 2005.

[13] Shabaikovych V.: Modern production of products. Joint venture business entity "Marusevych", Lviv 2014.

[14] Uniper SE: Methanation plant in Falkenhagen opens – important step for a successful energy transition. Press release, 2018, https://www.storeandgo.info/fileadmin/press_releases/2018-10-18_Press_Release_Political-Dinner.pdf

[15] Vasjukov D. A., Guseinov M. A., Konnova T.A., Solodilov L. N.: WIPO (PCT) Patent No. WO2012138260A1, 2012, https://patentimages.storage.googleapis.com/62/4e/a7/2e78886746b67f/WO2012138260A1.pdf

[16] Yang S., Lin X., Lewis W. et al.: A partially interpenetrated metal–organic framework for selective hysteretic sorption of carbon dioxide. Nature Materials 11(8)/2012, 710–716, [http://doi.org/10.1038/nmat3343].

[17] Yonhap News Agency.(2019). Scientists have discovered a way to obtain energy from carbon dioxid Researchers develop efficient way to make H_2, electricity from CO_2, https://en.yna.co.kr/view/AEN20190604006700320

D.Sc. (Eng.) Natalia Grigorieva
e-mail: vik_shabajkin@ukr.net

Lutsk National Technical University, Department of Instrumentation.
Specializes with the problems of machine and instrument technology, renewable electricity, automation of production processes, standardization and certification.
Has more than 200 publications in this area.

http://orcid.org/0000-0002-9787-5844

D.Sc. (Eng.) Viktor Shabaykovich
e-mail: vik_shabajkin@ukr.net

Lutsk National Technical University, Department of Automation and Computer-Integrated Technologies.
He deals with problems of quality and competitiveness of products, innovations, optimization of structural and technological solutions, organization of production.
Has more than 500 publications in this area.

http://orcid.org/0000-0001-6822-9520

Ph.D. Larysa Gumeniuk
e-mail: l.gumeniuk@lntu.edu.ua

Lutsk National Technical University, Ph.D. (technical). Head of Department of Automation and Computer-Integrated Technologies.
Research interests: Modeling of reliability and safety of the automated control systems.
Has more than 60 publications in this area.

http://orcid.org/0000-0002-7678-7060

Ph.D. Pavlo Humeniuk
e-mail: l.gumeniuk@lntu.edu.ua

Lutsk National Technical University, Ph.D. (technical), Department of Automation and Computer-Integrated Technologies.
Research interests: programming, robotics.

http://orcid.org/0000-0002-6251-8548

Ph.D. Lubov Dobrovolska
e-mail: lsobchuk@gmail.com

Lutsk National Technical University, Ph.D. (technical), Department of Electric Power Supply.
Research interests: Automation in mechanical engineering and power systems, renewable electricity.
Has more than 66 publications in this area.

http://orcid.org/0000-0001-8175-7635

Ph.D. Dmitry Sobchuk
e-mail: sobdim@gmail.com

Lutsk National Technical University, Ph.D. (technical), Department of Electric Power Supply.
Research interests: Energy systems and networks. Renewable energy sources.
Has more than 20 publications in this area.

http://orcid.org/0000-0001-5958-9612

otrzymano/received: 22.12.2019 *przyjęto do druku/accepted: 15.02.2020*

http://doi.org/10.35784/iapgos.826

SATURATION OF THE ABSORPTION OF THERMAL RADIATION BY ATMOSPHERIC CARBON DIOXIDE

Jan Kubicki, Krzysztof Kopczyński, Jarosław Młyńczak
Military University of Technology, Institute of Optoelectronics, Warsaw, Poland

Abstract. *The article presents a concise review of the works concerning the impact of an increase of the concentration of carbon dioxide in the atmosphere on the increase of its absorption of thermal radiation. Attention was paid to differences in the results of calculations presented in the works by various authors. Experimental verification was carried out, which confirmed the possibility of saturation of the process of thermal radiation absorption by CO_2 in the atmosphere. Possibilities of improving climate models by using direct measurement results of experimental works were pointed out.*

Keywords: greenhouse gases, radiation processes, Schwarzschild equation, climate sensitivity

NASYCENIE PROCESU ABSORPCJI PROMIENIOWANIA TERMICZNEGO W ATMOSFERYCZNYM DWUTLENKU WĘGLA

Streszczenie. *W artykule przedstawiono zwięzły przegląd prac dotyczących wpływu wzrostu stężenia dwutlenku węgla w atmosferze na wzrost w niej absorpcji promieniowania termicznego. Zwrócono uwagę na różnice wyników obliczeń w pracach różnych autorów. Przeprowadzono weryfikację eksperymentalną, która potwierdziła możliwość nasycenia się procesu absorpcji promieniowania termicznego dla CO_2 w atmosferze. Wskazano możliwości doskonalenia modeli klimatycznych poprzez wykorzystywanie bezpośrednich wyników pomiarów w pracach eksperymentalnych.*

Słowa kluczowe: gazy cieplarniane, procesy radiacyjne, równanie Schwarzschilda, wrażliwość klimatyczna

Introduction

Radiation processes occurring in the atmosphere, on the Earth's surface and in the surface layer of the ocean play a key role in the energy balance of the climate system [10]. Some of the solar radiation that illuminates the Earth is scattered and reflected by clouds and aerosols or absorbed by the atmosphere. The remaining radiation is absorbed or reflected by the Earth's surface. The energy of solar radiation is transformed into heat, latent energy (including various water states), potential energy and kinetic energy, and then it is emitted as long-wave radiation energy into space [13].

Finally, a state of equilibrium is established for which the average radiation flux from the Sun must be equal to the average radiation flux from the Earth.

The heated lithosphere is a gray body whose emission properties are similar to those of a black body. The Planck formula describing them clearly shows that the flux of the emitted radiation is an increasing function of the body temperature emitting this radiation. Thus, for a constant value of the radiation flux from the Sun, any reduction of radiation emission into space must cause an increase of the Earth's temperature (lithosphere). This is caused primarily by the processes of interaction of the lithosphere thermal radiation with active gases in the atmosphere. Thus, these gases, called greenhouse gases, have an uncontested effect on the Earth's climate and the related phenomena have been described, among others, in book [1] and in many other works on this subject [5, 6, 8, 9, 13].

Often, a special parameter is used to describe the effect of the greenhouse gas on the increase of the average temperature on the Earth's surface. This parameter, called climate sensitivity, determines the increase of the average temperature of the Earth when the amount of a greenhouse gas is doubled.

Concern for the Earth's climate inspires further work on this topic. In 1988, at the UN, upon request of the World Meteorological Organization (WMO) according to the United Nations Environment Program (UNEP), an intergovernmental scientific advisory body The Intergovernmental Panel on Climate Change (IPCC) was set up. Its purpose is to provide objective, scientific information on climate change.

However, despite the involvement in the climate change of many outstanding research centres equipped with the best apparatus, there is a lack of experimental work verifying the results of theoretical calculations. The necessity to undertake such work is justified by the fact that the described phenomena are relatively complex while some data taken for calculations may raise objections (due to the diversity of the analysed areas and the dynamics of the processes). As a result the final calculations may be very different.

In this work, taking into account the presented literature, an attempt to remind the processes of thermal radiation interaction with the active gases was made. Then, the possibilities of verification and supplementing existing knowledge with the help of conducted experiments and proposals of further research were shown.

1. Phenomenon of thermal radiation absorption in the atmosphere

Propagation of long-wave radiation with the intensity I and wavelength λ, emitted by a black body and passing through absorbing gaseous medium, neglecting scattering, can be described by the Schwarzschild equation in the form [10]:

$$\frac{dI_\lambda}{d\tau} = -I_\lambda + B_\lambda(T) \tag{1}$$

where: $d\tau = k_\lambda \rho ds$, τ – optical thickness measured rectilinearly (with neglecting refraction in the atmosphere), k_λ – mass absorption coefficient, ρ – density of the absorbing medium, s – propagation path, $B_\lambda(T)$ – Kirchhoff-Planck function.

When the temperature of the gas medium is much lower than the temperature of the radiator, the function $B_\nu(T)$ can be omitted and equation (1) will take the differential form of Lambert-Beer law. In the case of thermal radiation emission from the lithosphere (decreasing its temperature), the above situation occurs in the higher layers of the troposphere, where the temperature is much lower than on the Earth's surface. If the emitted radiation interacting with active gases in the atmosphere was monochromatic, its intensity during propagation in the atmosphere would decrease exponentially. Then at sufficiently high value of τ, increasing e.g. due to the increase of the concentration of the gases, the value of this intensity would become negligible. It could be said, then, that the saturation of the concentration of the absorbing substance occurred. Further increase of the concentration of the gases would not bring any effect, because there would be no radiation. However, in reality the situation is more complex. The radiation is not monochromatic because it is emitted by the lithosphere that is a grey body and the spectrum of this radiation is continuous similar to the spectrum of the black body described by the Planck formula

The carbon dioxide present in the atmosphere has a linear spectrum and with increase of optical thickness, these lines are deformed (Fig. 1). First, the saturation effect occurs at the central frequency ν_0, and then at farther frequencies.

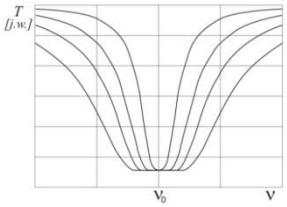

Fig. 1. Transmission line deformed by saturation

The final effect of such a process can be shown on the basis of the image of the transmission spectrum of layers of air of different thickness and with CO_2 concentration of 380 ppm (Fig. 2) [7].

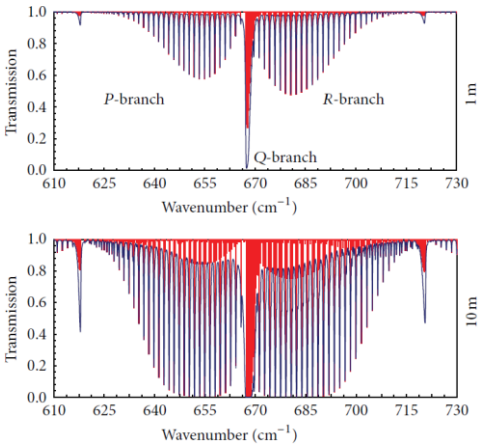

Fig. 2. Transmission spectra of dry air with CO_2 concentration of 380 ppm for two different thicknesses (air pressure: 1013 hPa, temperature: 288 K; red colour show transmission for central frequencies of the absorbing lines, while blue colour show total transmission for these lines) [7]

The phenomenon is quite complex and therefore in theoretical considerations various approximations are used to explain and estimate the effects of the happening processes. For example, in the work [5], it was shown that the absorption of the entire extended Lorenzian line (if there is a lot of absorbing substance) is equal to:

$$A = C + Dln(m) + Eln(p) \tag{2}$$

where: C, D i E – constants, m – amount of the absorbing substance, p – pressure.

This formula shows that when the concentration of the absorbing gas increases the absorption also increases. However, it should be noted that this is a logarithmic increase and thus the effect of the same amount of absorbing gas additionally introduced into the medium will depend on its initial concentration. Despite this, this work is cited by many authors, who try to prove that the so-called saturation effect for CO_2 in the atmosphere does not occur. They show the results of numerical calculations for their models, where each subsequent portion of the absorbing gas introduced into the atmosphere causes strong increase of the absorption of thermal radiation emitted by the lithosphere. The report [12], based on the presented reasoning, shows relatively high sensitivity of climate change to CO_2 emission (temperature increases by 3.2 K when CO_2 emission is doubled).

Meanwhile, in the work [7], it was shown that when CO_2 emission is doubled the temperature increases only by 0.6 K. In turn, work [3] shows that when CO_2 concentration is changed from 300 ppm to 600 ppm, the temperature on the Earth's surface increases by no more than 0.2 K.

In the report by Legalization Laboratory in Livermore [4], the authors point out the complexity of problems related to climate description and the very high uncertainty of the results obtained by computer calculations on the basis of assumed models. Attention is also drawn to the hasty adoption of visions of other planets, especially Venus, due to many different factors that are not taken into account in the models.

Thus, as already mentioned in the introduction, these differences inspire the experimental verification of the obtained results. The phenomenon of the absorption of infrared radiation (emitted by the lithosphere) by carbon dioxide contained in the higher cooler layers of the atmosphere, described very precisely in [7], cannot raise any doubts about its occurrence. However, doubts may relate to the amount of the saturation of the absorption when the concentration of CO_2 in the atmosphere increases. It should also be noted that other gases that absorb thermal radiation in the atmosphere have a significant impact on this phenomenon. Their absorption spectra overlap to some extend with the CO_2 absorption spectrum. Thus, the impact of the CO_2 concentration on the absorption of thermal radiation is reduced.

2. Application of radiation emitted by the Moon to study the atmosphere

Investigating the transmission spectrum of the atmosphere at small distances, especially horizontally, seems to be relatively simple. To make such measurement only the radiator (warmed-up body) and the monochromator with a photodetector set at the right distance from each other are required. However, if the greenhouse effect is considered, vertical tests using objects at a sufficiently high altitude should be carried out. Artificial satellites can be used for this experiment, but it is easier to use the natural satellite – the Moon. The temperature of its surface varies a lot, but for the part illuminated by the Sun, according to encyclopaedic information, it may slightly exceed 1100°C. Therefore, the spectrum of thermal radiation emitted by it can be described with a good approximation as a Planck distribution. This spectrum along with the CO_2 transmission spectrum are shown in Fig. 3.

It can be seen that part of the spectrum emitted by the black body overlaps with the carbon dioxide absorption spectrum (made using the HI-TRAN2004 software).

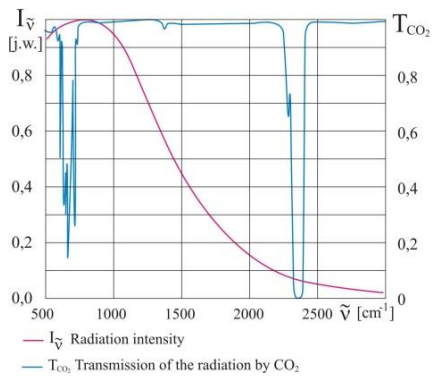

Fig. 3. Comparison of the spectrum of the black body radiation at 1100°C with the CO_2 transmission spectrum

Of course, it should be remembered that the surface of the moon is heated by solar radiation with a spectrum distribution corresponding to black body with a temperature of over 50,000 K. Part of this radiation is reflected by the surface of the Moon and, along with its thermal radiation, propagates towards the Earth. The spectrum of the combined radiation is, of course, continuous, but due to high temperature of the sun, its maximum should shift towards shorter wavelengths, better overlapping with the 4.3 μm (2326 cm^{-1}) absorption band of CO_2. Thus, infrared radiation coming from the moon should be more attenuated by carbon dioxide than radiation emitted by black body at 1100°C.

The concept of using the moon radiation to study the Earth's atmosphere is not a new issue. At the end of the nineteenth century the spectrum of radiation coming from the moon after passing through the Earth's atmosphere as well as absorption bands corresponding to various active gases were described [2].
At present, the Moon is also used in many experimental works to investigate the Earth's atmosphere [11, 14].

3. Experiment

The considerations presented in the previous chapters inspire to ask the question of what is the transmission of radiation with a continuous distribution, e.g. emitted by the black or grey body at a specific temperature, that vertically passes through the Earth's atmosphere with a CO_2 layer of appropriate thickness and pressure and temperature much lower than the temperature of the radiation source.

To answer this question, the experiment was performed where infrared radiation from the Moon reaching the Earth's surface after passing through the Earth's atmosphere was used to light the cuvette filled with the carbon dioxide. The appropriate experimental setup was assembled. The first experiments were carried out in a laboratory using an artificial source of radiation simulating the Moon. The experimental setup is presented in Fig. 4.

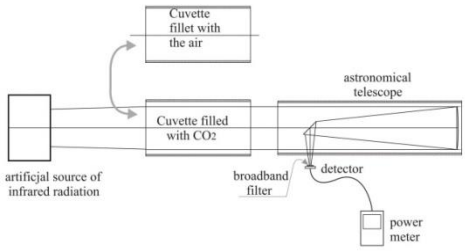

Fig. 4. Experimental setup for measuring the transmission of infrared radiation by a cuvette filled with CO_2

The setup uses two identical cuvettes in the form of plexiglass pipes with a diameter of 250 mm and a length of 500 mm closed with polyethylene foil windows. One cuvette was filled with carbon dioxide while the other was used as reference cuvette filled with air. The radiation emitted by the artificial source, after passing through the cuvette, was focused by the astronomical telescope Soligor MT-800/8"E on the S401C detector connected to PM200 power meter. The telescope was characterized by the diameter of the first mirror D = 200 mm, focal length F = 800 mm and the shading diameter of the second mirror d = 60 mm. The active surface of the detector was shielded by a broadband filter in the form of a flat-parallel germanium plate.

Polyethylene foil windows and a filter in the form of a flat-parallel germanium plate were chosen because of their appropriate transmission spectra. The comparison of these spectra with the carbon dioxide transmission spectrum and the emission spectrum of black body at the temperature of 1100°C (corresponding to the moon's temperature) are shown in Fig. 5.

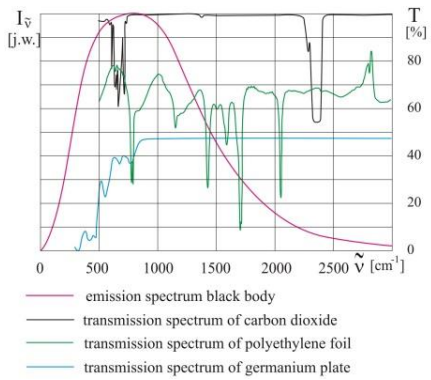

Fig. 5. Transmission spectra of polyethylene foil, germanium plate and CO_2 compared with the emission spectrum of black body at 1100℃

It can be seen that from the infrared spectrum emitted by black body at a temperature of 1100°C, the germanium plate cuts out unimportant part of low-frequency radiation and slightly reduces the radiation at ~ 15 μm (666 cm^{-1}) wavelength absorbed by CO_2. In turn, the polyethylene foil cuts out bands that do not overlap with CO_2 absorption bands. Finally, it can be stated that the setup's sensitivity to measure the absorption of black body radiation by CO_2 was increased. The photo of the developed experimental setup is shown in Fig. 6.

The experimental setup was assembled on a tripod enabling vertical full angle rotation and horizontal rotation from zero to ninety degrees.

The diagram of the artificial source of radiation simulating the Moon is shown in Fig. 7.

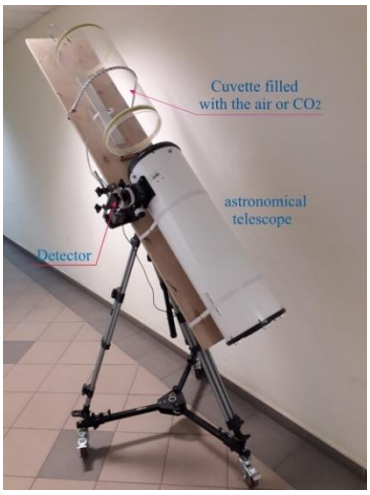

Fig. 6. Photo of the experimental setup

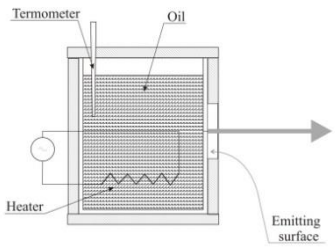

Fig. 7. Diagram of the artificial source of radiation simulating the Moon

The source consisted of a cylindrical glass vessel that was characterized by 100 mm diameter and 150 mm height. The vessel was filled with mineral oil and thermally insulated with 10 mm thick polyurethane foam with a hole of 40 mm diameter for emitting the radiation. The emissive surface of the vessel (behind the hole in the foam) was matted. With the help of an electric heater the oil was heated to 1100°C. The temperature was measured using the ETI 810-930 electronic thermometer. The radiation source was placed at a distance of 50 cm from the polyethylene window of the cuvette as shown in Fig. 4. Just before the right measurements the power meter was reset covering the radiation source with a plywood plate (at temperature of ~ 200°C).

The measurements of the power of the infrared radiation incident on the detector were made alternately for the cuvette filled with the carbon dioxide and filled with the air. In each case, 500 measurements every 0.01 seconds were made and the average power was determined. The measurement was repeated three times for the first cuvette and then three times for the second cuvette. The above measurements were repeated again six times. The results of the described experiment are shown in Tab. 1.

Table 1. The power of infrared radiation emitted by the artificial source after passing through the cuvettes

Subsequent measurements	Power for cuvette with CO_2, [μW]	Subsequent measurements	Power for cuvette with air, [μW]
1	267.2	2	310.4
	265.1		309.4
	263,7		308.5
3	264.6	4	309.2
	263.2		310.1
	262.9		308.9
5	264.2	6	307.9
	266.7		310.1
	263.9		308.7
Average value	**264.6**	Average value	**309.2**

The presented measurements show that the power of radiation incident on the detector in the case of the cuvette filled with air is equal to $I_p = 309.2$ μW while for the cuvette filled with CO_2 is equal to $I_{CO_2} = 264.6$ μW.

Assuming, that the power of radiation incident on the first cuvette window is I_0, the power of radiation incident on the detector for the carbon dioxide and the air can be expressed by the following formulas, respectively:

$$I_{CO_2} = I_0 \cdot T_{ok}^2 \cdot T_{CO_2} \cdot T_L \cdot T_F \quad (3)$$

$$I_p = I_0 \cdot T_{ok}^2 \cdot T_p \cdot T_L \cdot T_F \quad (4)$$

where: T_{ok} – transmission of the radiation for the polyethylene window, T_L – transmission of the radiation for the telescope, T_F – transmission of the radiation for the germanium plate, T_{CO2} – transmission of the radiation for CO_2 in the cuvette, T_p – transmission of the radiation for the air in the cuvette.

Using equations (3) and (4) and assuming that $T_p = 1$, the following formula can be derived:

$$T_{CO_2} = \frac{I_{CO_2}}{I_p} \quad (5)$$

By inserting the measured values from Tab. 1 into formula (5), the value of transmission of radiation for a 50 cm thick carbon dioxide layer at atmospheric pressure and temperature of 20ºC can be obtained and it is equal to $T_{CO_2} = 0.86$.

It should be remembered that this radiation was emitted by a grey body (matted glass surface) at a temperature of 1100°C and passed through two windows of polyethylene foil and the germanium plate, while it did not pass through the thick layer of the Earth's atmosphere, which is the main object of the investigation. The second part of the experiment was devoted to this issue. The infrared radiation from the moon after passing through the Earth's atmosphere was measured. The experiment was carried out at cloudless night, during the full moon, at ~ 2°C, on the roof of the IOE WAT building. The measurement system used for the experiment is shown in Fig. 8.

When the optical axis of the experimental setup was set towards the clear sky (away from the face of the Moon), the power meter was to zero. When the optical axis was set towards the face of the Moon, the power of the radiation incident on the detector was measured. During the measurement, the optical axis of the experimental setup was inclined from the vertical by an angle of ~ 35°.

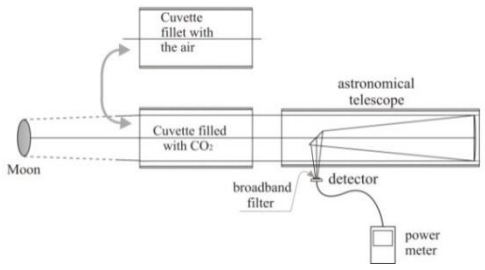

Fig. 8. Experimental setup for measuring the transmission of infrared radiation from the Moon by CO_2

The measurements were carried out in the same way as in case of the laboratory experiment exchanging the cuvette filled with CO_2 and with the air. The achieved results are shown in Tab. 2.

Table 2. The power of infrared radiation from the Moon after passing through the cuvettes

Subsequent measurements	Power for cuvette with CO_2, [μW]	Subsequent measurements	Power for cuvette with air, [μW]
1	123.2	2	122.4
	121.7		123.1
	119.5		120.0
3	120.7	4	119.4
	122.1		121.3
	119.5		122.0
5	121.5	6	120.8
	119.1		118.3
	120.7		122.1
Average value	**120.9**	Average value	**121.0**

The obtained results show that the average value of radiation power from the Moon, after passing through the cuvette filled with carbon dioxide and with the air, is the same this time. This means that according to formula (5), the value of infrared radiation coming from the moon to the Earth's surface through carbon dioxide at atmospheric pressure, temperature of ~ 2ºC and thickness of 50 cm is equal to $T_{CO_2} \cong 1$. Of course, it should be referred to the difference of temperature in laboratory (T = 20ºC) and on the terrace (T = 2ºC). Thus, according to the Schwarzschild equation (1) and analysis presented in [7], stronger attenuation of the infrared radiation by CO_2 should be expected at lower temperature than at a higher temperature. Thus, the temperature change could not cause an increase of transmission of CO_2.

4. Summary of the results of experimental work

The designed and carried out experiment has both methodological and cognitive value. It shows a relatively simple way to measure the attenuation of radiation emitted by grey body with a modified spectrum when passing through a specific gas with a defined thickness, temperature and pressure. The results of the measurements can be interpreted as follows. Infrared radiation from the moon, as a result of absorption by various gases dissolved in the atmosphere, especially by CO_2 and water vapour, changes its spectrum after reaching the Earth's surface. The "holes" in this spectrum overlaps with the carbon dioxide absorption bands in the cuvette. Of course, it can be argued whether this phenomenon can be called saturation of CO_2 concentration, because after all due to the overlapping of absorption bands, other gases also participate in it. However, the most important conclusion is that, unlike during the measurements in the laboratory, the additional layer of CO_2 with thickness of 50 cm at atmospheric pressure, placed on the Earth's surface, does not noticeably reduce the infrared radiation flux from the Moon, despite the fact that Moon's temperature is much higher than the temperature of carbon dioxide in this layer.

5. Proposal for further experiments

As was already mentioned, the flux of thermal radiation emitted by a solid, when passing through a gaseous media can decrease due to absorption in this gas only when the temperature of this gas is lower than the temperature of the solid. Therefore, active gases dissolved in the air at low altitudes, where the temperature is comparable to the surface temperature of the Earth, will not attenuate this radiation and only at higher altitudes, where the temperature is much lower, such attenuation may occur. Therefore, without going into all the complexities of the described phenomena, one can carry out a simple ideological experiment consisting in the measurement of the transmission of thermal radiation from the Earth by carbon dioxide in the cuvette (similarly to the conducted "moon" experiment) at appropriate subsequent heights. This can be accomplished by placing the cuvettes with focusing optics and measuring devices in the balloon basket, and after dropping subsequent portions of ballast, carry out measurements at the corresponding heights. Of course, the temperature and pressure in the cuvettes should be the same as outside of them, while the CO_2 concentration in the cuvette filled with carbon dioxide should always be 100%. In this way, assuming that carbon dioxide is evenly distributed throughout the globe, one can consider a layer with thickness equal to the length of the cuvette and estimate how much carbon dioxide is contained in it and how such amount of CO_2 at the considered height will reduce transmission of the radiation from the Earth.

After taking into account the results of the measurements carried out at different heights, a reliable model could be prepared to determine the effect of the increase of the concentration of CO_2 in the atmosphere on the decrease of transmission of thermal radiation from the lithosphere.

It is worth adding that in the balloon basket, in addition to the aforementioned apparatus and basic instruments for measuring air

parameters, it would also be possible to place a set of appropriate gas collection containers in order to accurately check the distribution of the concentration of individual gases in the atmosphere, and thus enable to provide more reliable data for currently used models.

It seems that the use of a balloon is an optimal solution, because it can be relatively easily to reach to all layers of the atmosphere that are important in climate processes and, additionally, the balloon stopping at the appropriate altitudes, should not introduce major distortion of gas concentrations in the surrounding atmosphere.

6. Conclusions

One could think that the cognitive value of the experiment is small and of little practical importance. Moreover, the measurements of transmission of infrared radiation from the Moon were done, not from the earth, as it is in case of the greenhouse effect. It is known that the Earth's temperature is much lower than Moon's temperature and therefore the emission spectrum of the Earth is slightly shifted towards longer wavelengths. Additionally, based on results presented in [7], in contrast to radiation from the Moon absorbed by the entire atmosphere, noticeable absorption of radiation from the Earth will occur only in the colder layers of the atmosphere located at higher altitudes. However, it should be noted that in both cases there is absorption of radiation of continuous spectrum, emitted by the grey body and passing through thick layers of the atmosphere. Thus, in both cases, the "widening" of absorption lines associated with saturation effects described at the beginning of this work will happen and the phenomena described in [5] will hace the impact on the absorption of radiation. Thanks to this, the presented work allows to look more critically at the frequently presented reality. As was already mentioned in the introduction, there is the conviction, that based on the formula (2) derived in paper [5], the increase of the concentration of absorbing gas in the air, regardless of its initial state, will cause strong increase of the absorption of the infrared radiation of continuous spectrum. Meanwhile, the experimental results obtained in this work, disprove this general theorem while it is the main basis for introducing restrictions on entities responsible for CO_2 emissions.

Nevertheless, disproval of one of the more serious arguments regarding this statement, based on the presented results of the measurement, it is not possible to determine what is the real impact of the increase of CO_2 concentration in the atmosphere on the decrease of the transmission of thermal radiation from the lithosphere. Only on the basis of measurements carried out in the proposed experiment, it would be possible to get closer to the true picture of reality.

Acknowledgements

The authors would like to thank Ph.D. Eng. Zbigniew Zawadzki from the Institute of Optoelectronics of the Military University of Technology for substantive discussion and comments during the preparation of the presented work.

References

[1] Andrews D. G.: An Introduction to Atmospheric Physics. Cambridge University Press, Cambridge 2010.
[2] Arrhenius S.: On the Influence of Carbonic Acid in the Air upon. Journal of Science 41/1896, 237–275.
[3] Beemt F.: On CO_2 and the global mean Earth's surface temperature. https://www.sciencetalks.nl/on-co2-and-the-global-mean-earths-surface-temperature/
[4] Covey C., Haberle R. M., McKay C. P., Titov D. V.: The Greenhouse Effect and Climate Feedbacks. Comparative Climatology of Terrestrial Planets, S. J. Mackwell, A. A. Simon-Miller, J. W. Harder, M. A. Bullock (eds.). University of Arizona Press, Tucson 2013, 163–179, [http://doi.org/10.2458/azu_uapress_9780816530595-ch007].
[5] Goody R. M., Yung Y. L.: Atmospheric Radiation: Theoretical Basis. Oxford University Press, New York 1989.
[6] Haman K.: Naturalne i antropogeniczne przyczyny zmian klimatu. Nauka 1/2008, 119–127.
[7] Harde H.: Was trägt CO_2 wirklich zur globalen Erwärmung bei Spektroskopische Untersuchungen und Modellrechnungen zum Einfluss von H_2O, CO_2, CH_4 und O_3 auf unser Klima. Books on Demand, Norderstedt 2011.
[8] Houghton J. T.: The Physics of Atmospheres. Cambridge University Press, Cambridge 2002.
[9] Jacobson M. Z.: Fundamentals of Atmospheric Modeling. Cambridge University Press, Cambridge 2005.
[10] Markowicz K.: Procesy radiacyjne w atmosferze – Materiały do wykładu. Instytut Geofizyki, Wydział Fizyki, Uniwersytet Warszawski, https://www.igf.fuw.edu.pl/m/documents/28/c7/28c7b491-658c-475a-9c03-fbb50707c9de/wykladradiacja.pdf
[11] Notholt J.: The Moon as a light source for FTIR measurements of stratospheric trace gases during the polar night: Application for HNO3 in the Arctic. Journal of Geophysical Research 99(D2)/1994, 3607–3614, [http://doi.org/10.1029/93JD03040].
[12] Randall D. A., Wood R. A., Bony S. et al.: Climate models and their evaluation, in Climate Change 2007: The Physical Science Basis – Assessment Report of the Intergovernmental Panel on Climate Change. Cambridge University Press, Cambridge 2007.
[13] Trenberth K. E., Fasullo J. T., Kiehl J.: Earth's global energy budget. Bulletin of the American Meteorological Society 90(3)/2009, 311–324, [http://doi.org/10.1175/2008BAMS2634.1].
[14] Vollmer M., Möllmann K.: Surface temperatures of the Moon: measurements with commercial infrared cameras. European Journal of Physics 33(6)/2012, 1703–1719, [http://doi.org/10.1088/0143-0807/33/6/1703].

Ph.D. Eng. Jan Kubicki
e-mail: jan.kubicki@wat.edu.pl

Dr. Eng. Jan Kubicki is a graduate of the Faculty of Technical Physics of the Military University of Technology. Currently works at the Institute of Optoelectronics of the Military University of Technology. He is the author or co-author of several dozen scientific publications in the field of laser physics, high power laser systems, laser spectroscopy, the interaction of laser radiation with matter and the use of pulsed electric discharges to modify metal surfaces. Author or co-author of technological studies and patents on the use of high-power laser pulses, pulsed electrical discharges in gases and liquids, and issues related to remote detection of alcohol vapors. Currently, he deals with remote detection of vapors and gases in open and closed spaces.

http://orcid.org/0000-0002-5191-7850

D.Sc. Eng. Krzysztof Kopczyński
e-mail: krzysztof.kopczynski@wat.edu.pl

D.Sc. Eng. Krzysztof Kopczyński is the director of the Institute of Optoelectronics of the Military University of Technology. In addition to managing the Institute, he is involved in research and teaching. He managed many domestic and foreign projects as part of KBN, NCBR, EU and EDA. Currently, he conducts research related to opto-electronic systems in the field of security and defense. He has won many gold medals and awards at the International Innovation Exhibitions in Moscow, Geneva and Brussels, as well as diplomas of the Minister of Science. He is the author of over 100 publications in Polish and foreign scientific journals. Member of SPIE International Society for Optics and Photonics, OSA Optical Society of America and EOS European Optical Society

http://orcid.org/0000-0002-3319-3940

D.Sc. Eng. Jarosław Młyńczak
e-mail: jaroslaw.mlynczak@wat.edu.pl

D.Sc. Eng. Jarosław Młyńczak is a university professor at the Institute of Optoelectronics of the Military University of Technology. He published dozens of articles in peer-reviewed scientific journals and many papers and communications at national and international conferences. He is also a co-author of 3 patents. He received 6 awards at international and national exhibitions of inventions SIIF, IWIS, IENA, BRUSSELS INNOVA. Currently, he conducts research in areas such as new active laser media, passive q-switches, laser heads for rangefinders, optoelectronic detection of chemical and biological contamination, remote alcohol detection as well as biometric identification of people.

http://orcid.org/0000-0002-0823-9302

otrzymano/received: 07.12.2019 *przyjęto do druku/accepted: 15.02.2020*

http://doi.org/10.35784/iapgos.909

CLASSIFICATION OF MULTIDIMENSIONAL POLARIZATION MICROSCOPY RESULTS IN THE TECHNOLOGY OF FORENSIC INTELLECTUAL MONITORING OF HEART DISEASES

Oleg Vanchulyak[1], Serhii Golub[2], Mariia Talakh[3], Vyacheslav Gantyuk[3]
[1]Bukovina State Medical University, Department of Forensic Medicine and Medical Law, Chernivtsi, Ukraine, [2]Cherkasy State Technological University, Department of Automated Systems Software, Cherkasy, Ukraine, [3]Yuriy Fedkovych Chernivtsi National University, Department of Computer Science, Chernivtsi, Ukraine

***Abstract**. The work combines methods of multidimensional polarization microscopy, statistical processing of data and inductive modeling with the purpose of constructing a methodology for creation of intelligent systems for multi-level forensic medical monitoring based on the example of the post-mortem diagnosis of coronary heart disease and acute coronary insufficiency. The task of classifying the results of the study of biological materials for obtaining a diagnosis was solved. To obtain informative features, a model of biological tissue of the myocardium was developed and the main diagnostic parameters were determined (statistical moments of 1–4 orders of coordinate distributions of the values of azimuths and the ellipticity of polarization and their autocorrelation functions, as well as wavelet coefficients of the corresponding distributions), which are dynamic due to its necrotic changes. The classification of these data was provided by constructing a deciding rule in the multi – raw algorithm of the GMDH. The effectiveness of the described methodology has been experimentally proved.*

Keywords: forensic medical monitoring, polarization microscopy, informative signs, classification

KLASYFIKACJA WYNIKÓW WIELOWYMIAROWEJ MIKROSKOPII POLARYZACYJNEJ W TECHNOLOGII INTELIGENTNEGO MONITOROWANIA CHORÓB SERCA W MEDYCYNIE SĄDOWEJ

***Streszczenie.** Praca łączy metody wielowymiarowej mikroskopii polaryzacyjnej, statystycznego przetwarzania danych i modelowania indukcyjnego w celu skonstruowania metodologii tworzenia inteligentnych systemów wielopoziomowego monitorowania w medycynie sądowej na przykładzie pośmiertnej diagnozy choroby wieńcowej i ostrej niewydolności wieńcowej. Wykonano zadanie sklasyfikowania wyników badań materiałów biologicznych w celu uzyskania diagnozy. Aby uzyskać cechy informacyjne, opracowano model tkanki biologicznej mięśnia sercowego i określono główne parametry diagnostyczne (momenty statystyczne 1–4 rzędów współrzędnych rozkładów wartości azymutów i eliptyczności polaryzacji oraz ich funkcji autokorelacji, a także jako współczynniki falkowe odpowiadających im rozkładów), które są dynamiczne z powodu jego zmian nekrotycznych. Klasyfikacja tych danych została zapewniona przez skonstruowanie decydującej reguły w algorytmie multi-raw GMDH. Skuteczność opisanej metodologii została eksperymentalnie udowodniona.*

Słowa kluczowe: monitoring medycyny sądowej, mikroskopia polaryzacyjna, znaki informacyjne, klasyfikacja

Introduction

Intelligent monitoring is a technology which provides information for decision-making processes, by organizing continuous observations and processing their results [1]. The main stages are to identify information about the objects' observation properties, which are needed to compare strategies during the decision-making, to identify the list of diagnostic parameters, which will be used for the formation of an array of input data (AID), to process and transform information by algorithms for synthesizing the models of the monitoring intellectual system (MIS). The set of the resulting classifier models is recorded in the base of model knowledge [2] and forms its hierarchical structure. It is always relevant to provide the AID informative, which is sufficient for constructing useful models by available methods and tools, which are implemented in the models synthesizer of MIS. Effective organization of research objects observations should involve of the latest scientific achievements in the subject area in which the monitoring technology is implemented.

The variety of medical monitoring facilities requires individual studies of the AID formation. The object of medical monitoring in this thesis are the processes of postmortem differentiation of coronary heart disease (CHD) and acute coronary insufficiency (ACI).

Cardiovascular diseases cause about a third part of the fatal consequences worldwide, taking the leading position among other causes of death [3,4]. Since 2000, cardiovascular diseases were the cause of 33.7% of the recorded deaths, and 42.5% among them were associated with CHD [5], in particular with sudden cardiac death due to ACI. The significant prevalence of ACI cases in the forensic practice and its suddenness, which causes suspicion of its violent nature, requires the use of objective and accurate methods. However, the ACI is difficult to diagnose through the non-specificity of macroscopic features, the necessity of using specific methods of coloring and through the role of the "human factor" [6].

At the same time, the task of operational establishing of the AI remains unresolved. The existing shortage of modern, objective methods of determining the AI encourages the search and development of new technologies for monitoring the pathological changes in the human myocardium.

Methods of multidimensional polarization microscopy make it possible to formulate a list of informative indicators for the AID and to obtain their numerical characteristics containing new, objective information about the dynamics of changes in laser polarimetric images of the morphological structure of biological tissues. They have been successfully tested in solving such tasks as determining the prescription of death, forming hematomas, diagnosing the time of emergence of injuries and whether they were intra vitam injuries, or not [7, 8]. In particular, the analysis results of distributions of polarization states (azimuths α and ellipticity β) and phases (δ) of light oscillations of myocardial images for the determination and displaying in numerical form of their changes associated with sources of AI in AID are quite informative [9, 10].

For the exploratory processing of the observation results obtained in this way and the construction of additional informative features, statistical, correlation, and wavelet analysis methods, followed by the definition of sensitivity (*Se*), specificity (*Sp*), and balanced accuracy (*Ac*) are used [11, 12].

Thus, a vector of characteristics that describes the properties of each of the studied objects is formed. The set of numerical characteristics of feature vectors forms the AID. On its basis, the problem of classifying objects is solved by formation a resolving rule, which is used for putting characteristics vector of certain disease in correspondence to each disease. This decision rule is built by the models synthesizer of MIS. Now more than 20 algorithms for synthesis of models (ASM) were implemented in the synthesizer of MIS. These are the basic algorithms of the GMDH [13], GMDH-like algorithms, neural networks of various topologies, genetic and hybrid algorithms, etc. The synthesizer provides a choice of the algorithm for synthesis of models

adaptively to the properties of the AID. The choice is based on the results of a sequential test of each of the ASM based on the quality of obtained model.

Thus, the process of disease diagnosis contains the stages of obtaining biological material, the formation of a list of its characteristics, the obtaining of a list of numerous characteristics, the formation of an array of input data, the construction of a decision rule by the synthesizer of MIS models, the classification of AID features, and interpretation of the results of the forensic expert classification. Models synthesizer used in the typical form, and the results of diagnostics depend on process of the AID formation. The studies results of biological samples using multidimensional polarization microscopy contain signs of the CHD and AID and allow to receive additional information for their diagnosis. Therefore, the study of the process of using multidimensional polarization microscopy for the formation of numerical features of the ACI and the synthesis of model-classifiers is relevant. This technology makes it possible to increase the accuracy and reliability, which can ensure the forensic medical expert's decision-making process as to differentiation of the cause of the patient's death.

1. Purpose and objectives of the study

Step 1. Obtaining biological material

The basic formulated hypothesis was that a list of informative features for classification of diseases by information technology of multi-level intellectual monitoring in the forensic medical examination relating to the causes of patients' death provoked by cardiovascular diseases should be obtained by using multidimensional polarization microscopy methods for image processing of myocardium histological sections. The aim of the work is to study the process of forming a list of characteristics and forming an AID for the classification of the causes of patients' death for forensic medical examination by sequential application of multidimensional polarization microscopy methods, statistical data processing and inductive modeling.

2. Results of the study

At first, the classes have been formed and classification features of research objects have been allocated. For this purpose, three groups have been distinguished and the criteria for including objects in the classes and the criteria for their exclusion have been developed. All the dead persons were residents of the city of Chernivtsi and the region, which, according to relatives and results of forensic histological examination, did not have a significant systemic disease and they were not registered in this regard.

The parts of the myocardium of the people's corpses were investigated. The samples were carried out from various anatomical structures, including the sites of the membrane, the right and left ventricular walls, the right and left atrium walls, as well as the apex region of the heart. Blocks with a volume of 1 cm^3 were formed, which were cut directly after sampling by freezing the microtome into sections of 30 ± 5 μm thick.

The characteristics of the classes of investigated objects are presented in the Table 1.

Stage 2. Formation of informative features of research objects

2.1. Multidimensional polarization microscopy of histological sections of the myocardium

Polarization microscopy was carried out at the standard location of the Stokes polarimeter [14].

The polarization irradiator consisted of two quarter-wave plates (Achromatic True Zero-Order Waveplate) and a polarizer (B + W Kaesemann XS-Pro Polarizer MRC Nano).

The myocardium cut was sequentially probed with a laser beam with the following types of polarization: linear with azimuths of 0°, 90°, 45° and right circulation (⊗). Polarization images of the myocardium sample with the help of a polarizing micro-len 7 (Nikon CFI Achromat P, focal length 30 mm, numerical aperture 0.1, magnification 4x) were projected into the plane of the photosensitive pad ($m \times n$ = 1280×960 pixels) of the CCD camera Imaging Source DMK 41AU02.AS, monochrome 1/2 "CCD, Sony ICX205AL (progressive scan) resolution – 1280×960, the size of the photosensitive pad is 7600×6200 μm, the sensitivity is 0.05 1x, the dynamic range is 8 bit. The analysis of images of the myocardial samples was carried out with the help of a polarizer and Quarter-wave plate.

Calculations of the coordinate distributions $V_i(p \times k)$ – Stokes vector parameters, $\alpha(p \times k)$ – polarization azimuths, $\beta(p \times k)$ – polarization ellipticities characterizing the microscopic images of the myocardial sections, were performed by using commonly known algorithms [15]:

$$\begin{aligned} V_{i=1}^{0;45;90;\otimes} &= I_0^{0;45;90;\otimes} + I_{90}^{0;45;90;\otimes} \\ V_{i=2}^{0;45;90;\otimes} &= I_0^{0;45;90;\otimes} - I_{90}^{0;45;90;\otimes} \\ V_{i=3}^{0;45;90;\otimes} &= I_{45}^{0;45;90;\otimes} - I_{135}^{0;45;90;\otimes} \\ V_{i=4}^{0;45;90;\otimes} &= I_{\otimes}^{0;45;90;\otimes} + I_{\oplus}^{0;45;90;\otimes} \end{aligned} \tag{1}$$

here $I_{0;45;90;135;\otimes;\oplus}$ is the radiation intensity transmitted by a linear polarizer with azimuth of rotation 0°, 45°, 90°, 135° , and right (⊗) and left (⊕) circularly polarized filter.

Determining, according to (2), in each pixel of the photosensitive pad the set of Stokes parameters one can obtain the azimuth and polarization ellipticity at the corresponding points of the image of the native myocardial section:

$$\begin{aligned} \alpha &= 0.5 arctg \frac{V_{i=3}}{V_{i=2}} \\ \beta &= 0.5 \arcsin \frac{V_{i=4}}{V_{i=1}} \end{aligned} \tag{2}$$

Figure 1 illustrates a series of polarization images of an optically anisotropic matrix (in the crossed planes of transmission of the polarizer and the analyzer of myocardial tissue samples for all groups.

Table 1. Characteristics of classes of objects under study

Class	Number of objects in the group	Inclusion criteria	Exclusion criteria
1. ACI	150	a) people's corpses of two genders aged from 18 to 45 years; b) histochemically confirmed by ACI	a) the presence of anamnestic, macroscopic, microscopic, including histochemical data of another pathology of the myocardium; b) laboratory confirmed presence of some exogenous intoxication
2. Chronic ischemic heart disease	160	a) people's corpses of two genders aged from 18 to 45 years; b) macroscopic signs: small focal myocardiosclerosis, the presence of atherosclerotic plaques in the lumen of the coronary arteries, hypertrophy of the ventricle left wall (wall thickness 1.6–2.0 cm), hypertrophy of the papillary muscles, shortening of the mitral valve tendon	a) postinfarction myocardiosclerosis; b) the presence of anamnestic, macroscopic, microscopic, including histochemical data of another pathology of the myocardium; c) laboratory confirmed presence of some exogenous intoxication
3. Control group	20	a) people's corpses of two genders aged from 18 to 45 years; b) violent death with an absent agonal period	a) the presence of anamnestic, macroscopic, microscopic, including histochemical data of another pathology of the myocardium; b) identification of agony features characteristic during the time of dying; c) laboratory confirmed presence of some exogenous intoxication

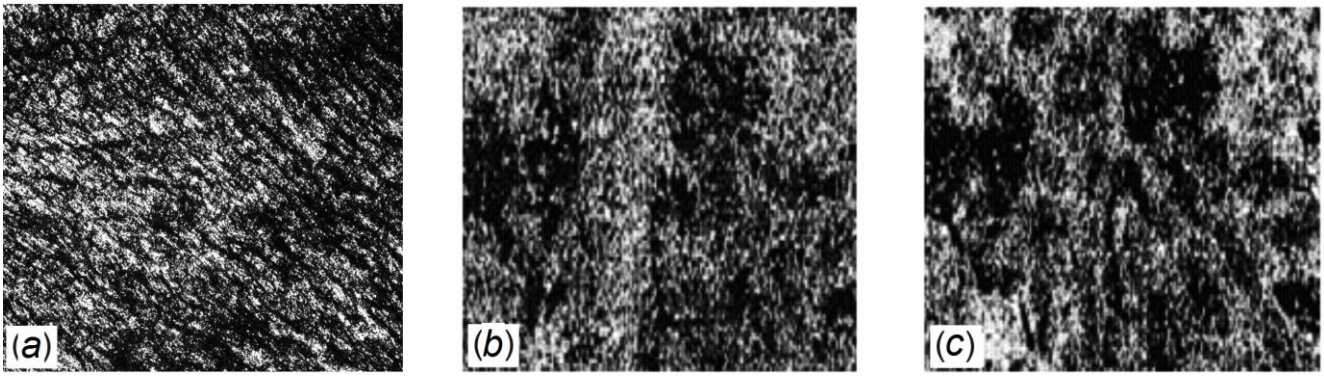

Fig. 1. Laser images of the fibrillar network of the histological section of the myocardium: (a) – an element of class 1; (b) an element of class 2; (c) an element of class 3

2.2. Examination of myocardial tissue

The following model representations are based on the description of the mechanisms of optical anisotropy of the myocardium [16, 17].

1. Amino acids and the polypeptide chains formed by them (the primary structure of the protein) have circular birefringence or optical activity and are characterized by the following matrix operator:

$$\{A\} = \begin{pmatrix} 1 & 0 & 0 & 0 \\ 0 & a_{22} & a_{23} & 0 \\ 0 & a_{32} & a_{33} & 0 \\ 0 & 0 & 0 & 1 \end{pmatrix} \tag{3}$$

where $a_{ik} = \{a_{22} = a_{33} = \cos 2\theta\}$, here θ – the angle of rotation of the polarization plane of the light beam relative to the plane of incidence.

Thus, by recording the polarization azimuth of polarization map, it is possible to obtain information about the manifestations of optically active structures of the proteins primary structure that form the morphological structure of the myocardium.

2. Fibrillar (secondary structure) protein networks, which are formed by polypeptide chains, have linear birefringence. An optical manifestation of the morphological structure of the fibrillar network is the formation of the coordinate distribution of intensity in the plane within the microscopic image of the histological section of the myocardium. Optical manifestations of such a mechanism are amply described by the following matrix operator:

$$\{B\} = \begin{pmatrix} 1 & 0 & 0 & 0 \\ 0 & b_{22} & b_{23} & b_{24} \\ 0 & b_{32} & b_{33} & b_{34} \\ 0 & b_{42} & b_{43} & d_{44} \end{pmatrix} \tag{4}$$

where $b_{ik} = \begin{cases} b_{22} = \cos^2 2\gamma + \sin^2 2\gamma \cos\varphi \\ b_{23} = b_{32} = \cos 2\gamma \sin 2\gamma (1 - \cos\varphi) \\ b_{33} = \sin^2 2\gamma + \cos^2 2\gamma \cos\varphi \\ b_{24} = -b_{42} = \sin 2\gamma \sin\varphi \\ b_{34} = -b_{43} = \cos 2\gamma \sin\varphi \end{cases}$

here γ – the direction of laying of fibrils, which determines the orientation of the optical axis; φ – phase shift between linearly polarized orthogonal components of the amplitude of the light beam.

Thus, by recording the elliptical polarization of polarization map, information can be obtained about the manifestations of the properties of fibrillar networks (networks) that form the secondary structure of the morphological structure of the myocardium.

3. Necrotic changes in the morphological structure of the myocardium lead to a structural and biochemical transformation of the primary and secondary structure of its protein components. Optically, such processes lead to changes in the coordinate distributions of azimuth maps (biochemical processes) and ellipticity (orientational changes in fibrillar networks) of microscopic images polarization within the histological sections of the myocardium.

4. The main idea of differentiation of myocardial tissue samples of people who died as a result IHD or ischemic heart disease lies in the possibility of multi-parametrical ($r \equiv \left[\begin{pmatrix} \alpha \\ \beta \end{pmatrix}\right]$) objectification of the microscopic images analysis of histological sections within the framework of statistical, correlation and wavelet analysis. Statistical analysis of the results was carried out by calculating statistical moments of 1, 2, 3, and 4 orders of magnitude (mean, variance, asymmetry, kurtosis) of digital camera pixels of the Stoks-Polarimeter which records the native cut and polarization-filtered microscopic images of the myocardium.

The correlation analysis was performed by calculating the auto-correlation function by the coordinate displacement along the rows of digital camera pixels of the coordinate distributions according to the known relation. In order to quantify the auto-correlation function *K(r)*, we used calculations of the statistical moments of the second (relation (4)) and the fourth (relations (6)) orders (here and further correlation moments K_2 and K_4). The wavelet analysis was performed for local estimation of coordinate distributions [18]. As an analytical probe, a special mathematical function (wavelet function) was used, which has a finite basis both in the coordinate and frequency space. Using the wavelet function, the values distribution of the calculated parameter *q* that characterizes the image structure of the native myocardium slice was decomposed into a mathematical series representing the convolution (correlation) of the displacement parameters (b) and scaling (a) and certain coefficients (wavelet coefficients). The result of the wavelet transformation of the one-dimensional parameter dependence is a two-dimensional array of amplitudes of the wavelet coefficients *W(a,b)*. The wavelet analysis makes it possible to investigate the multi-scale structure of polarization maps, which are interrelated with the morphological structure of myosinovirus myocardial networks.

To characterize the informative value of the diagnostic method the objective parameters, called operational characteristics were used. They include sensitivity (*Se*), specificity (*Sp*) and balanced accuracy (*Ac*) [10]. Sensitivity shows what will be the proportion of expert cases in which this study will give a positive result. The higher sensitivity of the test indicates that with the help of it the disease will be diagnosed more often, hence it is more effective. Having the determined specificity, it is possible to assume a priori what is the proportion of healthy individuals among which this study will give a negative result. The higher specificity of the method indicates reliability of the expert conclusion. So the higher specificity, thus it also proves the effectiveness of the test. Accuracy (balanced accuracy) shows how many correct results were obtained during the application of this investigation method. This criterion is also called diagnostic effectiveness.

Stage 3. Formation of an array of input data (AID)

Thus, the list of informative features contains statistical moments of 1–4 orders of coordinate distributions of the azimuths and ellipticity values of of polarization and their auto-correlation functions, as well as the wavelet coefficients of the corresponding distributions. An array of input data (AID) was formed by calculating the multiple specific characteristics and their combination into a two-dimensional array of data in accordance with methodology described here [1]. The numerical characteristics of the image of an individual biological sample make it possible to form a line in a two-dimensional AID table – the observation point in the multidimensional feature space. The AID contained 306 observation points, which were used to construct the model and 24 points – for testing the model.

Each observation point was classified expertly according to Table 1 – 1) ACI 2) CHD and 3) control without the features of these diseases. Affiliation to class 1 was affected by "+10", to class 2 – "10", in class 3 – "0". Table 2 shows a fragment of an array of input data, on the basis of which the model was synthesized.

Under the research conditions, the model-classifier provided the correct results of disease identification at all observation points. This means that the AID is quite informative. And the hypothesis of the formation of the AID based on the results of the consistent application of multidimensional polarization microscopy methods has been experimentally confirmed.

Table 2. Fragment of an array of input data

Class	x_1	x_2	x_3	x_4	x_5	…	x_{144}
10	0.6856	0.0901	0.2901	1.1917	0.2603	…	0.4404
10	0.6805	0.0901	0.2907	1.1914	0.2593	…	0.4416
10	0.6769	0.0902	0.2895	1.2127	0.2606	…	0.4425
10	0.6867	0.0902	0.2899	1.1885	0.2595	…	0.4399
…	…	…	…	…	…	…	…
-10	0.633	0.1099	0.2401	1.565	0.2301	…	0.3202
-10	0.6302	0.1010	0.2399	1.5279	0.2307	…	0.3200
-10	0.6282	0.1101	0.2396	1.565	0.2297	…	0.3196
-10	0.6264	0.1010	0.2391	1.5386	0.2295	…	0.3204
-10	0.6284	0.1100	0.2399	1.5371	0.2305	…	0.3205
…	…	…	…	…	…	…	…
0	0.1601	0.3398	0.6127	0.1300	0.1301	…	0.2099
0	0.1598	0.3403	0.6099	0.1302	0.1300	…	0.2099
0	0.1599	0.3398	0.6117	0.1300	0.1302	…	0.2100
0	0.1600	0.3398	0.6049	0.1300	0.1300	…	0.2100
0	0.1602	0.3394	0.6086	0.1299	0.1299	…	0.2101
…	…	…	…	…	…	…	…

Stage 4. Synthesis of model-classifiers

Model-classifiers were built using the multi-row algorithm of the GMDH [13]. Several algorithms for the synthesis of models implemented in the MIS were sequentially tested. Based on the test results, the ASM was selected, which provides the best performance characteristics of the model-classifier by the regularity criterion on the examination sequence of observation points.

The table 3 shows the results of the research. The value of the image indicated the belonging of the observation point to one of the 3 classes. The modeling result reflects the calculated value of the image.

Table 3. Results of testing the model-classifier on the examination (test) sequence

Class	Real value of affiliation	Real value of affiliation
1	10	9.99
1	10	10
1	10	9.99
1	10	10
1	10	9.99
	…	…
2	-10	-10
2	-10	-10
2	-10	-10
2	-10	-9.99
2	-10	-10
	…	…
3	0	-37
3	0	-30
3	0	-51
3	0	-99
3	0	-50

3. Conclusions

The use of monitoring information systems to provide information for decision-making processes in the field of forensic medical examination allows to solve successfully the classification problems of the samples. It was shown that the use of statistical processing of the results of the myocardial tissue studies by the methods of multivariate polarization microscopy allows to obtain statistical moments of 1, 2, 3, and 4 orders, which are informative and can be used to form the AID during the model-classifiers construction of the test samples.

The effectiveness of using inductive modeling methods, in particular the multi-row algorithm GMDH, is experimentally confirmed. It is used to synthesize the classifier models based on the AID with the results of image processing of myocardium sections by polarization microscopy methods.

A set of methods for obtaining biological samples, the formation of informative features, the construction of model-classifiers and the interpretation of modeling results are forming the information technology of intellectual forensic medical monitoring.

References

[1] Bachinskyi V. T., Boychuk T. M., Ushenko A. G., Dubolazov A. V., Vanchuliak O. Ya., Ushenko Yu. A., Ushenko V. A.: Laser polarimetry of biological tissues and fluids. LAP Lambert Academic Publishers, 2017.
[2] Davis C. S.: Statistical Methods of the Analysis of the repeated measurements. Springer-Verlag, New York 2002.
[3] Dubolazov O. V., Ushenko A. G., Bachynsky V. T. et al.: On the feasibilities of using the wavelet analysis of Mueller matrix images of biological crystals. Advances in Optical Technologies 2010, 162832.
[4] Garazdyuk M. S., Bachinskyi V. T., Vanchulyak O. Ya., Ushenko A. G., Dubolazov O. V., Gorsky M. P.: Polarization-phase images of liquor polycrystalline films in determining time of death. Appl. Opt. 55/2016, 67–71.
[5] Gerrard A., Burch J. M.: Introduction to Matrix Methods in Optics. Dover Publications, Inc., New York 1994.
[6] Golub S. V.: Multilevel modeling in environmental monitoring technologies. ChNU named after Bogdan Khmelnitsky, Cherkassy 2007.
[7] Ivakhnenko A. G.: Inductive method of self-organization of models of complex systems. Science. Thought, Kiev 1981.

[8] Lopera G., Curtis A. B.: Risk stratification for sudden cardiac death: current approaches and predictive value. Curr. Cardiol. Rev. 5/2009, 56–64.
[9] Mozaffarian D., Benjamin E. J., et al.: Heart disease and stroke statistics–2015 update: a report from the American Heart Association. Circulation 131(4)/2015, 329–322.
[10] Petrie B. Sabin: Medical Statistics at a Glance. Blackwell Publishing, 2005.
[11] Rubart M., Zipes D.: Mechanisms of sudden cardiac death. Journal of Clinical Investigation 115(9)/2005, 2305–2315.
[12] Sakhnovskiy M. Yu., Ushenko Yu. O., Ushenko V. O., Besaha R. M., Pavlyukovich N., Pavlyukovich O.: Multiscale polarization dianostics of birefringent networks in problems of necrotic changes dianostics. Proc. SPIE 10612, 2018, 106121K.
[13] Ushenko G., Dubolazov A.V., Ushenko V. A., Ushenko Yu. A., Pidkamin L. Y., Soltys I. V., Zhytaryuk V. G., Pavlyukovich G. N.: Mueller-matrix mapping of optically anisotropic fluorophores of molecular tissues in the diagnosis of death causes. Proc. SPIE 9971, 2016, 99712L.
[14] Ushenko Y. A., Arkhelyuk A. D., Sidor M. I., et al.: Laser polarization autofluorescence of endognous porphyrins of optically anisotropic biological tissues and fluids in diagnostics of necrotic and pathological changes of human organs. Appl. Opt. 53/2014, B181–B191.
[15] Ushenko Yu. A., Sidor M. I., Pashkovskaia N., Koval G. D., Marchuk Yu. F., Andreichuk D.: Laser polarization-variable autofluorescence of the network of optically anisotropic biological tissues: diagnostics and differentiation of early stages of cancer of cervix uteri. Journal of Innovative Optical Health Sciences 7(6)/2014, 1450024.
[16] Ushenko Yu. A., Bachynsky V. T., Vanchulyak O. Ya., Dubolazov A. V., Garazdyuk M. S., Ushenko V. A.: Jones-matrix mapping of the complex degree of mutual anisotropy of birefringent protein networks during the differentiation of myocardium necrotic changes. Appl. Opt. 55/2016, B113–B119.
[17] Ushenko Y. O., Dubolazov O. V., Karachevtsev A. O., Gorsky M. P., Marchuk Y. F.: Wavelet analysis of Fourier polarized images of the human bile. Appl. Opt. 51/2012, 133–C139.
[18] Van der Werf C., Hofman N., Tan H. L., et al.: Diagnostic yield in the young: the experience of a tertiary referral center in The Netherlands Heart Rhythm., 7(10)/2010, 1383–1389.
[19] Zhiriakova I. A., Golub S. V.: A new approach to the conceptualization of knowledge. Technical sciences and technology 2/2015, 78–82.

D.Sc. Oleg Vanchulyak
e-mail: sudmed@bsmu.edu.ua

Bukovina State Medical University
D.Sc. (medical), Associate Professor of Forensic Medicine and Medical Law. Research interests: forensic traumatology, diagnostics of limitation of onset of death, establishment of limitation and survivability of causing bodily injury, use of methods of correlation optics in forensic medicine.. Author of nearly 250 publications in this research area.

http://orcid.org/0000-0003-0243-1894

D.Sc. Serhii Golub
e-mail: fpkpk@ukr.net

Cherkasy State Technological University
D.Sc. (technical), Professor, of the Department of Automated Systems Software. Research interests: Information technologies of intellectual monitoring, inductive modeling, intellectual analysis of texts, systems of artificial intelligence, systems and methods of decision-making. Author of nearly 300 publications in this research area.

http://orcid.org/0000-0002-5067-6848

Ph.D. Mariia Talakh
e-mail: flaredreem@gmail.com

Yuriy Fedkovych Chernivtsi National University.
Ph.D. (biological), Assistant, Department of Computer Science. Research interests: methodology of creation of automated systems of ecological monitoring, geoinformation systems, intellectual analysis of geospatial data. Author of nearly 50 publications.

http://orcid.org/0000-0002-5523-6120

Ph.D. Student Vyacheslav Gantyuk
e-mail: Vgantyuk2@gmail.com

Yuriy Fedkovych Chernivtsi National University.
Ph.D Student at Department of Computer Science. Research interests: Data science methodology in life sciences.

http://orcid.org/0000-0003-0792-5113

otrzymano/received:15.11.2019 *przyjęto do druku/accepted: 15.02.2020*